University of
Reading

The Structure and Negative Thermal Expansion of Low-Dimensional Compounds

A thesis submitted for the degree of Doctor of Philosophy

Department of Chemistry

Edward Bilbé

September 2010

Declaration

I confirm that this is my own work and the use of all material from other sources has been properly and fully acknowledged.

Edward Bilbé

Abstract

The structures of mixed-metal group 11 cyanides of the form $(M_xM'_{1-x})CN$ (M= Cu, Ag, Au) have been determined using a combination of X-ray Bragg and total neutron diffraction, together with vibrational spectroscopy. In the gold- containing systems, only the line phases, $(Cu_{⅔}Au_{⅓})CN$, $(Cu_{½}Au_{½})CN$ and $(Ag_{½}Au_{½})CN$ are formed, whereas in $(Cu_xAg_{1-x})CN$, a solid solution exists with $(0 < x < 1)$. All the structures consist of one-dimensional chains in which, in the gold-containing systems and $(Cu_{0.50}Ag_{0.50})CN$, the metal atoms and cyanide groups order. The chains are packed on a hexagonal lattice to form, for the gold-containing compounds, the AuCN structure type and, for the copper-silver phases, the AgCN structure type. All these materials exhibit negative thermal expansion along the chain direction.

X-ray and total neutron diffraction studies show that "$Pd(CN)_2$" and "$Pt(CN)_2$" are nanocrystalline materials containing small sheets of vertex-sharing square-planar $M(CN)_4$ units (dimensions ~30 Å × 30 Å). The $Pd(CN)_2$ nanocrystallites are terminated by water and the $Pt(CN)_2$ nanocrystallites by ammonia, in addition to terminal cyanide groups. For these small particles, structural models predict compositions of $Pd(CN)_2{\cdot}xH_2O$ and $Pt(CN)_2{\cdot}yNH_3$ ($x \approx y \approx 0.29$), in good agreement with values obtained from thermal analysis and consistent with vibrational spectroscopy measurements. Related compounds, $Pd(CN)_2{\cdot}pNH_3$ and $Pt(CN)_2{\cdot}qH_2O$, in which the terminating groups are exchanged were also prepared. The sheet sizes, determined from modelling of the X-ray diffraction patterns, range from ~10 Å × 10 Å ($y \sim 0.67$) to ~80 Å × 80 Å ($p = q \sim 0.12$), varying with the method of synthesis. Removal of the final traces of water or ammonia by heating results in decomposition of the compounds to Pd and Pt metal, making it impossible to prepare the simple cyanides, $Pd(CN)_2$ or $Pt(CN)_2$, by this method.

Acknowledgements

Firstly I would like to thank Ann and Simon, who, from the beginning had faith in my ability to do some good science and so took me on to do a PhD. I believe that Simon is the cleverest person I am ever likely to know. His enthusiasm, experience and ability to explain things has driven my understanding throughout the project. Ann has shaped my ideas by posing the right questions to fortify my theories or expose their limitations. Her determination to get things finished without allowing standards to slip or untruths be told has ensured that my work is of a quality that I can be proud of. Without either of them I doubt this thesis would be worth reading.

I would like to thank Laura my fiancée who has stood by me and helped me especially through the first year, giving me the strength to carry on. My parents have also always been there for me and have kept my home life under control.

Thanks should also go to my Physical Family, Alex Hannon who taught me a great deal about neutron diffraction and showed me how to reduce and correct GEM data. He is a great beamline scientist and was always on-hand to help even in the wee hours of the morning. We will always see the world very differently and I hope that he thinks of me as less of an idiot now than when I started; either way I will always respect his work. The other members of this family, Emma Barney, Matt Tucker, Dave Keen and Andrew Goodwin, have all shown interest in my work and been sociable colleagues. The RAL and the BCA spring meetings would not have been the same without you.

Many thanks go to Alexander Pohl who showed me the ropes in the lab on the first day of my project, and was, until he left, always on hand with help and advice. I would also like to thank Elena who has helped keep me sane during my final year and for the Raman data she collected for me. Over the years I have also had dealings with a fair few project students and although I hope to have helped them, they have also been of help to me; some more than others! They

have all made the office and lab a brighter place even if they did “eat” every Monday and Tuesday during term time. I would especially like to thank Laura Jackaman for her work on copper and silver dicyanamides, which is not presented. I promise to get this work finished so it can be published soon.

This work would not have been possible without the help and moral support of the following people, in alphabetical order to stop fighting…

Allen M for his wise words of advice and encouragement when I was feeling down in my first year. Also for AA spectroscopy. Alix C for understanding synchrotrons and all their “joy”. Ann C for solving the structures of the single crystals I produced (sorry about the K_2SO_4), proof reading and for art and religious discussions. Ben S who has always been on hand with a pencil and a beer to keep me sane. Brian H especially for bending the “no chemicals in the glass blowing workshop” rule when I needed to get wet $(NH_4)_2Pt(CN)_4$ sealed in a tube. Cath B for sanity, it has often been in short supply. Chris B for help with the black art that is organic chemistry. Claire M for cake. Dave S for proof reading and help with error analysis. Gez G for reminding me that it can always be worse than it is. John S for mathematical terminology and promoting the use of graphs. Judy B for always being so very helpful. Junjuda U for her help preparing palladium and platinum compounds and for coming to Daresbury. Mark McC who fixed that which was broken and made things which couldn’t be bought, at least not at a price I was willing to pay! Marc M for spelling and grammar, although at times your suggestions have been fewer than helpful. Mike A from Sedimentology who ran my powder X-ray diffraction samples until the opening of the CAF lab. Simon H for a better appreciation of red wine and coffee and also for the reminders that science is fun as well as interesting. Philip M for having shown me that it is important to maintain standards.

Table of Contents

Chapter 1: Introduction

Chapter 2: Experimental Methods and Data Handling

Chapter 3: Preparation, Characterisation and Thermal Expansion Properties of Mixed Copper, Silver and Gold Cyanides, ($M_xM'_{1-x}$)CN

Chapter 4: The Structures of Mixed Copper, Silver and Gold Cyanides, $(M_xM'_{1-x})CN$

Chapter 5: The Structures of Nanocrystalline $Pd(CN)_2$ and $Pt(CN)_2$ 126

Chapter 1: Introduction

1.1 Transition-Metal Cyanides

Cyanide compounds have a long history including the first cheap stable blue pigment, known as Prussian Blue, $Fe_4(Fe(CN)_6)_3{\cdot}xH_2O$, which was used by European painters from 1709.[1] Cyanides have been of scientific interest from this point forward with many new cyanide compounds being synthesised. More recently a group of compounds, Prussian Blue analogues, have been shown to exhibit interesting magnetic behaviour which is dependent on their composition.[2] For example, $Cr_5(CN)_{12}{\cdot}10H_2O$ has a high Curie temperature, T_C = 240 K,[3] as does $V[Cr(CN)_6]_{0.86}{\cdot}2.8H_2O$, which is one of the two room-temperature organometallic magnets with $T_C < 315(5)$ K.[4] The other is $V(C_2(CN)_4)_x{\cdot}y(CH_2Cl_2)$, which is magnetic until it decomposes at 350 K.[5]

Many cyanide compounds, especially those containing platinum and gold, are noted for their luminescent properties. Most of the alkali-metal and alkaline-earth salts of tetracyanoplatinates fluoresce strongly under ultraviolet light, as do their hydrates.[6] Three of the four polymorphs of $Zn[Au(CN)_2]_2$ are luminescent. All four are constructed from tetrahedral Zn^{2+} linked together by linear $[Au(CN)_2]^-$ units to form diamond-like networks. These networks then interpenetrate to different degrees which changes the Au···Au distances over the range 3.11-3.33 Å. The emission energies are related to the Au···Au distances in the structures and also change on exposure to ammonia vapour.[7] Interestingly, a study of the family of compounds $(NH_3)_nM[M'(CN)_2]_2{\cdot}1\frac{1}{2}H_2O$, where M = Ni, Pd or Pt and M′

= Ag or Au, found that although $(NH_3)_4Pt[Au(CN)_2]_2\cdot1½H_2O$ is luminescent at 77 K, the isostructural silver salt is not luminescent at all. The other members of this family are also not luminescent.[8] Luminescence is not restricted to those cyanide materials just containing platinum or gold however. Silver cyanide complexes, all with Ag···Ag distances shorter than 3.33 Å, have also been shown to exhibit luminescence.[9] Both $La[Ag(CN)_2]_3\cdot3H_2O$ and $La[Au(CN)_2]_3\cdot3H_2O$ contain short metal-metal distances of 3.359(1) and 3.332(1) Å respectively, and are luminescent.[10] Of greater significance, is that by preparing mixed-metal samples, $La[Ag_{1-x}Au_x(CN)_2]_3\cdot3H_2O$ with different silver to gold ratios, the emission wavelength can be tuned and that the luminescence of the mixed compounds is stronger than that of the parents.[11] In order to understand these complex cyanide systems, there has recently been renewed interest in the “simple” cyanides, such as copper cyanide.[12] A further property of both simple and complex cyanide materials, which is of great relevance to this work, is that many of these cyanide materials demonstrate Negative Thermal Expansion (NTE), which is discussed in greater detail in Section 1.3.

1.1.1 Types of Cyanide Compounds

Cyanide compounds can be classified into two broad categories. The first group contains ionic cyanides, the simplest of which contain CN^- anions. More complex ionic cyanides, such as $KAg(CN)_2$, contain larger anions. In this example, the linear anion $[Ag(CN)_2]^-$ contains cyanide groups bound to the transition-metal *via* the carbon atoms.[13] The ionic cyanide compounds are often water soluble crystalline materials and the anions present in the solid are often stable in solution.[14] Indeed, concentrated aqueous solutions containing free CN^- anions are one of the few solvents which will dissolve palladium, platinum and gold through the formation of $[Pd(CN)_4]^{2-}$, $[Pt(CN)_4]^{2-}$ and $[Au(CN)_2]^-$ ions, respectively. Both the solids and their solutions are toxic and because transition-metal-cyanide anions are stable in solution, ionic cyanides can provide a pathway for heavy metals into the body, posing chronic health problems.

The second group of cyanide compounds are covalently bonded framework materials, such as the family of Prussian Blues, $Fe_4(Fe(CN)_6)_3{\cdot}xH_2O$, in which the most prominent mode of cyanide binding is $\mu_{1,2}$ bridging. The structures of these cyanide compounds are largely determined by the preferred geometry of the metal centres, with octahedral $[Fe(CN)_6]^{3-}$ in Prussian blue and tetrahedral $[Zn(CN)_4]^{2-}$ in $Zn(CN)_2$ both giving rise to three-dimensional (3-D) frameworks. In the case of Prussian Blues, the void space within the framework is occupied by water, (Figure 1.1(a)).[15] Zinc cyanide, on the other hand, has an interpenetrating structure consisting of two identical diamond-like frameworks with each occupying the void space in the other (Figure 1.1(b)).[16]

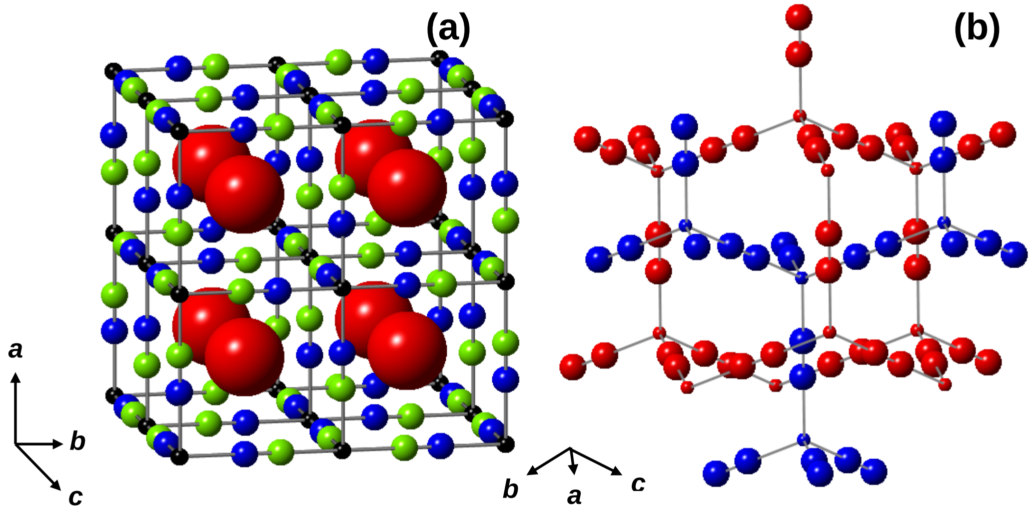

Figure 1.1(a) The average structure of Prussian Blue, $Fe_4(Fe(CN)_6)_3 \cdot xH_2O$ (Key: Iron (black), carbon (green), nitrogen (blue) and oxygen from disordered water molecules (red), hydrogen atoms have been excluded for clarity). (b) the structure of $Zn(CN)_2$, one diamond network is shown in red and the other is shown in blue to emphasise the interpenetration in this structure.

Cyanides of transition-metal ions with d^8 electron configuration, such as Ni^{2+}, would be expected to have structures incorporating square-planar units and indeed, $Ni(CN)_2$ does have a sheet structure based on 4,4 nets, (Figure 1.2(a)).[17] Both Ag^+ and Au^+, with d^{10} configuration, often adopt linear geometry and both AgCN and AuCN have structures based on infinite chains. (Figure 1.2(b)).[18-19]

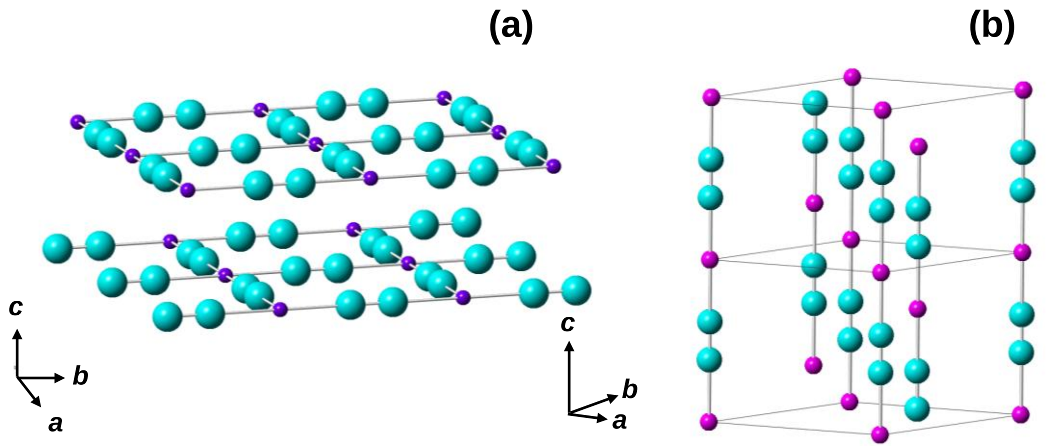

Figure 1.2 (a) two sheets from Ni(CN)$_2$, and (b) the structure of AgCN. (Key: Nickel (purple), silver (pink), and head-to-tail disordered cyanide (cyan)).

In mono-metallic systems, near equality of the M-C and M-N bond lengths is the rule rather than the exception and head-to-tail disorder of the C≡N group is very common.[20] A convenient way to describe disordered cyanide groups is as pairs of pseudo atoms, Z≡Z, where on average each Z atom is half a carbon and half a nitrogen atom (Figure 1.3 (a)).

—Z≡Z——M——Z≡Z——M——Z≡Z— **(a)**

—C≡N——M——C≡N——M——C≡N— **(b)**

—C≡N——M——N≡C——M——C≡N— **(c)**

Figure 1.3 Sections of MCN chain: (a) the average structure with disordered cyanide groups, (b) an ordered structure with only one metal environment and (c) an ordered structure with two different metal environments.

The Z≡Z unit describes the average structure very well but is not valid at the local level, where each cyanide group consists of one whole carbon atom and one whole nitrogen atom, giving rise to three possible metal environments within a chain. Figure 1.3(b) shows an ordered MCN chain in which each metal atom is bonded to one carbon atom and one nitrogen atom. Figure 1.3(c) shows a chain containing both of the other possible metal environments. In chains with this latter ordering, a metal atom can be bonded to two carbon or two nitrogen atoms, in an infinite chain. These metal environments have equal abundance. Magic Angle Spinning Nuclear Magnetic Resonance (MAS NMR) spectroscopy has shown that all three of these metal environments are present in copper and silver cyanides. In the copper-cyanide study,[21] the authors estimated 20 – 40 % of the copper sites were "disordered", defined in the paper as a metal environment with two identical neighbours. The same distribution of metal environments was found in the silver-cyanide study.[22] These results are in agreement with the total neutron diffraction experiments performed on copper and silver cyanides.[19, 23] These NMR experiments give detailed information on the local metal environments within a chain but no information on the packing of the chains in these materials.

Head-to-tail disorder is much less common in cyanide compounds containing more than one type of metal atom. For example, in the highly crystalline Heisenberg antiferromagnet,[*] $Cu(NH_3)_2[Ag(CN)_2]_2$,[24] each silver atom is bound to two carbon atoms and each Jahn-Teller distorted octahedrally coordinated

---

[*] The spins in antiferromagnetic materials with 2-dimentional structures can be described by the Heisenberg model, giving rise to the name Heisenberg antiferromagnet.

copper(II) atom has six nitrogen atoms, the axial of which are ammoniacal nitrogen atoms. This is not surprising given that the compound is synthesised by mixing solutions of $KAg(CN)_2$ and $CuSO_4$ causing the product to precipitate rapidly. In the family of compounds of formula $Cu(Sol.)_2[Au(CN)_2]_2$, (where Sol. = H_2O, NH_3, MeCN, DMF, DMSO, pyridine or dioxane), single-crystal X-ray diffraction studies have also shown ordering of the cyanide groups.[25] These compounds are not all isostructural, but in each case, the gold atoms are bound to the carbon of the cyanide groups. Interestingly these materials exhibit vapochromic behaviour and during resolvation, significant rearrangements of the crystal structures occur, as shown in (Figure 1.4) for the exchange of pyridine for DMSO in $Cu[Au(CN)_2]_2(DMSO)_2$. During these rearrangements, the cyanide ordering remains the same reflecting the preference of gold to bond to the carbon end of the C≡N group.

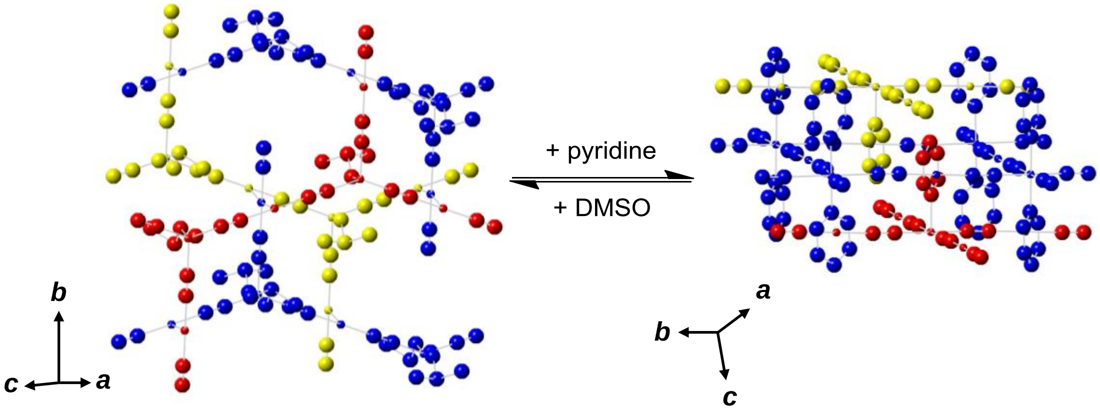

Figure 1.4 The structures of $Cu[Au(CN)_2]_2(DMSO)_2$ (left) and $Cu[Au(CN)_2]_2(py)_2$ (right). The layers are coloured and the hydrogen atoms excluded to aid clarity.

Head-to-tail cyanide ordering can occur in mono-metallic cyanide compounds because of differences in either the oxidation state of the metal, such as in

Prussian blue, or in the coordination geometry, for example in the nickel-cyanide hydrates. In anhydrous $Ni(CN)_2$, all the nickel atoms are equivalent, the Ni-C and Ni-N bond lengths are identical and the cyanide groups are disordered.[17] In all of the nickel-cyanide hydrates, $Ni(CN)_2 \cdot nH_2O$ (where n = 1, 1½, 2, 3) however, there are two chemically distinct nickel atoms.[26] One square-planar nickel is surrounded by four carbon atoms with Ni-C bond lengths of 1.87 Å, whilst the other is octahedral and surrounded by two oxygen atoms and four nitrogen atoms with Ni-N bond lengths of 2.05 Å.[26] (Figure 1.5)

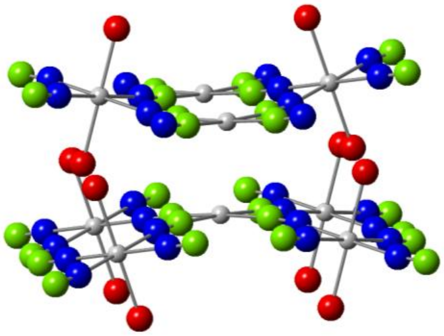

Figure 1.5 Two sheets from $Ni(CN)_2 \cdot 1½H_2O$, (Key: Nickel (grey), carbon (green), nitrogen (blue) and oxygen (red)).

Cyanide groups, like carbonyl groups, have many possible modes of bonding (Figure 1.6). Terminal and $\mu_{1,2}$ bridging cyanides are the most common as described above [27] and $\mu_{1,1}$, $\mu_{1,1,2}$ and $\mu_{1,2,2}$ bridging are well known.[27] Most unusual is the $\mu_{1,1,2,2}$ bonding seen in $3AgCN \cdot 2AgF \cdot 3H_2O$.[28]

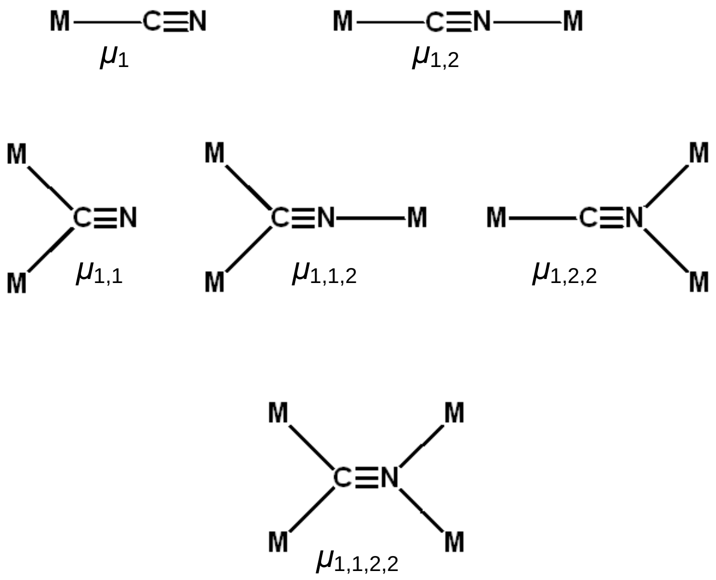

Figure 1.6 The different binding modes of cyanide groups.

1.1.2 Disordered Cyanide Compounds

In addition to head-to-tail disorder within the cyanide group, other forms of disorder are possible in covalently bonded cyanide materials. Of particular relevance to this work are the chain slipping[18-19, 23, 29] and sheet stacking disorders[17, 30] found previously in the cyanides of groups 10 and 11, respectively (Figure 1.3 and Figure 1.2). These chains and sheets are effectively infinite units which are highly crystalline in nature. However, because they do not pack in a perfectly ordered manner, the detailed structures of these materials remained elusive until the beginning of the 21st century. The successful determinations of their structures required total neutron diffraction techniques which yield interatomic distances and so directly measures bond lengths. This allowed the structures of copper, silver, gold and nickel cyanides to be solved in terms of both the average and local structures,[17-19, 23] the difference between average and local structure is explained below. In previous structure solutions using

Bragg diffraction techniques, the local structure was incorrectly determined. In particular, the bond lengths, which are of great interest to chemists, were significantly in error. The structures of silver and gold cyanides solved at room-temperature using Bragg neutron diffraction gave C≡N bond lengths of 1.26(9) and 1.21(3) Å, respectively.[31] The bond lengths, obtained using total neutron diffraction, are 1.1588(4) and 1.1499(2) Å,[18-19] for silver and gold cyanides respectively, which are much closer to the expected C≡N bond length of 1.16 Å as determined from ordered materials.[32] In addition, the Bragg diffraction studies give very different M-C and M-N bond lengths; at 300 K, $r_{\text{Ag-C}}$ = 2.15 Å, $r_{\text{Ag-N}}$ = 1.86 Å, and $r_{\text{Au-C}}$ = 2.06 Å, $r_{\text{Au-N}}$ = 1.82 Å,[31] whereas, in fact for each metal, $r_{\text{M-C}}$ and $r_{\text{M-N}}$ are identical or nearly identical. In AgCN, at 300 K, $r_{\text{Ag-C/N}}$ = 2.050(4) Å[19] and in AuCN $r_{\text{Au-C/N}}$ = 1.9703(5) Å.[18] The shortening of $r_{\text{Au-C/N}}$ relative to $r_{\text{Ag-C/N}}$ is a consequence of the lanthanide contraction. As expected, CuCN has the shortest $r_{\text{Cu-C/N}}$ bond lengths with $r_{\text{Cu-C/N}}$ = 1.8538(1) Å.[23] The equality or near equality of the M-C and M-N bond lengths appears to be a general phenomenon in monometallic polymeric cyanide compounds.[20]

1.2 Local Versus Average Structure

Conventional Bragg diffraction gives information on the size and shape of the unit cell, symmetry and atomic positions. This information describes the "average" structure of the material, as each unit cell is assumed to be identical. For highly ordered materials, this "average" structure also describes the "local structure", *i.e.* the environment around each atom. In disordered and amorphous materials however, the average structure does not explain the local structure. Sodium tungsten bronzes, Na_xWO_3 ($0 < x < 1$), have structures consisting of 3-D frameworks of corner sharing WO_6 octahedra which are charge balanced by sodium ions.[32] When $x = 1$, every sodium ion site is occupied, (Figure 1.7(a)), and when $x = 0$, every site is empty. In $Na_{0.54}WO_3$, the cation site is 54 % occupied.[33] In any individual cavity, however, the sodium site is either occupied or it is empty resulting in oxygen atoms with different local geometries.

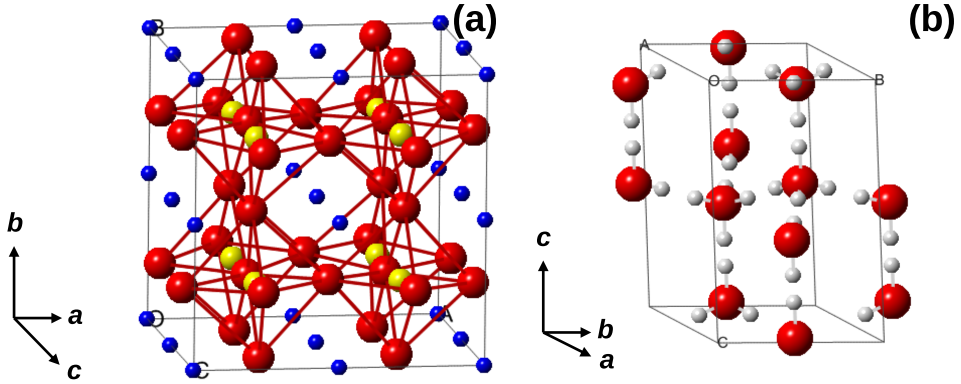

Figure 1.7 The structure of (a) $NaWO_3$ (Key: Sodium (blue), tungsten (yellow) and oxygen (red)) and (b) the average structure of hexagonal ice, (Key: oxygen (red) and hydrogen (grey)).

In the Bragg diffraction study of hexagonal ice[34] (Figure 1.7(b)), two hydrogen positions are found which generate four hydrogen sites around each oxygen, each with a 50% fractional occupancy. Locally only two of the four hydrogen sites around any particular oxygen will be occupied. The average structure might suggest that individual oxygen atoms can be bonded to any number of hydrogen atoms between zero and four. Chemical sense, as incorporated into Pauling's ice rules,[35] dictates that each oxygen atom will be bonded to two hydrogen atoms. Thus the results of the neutron diffraction study can be interpreted as each oxygen atom having two near-neighbour hydrogen atoms at ~0.85 Å with two more at ~2.0 Å all of which are involved in hydrogen bonding. In the case of ice, the chemical knowledge is well established and can be used to interpret the average structure from Bragg diffraction in terms of the local structure. This is not always the case and additional techniques are often required to obtain an accurate local structure.

Techniques used to investigate the immediate local environments around the atoms in a material include solid-state Nuclear Magnetic Resonance (NMR) spectroscopy and Extended X-ray Absorption Fine Structure (EXAFS) spectroscopy. However, both these techniques only provide short-range structural information. To determine the structure of a disordered material which is correct at both the local and average levels, a technique which is capable of determining longer range structure is required. The only methods available to do this involve the analysis of Pair Distribution Functions (PDFs) obtained from total diffraction data.

1.2.1 Pair Distribution Functions (PDFs)

1.2.1.1 Information From PDFs

The pair distribution function of a material shows the probability of finding an atom pair as a function of distance, *r*. At lower values of *r*, these interatomic distances can be ascribed to chemical bonds. Next-nearest neighbour distances can be seen at higher values of *r*. In highly crystalline materials, the limit to which peaks can be seen in the PDF is entirely dependent on the experiment. In contrast, the PDFs of materials with little long-range order, such as liquids and glasses, show no structural detail at values of r higher than ~6 Å. After this, the chance of finding an atom pair has a linear dependence on r.

Figure 1.8(a) shows a section of a graphene sheet marked with concentric circles whose radii correspond to the interatomic distances around the central carbon atom.

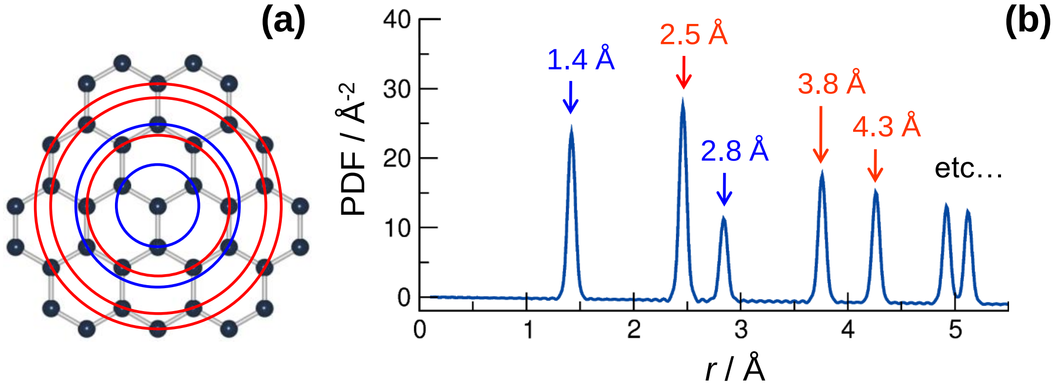

Figure 1.8(a) The local environment around a carbon atom in a graphene sheet showing the number of carbon atoms at each distance from the central atom (i.e., 3 carbon atoms at 1.4 Å (blue) and six carbon atoms at 2.5 Å (red)), and (b) the simulated PDF of a graphene sheet.

The first peak at 1.4 Å in the simulated PDF of graphene (Figure 1.8(b)), corresponds to the C-C bond length. The area of this peak is related to the number of atom pairs at this distance *i.e.* the coordination number. The coordination number of carbon at 1.4 Å in graphene is three. The coordination number, N, around an atom j, for the atom pair jk, can be calculated from the area of the peak A_{jk}, in the PDF at distance r,[36] (Equation 1.1)

$$N_{jk} = \frac{r_{jk} A_{jk}}{(2 - \delta_{jk}) c_j \bar{b}_j \bar{b}_k} \tag{1.1}$$

where c_j is the atomic fraction of j and $\bar{b}_j$ and $\bar{b}_k$ are the average coherent scattering lengths of atoms j and k respectively. The Kronecker delta, δ_{jk}, (where $\delta = 1$ if $j = k$ and $\delta = 0$ if $j \neq k$) accounts for the fact that when $j \neq k$ there is a second contribution to the area of the peak from the atom pair *kj*. From the first three peaks in the PDF of graphene, it is possible to describe much of its structure. The first peak shows that each carbon atom is bonded to three other carbon atoms at 1.4 Å. The positions of the second and third peaks in the PDF, along with the coordination numbers calculated from their areas, define the rest of the graphene sheet.

In highly crystalline materials, the bond lengths and coordination numbers can be calculated from the crystal structure, determined using Bragg diffraction techniques, so solving the structures of such materials from their PDFs is not necessary. Bragg diffraction gives no structural information on materials without long-range order. However, PDFs can be obtained even for amorphous materials and hence even in these materials, bond lengths and average coordination numbers can be determined. The advance of PDF techniques was initially driven by the desire to study glasses and liquids,[37] but the use of PDFs to solve the structures of other types of materials is becoming more common. For example, by using PDF analysis it is possible to solve the structures of low-dimensional materials, which have high levels of disorder between their chains or sheets. Of particular relevance to this work are the structures of copper, silver, gold and nickel cyanides, all of which have been solved using this method.[17-19, 23, 30] Studies of the local structure of $Li(Ni_{½}Mn_{½})O_2$, a potential electrode material for Li-ion batteries, have helped to explain why samples prepared using different synthetic routes have different performances.[38] The phase changes in the optical reading material, germanium antimony telluride, have also been investigated using total scattering in an attempt to understand better the properties of this material.[39] The emergence of nanotechnology has provided a large number of materials which have very small crystallites, which are too small for Bragg-diffraction studies. PDF analysis allows the local and average structures in these materials to be determined.[40-43]

1.2.1.2 Diffuse Scattering

Bragg diffraction is dependent on long range, regularly repeating, atomic spacing. Diffuse scattering yields information on local structure. The importance of this can be demonstrated using the “Square Ice” thought experiment presented by Dr Andrew Goodwin, University of Oxford, at the Annual British Crystallographic Meeting 2010 in Warwick.[44] In the first proposed structure for square ice (Figure 1.9 (a)), the oxygen atoms are square packed in a sheet and hydrogen atoms are placed such that the overall composition is H_2O with the O-H bond lengths correct. The diffuse scattering from this structure (Figure 1.9 (b)) is concentrated around the center spot. In the second structure (Figure 1.9 (c)), each oxygen atom is bonded to two hydrogen atoms and the effect of this extra constraint on the structure can be seen in the diffuse scattering, which is now evenly distributed inside the eight inner Bragg reflections (Figure 1.9 (d)). In the final structure (Figure 1.9 (e)), "ice rules" have been applied such that each pair of neighbouring oxygen atoms has one hydrogen atom between them, whilst still maintaining the O-H bond length. The diffuse scattering is structured (Figure 1.9 (f)).

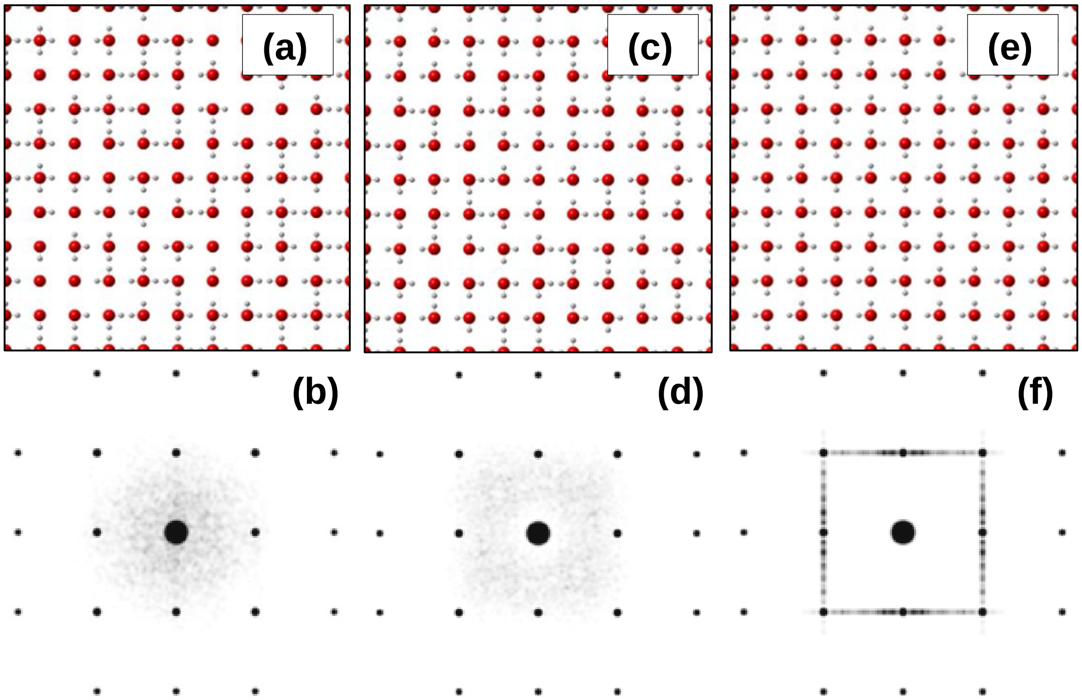

Figure 1.9 The 2-D structures and diffraction patterns of hypothetical square ice. In structure (a), the hydrogen atoms are placed randomly and generate diffraction pattern (b). In structure (c), H_2O molecules pack randomly and generate diffraction pattern (d). In structure (e), the H_2O molecules hydrogen bond according to "ice rules" which has a dramatic effect on the diffraction pattern (f).[44]

The Bragg diffraction from all three structures is identical and gives information on the positions of the regularly spaced oxygen atoms. The average structure of all three materials is the same, but the local structure is very different. The experiment demonstrates that changes in the local environment can be seen only in the diffuse scattering component of the diffraction patterns.

1.2.1.3 Obtaining a PDF

To obtain the pair distribution function for a material, a diffraction pattern must be collected which contains not only the peaks from Bragg diffraction but also the diffuse scattering which lies in the background regions (Figure 1.10).

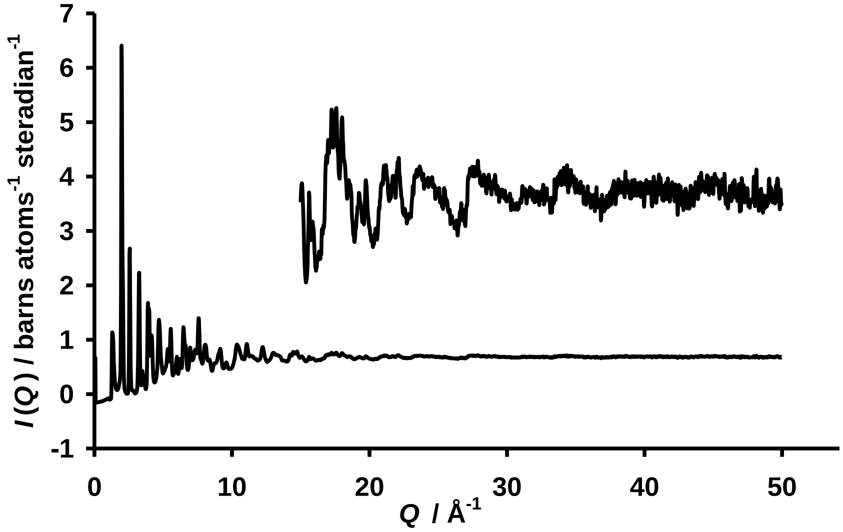

Figure 1.10 The neutron diffraction pattern of Ni(CN)$_2$ collected on the GEM time-of-flight diffractometer, at the ISIS spallation neutron source. Inset is a ×20 enlargement of the diffuse scattering in the 15 – 50 Q range.

The following describes the reduction of total neutron diffraction data to the PDF function, $T(r)$.[45] The diffraction pattern known as the differential cross section or total scattering, $I(Q)$, is measured over as wide a range of Q as possible (Figure 1.10), where Q is the magnitude of the scattering vector or momentum transfer for elastic scattering, given by (Equation 1.2).

$$Q = \frac{4\pi \sin\theta}{\lambda} \tag{1.2}$$

The total scattering is comprised of two components; namely, the self scattering and the distinct scattering. The self scattering, $I^S(Q)$, calculated using Equation 1.3, (Figure 1.11)

$$I^S(Q) = \sum c_l \, \overline{b_l}^2 \tag{1.3}$$

…Where c_l and $\overline{b}_l$ are respectively the atomic fraction and average coherent scattering length of element, l, is subtracted from the differential cross section, $I(Q)$, according to (Equation 1.4),

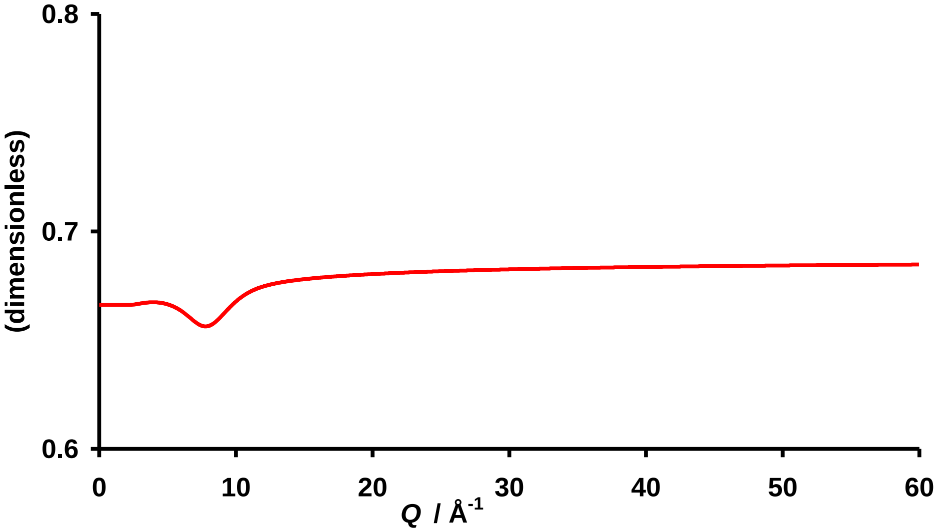

Figure 1.11 The calculated self scattering from Ni(CN)$_2$, calculated from (Equation 1.2).

$$i(Q) = I(Q) - I^S(Q) \tag{1.4}$$

…to give the distinct scattering, $i(Q)$, (Figure 1.12), which contains the information about the structure of the sample.

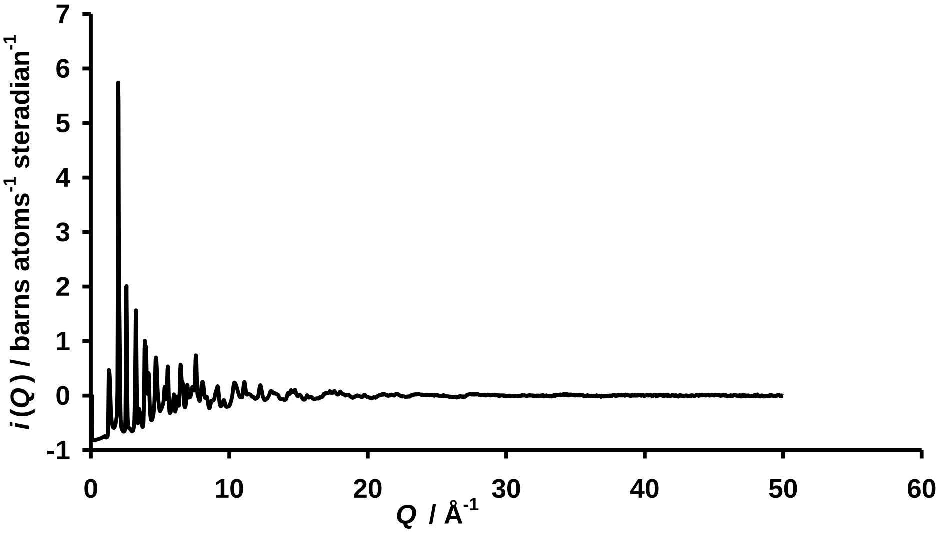

Figure 1.12 the distinct scattering, i(Q), which oscillates about zero.

The distinct scattering, *i*(*Q*), is multiplied by *Q*, (Figure 1.13) and Fourier transformed, using (Equation 1.5), to give the differential correlation function *D*(*r*), (Figure 1.14).

$$D(r) = \frac{2}{\pi}\int_0^{Q_{\max}} Q i(Q) M(Q) \sin(rQ) dQ \tag{1.5}$$

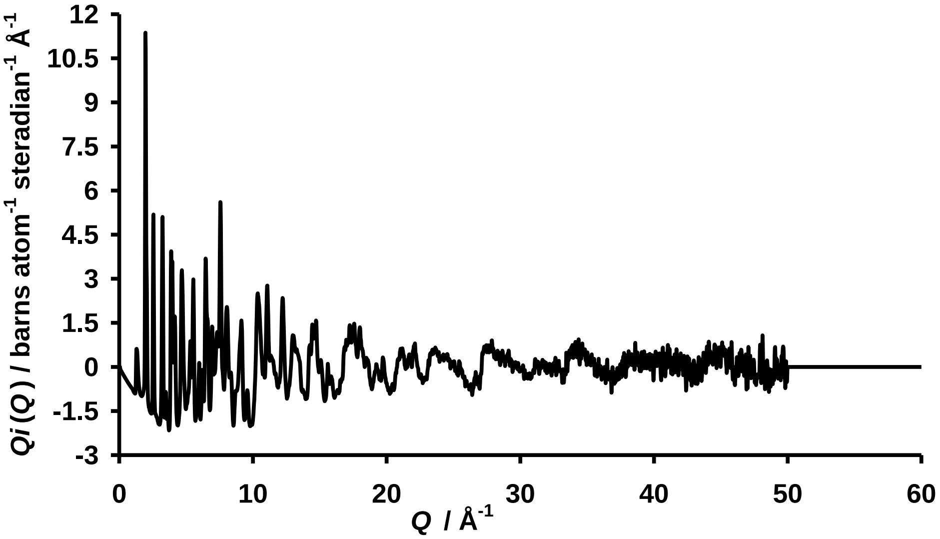

Figure 1.13 The function $M_{step}Qi(Q)$. e.g. The distinct scattering, i(Q), multiplied by Q and "extrapolated" to infinity where M_{step} $Qi(Q) = Qi(Q)$ where $Q<Q_{max}$ and $Qi(Q)_{step} = 0$ where $Q>Q_{max}$.

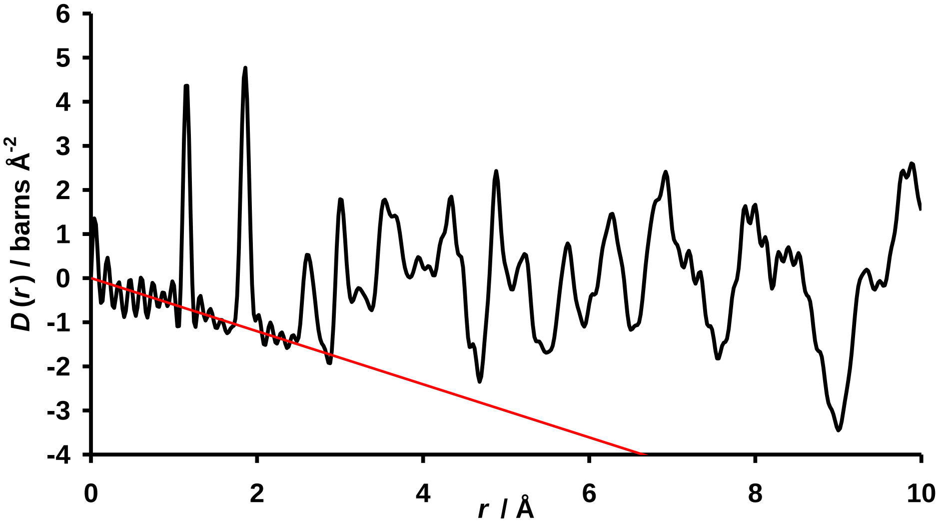

Figure 1.14 The correlation function, $D(r)_{step}$ (black), from the Fourier transform of $M_{step}Qi(Q)$. The slope of D(r) with respect to r is shown in red.

…Where $M(Q)$ is the modification function used to account for the fact that total scattering data are collected to a finite Q_{max}, and not to infinity. The simplest modification function is the step function, (Figure 1.15), where $M_{step}i(Q) = i(Q)$

when $Q < Q_{\max}$, and $M_{\text{step}}i(Q) = 0$ where $Q > Q_{\max}$. This abrupt cut in $M_{\text{step}}Qi(Q)$ at $Q = 50$ in Figure 1.13, leads to transform ripples around the peaks in $D(r)_{\text{step}}$ (Figure 1.14).

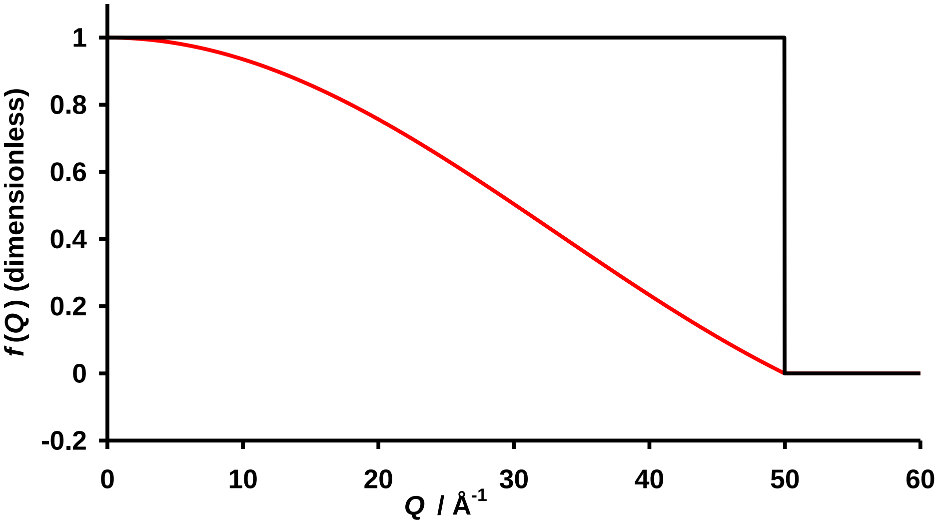

Figure 1.15 The step function (black) and the Lorch function (red), used to account for the experimental limits of Q_{max}.

The Lorch function, (Figure 1.15), (Equation 1.6),[46] is commonly used as a modification function because it greatly reduces transform ripples in $D(r)_{\text{Lorch}}$, (Figure 1.16)

$$M_{Lorch}(Q) = \frac{\sin(Q\Delta r)}{Q\Delta r} \text{ when } Q < Q_{\max}$$
$$\text{and } M_{Lorch}(Q) = 0 \text{ when } Q > Q_{\max} \qquad (1.6)$$

$$\text{where } \Delta r = \frac{\pi}{Q_{\max}} \qquad (1.7)$$

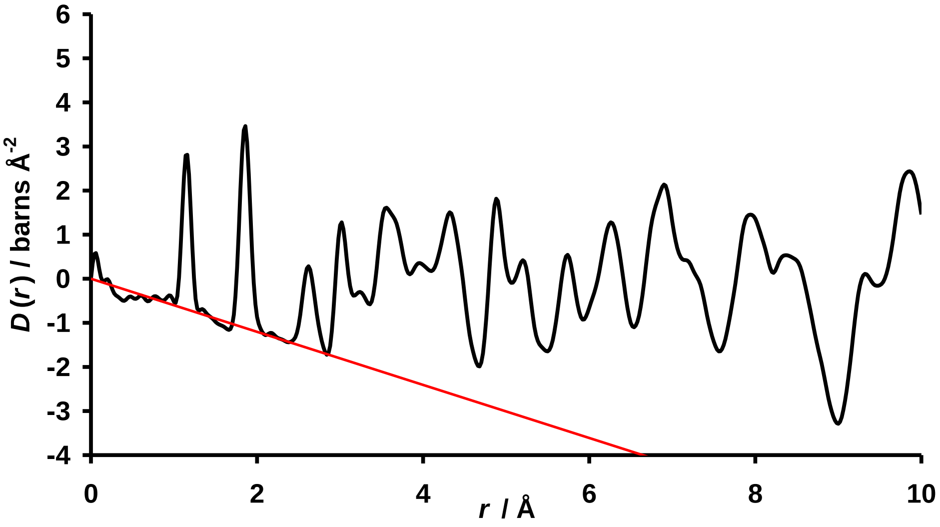

Figure 1.16 The correlation function D(r)$_{Lorch}$ (black) from the Fourier transform of M$_{Lorch}$Qi(Q). The slope of D(r) with respect to r is shown in red.

In addition to the reduction in transform ripples in *D*(*r*), there is also a reduction in peak resolution. *D*(*r*) is converted to the total correlation function *T*(*r*), (Figure 1.17), by adding the $T^0(r)$ constant, (Equation 1.8), which is equal to the slope of *D*(*r*).

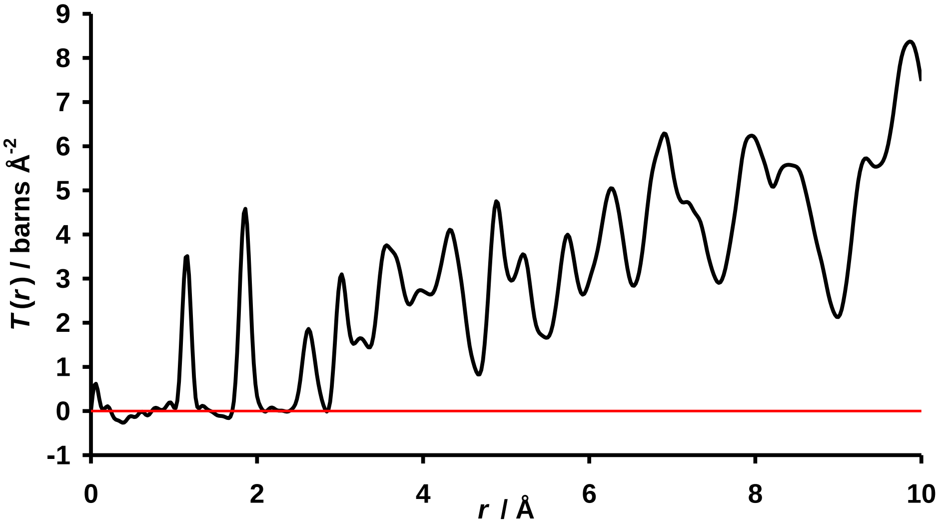

Figure 1.17 T(r)$_{Lorch}$ (black) from D(r)$_{Lorch}$, Zero line (red)

$$T(r) = D(r) + T^0(r) \tag{1.8}$$

$$\text{where } T^0(r) = 4\pi r g^0 \left(\sum_l c_l \overline{b_l} \right)^2 \tag{1.9}$$

…Where g^0 (=N/V) is the macroscopic number density of the sample, with units of (atoms Å^{-3}).

Several research groups analyse PDF data and a consequence of this is that each group has a slightly different PDF language. The data collection and the information obtained are very similar but the presentations of results are not. A paper by David Keen[47] comparing some of the different terminology and related equations gives a good summary of the field. Although it is relatively easy to calculate the PDF of any material from its crystallographic model, $T(r)$ has peaks which can be modelled using Gaussian functions, which at low r model simple harmonic motion.[36] In addition, the broadening of the peaks in some PDF functions has an r dependence. This is not true for $T(r)$, making it possible to compare directly the broadening of peaks in $T(r)$ at different values of r.[48]

It is also worth mentioning at this point that it is possible to collect total scattering data using X-rays, although total neutron diffraction is generally accepted to be a more powerful technique. It can be seen from Equation 1.2 that Q_{max} is determined by both λ and the scattering angle. When the scattering angle is 90 ˚, $Q_{\text{max}} = 4\pi/\lambda$, making Q_{max} entirely dependent on wavelength. Laboratory X-ray sources, $\mathrm{Cu}_{K\alpha}$, $\mathrm{Mo}_{K\alpha}$ and $\mathrm{Ag}_{K\alpha}$, yield Q_{max} of 8.2, 1.7 and 22.5 Å^{-1} respectively. The resolution, Δr, in $T(r)$ is determined by Q_{max}, as calculated using Equation 1.7. Higher values of Q_{max} give higher resolution peaks in $T(r)$. The maximum resolution in $T(r)$, measured using $\mathrm{Cu}_{K\alpha}$, $\mathrm{Mo}_{K\alpha}$ and $\mathrm{Ag}_{K\alpha}$ are 0.38, 0.18 and 0.14 Å. In comparison, data measured at a spallation neutron source have values of Q_{max} in the range 40 – 60 Å^{-1}. This gives maximum resolutions of 0.08 and 0.05 Å respectively. Although the use of X-ray synchrotron radiation allows a much higher theoretical Q_{max} to be obtained, as shorter wavelengths can be employed, very long count times are required to acquire good signal-to-noise ratios at higher values of Q. This is because X-ray scattering is strongly dependent on scattering angle, which is not the case in neutron diffraction. The difference in resolution at a range of values for Q_{max} can be seen in Figure 1.18.

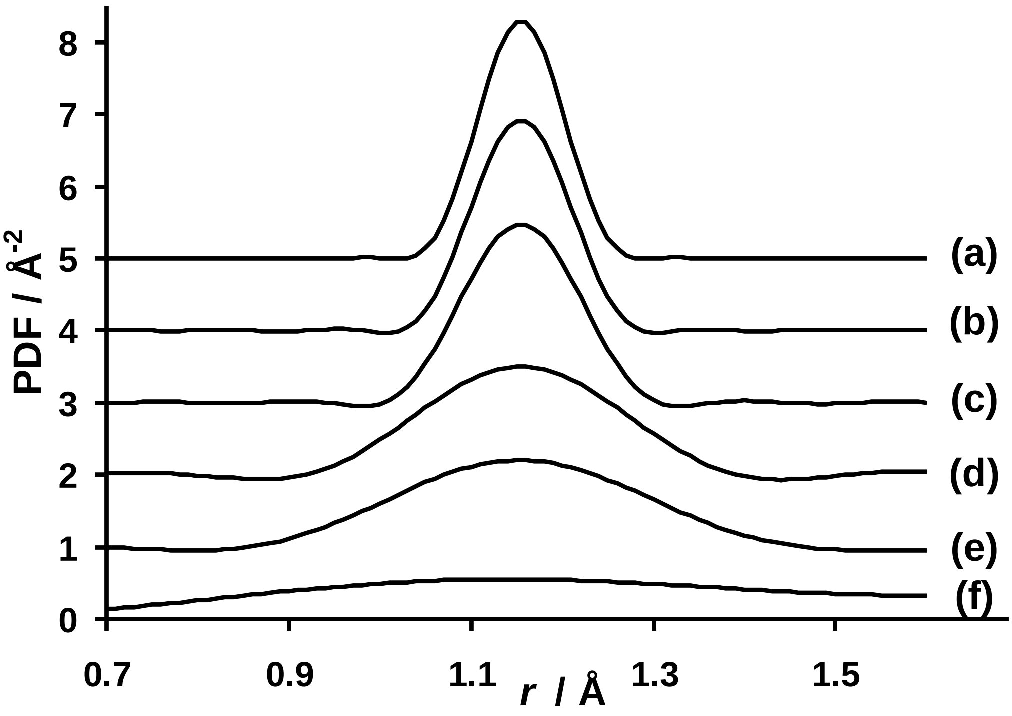

Figure 1.18 A simulated CN peak using a Lorch modification function and Q_{max} = (a) 60.0, (b) 50.0, (c) 40.0, (d) 22.5, (e) 17.7 and (f) 8.2 Å^{-1}. These are shifted along the y axis by 5, 4, 3, 2, 1 and 0 respectively.

The second major advantage of PDF work using neutron diffraction rather than X-ray diffraction is that the X-ray scattering lengths of elements depend on their number of electrons. As a result, it is very difficult to determine the positions of light elements in the presence of heavier ones. Neutrons, on the other hand, are scattered by the nucleus and have a smaller range of scattering lengths for non-isotopically enriched samples; $\bar{b}_{Mn}$ = -3.73(2) to $\bar{b}_{Dy}$ = 16.9(2) fm. This is especially important when looking at samples containing both heavy and light atoms, for example, metal oxides or metal cyanides. The opportunity for isotopic enrichment of samples to change the contrast between the scattering lengths of the atoms also adds versatility to neutron diffraction experiments. There are, as with any technique, some disadvantages to total neutron diffraction. For example, the large incoherent scattering length of hydrogen means that samples must be very dry and that hydrated samples must be prepared using D_2O. Neither of these are insurmountable problems. More importantly, samples containing strong neutron absorbers or fissile elements are not suitable for neutron diffraction. With this in mind, X-ray and neutron scattering experiments should be considered as complementary methods, with each having their place in the scientists' tool box.

1.3 Negative Thermal Expansion (NTE)

Most materials expand on heating but this is not universally true. Transition-metal cyanides not only provide examples of materials which contract in one, two or three dimensions on heating, but also show the most dramatic changes with temperature.

The overall changes in volume, V, or length of a crystallographic axes, l, of a material are described by the thermal expansion coefficients α_V and α_l respectively, which are defined in (Equation 1.10).

$$\alpha_V = \frac{(V_T - V_0)}{V_0(T - T_0)} \quad \text{and} \quad \alpha_l = \frac{(l_T - l_0)}{l_0(T - T_0)} \tag{1.10}$$

Values of α_l vary from 40×10^{-6} K^{-1} for NaCl and α-Quartz, down to Invar steel, $Fe_{64\%}Ni_{36\%}$, and β-Quartz which have coefficients of thermal expansion close to zero.[49] Materials with very small values of α_V are used to make oven-to-table cookware, ceramic hobs for electric ovens,[50] precision instruments and satellite components. More interesting are materials which have negative values of α_V, reflecting the fact that they contract on heating.

The best known example of NTE is the phase transition of water at 0 ˚C, but this expansion on cooling occurs over a very limited range of temperature, *i.e*. 0 - 4 ˚C.[51] The first materials to be studied which showed negative thermal expansion (NTE), as opposed to positive thermal expansion (PTE), over a wide range of temperature were the zeolites.[52] The contraction in ZrW_2O_8, on heating, $\alpha_a = -9.07\times10^{-6}\ K^{-1}$, has also been well studied.[53-55] The mechanism responsible for NTE in these materials has been attributed to Rigid Unit Modes (RUMs), in which precession of the bridging oxygen atoms displaces them from their average position, drawing the metal atoms closer together. (Figure 1.19 (a+b))

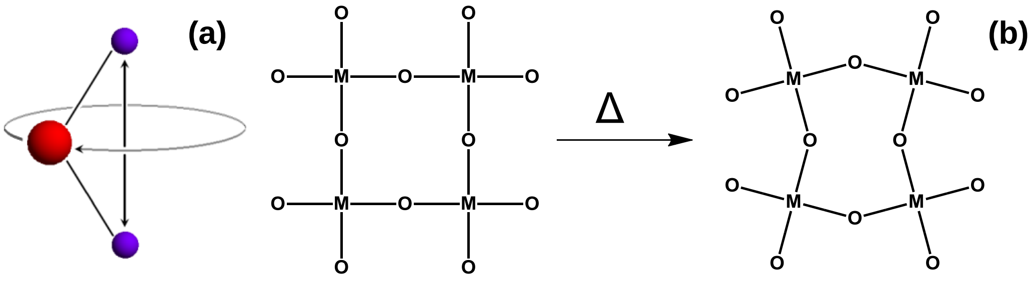

Figure 1.19 (a) Displacement of a bridging oxygen atom from its equilibrium position and (b) the contraction in the M···M distance in an MO_2 sheet from this displacement of the oxygen atom.

For a vibrational mode to contribute to negative thermal expansion, it must be excited by thermal energy. This means that the modes must be of low energy, and so are expected to have a long wavelength spanning multiple unit cells.

In 1997, a structural study of $Zn(CN)_2$ noted that it showed negative thermal expansion, α_a = -17×10^{-6} K^{-1}.[20] It was proposed that cyanide links allowed greater flexibility of the framework because there are two possible displacements of the cyanide group, (Figure 1.20).

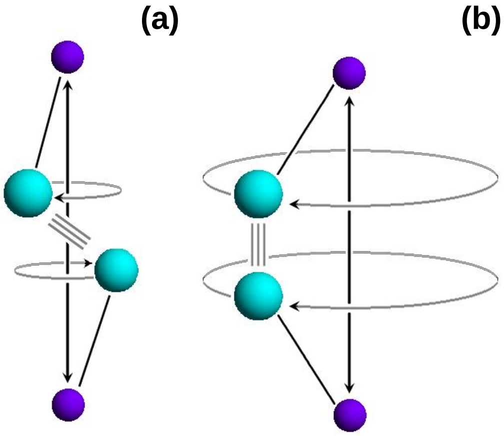

Figure 1.20 The two possible displacements of a bridging cyanide, (a) where the atoms are displaced in opposite directions and (b) where the atoms are displaced in the same direction.

Both these displacements of the cyanide group cause a contraction of the M···M distance giving rise to two predicted RUMs. These are shown in Figure 1.21 and Figure 1.22.[56]

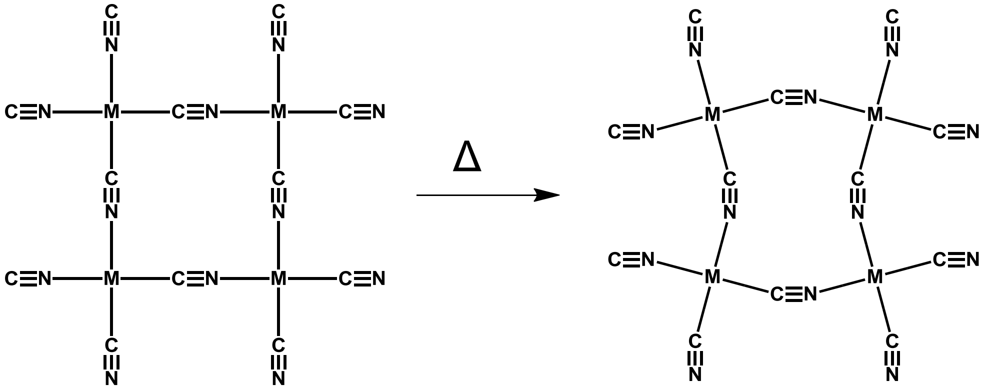

Figure 1.21 Distortion of an $M(CN)_2$ square with increasing temperature in a side-step RUM vibration.

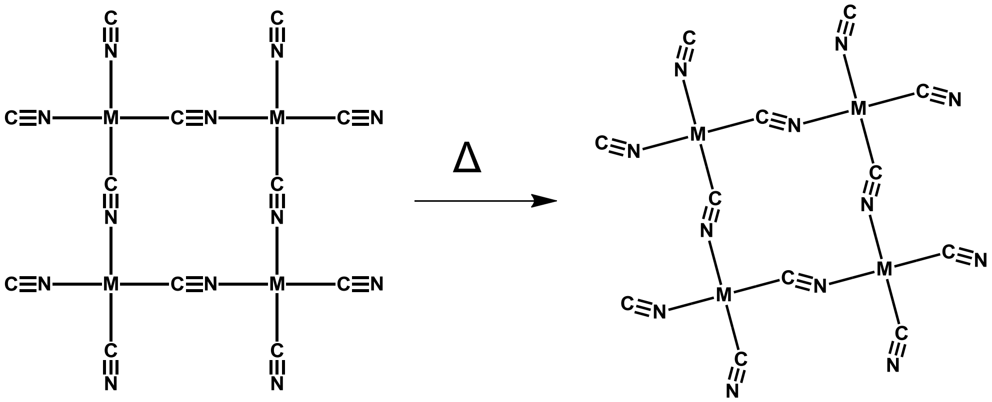

Figure 1.22 Distortion of an $M(CN)_2$ square with increasing temperature in a kinky RUM vibration.

Further work on $Zn(CN)_2$ seemed to suggest that that the predominant type of RUM was of type shown in Figure 1.20(b). In contrast to the 3-D NTE seen in $Zn(CN)_2$, 1-D NTE has been observed in copper, silver and gold cyanides. This behaviour has been attributed to long-wavelength motions within the chains.[57] The thermal behaviour of these materials has been further investigated using variable-temperature powder X-ray diffraction, to measure changes in the average structure, and RMC modelling, to investigate the local motions within these materials.[58] Two possible vibrations which would lead to an apparent contraction of the chain length, but which maintain linear geometry around the metal atoms, are shown in Figure 1.23 (b)+(c).

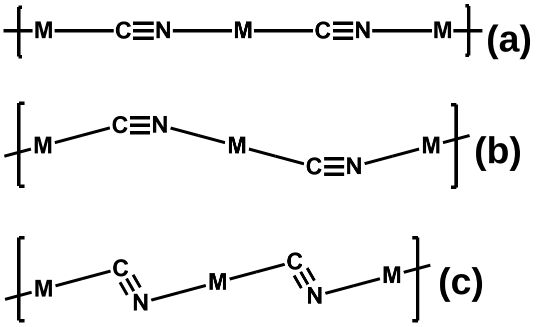

*Figure 1.23 (a) the straight MCN chain expected at absolute zero, (b) a skipping-rope mode with a wavelength of 2*$r_{M\cdots M}$ *(c) a kinked mode with a wavelength of 1*$r_{M\cdots M}$.

The skipping-rope mode (Figure 1.23(b)) has a wavelength of two M···M repeats, while the kinked mode (Figure 1.23(c)) has a wavelength of one M···M repeat. This shorter wavelength results in M-C-N bond angles which are further from 180 ° resulting in a greater decrease in the M···M distance.

Given that cubic materials such as ZrW_2O_8 and $Zn(CN)_2$ show isotropic 3-D NTE and structures constructed from chains exhibit 1-D NTE, it was predicted that a material constructed from sheets should exhibit 2-D NTE. Indeed in schematic diagrams used to explain 3-D NTE (Figure 1.19 (b), Figure 1.21 and Figure 1.22), the modes shown are, in fact, 2-D RUMs.[49] The structure of $Ni(CN)_2$, which consists of infinite sheets (Figure 1.2(a)), has been solved at 100 and 300 K. The *a* lattice parameter contracts with increasing temperature, $\alpha_a = -6.5 \times 10^{-6}$ K^{-1}, whilst the *c* lattice parameter increases with temperature, $\alpha_c = 61.8 \times 10^{-6}$ K^{-1}, proving that layered structures can exhibit 2-D NTE behaviour.[17] Further investigation of the thermal behaviour of $Ni(CN)_2$ has shown that there are multiple vibrational modes which when excited cause a contraction in the plane of the sheet.[30] Several of these modes involve atoms moving out of the plane of the sheet and this rippling of the sheets would be expected to force them apart .[30]

The expectation that compounds containing longer, more flexible, linkers should show increased NTE behaviour, has led to theoretical studies of materials with very long linkers, particularly MOFs.[59] Although the linkers in MOFs can be very long, *e.g.* in 4,4′-bipyridyl $r_{\mathrm{N}\cdots\mathrm{N}'} \approx 7.1$ Å, they often contain rigid units such as *para*-substituted benzene rings which reduce the flexibility of the linkers. Cyanide compounds can also have structures containing long linking units, *e.g.* $[\mathrm{Ag(CN)_2}]^{1-}$ where $r_{\mathrm{N}\cdots\mathrm{N}} \approx 6.3$ Å.

In 1968, Pauling determined the structure of $\mathrm{Ag_3Co(CN)_6}$.[60] The structure consists of octahedrally coordinated $\mathrm{Co^{3+}}$ ions linked by linear $[\mathrm{Ag(NC)_2}]^{1-}$ units to form a very open 3-D framework (Figure 1.24(a)). The crystal structure contains three such frameworks which interpenetrate one another (Figure 1.24(b)).

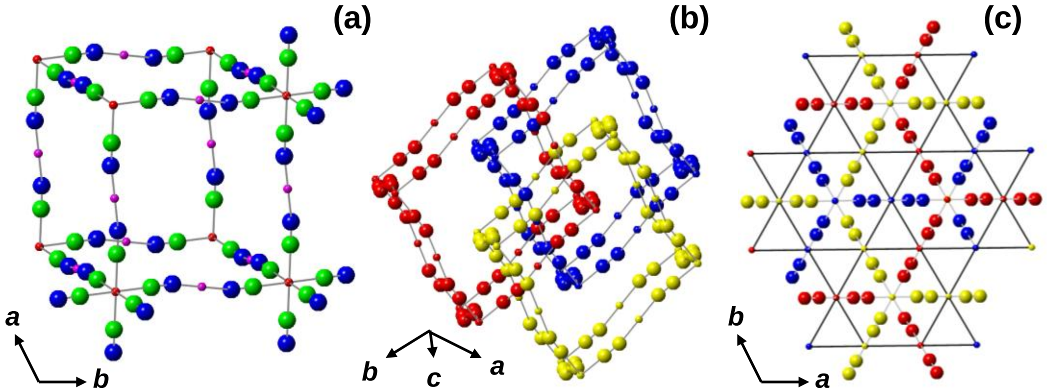

Figure 1.24 (a) a section of the $Ag_3Co(CN)_6$ framework (Key: Silver (pink), cobalt (red), carbon (green) and nitrogen (blue)), (b) three sections of $Ag_3Co(CN)_6$ framework, the networks are shown in blue, red and yellow to emphasise their interpenetration. (c) the kagome lattice[61] formed by the silver atoms in all three frameworks using the same colour scheme as in (b).

The silver atoms in neighbouring $Ag_3Co(CN)_6$ frameworks are arranged in a kagome lattice in the *ab* plane, Figure 1.24(c). The nearest Ag···Ag distance is quite short, at 3.515 Å, suggestive of argentophilic interactions similar to aurophilic interaction.[62] Forty years later, the structure of this material was re-examined as a function of temperature.[63] It was proposed that due to the length, ~10.2 Å, and flexibility of the Co-CN-Ag-NC-Co links, $Ag_3Co(CN)_6$ should show interesting thermal expansion behaviour. The results of this investigation were ground breaking. Whilst previous studies have reported $\alpha_a \approx -10 \times 10^{-6}$ K^{-1}, for zeolites and $\alpha_a \approx -20 \times 10^{-6}$ K^{-1}, for cyanide bridged materials, the contraction in the *c* lattice parameter of $Ag_3Co(CN)_6$ was found to be an order of magnitude larger, $\alpha_c = -125 \times 10^{-6}$ K^{-1}. This contraction was accompanied by 2-D PTE where $\alpha_a = 140 \times 10^{-6}$ K^{-1}, the mechanism behind these "colossal" changes in the lattice parameters have been investigated using RMC modelling and are linked to thermal motion disrupting the argentophilic interaction within the kagome lattices.[64] Other coordination polymers with structures which incorporate metallophilic bonding have also been shown to exhibit colossal NTE and PTE behaviour.[65]

Interestingly, the structure of the mineral β-eucryptite, $LiAlSiO_4$, which is used in the manufacture of ceramic hobs for electric ovens because of its very low α_V,[50] is hexagonal and not cubic. Like $Ag_3Co(CN)_6$, it contracts on heating along its c lattice parameter, α_c = -18.4 $\times 10^{-6}$ K^{-1}, and expands along its a lattice parameter, α_a = 8.6 $\times 10^{-6}$ K^{-1}. The overall volume does not change greatly with temperature because $V_{hex} = 2a(\sin 120°) \times c$ and in β-eucryptite, $\alpha_c \approx -2\alpha_a$.

Understanding a material's thermal behaviour, requires a detailed knowledge of both the average and the local structures. Measuring the expansion or contraction of the average structure using Bragg diffraction allows the macroscopic properties of the material to be measured accurately. Studying the local structure as a function of temperature using PDF techniques is very useful in investigating the motions responsible for this behaviour.

1.4 Scope of the Current Work

Based on the previously established structural similarities of HT-CuCN,[23] AgCN[19] and AuCN,[18] it was expected that it would be possible to prepare mixed group 11 transition-metal cyanides of the form $(M_xM'_{1-x})CN$. This is demonstrated in this thesis and the phase diagram for each system is established. All these materials are disordered polycrystalline powders and powder X-ray diffraction has shown that the mixed compounds are isostructural with the parent metal cyanides. The detailed local structures of $(Cu_{1/2}Ag_{1/2})CN$, $(Cu_{1/2}Au_{1/2})CN$ and $(Ag_{1/2}Au_{1/2})CN$ have all been determined using total neutron diffraction, confirming the predictions made about chain ordering based on infrared measurements.

Following on from the successful structure determination of nickel cyanide,[17] the structures of $Pd(CN)_2$ and $Pt(CN)_2$ have been solved using total neutron diffraction. However, unlike nickel cyanide, which is a disordered polycrystalline material, the structures of $Pd(CN)_2$ and $Pt(CN)_2$ are in fact disordered nanocrystalline materials consisting of small $M(CN)_2$ sheets terminated by H_2O or NH_3 groups. The sizes of the platinum- and palladium-based sheets vary with the method of synthesis and there is significantly less order between the sheets in these materials than is found in $Ni(CN)_2$. Because of the small sizes of the sheets in $Pd(CN)_2$ and $Pt(CN)_2$, the edges make up a significant proportion of the materials and it has been possible to determine not only the bulk structure of the materials but also to characterise the nature of the edges using a range of methods. Commercial samples, for example, have the formulae $Pd(CN)_2{\cdot}0.29H_2O$ and $Pt(CN)_2{\cdot}0.29NH_3$.

All the materials studied in this work show NTE. Both the parent group 11 metal cyanides and the mixed compounds show 1-D NTE along the chain direction and the likely mechanism behind this is discussed in some detail. Both $Pd(CN)_2 \cdot 0.29H_2O$ and $Pt(CN)_2 \cdot 0.29NH_3$ show 2-D NTE, which is quite unusual, and the mechanism responsible for this behaviour is also discussed in detail. Preliminary results suggest that $(Cu_{⅔}Au_{⅓})CN$, $(Cu_{½}Au_{½})CN$, $Pt(CN)_2 \cdot 0.29NH_3$, $(NH_4)_2Pt(CN)_4$ and, $(NH_4)_2Pt(CN)_4 \cdot 2H_2O$ are luminescent. Samples have been given to Professor Franti Hartl, University of Reading, for a detailed study of this phenomenon.

1.5 References

1. J. Bartoll, in *The 9th International Conference on NDT of Art*, Jerusalem, Editon edn., 2008.
2. D. Gatteschi, *Solid State Mater. Sci.*, 1996, 192.
3. T. Mallah, S. Thiebaut, M. Verdaguer and P. Veillet, *Science*, 1993, **262**, 1554.
4. S. Ferlay, T. Mallah, R. Ouahes, P. Veillet and M. Verdaguer, *Nature*, 1995, **378**, 701.
5. J. M. Manriquez, G. T. Yee, R. S. McLean, A. J. Epstein and J. S. Miller, *Science*, 1991, **252**, 1415.
6. H. E. Williams, *Cyanogen Compounds*, 2nd edn., Edward Arnold & Co., London, 1945.
7. M. J. Katz, T. Ramnial, H.-Z. Yu and D. B. Leznoff, *J. Am. Chem. Soc.*, 2008, **130**, 10662.
8. M. Stender, R. L. White-Morris, M. M. Olmstead and A. L. Balch, *Inorg. Chem.*, 2003, **42**, 4504.
9. X. Liu, G. C. Guo, M. L. Fu, X. H. Liu, M. S. Wang and J. S. Huang, *Inorg. Chem.*, 2006, **45**, 3679.
10. J. C. F. Colis, C. Larochelle, R. Staples, R. Herbst-Irmer and H. Patterson, *Dalton Trans.*, 2005, **109**, 675
11. J. C. F. Colis, C. Larochelle, E. J. Fernandez, J. M. Lopez-de-Luzuriaga, M. Monge, A. Laguna, C. Tripp and H. Patterson, *J. Phys. Chem.*, 2005, **B109**, 4317.
12. C. A. Bayse, T. P. Brewster and R. D. Pike, *Inorg. Chem.*, 2009, **48**, 174.
13. J. L. Hoard *Z. Kristallogr.*, 1933, **84**, 231.
14. J. J. Pesek and W. R. Mason, *Inorg. Chem.*, 1982, **22**, 2958.
15. F. Herren, P. Fischer, A. Ludi and W. Haelg, *Inorg. Chem.*, 1980, **19**, 956.
16. B. F. Hoskins and R. Robson, *J. Am. Chem. Soc.*, 1990, **112**, 1546

17. S. J. Hibble, A. M. Chippindale, A. H. Pohl and A. C. Hannon, *Angew. Chem. Int. Ed.*, 2007, **46**, 7116.
18. S. J. Hibble, A. C. Hannon and S. M. Cheyne, *Inorg. Chem.*, 2003, **42**, 4724.
19. S. J. Hibble, S. M. Cheyne, A. C. Hannon and S. G. Eversfield, *Inorg. Chem.*, 2002, **41**, 1042.
20. D. J. Williams, D. E. Partin, F. J. Lincoln, J. Kouvetakis and M. O'Keeffe, *J. Solid State Chem.*, 1997, **134**, 164.
21. S. Kroeker, R. E. Wasylishen and J. V. Hanna, *J. Am. Chem. Soc.*, 1999, **121**, 1582.
22. D. L. Bryce and R. E. Wasylishen, *Inorg. Chem.*, 2002, **41**, 4131.
23. S. J. Hibble, A. C. Hannon, S. M. Cheyne and S. G. Eversfield, *Inorg. Chem.*, 2002, **41**, 4990.
24. A. Vlcek, M. Orendac, A. Orendacova, M. Kajnakova, T. Papageorgio, J. Chomic, J. Cernak, W. Massa and A. Feher, *Solid State Sci*, 2007, **9**, 116.
25. J. Lefebvre, R. J. Batchelor and D. B. Leznoff, *J. Am. Chem. Soc.*, 2004, **126**, 16117.
26. A. H. Pohl, PhD Thesis, The University of Reading, 2008.
27. R. K. Dunbar and R. A. Heintz, *Prog. Inorg. Chem.*, 1997, **45**, 283.
28. G. C. Guo and T. C. W. Mak, *Angew. Chem. Int. Ed.*, 1998, **37**, 3183.
29. J. K. Harris and R. E. Wasylishen, *Inorg. Chem.*, 2009, **48**, 2316.
30. A. L. Goodwin, M. T. Dove, A. M. Chippindale, S. J. Hibble, A. H. Pohl and A. C. Hannon, *Phys. Rev. B*, 2009, **80**, 054101.
31. G. A. Bowmaker, B. J. Kennedy and J. C. Reid, *Inorg. Chem.*, 1998, **37**, 3968.
32. A. F. Wells, *Structural Inorganic Chemistry 4th edition*, Clarendon Press, Oxford, 1975.
33. P. J. Wiseman and P. G. Dickens, *J. Solid State Chem.*, 1976, **17**, 91.
34. A. Goto, T. Hondoh and S. Mae, *Acta Cryst.*, 1994, **B50**, 644.
35. L. Pauling, *J. Am. Chem. Soc.*, 1935, **57**, 2680.
36. A. C. Hannon, *XTAL: A program for calculating interatomic distances and co-ordination numbers for model structures*, Rutherford Appleton Laboratory 1993.
37. A. C. Wright, *Experimental techniques of glass science*, American Ceramic Society, New York, 1993.
38. J. Breger, K. Kang, J. Cabana, G. Ceder and C. P. Grey, *J. Mater. Chem.*, 2007, **17**, 3167.
39. S. I. Shamoto, K. Kodama, S. Iikubo and T. Taguchi, *Nucl. Instrum. Methods Phys. Res., Sect. A*, 2009, **600**, 229.
40. K. Mullen, V. Krayzman and I. Levin, *J. Appl. Crystallogr.*, 2010, **43**, 483.
41. S. J. L. Billinge, *Z. Kristallogr.*, 2007, 17.
42. S. J. L. Billinge, *J. Solid State Chem.*, 2008, **181**, 1695.
43. S. J. L. Billinge and M. G. Kanatzidis, *Chem. Commun.*, 2004, 749.
44. N. Funnell, The Annual British Crystallographic Spring Meeting Warwick University, 2010.
45. S. J. Hibble, A. C. Hannon and I. D. Fawcett, *J. Phys.: Condens. Matter*, 1999, **11**, 9203.

46. E. A. Lorch, *J. Phys. Commun.*, 1969, **2**, 229.
47. D. A. Keen, *J. Appl. Crystallogr.*, 2001, **34**, 172.
48. S. J. Hibble and A. C. Hannon, *Local structure: the realm of the chemist?* in “From semiconductors to proteins: beyond the average structure”, Eds. S. J. L. Billinge and M. F. Thorpe (Kluwer Academic Publishers, New York) p.129 (2002).
49. J. S. O. Evans, *Dalton Trans.*, 1999, 3317.
50. A. I. Lichenstein and R. O. Jones, *Phys. Rev. B*, 1998, **58**, 6219.
51. L. Pauling, *The Nature of the Chemical Bond*, 3rd edn., Cornell University Press, 1960.
52. S. H. Park, R. W. Grosse-Kunstleve, H. Graetsch and H. Gies, 11th IZA conference 1996, Amsterdam, 1996.
53. A. W. Sleight, *Inorg. Chem.*, 1998, **37**, 2854.
54. J. S. O. Evans, W. I. F. David and A. W. Sleight, *Acta Cryst.*, 1999, **B55**, 333.
55. T. A. Mary, J. S. O. Evans, T. Vogt and A. W. Sleight, *Science*, 1996, **272**, 90.
56. A. L. Goodwin, *Phys. Rev. B*, 2006, **74**, 134302.
57. A. C. Hannon, *Nucl. Instrum. Methods Phys. Res., Sect. A*, 2005, 88.
58. S. J. Hibble, G. B. Wood, E. J. Bilbe, A. H. Pohl, M. G. Tucker, A. C. Hannon and A. M. Chippindale, *Z. Kristallogr.*, 2010, **225**, 457-462.
59. D. Dubbeldam, K. S. Walton, D. E. Ellis and R. Q. Snurr, *Angew. Chem. Int. Ed.*, 2007, **46**, 4496.
60. L. Pauling and P. Pauling, *Proc. Natl. Acad. Sci. U.S.A*, 1968, **60**, 362.
61. I. Syozi, *Prog. Theor. Phys.*, 1951, **6**, 306 - 308.
62. P. Pyykko, *Angew. Chem. Int. Ed.*, 2004, **43**, 4412.
63. A. L. Goodwin, J. S. O. Evans and M. G. Tucker, *Science*, 2008, **319**, 794.
64. M. J. Conterio, A. L. Goodwin, M. G. Tucker, D. A. Keen, M. T. Dove, L. Peters and J. S. O. Evans, *J. Phys.: Condens. Matter*, 2008, **20**.
65. J. L. Korčok, M. J. Katz and D. B. Leznoff, *J. Am. Chem. Soc.*, 2009, **131**, 4866.

Chapter 2: Experimental Methods and Data Handling.

2.1 Determining the Total Structures of Materials

This thesis describes the synthesis and structural characterisation of a number of Group 10 and 11 transition-metal cyanides, including platinum and palladium cyanides, $Pt(CN)_2$ and $Pd(CN)_2$ and the mixed-metal series $(Cu_xAg_{1-x})CN$, $(Ag_xAu_{1-x})CN$ and $(Ag_xAu_{1-x})CN$. The methods of synthesis of these materials are described in detail in the chapters containing their structure determinations. The principal techniques used to characterise the compounds were X-ray diffraction (powder and single crystal) and total neutron diffraction, supplemented by spectroscopic methods (IR and Raman), thermal analysis and density determination.

Most of the cyanide materials discussed in this thesis could only be prepared as powdered samples of poor crystallinity. At the start of the project, they were anticipated to have relatively simple structures, describable to a first approximation using a small unit cell of volume < 300 Å^3, with high symmetry. The small unit cells, combined with the disorder in these materials, described in Chapter 1, afford powder X-ray diffraction patterns containing only a small number of broad peaks, none of which occur at high *d*-spacing. The presence of very sharp peaks or overly complex powder patterns are both indications that the samples contain impurities, such as metal formed by reduction or other crystalline materials such as synthetic by-products. Infrared spectroscopy is very sensitive when identifying possible impurities from synthesis such as sulphates or nitrates. It also provides structural information about the presence of coordinated water or ammonia within the compound, which proved essential in the cases of the platinum and palladium cyanides (Chapter 5), and also about the bonding mode of the cyanide group. Bridging CN groups give rise to stretching modes, $v_{(C\equiv N)}$, at the higher end of the 2300 – 2000 cm^{-1} range, *e.g.* $v_{(C\equiv N)}$ in AgCN and AuCN are at 2170 and 2236 cm^{-1},[1] respectively. Terminal CN groups, on the other hand, give rise to $v_{(C\equiv N)}$ modes in the middle of this range. For example, dicopper(II) trihydroxide cyanoureate dihydrate shows $v_{(C\equiv N)}$ bands at 1657 and 1650 cm^{-1}.[2] The $v_{(C\equiv N)}$ of free $CN^-_{(aq)}$ occurs at 2080 cm^{-1},[3] very similar to the value of 2077 cm^{-1} seen in solid KCN. If the powder X-ray diffraction pattern and infrared spectra are consistent with a pure single-phase material, then attempts at a full structure determination can begin.

2.2 Diffraction

2.2.1 Powder X-Ray Diffraction

2.2.1.1 Data Collection

During the period from October 2006 to October 2009, powder X-ray diffraction data were collected at room temperature by Mr Mike Andrews, Sedimentology Department, Reading, on a Siemens D5000 powder X-ray diffractometer using graphite {111} monochromated Cu K_α radiation (λ = 1.54051 Å). After October 2009, powder X-ray diffraction data were collected at room temperature in the Chemical Analysis Facility (CAF), Department of Chemistry, using a Bruker D8 powder diffractometer with germanium {111} monochromated Cu $K_{\alpha1}$ radiation (λ = 1.54060 Å). The D8 instrument was equipped with a Lynx eye area detector allowing high-resolution data to be collected quickly. In each case, bulk samples were finely ground in a pestle and mortar and pressed into the well of a sample holder. Samples of mg quantity, for example from TGA experiments were sprinkled onto a cut {100} silicon wafer. Data were collected in reflection geometry for all experiments and in each case, the sample was rotated during the collection to ensure a good powder average.

The thermal expansion behaviour for the Group 11 cyanides was determined by measuring powder X-ray diffraction patterns as a function of temperature over the temperature range $90 \leq T/\mathrm{K} \leq 490$, using an Oxford Gemini S-Ultra single-crystal diffractometer with Cu K_{α} radiation (λ = 1.54051 Å). Each finely ground sample was mounted on a drawn glass fibre using Superglue and cooled to 90 K under flowing nitrogen using an Oxford Cryojet™, and a diffraction pattern collected. The temperature was raised to 110 K and another data set collected. Subsequent data sets were collected every 20 K reaching a maximum temperature of 490 K.

2.2.1.2 Powder Diffraction Data Processing

Powder X-ray diffraction data from all three instruments were processed to obtain unit-cell parameters using the following method. The data were converted to cpi format using the Convex program and loaded into XFIT.[4] For each data set, the background was modelled using a fifth-order Chebyshev polynomial, the peaks were fitted using a mixed Gaussian-Lorentzian peak shape to determine their position and full width half maximum (FWHM). The measured peak positions were exported to CellRef,[5] where they were used for pattern indexing, unit-cell refinement and, where possible, spacegroup prediction. It was possible to index the powder patterns of the mixed Group 11 cyanides based on the unit-cell parameters and spacegroups of the parent materials CuCN, AgCN and AuCN. This method, which is similar to the Le Bail method,[6] has proved to be fast and reliable but because the intensities of the peaks are not considered, it does not provide information on the atomic positions.

2.2.2 Single-Crystal X-Ray Diffraction

During the course of this work single-crystal structure determinations of precursor materials were undertaken by Dr Ann Chippindale. Diffraction data were recorded using the Oxford Gemini S Ultra single-crystal diffractometer with Mo K_α radiation (λ = 0.71073 Å) or with Cu K_α radiation (λ = 1.54051 Å). The selected crystal was suspended in Paratone oil in a hair loop and cooled to 150 K using a Cryojet. Intensity data were merged and corrected for absorption within the program CrysalisPro.[7] The structures were solved using SIR92[8] and the models refined using CRYSTALS.[9] Thermal decomposition reactions of single crystals could be studied *in situ* up to 490 K using the Gemini instrument and the powder X-ray diffraction patterns of the final products were measured using Cu K_α radiation (λ = 1.54051 Å).

2.2.3 Neutron Diffraction

2.2.3.1 Data Collection

Neutron diffraction data were collected at the ISIS spallation neutron source at the Rutherford Appleton Laboratory on the GEM (GEneral Materials) diffractometer (Figure 2.1) which is designed for total neutron diffraction work on amorphous and disordered materials as well as crystalline materials.[10] The ISIS neutron source produces a neutron current of ~100-200 *μ*A by bombardment of protons onto a tantalum target. GEM is a time-of-flight neutron diffractometer which has a very large detector area resulting in high count rates and a good signal-to-noise ratio. High resolution data can be collected over a wide Q range by virtue of having detector banks at a variety of scattering angles.

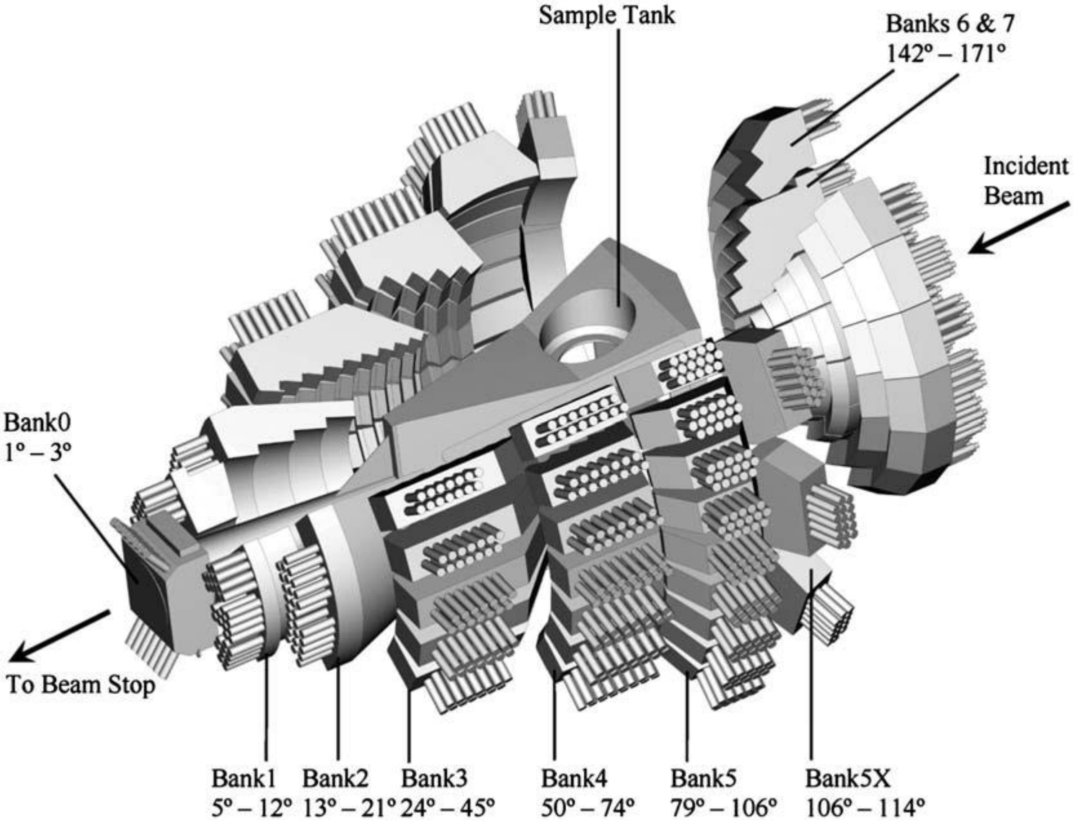

Figure 2.1 The arrangements of the detector banks on the GEM diffractometer.[10]

GEM can accommodate a number of sample environments so that samples can be studied under a variety of conditions, such as temperature and pressure. Data for the work presented here were collected on powdered samples (1-5 g) which were loaded into thin foil vanadium cans and mounted either directly inside the sample tank, for data collection at 300 K, or in a close-circuit refrigerator (CCR), for collection at 10 K. A typical length data collection for a sample to give good counting statistics, was ~800 μAh (that is 4 hours in the beam if the average beam current is 200 μA). Shorter runs of ~100 μAh were collected for use during the data correction on an empty sample can, the empty spectrometer and the empty CCR where used. A short data set was also collected for a solid vanadium rod, which is used to correct for the shape of the neutron flux arising from the pulsed nature of the ISIS spallation source.

2.2.3.2 Processing of Neutron Diffraction Data

All manipulations of neutron data were performed using the in-house ISIS software. The reduction and correction of total neutron diffraction data discussed below is summarised in Figure 2.2. Each dataset was initially screened using the purge_det program and data collected using detectors which were not functioning properly were removed. The data were then corrected for attenuation and multiple scattering using GUDRUN.[11] The data were also normalised to vanadium to produce a set of differential cross section curves, $I(Q)$, one for each detector bank. Contributions to the data from the sample environments were also subtracted. The ATLAS[12] suite of programs within Open GENIE was then used to subtract the self-scattering $I^S(Q)$ as calculated by Platom[12] from the total scattering for each detector bank. The data from each detector bank were then corrected by inspection, with a linear component subtracted from each, to ensure that they oscillated about zero. The *i(Q)* curves from detector banks 2, 3, 4 and 5 were merged into a single *i(Q)* curve whilst ensuring good overlap between data from neighbouring detector banks. The final $i(Q)$ was then extrapolated from $Q \approx 1$ to zero using the LowQ program, which fits a quadratic function to the data before the first Bragg peak. Only data for which $i(Q) = 0$ is overwritten. A preliminary Fourier transform was performed on the $i(Q)$ to generate $D(r)$. Inspection of the low r region, which should have minimum noise, gave a good indication of how well the data reduction had gone. The occurrence of a large peak, intensity ≥ 1 at $r \approx 0.1$, was a sign that the final $i(Q)$ did not oscillate about zero. If this occurred, the linear corrections needed to be adjusted and the $i(Q)$ data remerged. The slope of $D(r)$ was fitted using the pfit program and compared with the $T^0(r)$ constant calculated using Xsect.[13] The area and position of the first “real” peak in $D(r)$, which arises from C≡N correlations, were also fitted using the pfit program. These were then used to calculate the C≡N coordination number. Ideally, this value should be 1.00. A calculated value not within a few percent of 1.00 indicated that the data reduction had not been entirely successful and the $i(Q)$ data were then scaled. The fully corrected $i(Q)$ curve was used to generate a preliminary $T(r)$ by addition of the $T^0(r)$ constant, calculated from the measured density (section 2.3.4), using the Xsect program.[13] Once the structural model has been confirmed, the final $T(r)$ is generated by addition of a slightly different $T^0(r)$ constant, also calculated by Xsect, but based on the density of the crystallographic model. Use of the $T^0(r)$ constant calculated using the density of the model ensures that the data and the model are entirely consistent at higher values of r. The density of a correct structural model should be very close to that measured, and therefore the two $T^0(r)$ values should also be very close.

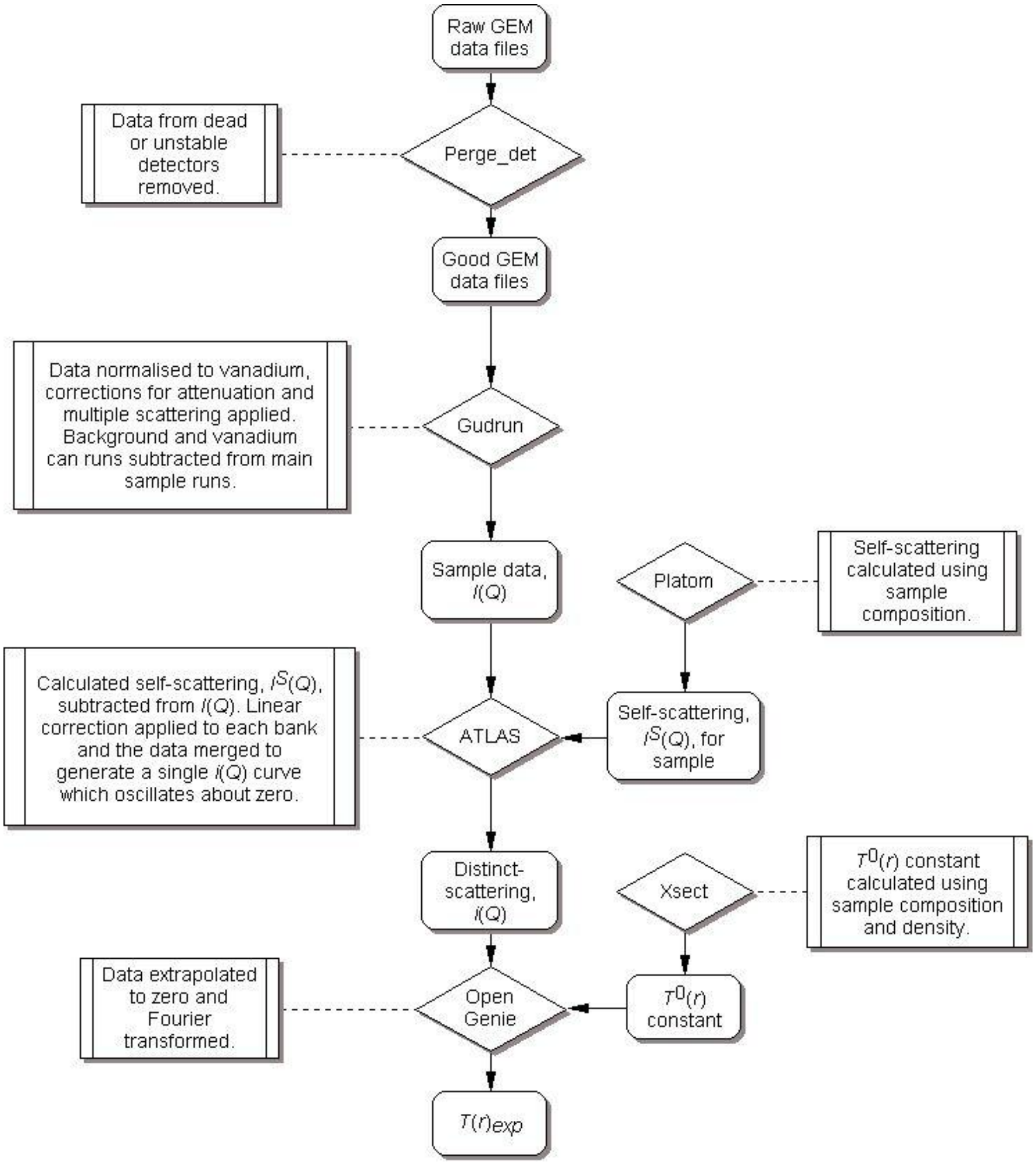

Figure 2.2 Flowchart detailing the data reduction process, rounded boxes are the input/output data, diamond boxes are the programs used and the rectangles to their sides explain their function.

2.2.3.3 Modelling *T*(*r*)

The iterative modelling process described below is summarised in Figure 2.3. The first two or three peaks in *T*(*r*) correspond to the C≡N and M-C/N bond lengths and it should be stressed that the positions of these peaks are not dependent on the data reduction process. By fitting the positions of these peaks, a low-dimensional bonded section of the structural model, such as a chain or sheet, was constructed using “chemical knowledge” of local structure.[14] From this model, a set of delta functions were calculated using the Xtal program,[15] which not only give information about the atomic distances within the model but also information about the number of occurrences of the correlations weighted by the bound coherent scattering lengths, $\bar{b}$, of the atoms involved. Crystallographic models with different packing sequences of these bonded sections were then proposed and a set of delta functions for each were calculated. The first set of delta functions from the bonded section were then subtracted from the set of delta functions from the total models to give a set delta functions arising from the interchain or interlayer contributions from the different models. To generate a complete model, the delta functions from the bonded and non-bonded sections were broadened independently using the RDF program, and then summed in a similar manner to that used previously to model AgCN[16] and Ni(CN)$_2$.[17] Interchain and intersheet correlations were broadened more rapidly with *r* than intrachain and intrasheet contributions, reflecting the possibility of static disorder between the bonded sections. Inspection showed that some models were inconsistent with the data and where two models looked quite close to the data, the goodness of fit *R* factor, $R_{T(r)}$, was calculated (2.1).[18]

$$R_{T(r)} = \sqrt{\sum \left| T(r_i)_{obs} - T(r_i)_{model} \right|^2 \Big/ \sum \left| T(r_i)_{obs} \right|^2} \qquad (2.1)$$

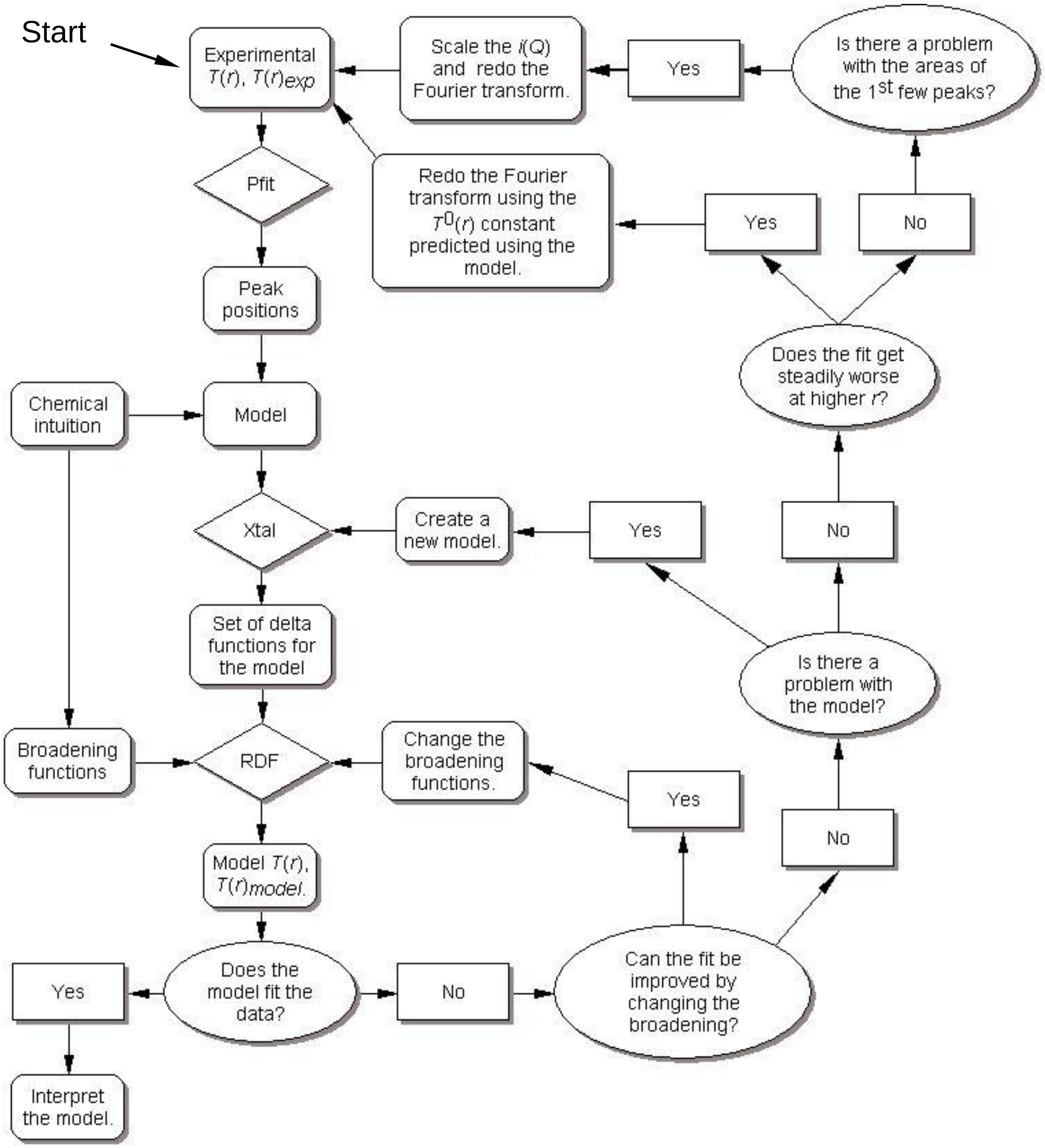

Figure 2.3 Flowchart detailing the modelling process, the rounded boxes are the input/output, diamond boxes are the programs used, round boxes are questions and the answers are in small rectangles.

All the data sets modelled in this work have been through all of the stages described above. Further details are given in each relevant chapter.

2.3 Other Methods of Sample Characterisation

2.3.1 Infrared and Raman Spectroscopy

Prior to October 2009, infrared spectra were recorded on a Perkin Elmer 1720-X Fourier transform spectrometer at a resolution of 4 cm^{-1} over the range 4000 - 500 cm^{-1}. The samples were prepared as Spectrasol® mulls mounted between polished NaCl or KBr disks. Spectrasol® is a light fraction hydrocarbon containing C-H and C-C bonds giving rise to bands around 3000 – 2650 cm^{-1} (strong) and most notably <1500 cm^{-1} at 1450 - 1370 cm^{-1} (strong) and 720 cm^{-1} (medium). Following the opening of the CAF in October 2009, IR spectra were recorded using a Perkin Elmer Spectrum 100 FT-IR spectrometer with a Universal Attenuated Total Reflection (ATR) sampling accessory. Samples were presented in powder form and pressed onto the surface of a diamond window. Spectra were collected at a resolution of 4 cm^{-1} over the range 4000 – 520 cm^{-1}. Raman spectra were measured using a Renishaw Raman microscope fitted with two lasers with wavelengths 532, and 785 nm, all of which were calibrated using an internal silicon standard. Spectra were measured at a resolution of ~1 cm^{-1} over the range 4000 – 100 cm^{-1}, with acquisition times of around 10 seconds and using statistical cosmic ray removal. Samples were presented on a glass slide covered in aluminium foil to eliminate the fluorescence from the glass slide.[19] The Raman spectra presented in Chapter 5 were measured by Miss Elena Marelli.

2.3.2 Atomic Absorption Spectroscopy

Atomic absorption measurements were measured by Allen Munday using a Perkin Elmer 1100B atomic absorption spectrometer. Alexander Pohl prepared the samples by dissolving 0.1 – 0.2 g of the sample in 10 mL boiling nitric acid which was diluted with 100 mL of distilled water. This was sprayed into the ionisation chamber at 2400 - 2700 K.

2.3.3 Thermal Analysis

Simultaneous thermogravimetric analysis and differential thermal analysis (TGA-DTA) measurements were made using a Thermal Analysis Q600 thermal analyser. A few milligrams of sample were placed in an alumina crucible and heated at 1 ˚C min^{-1} under flowing nitrogen over the temperature range ($20 \leq T$ / ˚C ≤ 300) for studying dehydration or deammoniation and over the range ($20 \leq T$ / ˚C ≤ 800) when following decomposition.

2.3.4 Density Measurements

Bulk crystallographic density measurements were made on powdered samples using a Quantachrome micropycnometer at the Rutherford Appleton Laboratory. The volume of sample is calculated using the ideal gas law by changing the partial pressure of helium in a sealed system. This value, together with the exact weight of the sample, allows the bulk density of the solid to be calculated. The crystallographic density is used to calculate the $T^0(r)$ constant, using the program Xsect, as part of the reduction of neutron diffraction data (section 2.2.3.2). Agreement between the measured density and that calculated from a proposed crystallographic model provides additional confirmation that the model is correct.

2.4 References

1. G. A. Bowmaker, B. J. Kennedy and J. C. Reid, *Inorg. Chem.*, 1998, **37**, 3968.
2. A. M. Chippindale, S. J. Hibble and E. J. Bilbe, *Acta Cryst. C*, 2009, **65**, I39.
3. K. Nakamoto, *Infrared and Raman Spectra of Inorganic and Coordination Compounds*, 3rd edn., Wiley-Interscience, New York, 1978.
4. R. W. Cheary and A. A. Coelho, EPRSC, Daresbury Laboratory, Warrington, 1996.
5. R. P. Hugel and Kappenstein, *Inorg. Chem.*, 1994, **17**, 1945.
6. A. Le Bail, H. Duroy and J. L. Fourquet, *Mater. Res. Bull.*, 1988, 447.
7. Oxford Diffraction Ltd. Abingdon, Oxford, 2006.
8. A. Altomare, G. Cascarano, C. Giacovazzo, A. Guagliardi, M. C. Burla, G. Polidori and M. Camalli, *J. Appl. Crystallogr.*, 1994, **27**, 435.
9. D. J. Watkin, C. K. Prout and L. J. Pearce, Chemical Crystallography Laboratory, University of Oxford, Oxford, 1996.
10. A. C. Hannon, *Nucl. Instrum. Methods Phys. Res., Sect. A*, 2005, 88.
11. S. E. McLain, D. T. Bowron, A. C. Hannon and A. K. Soper, ISIS Facility, Rutherford Appleton Laboratory, Didcot, 2006.
12. A. C. Hannon, W. S. Howells and A. K. Soper, Conference on Neutron Scattering Data Analysis, 1990.
13. A. C. Hannon, ISIS Facility, Rutherford Appleton Laboratory, Didcot, 1990.
14. S. J. Hibble and A. C. Hannon, *Local structure: the realm of the chemist?* in “From semiconductors to proteins: beyond the average structure”, Eds. S. J. L. Billinge and M. F. Thorpe (Kluwer Academic Publishers, New York) p.129 (2002).
15. A. C. Hannon, ISIS Facility, Rutherford Appleton Laboratory, Didcot, 1990.
16. S. J. Hibble, S. M. Cheyne, A. C. Hannon and S. G. Eversfield, *Inorg. Chem.*, 2002, **41**, 1042.
17. S. J. Hibble, A. M. Chippindale, A. H. Pohl and A. C. Hannon, *Angew. Chem. Int. Ed.*, 2007, **46**, 7116.
18. S. J. Hibble, S. P. Cooper, S. Patat and A. C. Hannon, *Acta Cryst. B*, 1999, **55**, 683.
19. J. V. Miller and E. J. Bartick, *Appl. Spectrosc.*, 2001, **55**, 1729.

Chapter 3: Preparation, Characterisation and Thermal Expansion Properties of Mixed Copper, Silver and Gold Cyanides, $(M_xM'_{1-x})CN$

3.1 Introduction

The detailed structures of copper, silver and gold cyanides have only recently been determined.[1-4] All consist of infinite one-dimensional (1-D) chains of the form –[M-C≡N]–. Copper(I) cyanide exists in two polymorphs; the low-temperature phase, LT-CuCN, and the high-temperature phase, HT-CuCN. On heating LT-CuCN to 563 K, it converts to the high-temperature form,[1] this form is metastable and can also form as the kinetic product at lower temperatures.[2] HT-CuCN has a simple structure in which the linear chains pack hexagonally parallel to the *c* axes. Adjacent chains are offset alternatively by +⅓ and -⅓ *c*.[3] Silver cyanide is isostructural with HT-CuCN (Figure 3.1). Gold cyanide adopts a similar structure to high-temperature copper cyanide and silver cyanide. The infinite linear chains still pack hexagonally, however the chains align to form sheets of gold atoms in the *ab* plane, giving AuCN true hexagonal symmetry. It seems plausible that it is aurophilic interactions that cause the AuCN chains to line up in this manner.[4] This is supported by an interchain distance in AuCN of 3.3915(1) Å, which is shorter than those seen in either HT-CuCN or AgCN, which are 3.482092(6) and 3.460638(6) Å respectively.

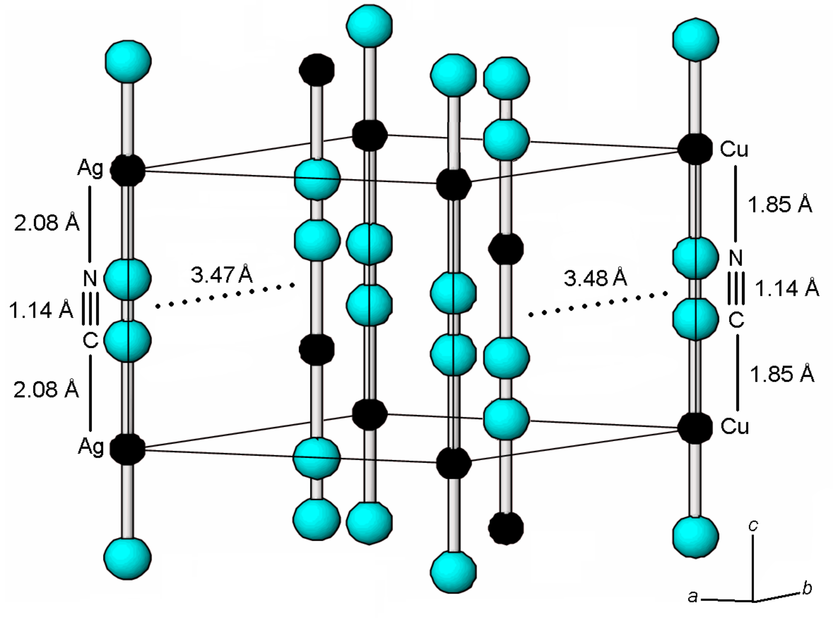

Figure 3.1 The structure of high-temperature copper cyanide and silver cyanide in spacegroup R-3m. (Key: Copper / silver (black) and head-to-tail disordered cyanide (cyan)). The C-N, M-C/N and interchain distances are shown for both compounds.

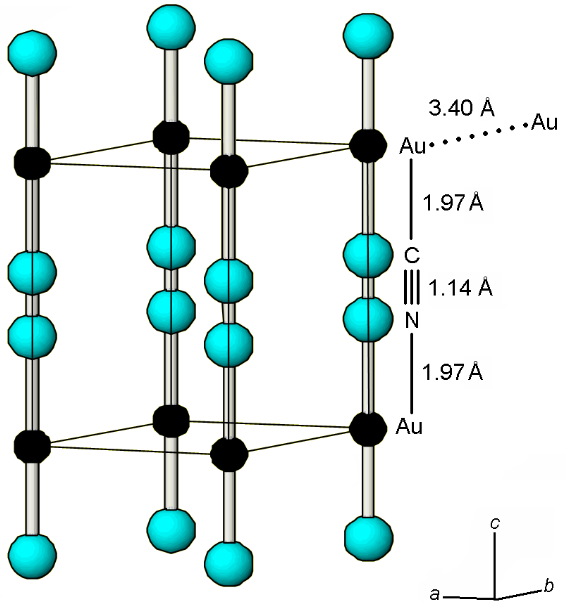

Figure 3.2 The structure of gold cyanide in spacegroup P6/mmm.. (Key: Gold (black) and head-to-tail disordered cyanide (cyan)). The C-N, M-C/N and interchain distances are shown

Low-temperature copper cyanide, LT-CuCN, adopts a more complex crystal structure, first identified in 1957[5] and solved in 2004,[6] in which the –[Cu-C≡N]– chains deviate from linearity and pack into rippled sheets in the *ac* plane. These sheets then stack in an *AB* fashion, with adjacent sheets being rotated relative to one another by 49 ˚(Figure 3.3)

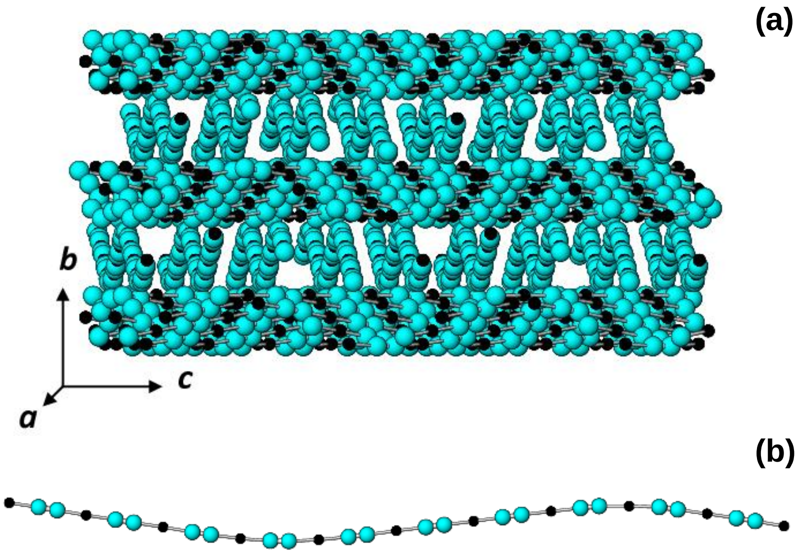

Figure 3.3 The structure of the low-temperature polymorph of copper cyanide. (a) a view showing layers of -(Cu-CN)- chains, which lie in the [150] direction. (b) a portion of a single -(Cu-CN)- chain showing the repeat distance of the wave. (Key: Copper (black) and head-to-tail disordered cyanide (cyan)).

The thermal expansion behaviour of HT-CuCN, AgCN and AuCN have been studied recently by the present author and others.[7] The behaviour of the lattice parameters of HT-CuCN (high-temperature polymorph), AgCN and AuCN was investigated as a function of temperature over the temperature range 90-490 K (Figure 3.4). All the materials show one-dimensional negative thermal expansion (NTE) along the –[M-C≡N]– chain direction *c* (α_c(HT-CuCN) = -32.1×10^{-6} K^{-1},

α_c(AgCN) = -23.9 × 10^{-6} K^{-1} and α_c(AuCN) = -9.3 × 10^{-6} K^{-1} over the temperature range 90-490 K). The one-dimensional contraction can be viewed in terms of local modes (Figure 3.5) or longer-range motions (phonons) resembling the static distortion seen in the –[Cu-C≡N]– chains in LT-CuCN (Figure 3.3(b)).

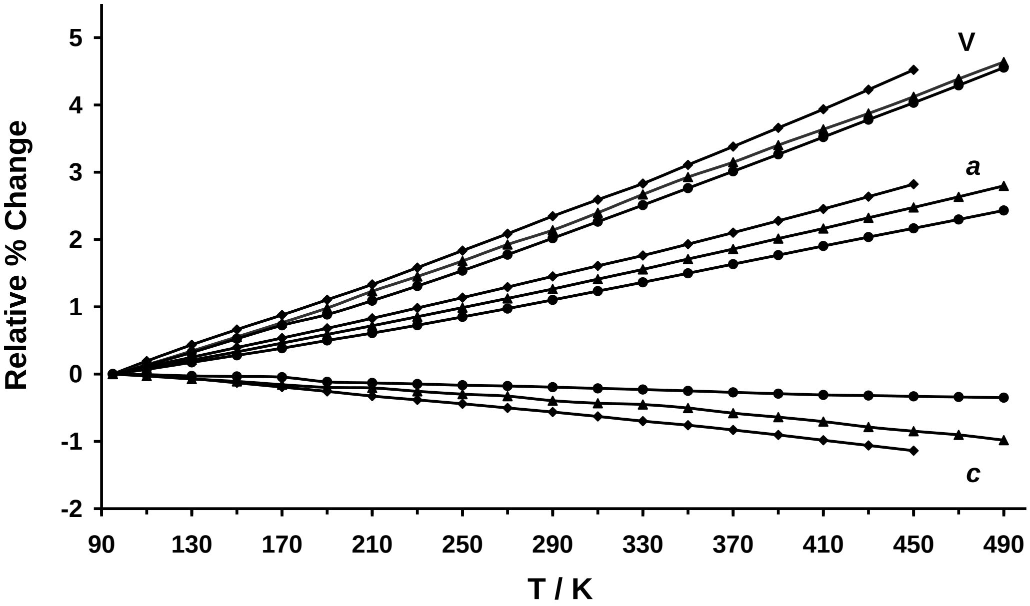

Figure 3.4 The relative percentage changes with temperature of the a and c lattice parameters and cell volume, V, for HT-CuCN (diamonds), AgCN (triangles) and AuCN (circles).

RMC modelling of Bragg and total neutron diffraction data from AgCN and AuCN at 10 and 300 K has been undertaken. The –[M-C≡N]– chains in AgCN show a much greater degree of oscillatory motion as the temperature is raised compared to those of AuCN, accounting for the larger NTE effect observed along the chain direction in AgCN. In AgCN, the “kinky” mode, in Figure 3.5(b), does not seem to occur, whereas modes similar to the “skipping-rope” mode, Figure 3.5(a), can be clearly seen. In contrast, in AuCN, both kinky and skipping-rope modes can be seen.

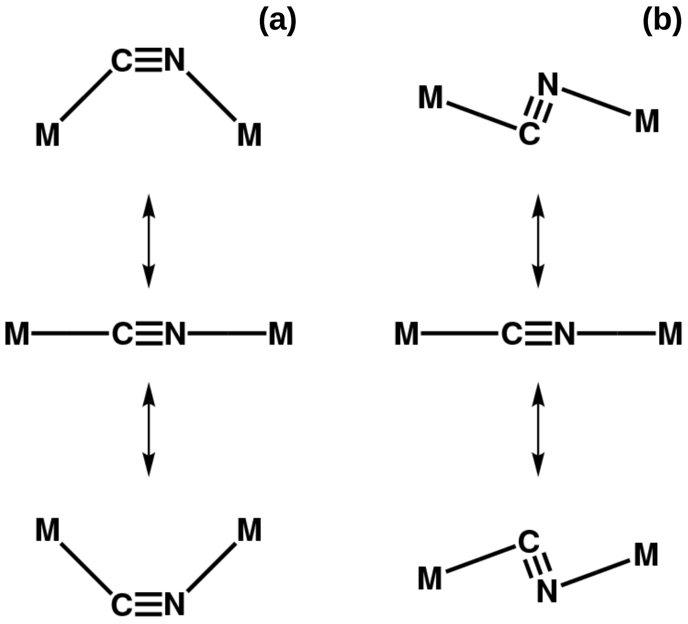

Figure 3.5 Local vibrational modes which lead to decreased metal-metal distances and NTE behaviour in M–C≡N–M units. (a) a skipping-rope mode and (b) a kinky mode.

Given that HT-CuCN and AgCN are isostructural, it seemed likely that it should be possible to prepare mixed copper-silver cyanides. The work in this chapter describes the preparation of such materials and other group 11 mixed-metal cyanides. A number of compounds of formula $(M_xM'_{1-x})CN$ have been prepared, their structure type identified *i.e.* LT-CuCN, AgCN or AuCN, and their phase limits determined. The thermal expansion properties of these mixed-metal cyanides have been determined from powder X-ray diffraction data and are compared with those of the parents HT-CuCN, AgCN and AuCN. The detailed structures of $(Cu_{0.50}Ag_{0.50})CN)$, $(Cu_{1/2}Au_{1/2})CN$ and $(Ag_{1/2}Au_{1/2})CN$, determined by total neutron diffraction, are described in Chapter 4.

3.2 Experimental

Three methods for the synthesis of mixed-metal group 11 cyanides were explored. The most general method involved precipitation of the cyanides from solutions of the parent cyanides dissolved in aqueous potassium cyanide by acid addition. This method was used to prepare Cu-Ag, Cu-Au and Ag-Au phases. The second method, the ‘coordination chemistry method’, specific to the Ag-Au system, was the addition of $[Au(CN)_2]^-$ to a solution containing Ag^+ ions. Finally, the third method involved the thermal decomposition of crystalline precursors with known metal-atom ratios. In this method, the metals are already mixed on a microscopic scale in fixed proportions and are prearranged in space. This might lead to products with different degrees of order within and/or between chains. All products were characterised using powder X-ray diffraction.

3.2.1 Acid Addition Method

To prepare mixed-metal cyanide phases, the parent metal cyanides were first dissolved in a slight excess of KCN or NaCN to form the ions $[Cu(CN)_4]^{3-}$, $[Ag(CN)_2]^-$ and $[Au(CN)_2]^-$. The solutions were mixed in appropriate ratios of any two of the metals. The resulting solution was rapidly acidified by addition of excess 1 M or 2M nitric acid to precipitate the mixed-metal cyanide phase and ensure that all the remaining CN^- was converted into HCN. The acid addition was performed under flowing nitrogen so that all exhaust gases from the experiment were passed though an alkaline bleach trap (Figure 3.6). Oxidation of cyanide containing solutions is a well recognised method for the destruction of cyanide and is used in industry.[8-9]

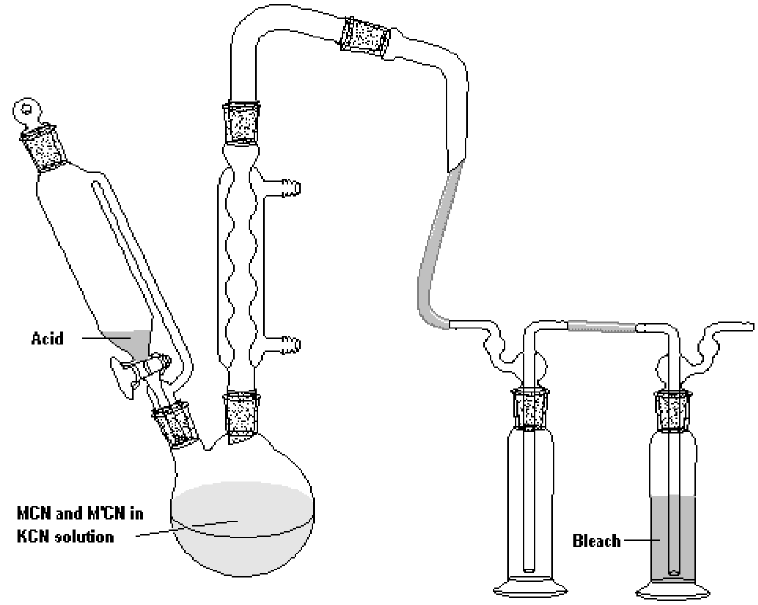

Figure 3.6 Apparatus for the addition of acid to cyanide containing solutions, (left) and scrubbing the HCN which is evolved (right).

The insoluble mixed-metal cyanide product was then filtered and washed well with water and dried in air. For each of the Cu-Ag, Cu-Au and Ag-Au systems, a range of molar ratios of the parent metal cyanides were dissolved in an attempt to create products with different compositions. Typical quantities of reagents used for preparations in the Cu-Ag system are given in (Table 3.1).

Table 3.1 Quantities of reagents used to prepare mixed Cu-Ag cyanide compounds with the AgCN structure via fast excess acid addition.

Composition	CuCN	AgCN	KCN	2M HNO_3
$(Cu_{0.83}Ag_{0.17})CN$	1.4927 g (16.7 mmol)	0.4463 g (3.3 mmol)	3.4729 g (53.3 mmol)	27 mL (54 mmol)
$(Cu_{0.66}Ag_{0.33})CN$	1.1942 g (13.3 mmol)	0.8926 g (6.7 mmol)	3.0388 g (46.7 mmol)	24 mL (48 mmol)
$(Cu_{0.50}Ag_{0.50})CN$	0.8956 g (10.0 mmol)	1.3389 g (10.0 mmol)	2.6046 g (40.0 mmol)	21 mL (42 mmol)
$(Cu_{0.33}Ag_{0.66})CN$	0.5971 g (6.7 mmol)	1.7852 g (13.3 mmol)	2.1705 g (33.3 mmol)	17 mL (34 mmol)
$(Cu_{0.17}Ag_{0.83})CN$	0.2986 g (3.3 mmol)	2.2314 g (16.7 mmol)	1.7364 g (26.7 mmol)	14 mL (28 mmol)

Powder X-ray diffraction patterns provided a useful means of identifying the structure type of the polycrystalline materials formed and checking their phase purity. For example, all the peaks in the powder X-ray diffraction patterns of the materials given in Table 3.1 could be indexed on the basis of hexagonal unit cells in R-3m with $a = b \approx 6$ Å and $c \approx 5$ Å, indicating that they all have the AgCN / HT-CuCN structure. This information, together with atomic absorption analysis (Table 3.2) confirmed that all of the parent metal cyanides had been incorporated into the products to give compounds of the form $(Cu_xAg_{1-x})CN$. The LT-CuCN structure has an orthorhombic unit cell with $a = 7.84$, $b = 12.80$ and $c = 18.15$ Å and the powder X-ray pattern is easily distinguished from that generated from the AgCN structure. The powder X-ray diffraction patterns for all the mixed-metal series, all of which are of the form $(M_xM'_{1-x})CN$, and the relationships between the product compositions and their lattice parameters are analysed in more detail in 3.3.1 and 3.3.2.

Table 3.2 Compounds in the Cu-Ag cyanide system formed by the acid addition method and atomic absorption results. Analysis results for the parent cyanides are given for comparison.

Compound	% Cu calc.	% Cu obs.	% Ag calc.	% Ag obs.
HT-CuCN	100	104	0	0
$(Cu_{0.83}Ag_{0.17})CN$	83	84	17	18
$(Cu_{0.67}Ag_{0.33})CN$	67	62	33	35
$(Cu_{0.50}Ag_{0.50})CN$	50	52	50	53
$(Cu_{0.33}Ag_{0.67})CN$	33	33	67	70
$(Cu_{0.17}Ag_{0.87})CN$	17	16	83	87
AgCN	0	0	100	99

** the estimated standard deviation for the observed values are 2%.*

A detailed description, including any variations in the general method, is given below for preparation of the bulk samples used in the neutron diffraction studies described in Chapter 4.

3.2.1.1 $(Cu_{0.50}Ag_{0.50})CN$

Copper cyanide (2.06 g, 23 mmol), silver cyanide (3.08 g, 23 mmol) and potassium cyanide (6.00 g, 92 mmol) were dissolved in 50 mL of water. 2 M nitric acid (52 mL, 104 mmol) was then added and the solution was vigorously stirred whilst under a steady flow of nitrogen gas. A curdy white precipitate appeared immediately. After 15 minutes, no further gas could be seen to be evolved and the solid was allowed to settle. As much as possible of the solution above the solid was pipetted off and treated with an alkaline bleach solution. The solid was twice stirred with 250 mL of water for 10 minutes, after which the solid and solution were separated. The pure white solid was then transferred, using 500 mL of water, to a Buchner funnel where it was washed with a further 500 mL of water and dried in air overnight and then under vacuum at 80 °C for 14 h.

3.2.1.2 ($Cu_{1/2}Au_{1/2}$)CN

Copper cyanide (0.86 g, 9.6 mmol), gold cyanide (2.14 g, 9.6 mmol) and potassium cyanide (2.50 g, 38.4 mmol) were dissolved in 50 mL of water. This solution was vigorously stirred under a steady flow of nitrogen gas and 1 M nitric acid (40 mL, 40 mmol) added to precipitate a pale yellow solid. This precipitate was then washed and dried in the same manner as ($Cu_{0.50}Ag_{0.50}$)CN above.

3.2.1.3 ($Cu_{2/3}Au_{1/3}$)CN

Copper cyanide (1.34 g, 15 mmol), gold cyanide (1.66 g, 7.5 mmol) and potassium cyanide (3.40 g, 52 mmol) were dissolved in 50 mL of water. This solution was vigorously stirred under a steady flow of nitrogen gas and 1 M nitric acid (55 mL, 55 mmol) added to precipitate a very pale yellow solid. This precipitate was then washed and dried in the same manner as above. (It should be noted that there is a small amount of LT-CuCN present with the mixed copper-gold cyanide in this sample).

3.2.2 Coordination Chemistry Method

3.2.2.1 ($Ag_{1/2}Au_{1/2}$)CN

Attempts to make ($Ag_{1/2}Au_{1/2}$)CN *via* the acid addition method resulted in the formation of ($Ag_{1/2}Au_{1/2}$)CN contaminated with a very small amount of AgCN. To avoid this complication, the ($Ag_{1/2}Au_{1/2}$)CN sample for the GEM experiments was prepared using a coordination-chemistry style synthesis. A solution of $[Au(CN)_2]^-$ was prepared by dissolving gold cyanide (1.59 g, 7 mmol) with potassium cyanide (0.46 g, 7 mmol) in 50 mL of water. A silver nitrate solution, prepared by dissolving $AgNO_3$ (1.2 g, 7 mmol) in 50 mL water, was added to the rapidly stirred $[Au(CN)_2]^-$ solution, throwing down an off-white precipitate. After stirring for a further 10 minutes, the solid was filtered, rinsed well with water and allowed to air dry.

3.2.3 Thermal Decomposition of Crystalline Precursors

An alternative route to mixed-metal cyanides is the decomposition of precursors already containing metal atoms in fixed ratios. Three new precursors of this type: $[Ag(NH_3)_2][AgCu_3(CN)_5]$, $[Ag_4Cu(CN)_5(NH_3)_3]$ and $[Au(NH_3)_2][Cu_2(CN)_4]$ were prepared as single crystals either under hydrothermal conditions or on ageing in ammoniacal solution under ambient conditions. The structures of these new materials were determined by single-crystal X-ray diffraction and these are presented in Appendices 1-3.

3.2.3.1 Synthesis of Crystalline Precursors

$[Ag(NH_3)_2][AgCu_3(CN)_5]$

Single crystals of $Cu[Ag(CN)_2][(NC)Ag(NH_3)]_3$ were prepared using hydrothermal methods. Copper cyanide (0.1791 g, 2 mmol), silver cyanide (0.2678 g, 2 mmol) and potassium cyanide (0.5215 g, 8 mmol) were dissolved in water (10 mL) with stirring. The resulting solution was placed in a Teflon lined autoclave and heated at 140 ˚C for one week. On opening the autoclave, the liner smelled strongly of ammonia and contained colourless rods of $[Ag(NH_3)_2][AgCu_3(CN)_5]$.

$[Ag_4Cu(CN)_5(NH_3)_3]$

Single crystals of $[Ag_4Cu(CN)_5(NH_3)_3]$ were prepared using hydrothermal methods. Silver cyanide (1.0719 g, 8 mmol) and sodium cyanide (0.3925 g, 8 mmol) were dissolved in ammonia solution (35 %, 20 mL). The resulting solution was divided equally between two Teflon lined autoclaves, each of which contained $CuSO_4 \cdot 5H_2O$ (0.2590 g, 1 mmol). After heating at 100 or 150 ˚C for 25 days, both bombs contained crystals of $[Ag_4Cu(CN)_5(NH_3)_3]$ in the form of colourless diamond-shaped plates.

$[Cu(NH_3)_4Cu(CN)_2][Au(CN)_2]$

Gold cyanide (0.2227 g, 1 mmol) and potassium cyanide (0.0841 g, 1.3 mmol) were dissolved in water (5 mL). This solution was added to a solution of $CuSO_4 \cdot 5H_2O$ (0.2497 g, 1 mmol) in ammonia solution (35 %, 5 mL) to form a blue solid. After two weeks, in a covered beaker, block-like crystals of sufficient size for single crystal X-ray diffraction had grown.

3.2.3.2 Thermal Decomposition Reactions

Single crystals were mounted on the Oxford Diffraction Gemini diffractometer and heated *in situ* under a nitrogen stream up to 490 K. The decomposition reactions were followed by monitoring the powder X-ray diffraction patterns. In all cases compounds of the type $(M_xM'_{1-x})CN$ were formed with loss of ammonia to produce polycrystalline products (Table 3.3). The powder pattern of $(Cu_{0.20}Ag_{0.80})CN$ prepared from $[Ag_4Cu(CN)_5(NH_3)_3]$ is shown in Figure 3.7.

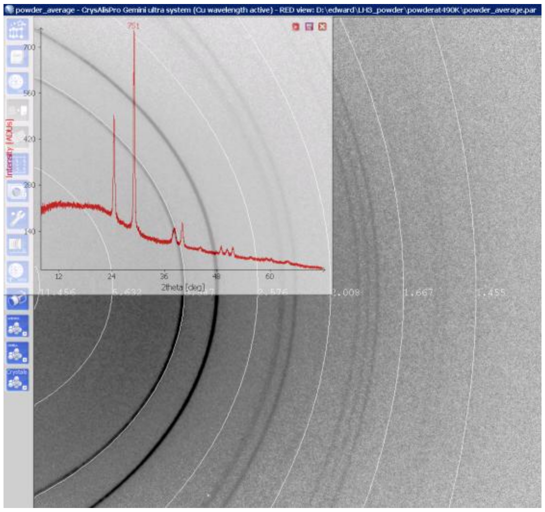

Figure 3.7 The powder X-ray diffraction pattern of $(Cu_{0.20}Ag_{0.80})CN$ *prepared in situ* on the Oxford Gemini diffractometer *from* $[Ag_4Cu(CN)_5(NH_3)_3]$

In the case of $[Cu(NH_3)_4Cu(CN)_2][Au(CN)_2]$, Cu(II) is reduced to Cu(I) during the decomposition, accompanied by the solid changing colour from blue to pale yellow, and cyanogen is also liberated, equation below.

$$[Cu(NH_3)_4Cu(CN)_2][Au(CN)_2]_{(s)} \rightarrow 3(Cu_{2/3}Au_{1/3})CN_{(s)} + 4NH_{3(g)} + \tfrac{1}{2}(CN)_{2(g)}$$

Table 3.3 Crystalline precursors, their decomposition temperatures and the mixed-metal phases formed.

Starting material	Decomposition temperature / K	Final product
$[Ag(NH_3)_2][AgCu_3(CN)_5]$	490	$(Cu_{0.60}Ag_{0.40})CN$
$[Ag_4Cu(CN)_5(NH_3)_3]$	435	$(Cu_{0.20}Ag_{0.80})CN$
$[Cu(NH_3)_4Cu(CN)_2][Au(CN)_2]$	440	$(Cu_{2/3}Au_{1/3})CN$

3.3 Results

A number of compositions have been made for the three bimetallic systems, $(Cu_xAg_{1-x})CN$, $(Cu_xAu_{1-x})CN$ and $(Ag_xAu_{1-x})CN$.

3.3.1 $(Cu_xAg_{1-x})CN$ phases

Mixed copper-silver cyanides, $(Cu_xAg_{1-x})CN$, with compositions in the range ($0.0 \le x \le 1.0$) were prepared and characterised using powder X-ray diffraction (Figure 3.8). Compositions formed, together with their refined lattice parameters, are given in Table 3.4. For some compositions, more than one sample was prepared. All these compounds are isostructural with AgCN and are white in colour.

Table 3.4 Compositions *of* $(Cu_xAg_{1-x})CN$ ($0 \le x \le 1$) prepared, together with *their lattice parameters at room temperature and the interchain distances.*

Sample	Formula	*a* / Å	*c* / Å	Interchain distance / Å*
	AgCN[$]	6.0069(22)	5.2593(31)	3.4681(13)
1a	$(Cu_{0.17}Ag_{0.83})CN$	6.0219(30)	5.2013(46)	3.4767(17)
1b	$(Cu_{0.17}Ag_{0.83})CN$	6.0116(26)	5.1691(29)	3.4708(15)
2a	$(Cu_{0.33}Ag_{0.67})CN$	6.0311(18)	5.1076(25)	3.4821(10)
2b	$(Cu_{0.33}Ag_{0.67})CN$	6.0284(21)	5.095(27)	3.4805(12)
3a	$(Cu_{0.50}Ag_{0.50})CN$	6.0215(47)	5.007(48)	3.4765(27)
3b	$(Cu_{0.50}Ag_{0.50})CN$	6.0341(71)	5.0221(105)	3.4838(41)
4a	$(Cu_{0.67}Ag_{0.33})CN$	6.0304(87)	4.9257(114)	3.4817(50)
4b	$(Cu_{0.67}Ag_{0.33})CN$	6.0379(16)	4.9556(16)	3.4860(9)
5a	$(Cu_{0.83}Ag_{0.17})CN$	6.0263(30)	4.8772(28)	3.4793(17)
5b	$(Cu_{0.83}Ag_{0.17})CN$	6.0369(27)	4.8948(34)	3.4854(16)
6a	$(Cu_{0.93}Ag_{0.07})CN$[§]	6.0309(28)	4.8453(33)	3.4819(16)
	HT-CuCN[†]	6.0306(23)	4.8286(27)	3.4818(13)
	HT-CuCN[†]	6.0308(33)	4.8238(39)	3.4819(19)

*Notes: * Interchain distance calculated from a /√3*

[$] AgCN precipitated from an equimolar mixture of $AgNO_3$ *and KCN aqueous solutions*

[§] High-temperature polymorph formed on heating LT-$(Cu_{0.93}Ag_{0.07})CN$ *at 320°C under vacuum*

[†] HT-CuCN prepared by heating LT-CuCN at 320 °C under vacuum

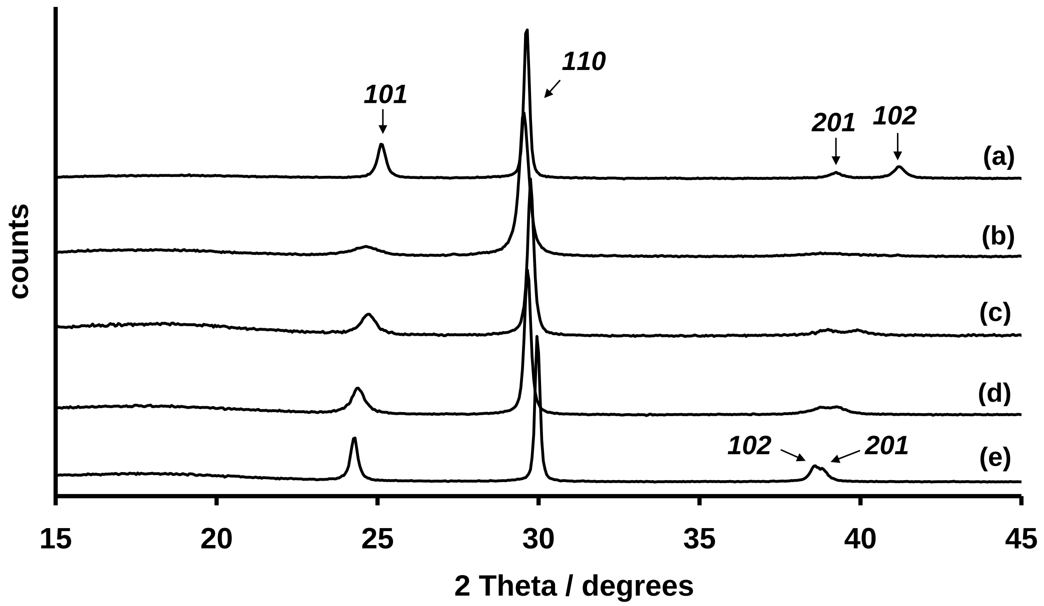

Figure 3.8 Powder X-ray diffraction patterns of (a) HT-CuCN, (b) $(Cu_{0.67}Ag_{0.33})CN$, (c) $(Cu_{0.50}Ag_{0.50})CN$, (d) $(Cu_{0.33}Ag_{0.67})CN$ and (e) AgCN

Copper rich mixed copper-silver cyanides where $x > 0.83$ were also investigated. Three further compounds, $(Cu_xAg_{1-x})CN$, with $x = 0.93$, 0.95 and 0.98 were prepared. These adopt the LT-CuCN structure.[2] For $(Cu_{0.93}Ag_{0.07})CN$, the refined orthorhombic lattice parameters are: $a = 7.67(3)$, $b = 12.77(4)$ and $c = 18.13(6)$ Å. On heating these off-white powders at 320°C under vacuum, they convert to the AgCN structure (Table 3.3). The low-temperature polymorph of copper cyanide, LT-CuCN, also converts to the AgCN structure (*i.e.* HT-CuCN) at 320 °C under vacuum. Attempts to prepare $(Cu_xAg_{1-x})CN$ with compositions in the range $(0.88 \leq x \leq 0.93)$ resulted in a mixture of products being formed. For $x = 0.88$ and 0.90, the majority of peaks found in the powder X-ray patterns correspond to a phase with the AgCN structure, with additional peaks corresponding to a phase with the LT-CuCN structure. The refined lattice parameters for the AgCN-type component within $(Cu_{0.88}Ag_{0.12})CN$ are a = 6.0375(3) and c = 4.8797(4) Å and for that within $(Cu_{0.90}Ag_{0.10})CN$ are a = 6.0360(47) and c = 4.8761(63) Å. Note: In the area of the phase diagram where $x \geq 0.88$, sodium cyanide had to be used in place of potassium cyanide to dissolve the parent metal cyanides. When KCN was used, $K[Cu_2(CN)_3].H_2O$[10] was the only product as identified by powder X-ray diffraction.

3.3.2 Discussion of $(Cu_xAg_{1-x})CN$ phases

In the copper-silver system, $(Cu_xAg_{1-x})CN$, it is possible to prepare phases with $(0.0 \leq x \leq 0.83)$ both at room temperature by acid addition and by thermal decomposition of crystalline precursors, that are isostructural with silver cyanide. Phases prepared at room temperature in the range $(0.93 \leq x \leq 1.00)$, have the LT-CuCN structure but these transform to the HT-CuCN (AgCN) structure on heating. Intermediate between these compositions, a mixture of phases is produced. Plotting the c lattice parameter as a function of composition for the $(Cu_xAg_{1-x})CN$ system, (Figure 3.9), shows that the c lattice parameter decreases with increasing values of x.

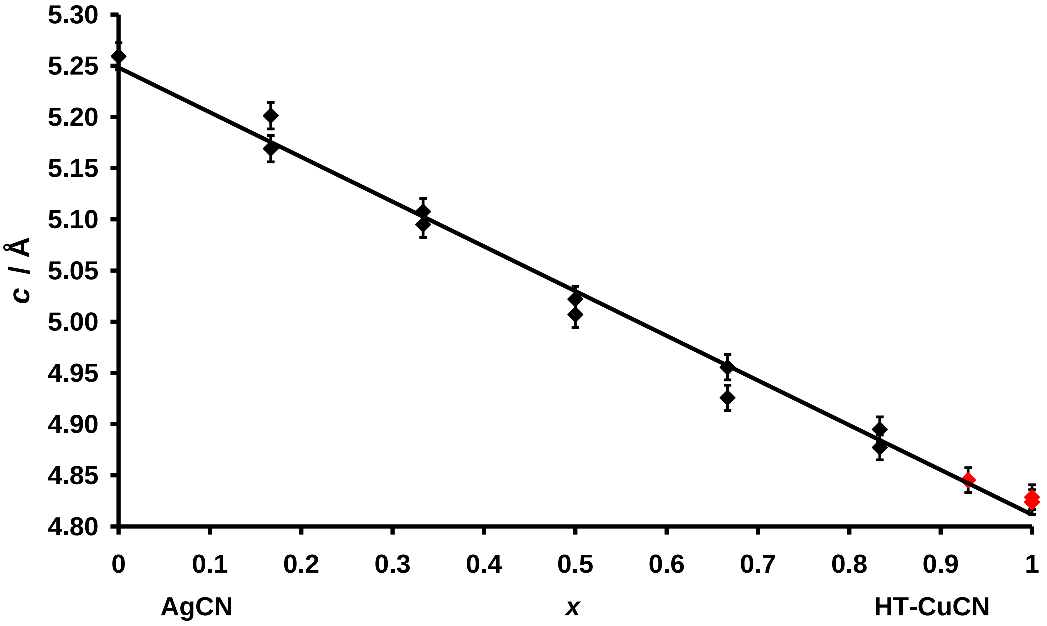

Figure 3.9 The c lattice parameter variation for (Cu_xAg_{1-x})CN as a function of composition x. The black diamonds correspond to compounds prepared at room temperature with the AgCN structure. The red diamonds correspond to compounds prepared at room temperature with the LT-CuCN structure (($Cu_{0.93}Ag_{0.07}$)CN and LT-CuCN) which transform to the AgCN structure on heating to 320 °C under vacuum. The least-squares fit line shows that the c lattice parameter obeys Vegard's law.

This decrease in the *c* lattice parameter as *x* increases reflects the difference in the average M-C/N bond lengths in CuCN and AgCN, which are 1.85 and 2.09 Å, respectively.[11] This behaviour is in accordance with Vegard's law[12] and suggests that the (Cu_xAg_{1-x})CN system forms a solid solution over the range ($0.0 \le x \le 1.0$). The phases in the range ($0.93 \le x \le 1.00$) on heating also lie on the Vegard's law straight line. The interchain distances in HT-CuCN and AgCN are quite similar, 3.482092(6) and 3.460638(6) Å, and so it is not surprising that the interchain distance, which is calculated as $a/\sqrt{3}$, does not vary greatly with composition in the mixed-metal phases (Figure 3.10).

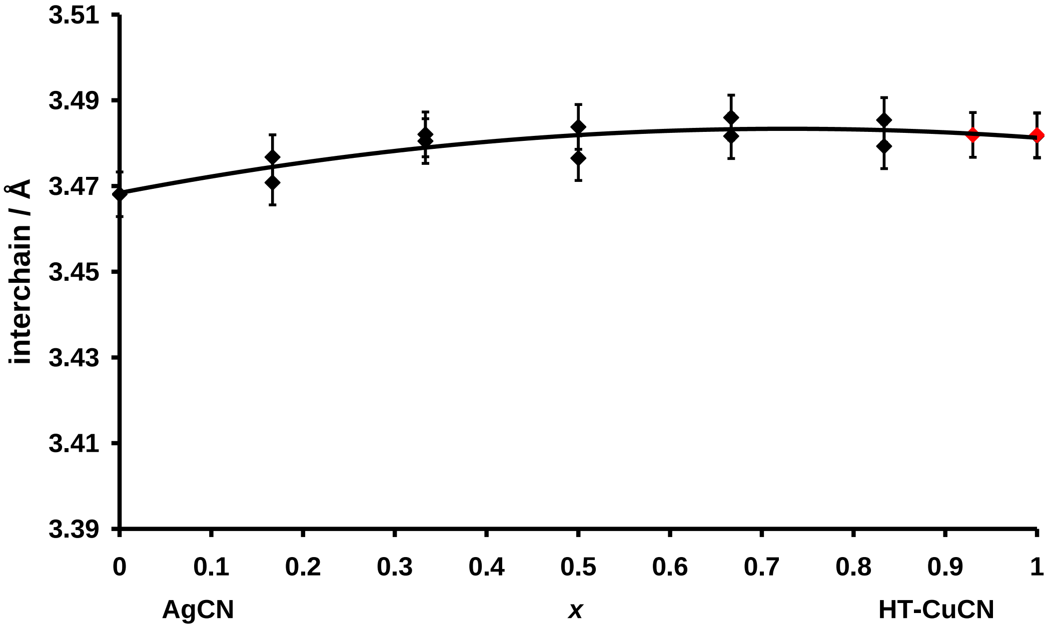

Figure 3.10 The interchain distance against composition x for (Cu_xAg_{1-x})CN. The line drawn is a second-order polynomial fit.

The maximum in the interchain distance versus composition plot can be attributed to the less efficient packing of the mixed-metal chains relative to the parents. The absence of superlattice lines in the powder X-ray diffraction patterns indicates a lack of long-range order. The question as to whether this is only between or also within the chains is discussed in the following chapter.

3.3.3 (Cu_xAu_{1-x})CN phases

In the (Cu_xAu_{1-x})CN system, two phases, ($Cu_{2/3}Au_{1/3}$)CN and ($Cu_{1/2}Au_{1/2}$)CN, have been prepared by rapid addition of acid and the former has also been prepared by thermal decomposition of $[Cu(NH_3)_4Cu(CN)_2][Au(CN)_2]$. Both are pale yellow solids, the 1:1 copper gold composition being slightly brighter yellow than the 2:1 composition. Both phases have the AuCN structure identified from their diffraction patterns (Figure 3.11, Table 3.5). The preparations of other compositions in the range (0 ≤ x ≤ 1) were also attempted but were unsuccessful in producing single phases incorporating all the metal ions from the synthesis (Figure 3.12). In preparations containing more than 66% copper cyanide, LT-CuCN was seen as an small impurity in the X-ray diffraction pattern of ($Cu_{2/3}Au_{1/3}$)CN. In preparations containing more than 50% gold cyanide, the X-ray diffraction patterns of the solid product corresponded to that of ($Cu_{1/2}Au_{1/2}$)CN. After standing for several days, the washings precipitate a bright yellow solid identified by infrared spectroscopy as gold cyanide.

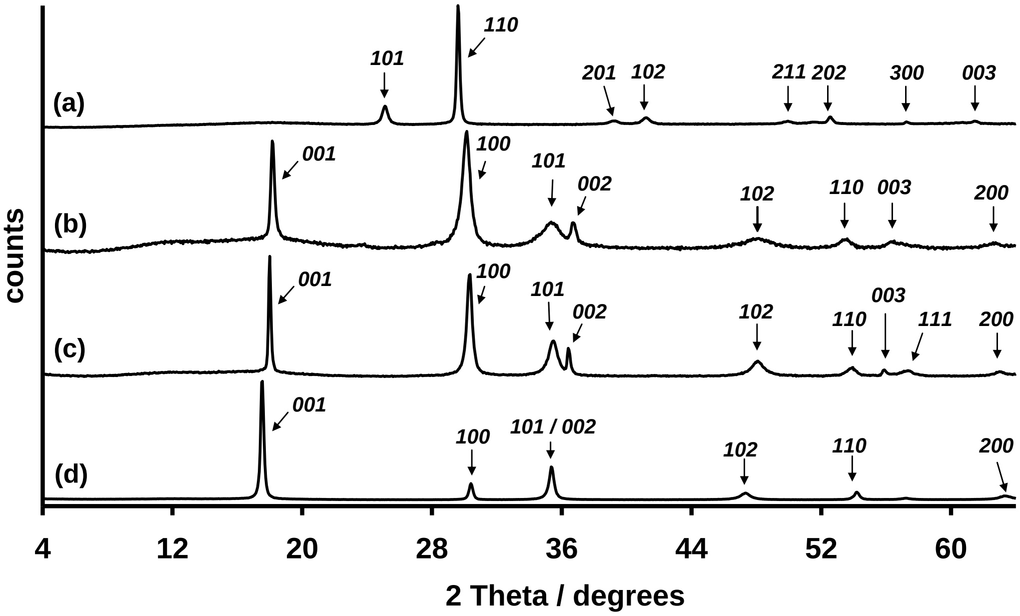

Figure 3.11 The indexed powder X-ray diffraction patterns of (a) HT-CuCN, (b) ($Cu_{2/3}Au_{1/3}$)CN, (c) ($Cu_{1/2}Au_{1/2}$)CN, and (d) AuCN, showing that b, c and d are isostructural.

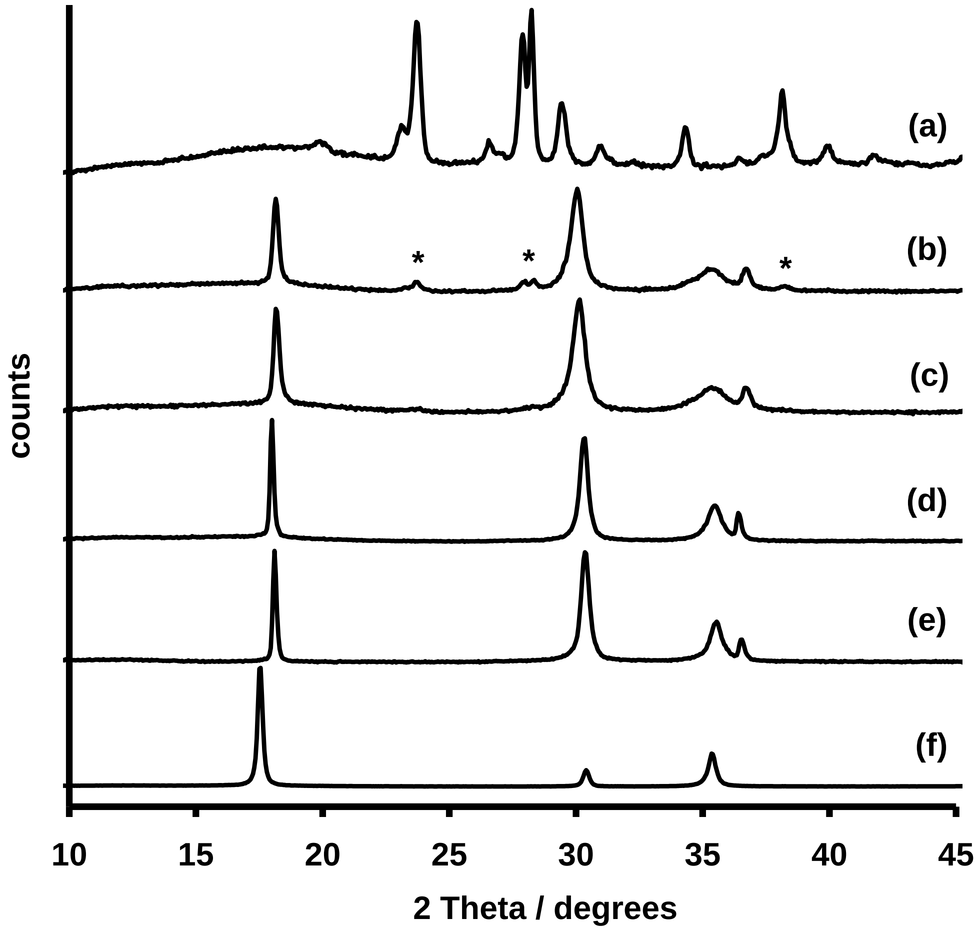

*Figure 3.12 The powder X-ray diffraction patterns of (a) LT-CuCN and the products formed attempting to make (Cu_xAu_{1-x})CN with x values of (b) 0.75, (c) 0.67, (d) 0.50 and (e) 0.25, together with (f) AuCN. The peaks in (b) marked * correspond to LT-CuCN.*

Table 3.5 Compositions of (Cu_xAu_{1-x})CN ($0 \leq x \leq 1$) prepared, together with their lattice parameters at room temperature.

sample	Formula	a / Å	c / Å	comments
1	($Cu_{0.75}Au_{0.25}$)CN	3.4347(32)	4.8998(28)	($Cu_{2/3}Au_{1/3}$)CN + LT-CuCN
2a	($Cu_{2/3}Au_{1/3}$)CN	3.4253(62)	4.8928(53)	+ trace LT-CuCN
2b	($Cu_{2/3}Au_{1/3}$)CN	3.4235(54)	4.8823(53)	+ LT-CuCN
3a	($Cu_{1/2}Au_{1/2}$)CN	3.3955(49)	4.9305(56)	
3b	($Cu_{1/2}Au_{1/2}$)CN	3.4005(37)	4.9317(47)	
4	($Cu_{0.25}Au_{0.75}$)CN	3.4074(52)	4.9283(59)	($Cu_{1/2}Au_{1/2}$)CN + AuCN in washings
	AuCN§	3.3931(85)	5.0663(69)	Aldrich

§sample from Aldrich

3.3.4 Discussion of (Cu_xAu_{1-x})CN phases

In the (Cu_xAu_{1-x})CN system, two line phases have been identified, both of which are isostructural with gold cyanide. A plot of the *c* lattice parameter against composition shows, as for the copper-silver system, a decrease in the *c* lattice parameter with increasing copper content (Figure 3.13). This decrease in the *c* lattice parameter is as expected given that the Cu-C/N bond length (1.85 Å)[3] is shorter than the Au-C/N bond length (1.97 Å)[13].

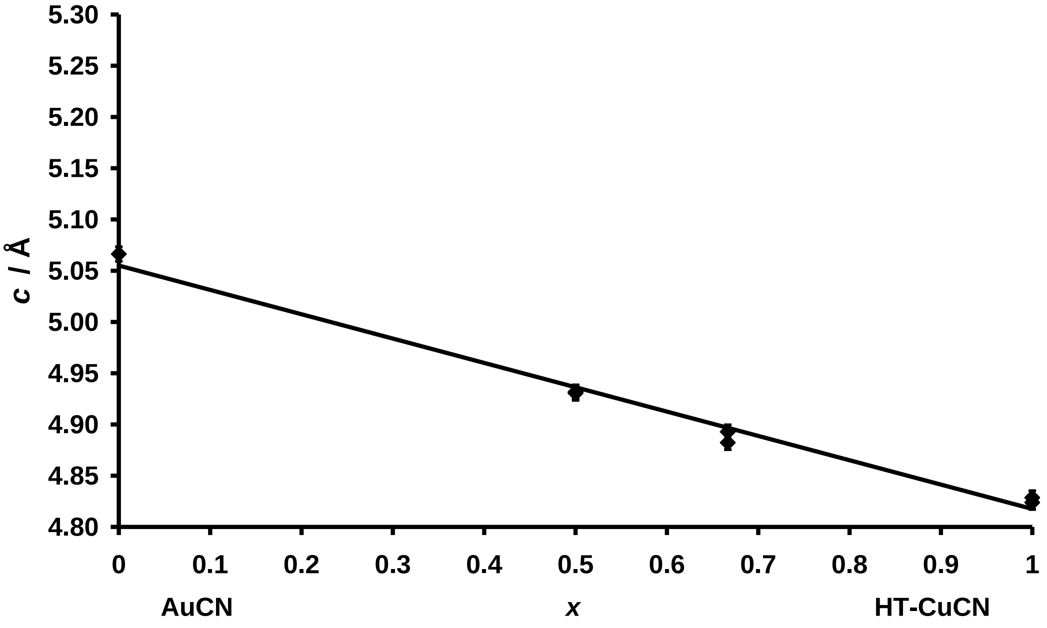

Figure 3.13 The behaviour of the c lattice parameter for (Cu_xAu_{1-x})CN as a function of composition. The least-squares fit line shows that the c lattice parameter obeys Vegard's law.

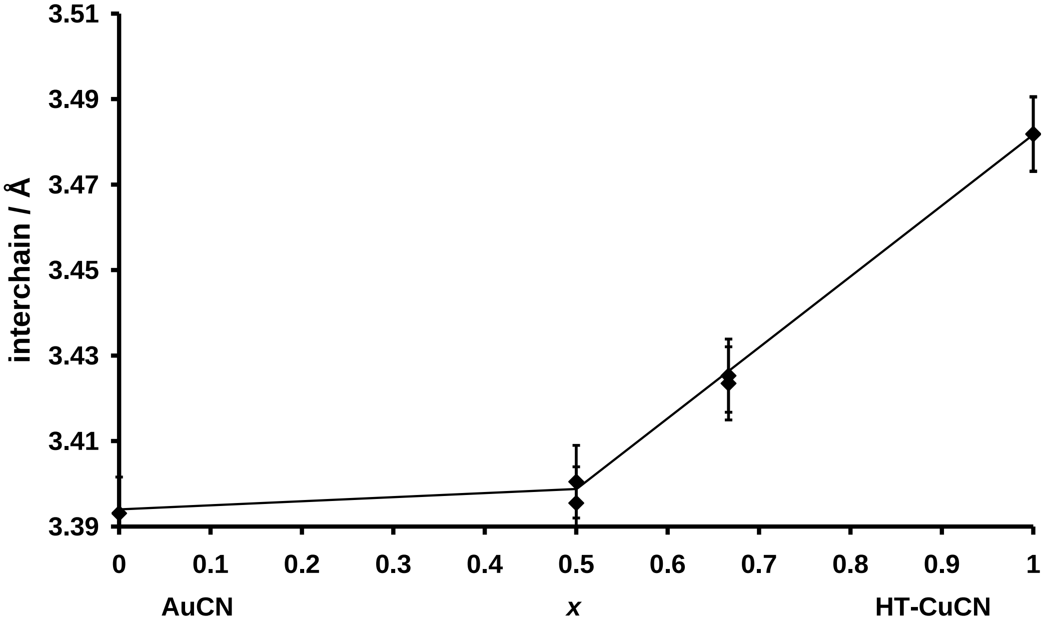

Figure 3.14 The interchain distance, equal to the a lattice parameter, against composition for the (Cu_xAu_{1-x})CN compounds. The line is drawn as an aid to the eye.

The interchain distances in ($Cu_{1/2}Au_{1/2}$)CN and gold cyanide are very similar, at 3.4005(37) and 3.3931(85) Å, respectively, suggesting that aurophilic bonding is also important in the mixed-metal system. In ($Cu_{2/3}Au_{1/3}$)CN, the chains also appear to be pulled closer together than would be expected without any aurophilic interaction since the chains are closer together than in HT-CuCN. Again the absence of superlattice reflections in the powder X-ray diffraction patterns for the mixed copper-gold phases shows that these materials lack long-range order but in this system, the existence of line phases is highly suggestive of order in individual chains. The full structural characterisation of $Cu_{1/2}Au_{1/2}CN$ is presented in Chapter 4, along with spectroscopic evidence for ordered chains in both ($Cu_{2/3}Au_{1/3}$)CN and ($Cu_{1/2}Au_{1/2}$)CN

3.3.5 ($Ag_{1/2}Au_{1/2}$)CN phases

In the silver-gold cyanide system, only one mixed-metal phase is formed and this is the line phase with composition ($Ag_{1/2}Au_{1/2}$)CN (Table 3.6). This phase was best prepared using the ‘coordination chemistry’ route (Section 3.2.2.1) in which $[Au(CN)_2]^-$ reacts with Ag^+. Powder X-ray diffraction demonstrated that the white product is isostructural with gold cyanide. Compositions made up to the silver rich side of ($Ag_{1/2}Au_{1/2}$)CN produced this phase together with AgCN. Those to the gold rich side also produced ($Ag_{1/2}Au_{1/2}$)CN but $HAu(CN)_2$ also forms precipitating gold cyanide in the washings.

Table 3.6 Compositions of (Ag_xAu_{1-x})CN ($0 \leq x \leq 1$) prepared, together with their lattice parameters at room temperature.

Sample	Formula	*a* / Å	*c* / Å	comments
	$AgCN^{\#}$	6.0069(22)	5.2593(31)	
1	$(Ag_{0.67}Au_{0.33})CN^{\dagger}$	3.4324(38)	5.1627(20)	+ AgCN
2a	$(Ag_{1/2}Au_{1/2})CN^{\dagger}$	3.4362(27)	5.1508(39)	+ AgCN
2b	$(Ag_{1/2}Au_{1/2})CN^{\$}$	3.4252(45)	5.1582(58)	
2c	$(Ag_{1/2}Au_{1/2})CN^{\$}$	3.4166(34)	5.1537(47)	
3	$(Ag_{0.30}Au_{0.70})CN$	3.4228(54)	5.1536(9)	$+HAu(CN)_{2(aq)}$
4	$(Ag_{0.17}Au_{0.83})CN$	3.4187(50)	5.1469(68)	
5	$(Ag_{0.10}Au_{0.90})CN$	3.4206(43)	5.1487(23)	
	$AuCN^{\S}$	3.3931(85)	5.0663(69)	

Note: all samples prepared by acid addition unless otherwise stated

 # Sample prepared by addition of KCN to $AgNO_3$

† AgCN impurity identified in the X-ray diffraction powder pattern

\$ sample prepared by coordination chemistry approach ($[Au(CN)_2]^-$ + Ag^+)

§ sample from Aldrich

3.3.6 Discussion of $(Ag_{1/2}Au_{1/2})$CN phase

For the system (Ag_xAu_{1-x})CN ($0 \leq x \leq 1$), there is only one mixed-metal phase, ($Ag_{1/2}Au_{1/2}$)CN, in contrast to the two phases found in the (Cu_xAu_{1-x})CN system (Figure 3.15). The *c* lattice parameter for ($Ag_{1/2}Au_{1/2}$)CN is the average of the values for the parent cyanides, AgCN and AuCN (Figure 3.16). The interchain distance in ($Ag_{1/2}Au_{1/2}$)CN is shorter than that found in AgCN (Figure 3.17), reflecting the importance of aurophilic bonding.

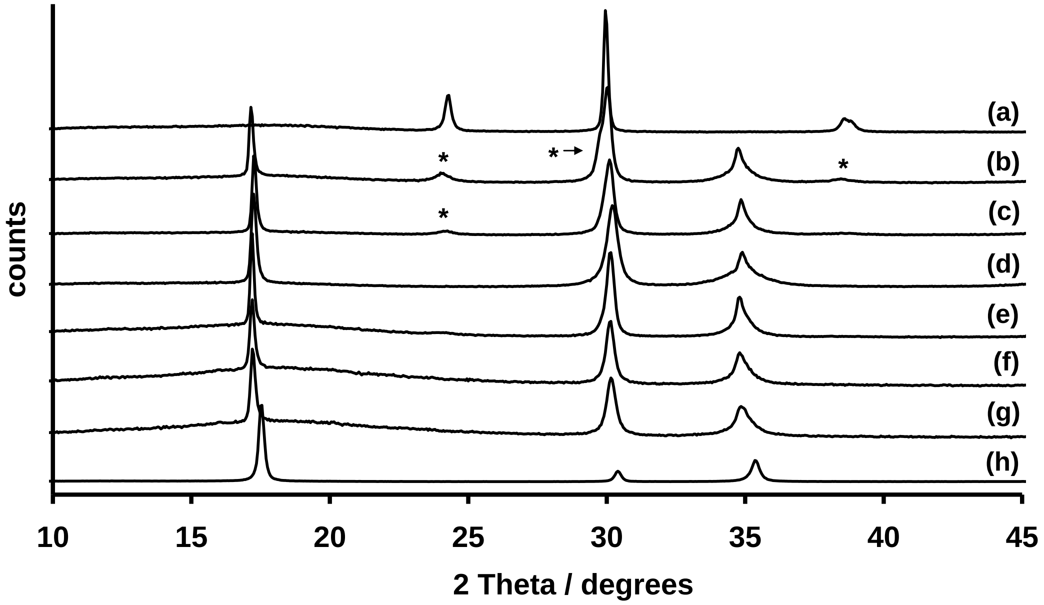

*Figure 3.15 The powder X-ray diffraction patterns of (a)AgCN and the products formed attempting to make (Ag_xAu_{1-x})CN with x values of (b) 0.67, (c) 0.50 (acid addition method), (d) 0.50 (coordination chemistry route), (e) 0.30, (f) 0.17 and (g) 0.10, together with (h) AuCN. The peaks in (b) and (c) marked * correspond to AgCN.*

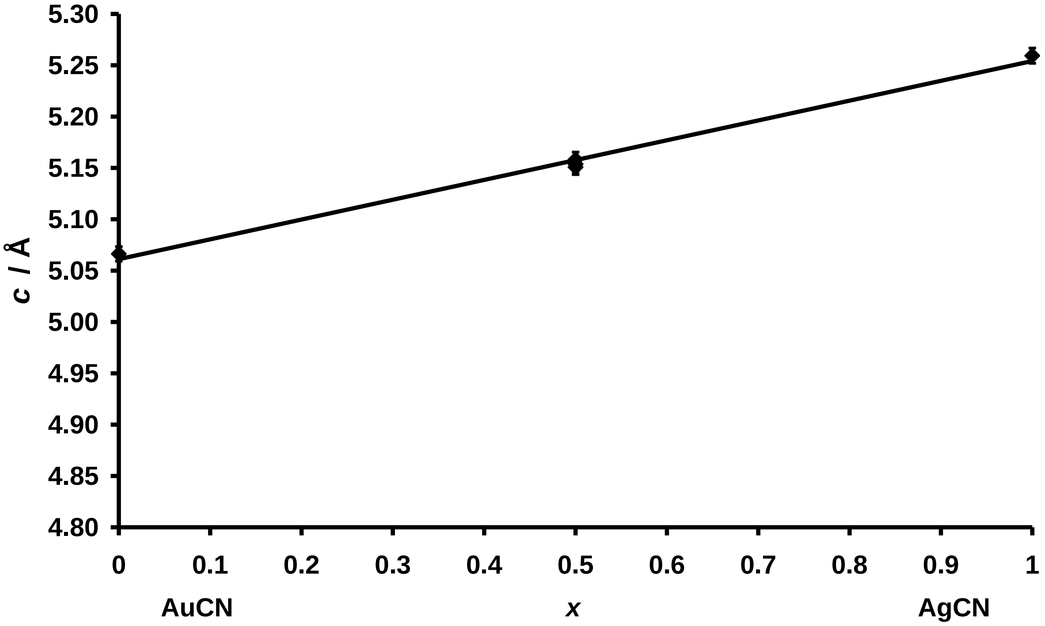

Figure 3.16 The behaviour of the c lattice parameter for (Ag_xAu_{1-x})CN as a function of composition. The line is a least-squares fit.

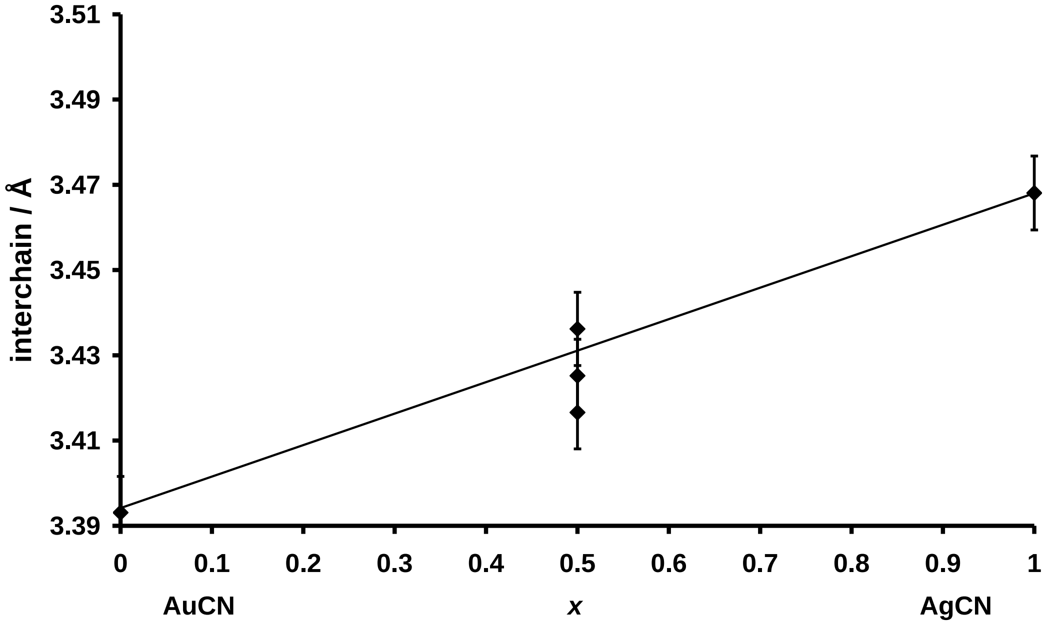

Figure 3.17 The interchain distance, equal to the a lattice parameter for the gold containing compounds, against composition for (Ag_xAu_{1-x})CN. The line is an aid to the eye.

Although the formation of a single mixed-metal phase suggests that the chains in ($Ag_{1/2}Au_{1/2}$)CN are ordered there is no evidence from the Bragg diffraction that this is the case.

3.4 Conclusions on the formation of mixed-metal cyanides ($M_xM'_{1-x}$)CN

In this chapter it has been shown that it is possible to prepare mixed metal cyanides in the CuCN-AgCN, CuCN-AuCN and AgCN-AuCN systems. In the CuCN-AgCN system, where the end members are isostructural, a solid solution exists across the complete compositional range. In the CuCN-AuCN and AgCN-AuCN systems, only line phases exist. All the intermediate phases formed,

$(Cu_{1/2}Au_{1/2})CN$, $(Cu_{2/3}Au_{1/3})CN$ and $(Ag_{1/2}Au_{1/2})CN$ have the gold-cyanide structure type. The existence of line phases in the gold-containing systems can be accounted for because only with rational ratios can the metal atoms remain aligned in layers. Accounting for the particular ratios adopted is more difficult. It is clear that large ratios of Cu:Au or Ag:Au might be unfavourable because the loss of the favourable aurophilic interaction becomes outweighed by the repulsive forces between non metals in the chains when held in the gold-cyanide structure. The occurrence of the phases, $(Cu_{1/2}Au_{1/2})CN$ and $(Ag_{1/2}Au_{1/2})CN$, can be explained if individual chains order as it seems likely that the enthalpy of formation of the two possibilities, M-NC-Au-CN-M and M-CN-Au-NC-M, will differ. In the $(Cu_{2/3}Au_{1/3})CN$ case, the enthalpic payback from forming links with NC-Au-CN-Cu-(ZZ′)-Cu-NC-Au or CN-Au-NC-Cu-(ZZ′)-Cu-CN-Au with CN order between the gold and copper atoms must outweigh the loss of the favourable aurophilic interactions. Figure 3.18 shows a possible local arrangement for $(Ag_{1/2}Au_{1/2})CN$. If there was long-range order in *a* and *b* as well as within the chains, superlattice peaks would be seen in the powder X-ray diffraction pattern. These are not observed however and so there must be disorder at least in the *a* and *b* directions. The structures of these materials are determined in Chapter 4.

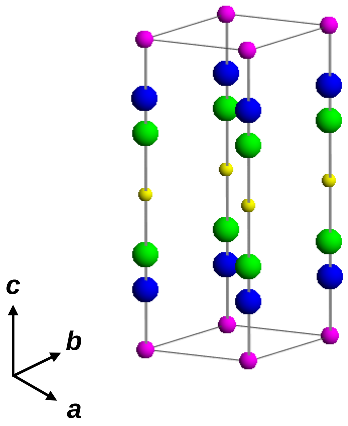

Figure 3.18 A possible model of $(Ag_{1/2}Au_{1/2})CN$ *containing ordered -[Au-CN-Ag]- chains. (Key: gold (yellow); silver (pink); carbon (green) and nitrogen (blue)).*

3.5 <u>Thermal expansion behaviour of the mixed-metal cyanides</u>

3.5.1 Determination of the thermal expansion coefficients

To investigate the thermal expansion (NTE) behaviour of the mixed-metal cyanides, their lattice parameters were measured on the Oxford Diffraction Gemini diffractometer between 95 and 490 K. The relative percentage changes in the lattice parameters and unit-cell volume as a function of temperature are shown in Figures 3.19 - 3.22.

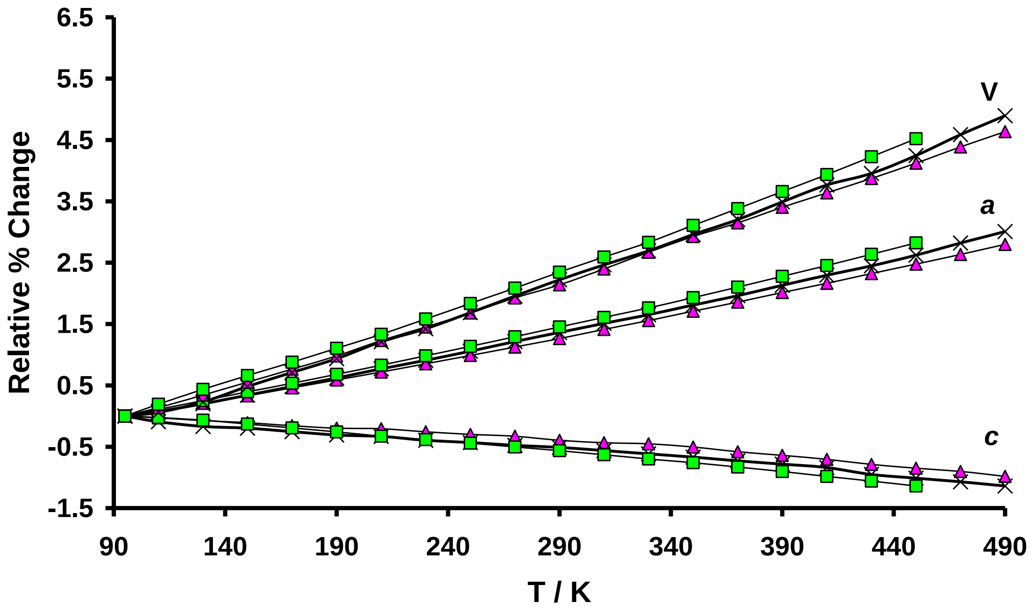

Figure 3.19 The relative percentage changes in the volume, a and c lattice parameters for HT-CuCN (green squares), $(Cu_{0.50}Ag_{0.50})CN$ (crosses) and AgCN (pink triangles).

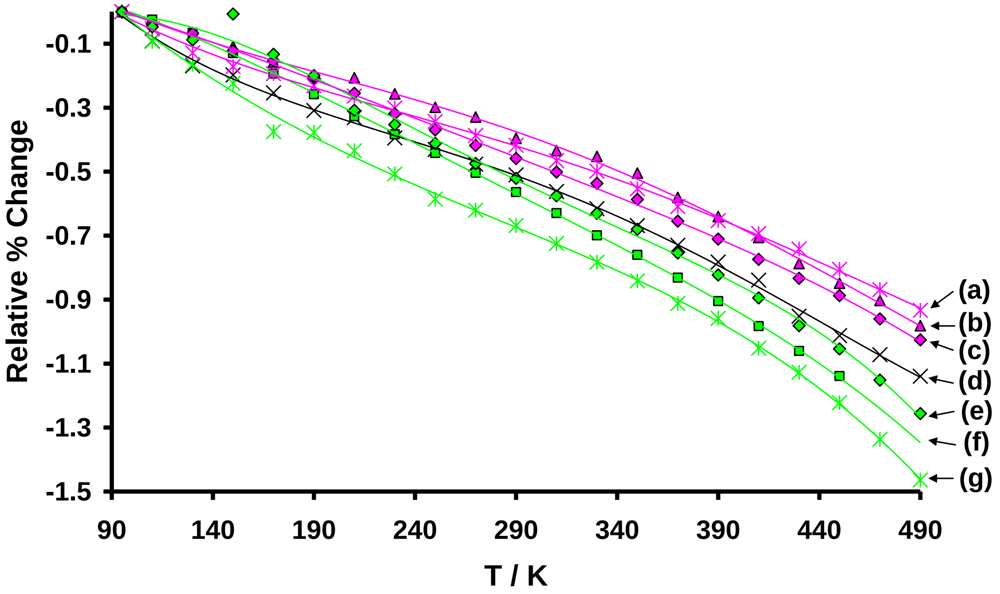

Figure 3.20 The relative percentage changes in the c lattice parameter for (a) $(Cu_{1/3}Ag_{2/3})CN$, (b) AgCN, (c) $(Cu_{1/6}Ag_{5/6})CN$, (d) $(Cu_{0.50}Ag_{0.50})CN$, (e) $(Cu_{5/6}Ag_{1/6})CN$, (f) HT-CuCN and (g) $(Cu_{2/3}Ag_{1/3})CN$. The data are all fitted using 4th order polynomials.

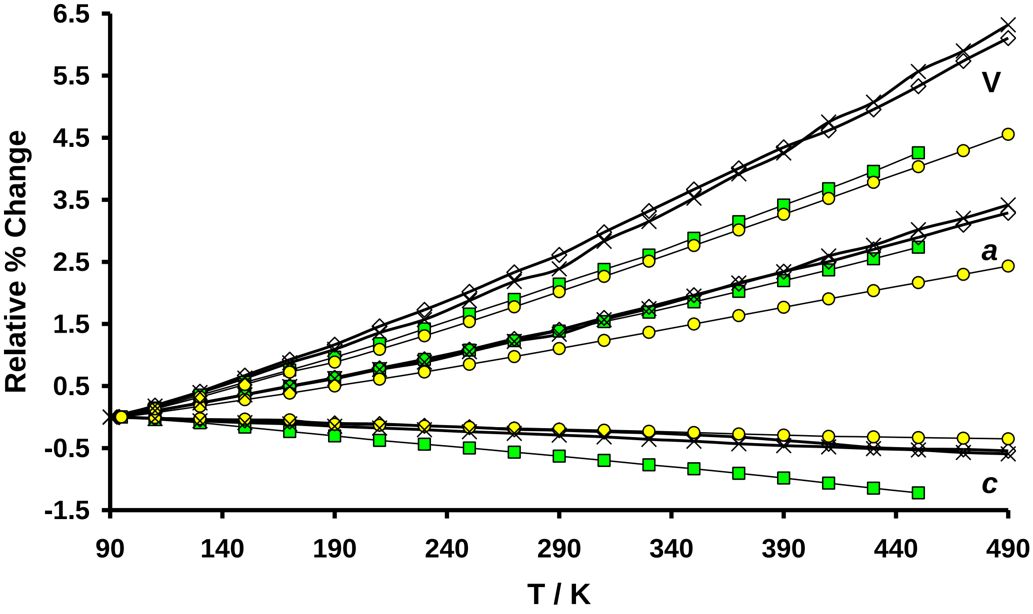

Figure 3.21 The relative percentage changes in the volume, a and c lattice parameters for CuCN (green squares), ($(Cu_{1/2}Au_{1/2})CN$ (crosses), $(Cu_{2/3}Au_{1/3})CN$ (open diamonds) and AuCN (yellow circles).

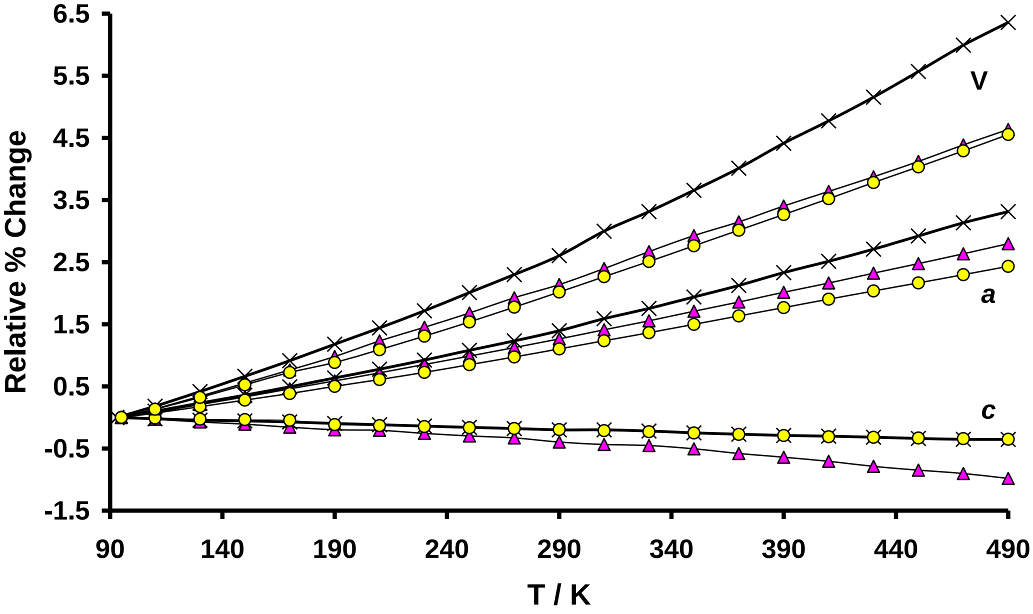

Figure 3.22 The relative percentage changes in the volume, a and c lattice parameters for AgCN (pink triangles), $(Ag_{1/2}Au_{1/2})CN$ (crosses) and AuCN (yellow circles).

Values of thermal expansion coefficients, α, were calculated using Equation 1.10 in Chapter 1, from the change in lattice parameters between 95 and 450 K to allow direct comparison with the data measured for HT-CuCN and the other parent cyanides (Table 3.7).

Table 3.7 Values of thermal expansion coefficients, α, for simple and mixed group 11 metal cyanides.

	α_a^* / 10^{-6} K^{-1}	α_c / 10^{-6} K^{-1}	α_{vol}^* / 10^{-6} K^{-1}
HT-CuCN	79.5	-32.1	127.4
AgCN	69.8	-23.9	116.1
AuCN	61.0	-9.3	113.6
$(Cu_{0.83}Ag_{0.17})CN$	77.4	-29.7	125.6
$(Cu_{0.67}Ag_{0.33})CN$	73.2	-34.4	112.0
$(Cu_{0.50}Ag_{0.50})CN$	73.9	-28.5	119.6
$(Cu_{0.33}Ag_{0.67})CN$	74.7	-22.7	127.6
$(Cu_{0.17}Ag_{0.83})CN$	72.6	-25.0	120.7
$(Cu_{2/3}Au_{1/3})CN$	83.8	-14.7	154.6
$(Cu_{1/2}Au_{1/2})CN$	81.3	-14.4	149.7
$(Ag_{1/2}Au_{1/2})CN$	82.3	-9.5	156.9

Note: $^*\alpha_a = (a_{T=450K} - a_{T=95K}) / a_0(450 - 95)$ and $\alpha_V = (V_{T=450K} - V_{T=95K}) / V_0(450 - 95)$.

3.5.2 Discussion of the thermal expansion behaviour

All the mixed-metal cyanides show negative thermal expansion in the *c* direction. This is accompanied by positive thermal expansion in the *ab* plane. This behaviour is similar to that shown by the parent cyanides.[7] It is notable that the NTE, which occurs along the chain direction *c*, is much smaller in the gold-containing systems, which have the AuCN structure type, than in the copper-silver system, with the AgCN structure type. This suggests that the magnitude of the NTE effect depends not only on the intrinsic flexibility of individual chains, but also on the way the chains are packed together. Motions such as that shown in Figure 3.23 must be more constrained in the gold-cyanide structure type because they are closer together which would be expected to increase repulsion between the chains. Other types of local motion have been suggested as contributing to the contraction in the *c* direction.[7] All of these motions involve lateral displacements of the atoms in the *ab* plane normal to the chain. These would be expected to force the chains apart causing the expansion in the *ab* plane which is indeed observed. It is notable that the thermal expansion coefficient, α_a (= α_b), is similar for all materials.

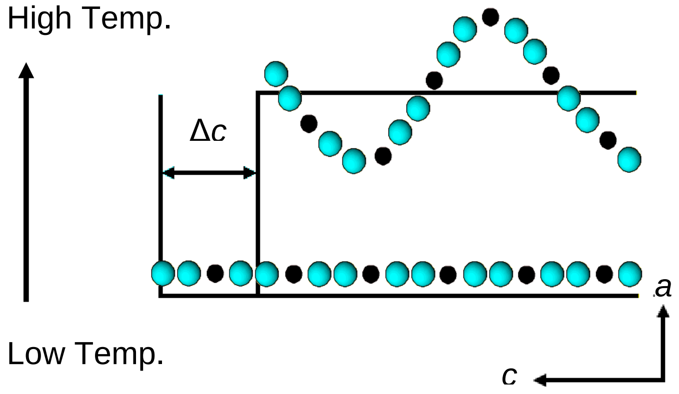

Figure 3.23 The thermal behaviour of an –(M-ZZ)– chain. (Key: metal (black) and disordered cyanide groups (cyan)). With increasing temperature the c lattice parameter contracts while the a lattice parameter expands.

3.6 Conclusions and further work

In this chapter, it has been demonstrated that mixed-metal cyanides of the group 11 metals can be prepared with general formula $(M_xM'_{1-x})CN$. In the copper-silver cyanide system, a solid solution, $(Cu_xAg_{1-x})CN$ ($0.0 \leq x \leq 1.0$), is formed which has the AgCN structure type. The gold-containing systems form the line phases, $(Cu_{1/2}Au_{1/2})CN$, $(Cu_{2/3}Au_{1/3})CN$ and $(Ag_{1/2}Au_{1/2})CN$, all with the AuCN structure. The thermal expansion behaviour of these materials has been measured and all compounds, like the simple parents HT-CuCN, AgCN and AuCN, show negative thermal expansion along the direction of the metal-cyanide chains. All the gold-containing materials show markedly lower NTE values compared to the copper-silver system. Future work could include a detailed study using total neutron diffraction together with RMC modelling to determine how the motions in the $M(CN)_2$ units and links between the chains varies with structure type.

3.7 References

1. J. Wang, M. F. Collins and G. P. Johari, *Phys. Rev. B*, 2002, **65**, 214201.
2. A. M. Chippindale, S. J. Hibble and A. R. Cowley, *Inorg. Chem.*, 2004, **43**, 8040.
3. S. J. Hibble, A. C. Hannon, S. M. Cheyne and S. G. Eversfield, *Inorg. Chem.*, 2002, **41**, 4990.
4. M. O. Hakala and P. Pyykko, *Chem. Comm.*, 2006, 2890.
5. D. T. Cromer, R. M. Douglass and E. Staritzky, *Anal. Chem.*, 1957, **29**, 316.
6. S. J. Hibble, S. G. Eversfield, A. R. Cowley and A. M. Chippindale, *Angew. Chem. Int. Ed.*, 2004, **43**, 628.
7. S. J. Hibble, G. B. Wood, E. J. Bilbe, A. H. Pohl, M. G. Tucker, A. C. Hannon and A. M. Chippindale, *Z. Kristallogr.*, 2010, **225**, 457.
8. L. F. Oeming, *Sewage Works Journal*, 1946, **18**, 678.
9. A. N. Corcoran, *Sewage and Industrial Waste*, 1950, **22**, 228.
10. D.T. Cromer and A.C. Larson, *Acta Crystallographica Section E*, 1962, **15**, 397.
11. S. M. Cheyne, PhD Thesis, The University of Reading, 2004.
12. A. R. Denton and N. W. Ashcroft, *Physical Review A*, 1991, **43**, 3161.
13. S. J. Hibble, A. C. Hannon and S. M. Cheyne, *Inorg. Chem.*, 2003, **42**, 4724.

Chapter 4: The Structures of Mixed Copper, Silver and Gold Cyanides, $(M_xM'_{1-x})CN$

4.1 Introduction

In Chapter 3, it was established that mixed-metal cyanides of the group 11 metals can be synthesised. The structure types adopted, together with the phase limits of the mixed metal phases, were determined using powder X-ray diffraction. This chapter describes further the structural characterisation of these materials. The principal method used is total neutron diffraction with additional information gleaned from vibrational spectroscopy and powder X-ray diffraction. Figure 4.1(a) shows the structure of AgCN, which is adopted by the mixed-metal compounds, $Cu_xAg_{1-x}CN$ ($0 \leq x \leq 1$). Figure 4.1(b) shows the structure of AuCN adopted by the mixed-metal compounds, $Cu_{1/2}Au_{1/2}CN$, $Cu_{2/3}Au_{1/3}CN$ and $Ag_{1/2}Au_{1/2}CN$. Important bond lengths and distances for the parent compounds, determined from total neutron diffraction, are marked on Figure 4.1. The M-C and M-N bond lengths for a particular metal are identical or nearly so. This suggests that head-to-tail disorder of the cyanide group might occur. Although this disorder is difficult to establish even using total neutron diffraction, it has been confirmed in CuCN, AgCN and AuCN by solid-state NMR measurements.[1-3] It is clear from previous neutron diffraction experiments that there are substantial differences in the M-C/N bond lengths for different metals. How the different M-C/N bond lengths are accommodated in the mixed-metal systems, and whether the cyanide groups order when there are different metals in the M-CN chains, are questions that can be answered using total neutron diffraction when the bond lengths are different and the metals have different scattering lengths.

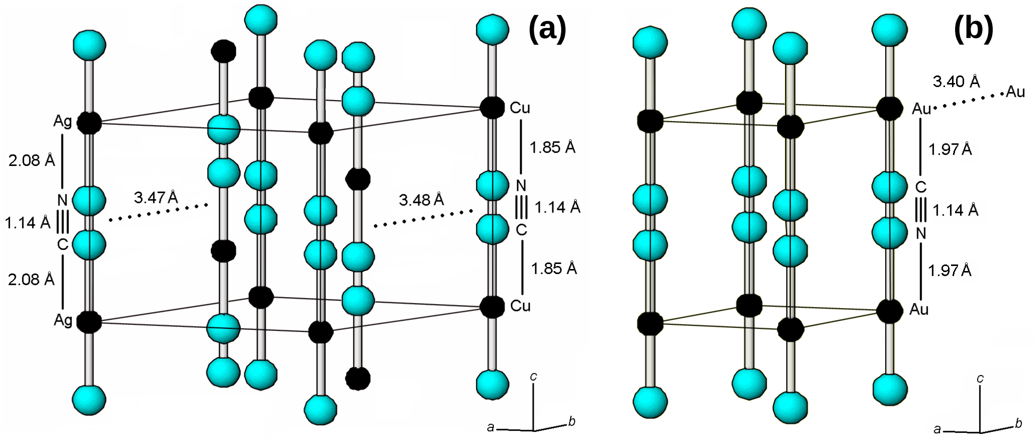

Figure 4.1 The structures of (a) high-temperature copper and silver cyanides in R-3m and (b) gold cyanide in P6/mmm. (Key: Copper, silver and gold (black) and head-to-tail disordered cyanide groups (cyan)). The C≡N, M-C/N and interchain distances are shown for all compounds.

Below is presented the evidence from vibrational spectroscopy for cyanide and metal ordering within individual chains in the mixed-metal cyanides containing gold; $(Cu_{1/2}Au_{1/2})CN$, $(Cu_{2/3}Au_{1/3})CN$ and $(Ag_{1/2}Au_{1/2})CN$. In the cases of $(Cu_{1/2}Au_{1/2})CN$ and $(Ag_{1/2}Au_{1/2})CN$, the conclusions are confirmed using total neutron diffraction. Neutron diffraction also yields accurate bond lengths and shows that it is the carbon end of the cyanide ligand that is bound to the gold atoms in all cases. Powder X-ray diffraction shows no evidence for long-range order *i.e.* all of the diffraction patterns from all of the materials have patterns which can be indexed on the basic cells shown in Figure 4.1. The reasons for the lack of long-range order, but at the same time the existence of only line phases for the gold containing systems, are discussed. Vibrational spectroscopy is not as useful in the case of the mixed-metal copper-silver cyanide phases and neutron diffraction is needed to prove that $(Cu_{0.50}Ag_{0.50})CN$ has both metal and cyanide order within individual chains. In this case, the carbon end of the cyanide ligand is bound to silver.

4.2 IR and Raman Spectroscopy

Infrared spectra were recorded for all the mixed-metal cyanide phases and Raman spectra measured for the parent cyanides CuCN, AgCN and AuCN and for $(Cu_{0.50}Ag_{0.50})CN$, $(Cu_{2/3}Au_{1/3})CN$, $(Cu_{1/2}Au_{1/2})CN$ and $(Ag_{1/2}Au_{1/2})CN$ (Figures 4.2 - 4.4, Table 4.1).

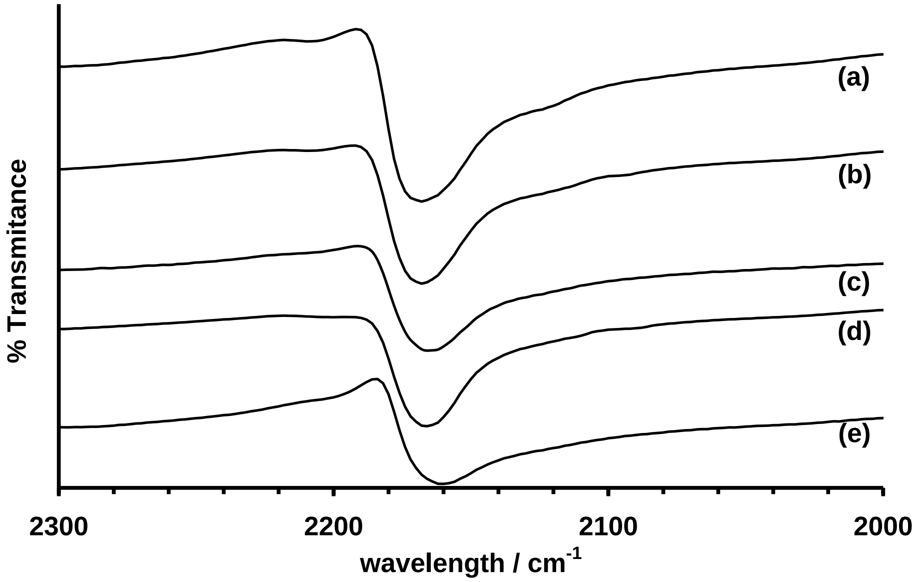

Figure 4.2 Infrared spectra in the $\nu_{C\equiv N}$ *region of (a)* $(Cu_{0.83}Ag_{0.17})CN$*, (b)* $(Cu_{0.67}Ag_{0.33})CN$*, (c)* $(Cu_{0.50}Ag_{0.50})CN$*, (d)* $(Cu_{0.33}Ag_{0.67})CN$ *and (e)* $(Cu_{0.17}Ag_{0.83})CN$*.*

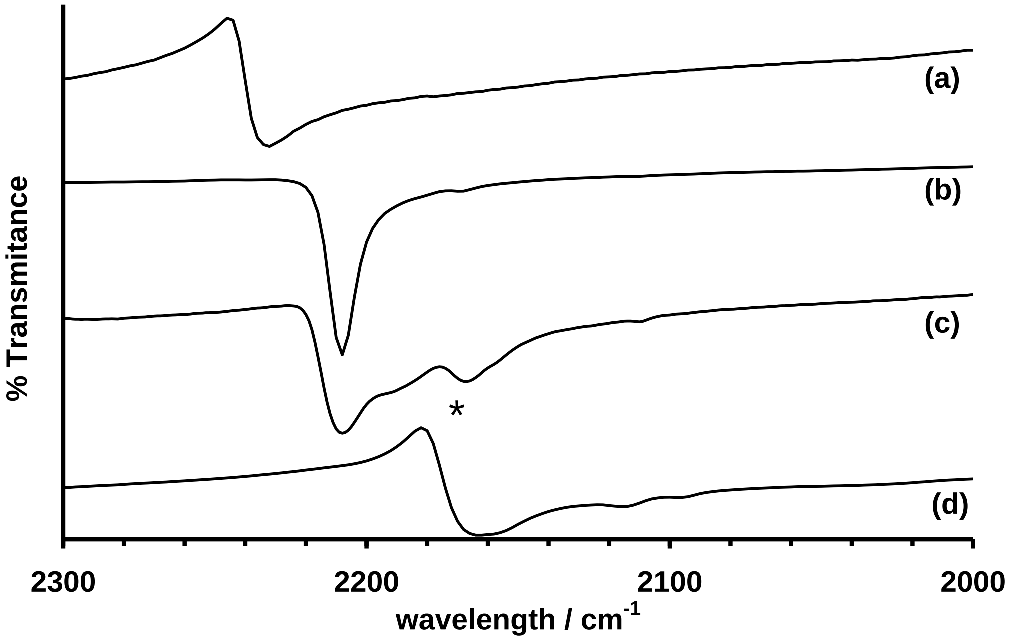

*Figure 4.3 Infrared spectra in the $\nu_{C\equiv N}$ region of (a) AuCN, (b) $(Cu_{1/2}Au_{1/2})CN$, (c) $(Cu_{2/3}Au_{1/3})CN$ and (d) LT-CuCN. The * indicates the band arising from LT-CuCN*

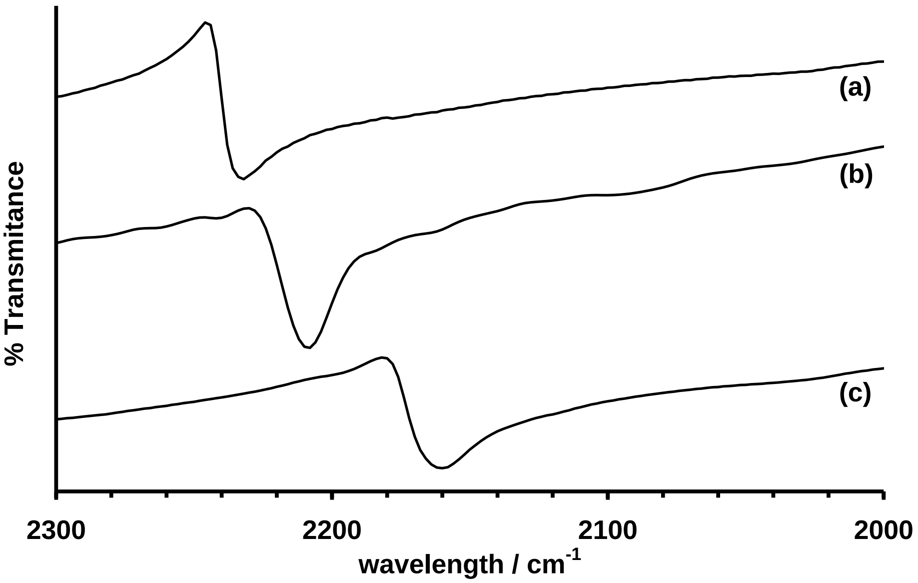

Figure 4.4 Infrared spectra in the $\nu_{C\equiv N}$ region of (a) AuCN, (b) $(Ag_{1/2}Au_{1/2})CN$, (c) and (c) AgCN.

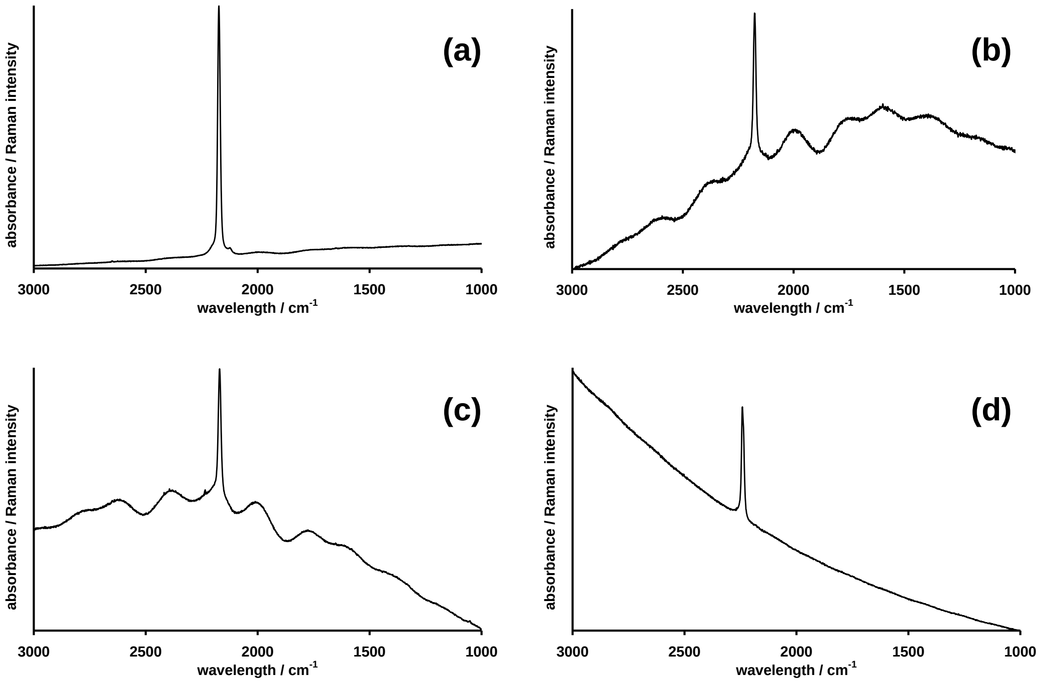

Figure 4.5 The Raman spectra in the 3000 - 1000 cm^{-1} region of (a) LT-CuCN, (b) HT-CuCN, (c) AgCN and (d) AuCN.

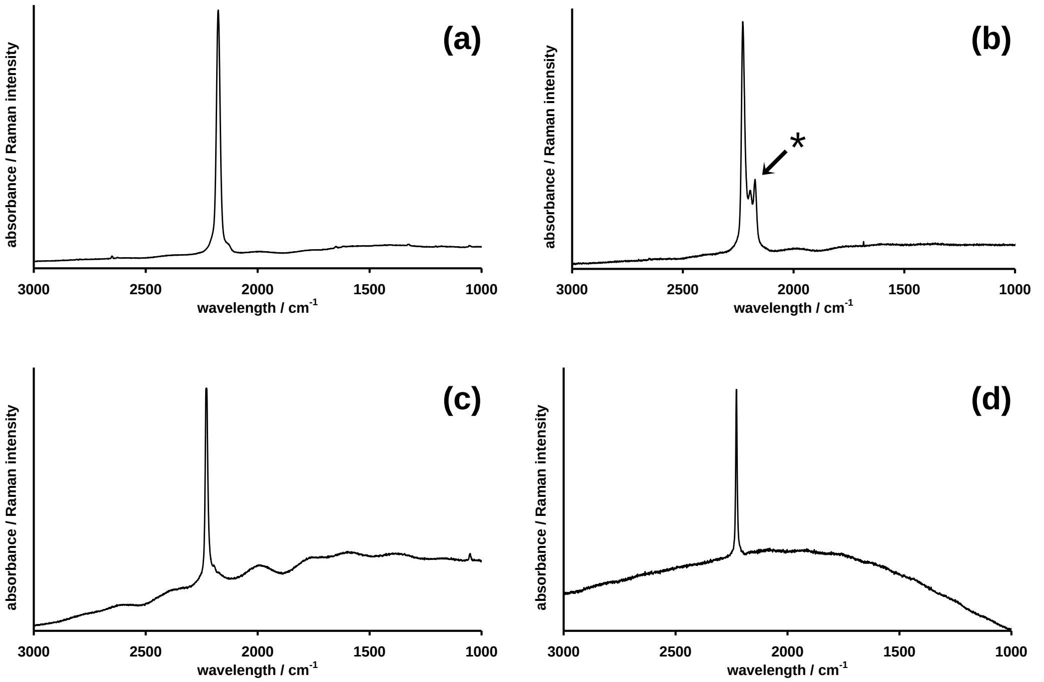

*Figure 4.6 The Raman spectra in the 3000 - 1000 cm^{-1} region of (a) $(Cu_{0.5}Ag_{0.5})CN$, (b) $(Cu_{2/3}Au_{1/3})CN$, (c) $(Cu_{1/2}Au_{1/2})CN$ and (d) $(Ag_{1/2}Au_{1/2})CN$. The * in (b) indicates the band arising from LT-CuCN.*

Table 4.1 Cyanide stretching frequencies in mixed-metal cyanide systems.

Compound	IR $v_{C≡N}$ / cm^{-1}	Raman $v_{C≡N}$ / cm^{-1}
HT-CuCN	2167[4]	2175
LT-CuCN	2166[4]	2173
AgCN	2164[5]	2168[5]
AuCN	2233	2236
$(Cu_{0.17}Ag_{0.83})CN$	2161	
$(Cu_{0.33}Ag_{0.67})CN$	2167	
$(Cu_{0.50}Ag_{0.50})CN$	2165	2176
$(Cu_{0.67}Ag_{0.33})CN$	2168	
$(Cu_{0.83}Ag_{0.17})CN$	2168	
$(Cu_{1/2}Au_{1/2})CN$	2208	2227
$(Cu_{2/3}Au_{1/3})CN$*	2208, 2190 (2167)	2229, 2193 (2173)
$(Ag_{1/2}Au_{1/2})CN$	2209	2228

*Note: *This sample contains LT-CuCN*

4.3 Discussion of Vibrational Spectroscopy Data

Vibrational spectroscopy is very informative in the gold-containing mixed-metal cyanides. This is because there is a significant difference between $v_{C≡N}$ in gold cyanide (2233 cm^{-1}) and the corresponding values in HT-CuCN and AgCN (2167 and 2164 cm^{-1}, respectively) enabling the nearest metal neighbours around different cyanide groups in the chains to be identified. The number of $v_{C≡N}$ stretching frequencies observed gives additional information about the number of different cyanide environments in the different compounds and the local symmetry within the chains. Figure 4.7 shows the possible vibrational modes arising from C≡N stretches in ordered chains.

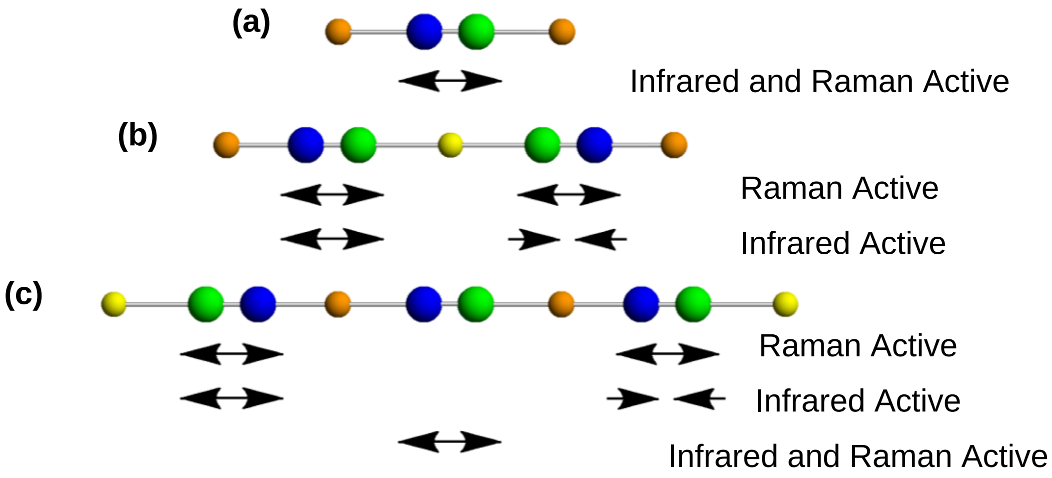

Figure 4.7 The infrared and Raman active vibrational modes in (a) MCN, $C_{\infty v}$, (b) ordered $(M_{1/2}M'_{1/2})CN$, $D_{\infty h}$ and (c) ordered $(M_{2/3}M'_{1/3})CN$, $C_{\infty v}$, chains. (Key: Metal M (orange), metal M' (yellow), carbon (green) and nitrogen (blue)).

In the infrared spectra of $(Cu_{1/2}Au_{1/2})CN$ and $(Ag_{1/2}Au_{1/2})CN$, there are single C≡N stretches at 2208 and 2209 cm^{-1}, respectively, Figure 4.3, Figure 4.4 and Table 4.1. The occurrence of a single $\nu_{C≡N}$ band indicates that there is only one C≡N environment in each of these compounds. The $\nu_{C≡N}$ values for the mixed systems are intermediate between those of the parent metal cyanides consistent with the C≡N group bridging two different metal atoms *i.e.* –M-CN-M′-NC-M-. The observation of a single band in the Raman spectra of $(Cu_{1/2}Au_{1/2})CN$ and

$(Ag_{1/2}Au_{1/2})CN$, which is not coincident with their infrared bands, also agrees with this interpretation (Figure 4.6 (c) and (d)).

In $(Cu_{2/3}Au_{1/3})CN$, three peaks are observed in both the infrared and Raman spectra (Figure 4.3(c) and Figure 4.6(b)). On inspection, the bands at 2167 cm^{-1} in the IR and 2173 cm^{-1} in the Raman can be associated with LT-CuCN (traces of LT-CuCN were observed in the powder X-ray pattern of the sample, Section 3.3.3). The two remaining bands in each spectrum are assumed to belong to $(Cu_{2/3}Au_{1/3})CN$. The band at 2190 cm^{-1} in the IR is coincident, within experimental error, with the band at 2193 cm^{-1} in the Raman. This can be assigned to the $v_{C\equiv N}$ between two copper atoms (Figure 4.7(c)). It is notable that the wavenumber is significantly different from that observed for C≡N groups in HT-CuCN. This shift in band position must reflect the fact that bonding within the Cu-C≡N-Cu unit has changed on going from the AgCN structure type to the AuCN structure type which $(Cu_{2/3}Au_{1/3})CN$ adopts. The occurrence of two further noncoincident bands, at 2208 cm^{-1} in the IR and 2229 cm^{-1} Raman, is consistent with chains ordered in the sense -Au-CN-Cu-NC-Cu-NC-Au- or -Au-NC-Cu-NC-Cu-CN-Au-. In each of the mixed copper-silver cyanides, $Cu_xAg_{1-x}CN$ ($0 \leq x \leq 0.83$), a single $v_{C\equiv N}$ stretch is also observed in the range 2161-2168 cm^{-1}. These values are very close to the values of 2167 cm^{-1} and 2164 cm^{-1} found for CuCN and AgCN respectively (Table 4.1).

In summary, vibrational spectroscopy shows that in the gold-containing compounds, the metal atoms within individual chains are ordered. In the mixed copper-silver cyanides however, no information about the possible ordering within the chains is obtained because of the similarity in the cyanide stretching frequencies to those of the parent-metal cyanides. To obtain information on the packing of the chains in these compounds, the predicted powder X-ray diffraction patterns from models based on ordered chains were compared with the experimental diffraction patterns.

4.4 Powder X-Ray Diffraction

For the mixed-metal gold-containing cyanides, the vibrational studies have established that there is metal order within individual chains. The three simplest ways to pack these chains in an ordered way on a hexagonal lattice are shown in Figure 4.8. Ordering of the chains would lead to a doubling of the repeat in the *c* direction compared to the AuCN parent. Packing the chains in differently ordered manners means that although the hexagonal metric is maintained, the true symmetry is reduced from *P*6*/mmm* to *Immm* or *R*-3*m*. The new unit cells with these lower symmetry are shown in Figure 4.8, together with their relationship to the simplest hexagonal cell. The resulting 3-D cells are shown in Figure 4.9 and are identified by their spacegroups with the multiple of the simplest *P6/mmm* cell, *i.e. P6/mmm*[1], contained within the square brackets.

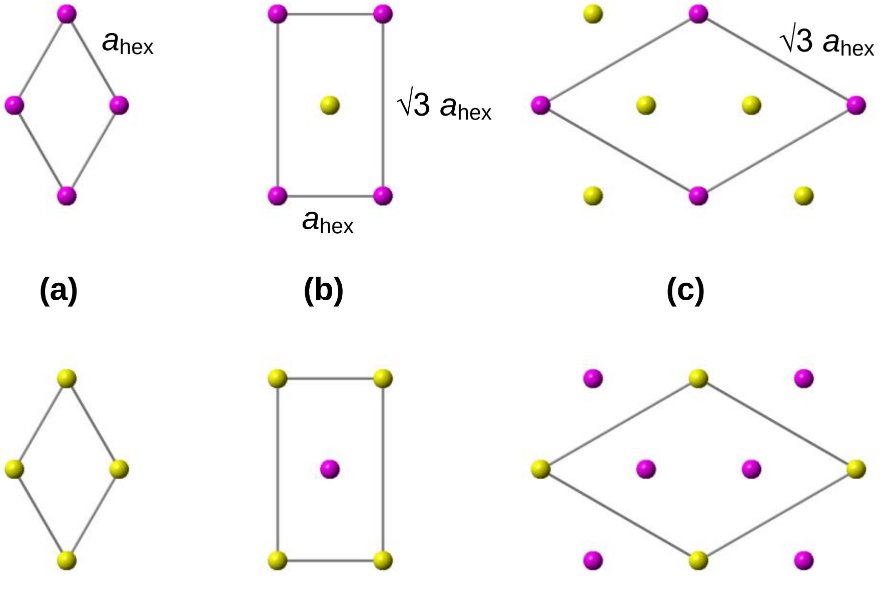

Figure 4.8 The different packing arrangements of ordered chains on a hexagonal lattice with the resulting 2-dimensional unit cells: (a) shows two adjacent layers of metal atoms for the simplest hexagonal cell where single layers contain only one type of metal atom, (b) shows the situation when sheets have an ordered 50:50 metal occupancy and (c) shows the situation when sheets have an ordered 2/3:1/3 metal occupancy. Stacking of these pairs of sheets produces an overall composition $(M_{1/2}Au_{1/2})CN$.

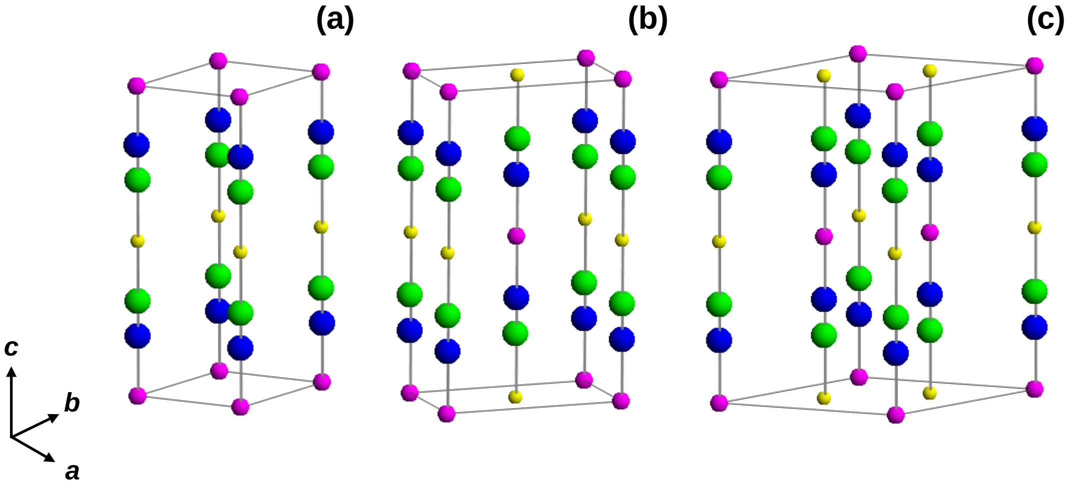

Figure 4.9 Three proposed models containing ordered -[Au-CN-Ag]- chains. (a) P6/mmm[1], (b) Immm[2] and (c) P6/mmm[3]. (named from the space group with number of $AgAu(CN)_2$ *units in the unit cell). (Key: gold (yellow); silver (pink); carbon (green) and nitrogen (blue)).*

The positions of the Bragg reflections in the powder X-ray patterns predicted for all three of the models in which the chains are packed in an ordered manner are shown in Figure 4.10, together with the measured pattern. The calculated Bragg positions for a model in which the chains pack at random, but maintain the AuCN structure type *i.e.* the metal atoms still all occur in sheets, is also shown. In this model, the chain repeat is from the average cell determined in the previous chapter. The predicted powder X-ray diffraction patterns for each of the ordered structures generate additional Bragg reflections. The absence of any superlattice peaks in the measured diffraction patterns shows that there is no long-range order between the chains. However, this absence does not preclude a local preference for particular packing arrangements.

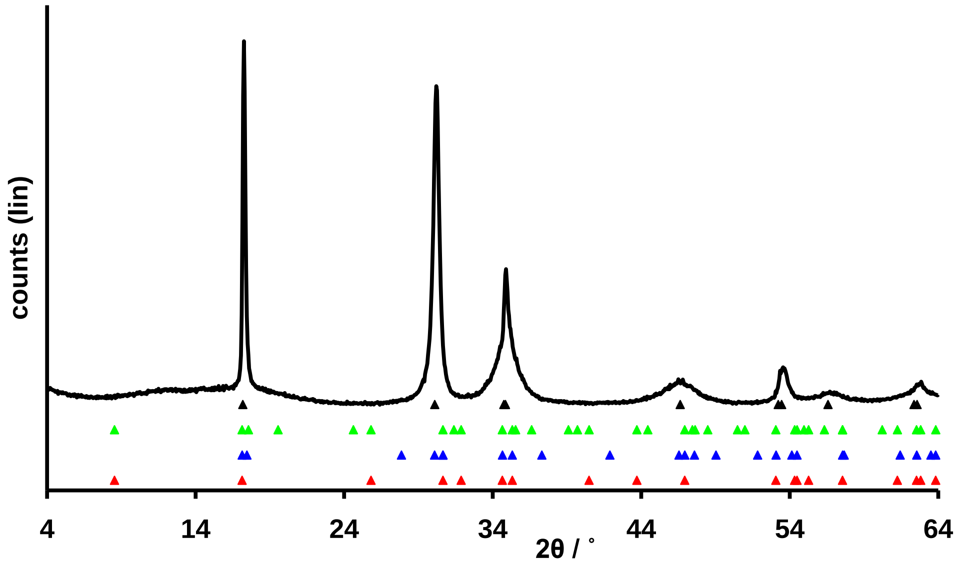

Figure 4.10 Measured powder X-ray diffraction data for ($Ag_{1/2}Au_{1/2}$)CN (top) compared with the predicted peak positions from a model using an average cell (black) and the three different ordered chain models shown in Figure 4.9, P6/mmm[1] (red), Immm[2] (blue), P6/mmm[3] (green).

A similar set of ordered chain models was constructed for ($Cu_{1/2}Au_{1/2}$)CN. Again the ordered chain models predict peaks which are not observed in the experimental data, (Figure 4.11), precluding long-range order between the chains.

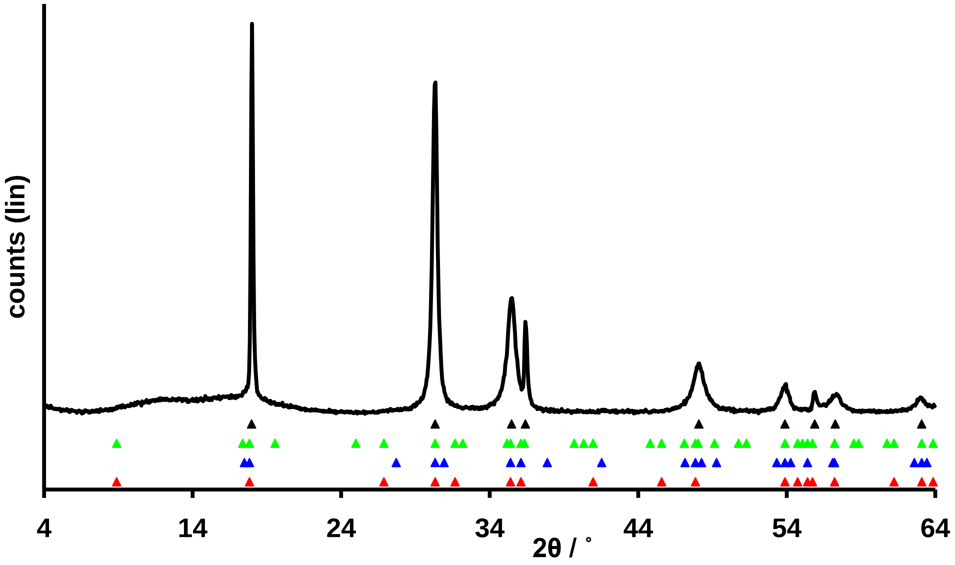

Figure 4.11 Measured powder X-ray diffraction pattern for ($Cu_{1/2}Au_{1/2}$)CN (top) compared with the predicted peak positions from a model using an average cell (black) and the three different ordered chain models shown in Figure 4.9, P6/mmm[1] (red), Immm[2] (blue), P6/mmm[3] (green).

Figure 4.12 shows a possible ordered arrangement of chains for ($Cu_{2/3}Au_{1/3}$)CN. Figure 4.13 shows the corresponding calculated positions of the Bragg reflections from the ordered model and also from the average unit cell, together with the measured pattern. Again, as in the cases above, there does not appear to be any long-range order in the chain packing.

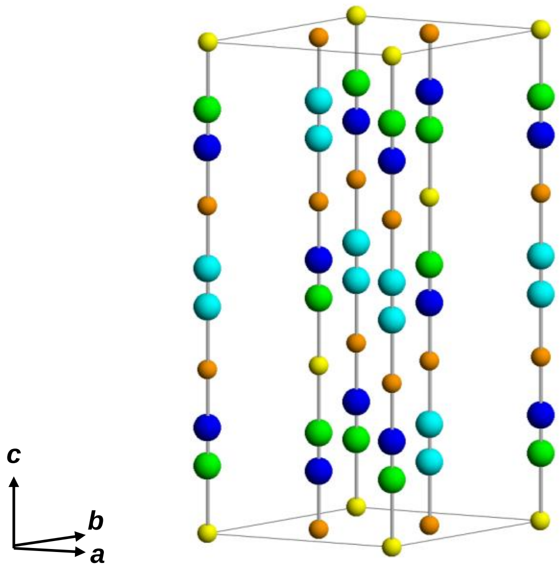

Figure 4.12 A proposed model for ($(Cu_{2/3}Au_{1/3})CN$) in R-3m containing chains with metal ordering and some cyanide ordering. (Key: Copper (orange), gold (yellow), carbon (green), nitrogen (blue) and head-to-tail disordered cyanide groups (cyan)).

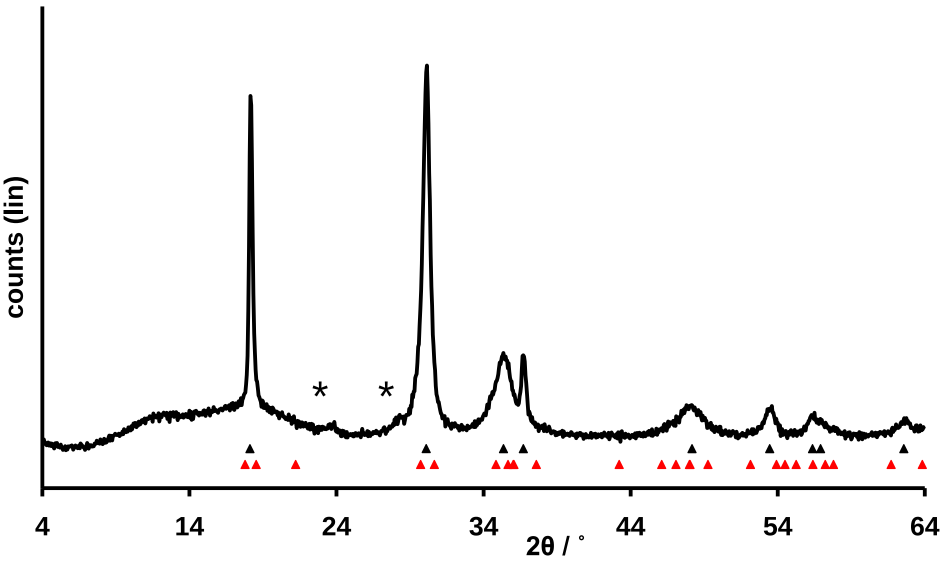

*Figure 4.13 Measured powder X-ray diffraction pattern for ($(Cu_{2/3}Au_{1/3})CN$) (top) compared with the predicted peak positions from a model using an average cell (black) and the ordered chain model in R-3m (red). The * indicate peaks from the LT-CuCN impurity.*

In the Cu-Ag cyanide system, vibrational spectroscopy is unable to determine whether or not there is order within the chains because the vibrational frequencies in the two parent cyanides are so similar. Other methods are necessary to determine if there is any order within or between chains. Two packing models for $(Cu_{0.50}Ag_{0.50})CN$ were constructed in *R-3m* and *P1* (Figure 4.14). The models both have ordered chains packed on a hexagonal lattice and with neighbouring chains displaced by ± 1/3*c* to give the same relationship between chains as found in both the HT-CuCN and AgCN parents.

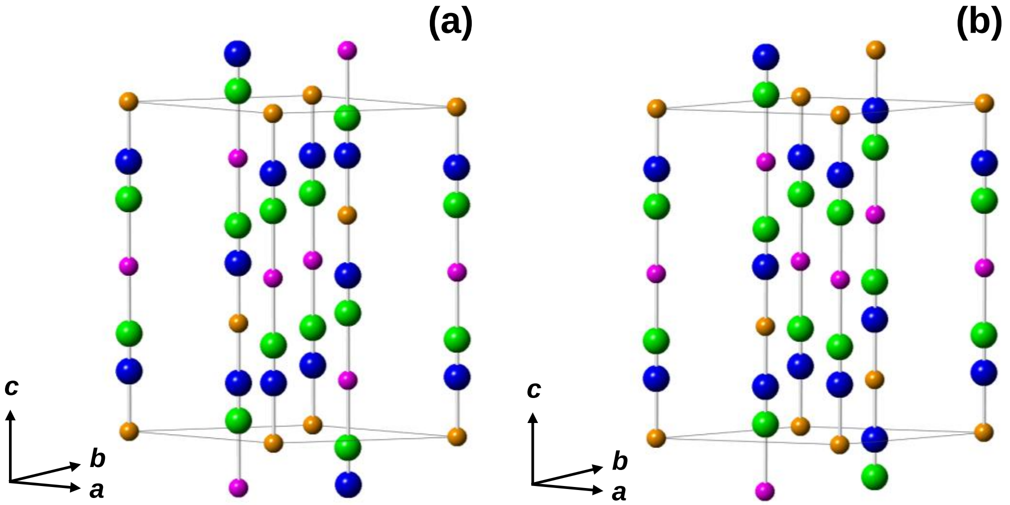

Figure 4.14 Ordered chain models for $(Cu_{0.50}Ag_{0.50})CN$ (a) in R-3m and (b) in P1 (Key: copper (orange); silver (pink); carbon (green) and nitrogen (blue)).

Again these ordered chain models predict peaks in the diffraction patterns which are not observed in the experimental data (Figure 4.15).

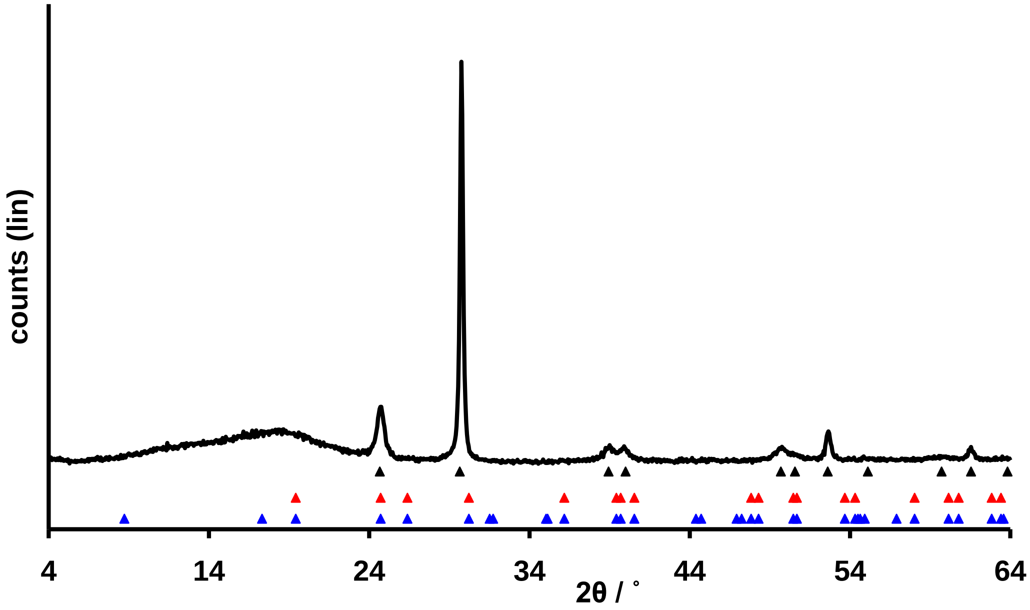

Figure 4.15 The powder X-ray diffraction pattern for $(Cu_{0.50}Ag_{0.50})CN$ *along with the predicted peak positions from a model using an average cell (black), ordered chains in R-3m (red) and ordered chains in P1 (blue).*

To further investigate the structures of these materials, total neutron diffraction data were collected for $(Cu_{1/2}Au_{1/2})CN$, $(Ag_{1/2}Au_{1/2})CN$ and $(Cu_{0.50}Ag_{0.50})CN$ and reduced to $T(r)$.

4.5 Total neutron diffraction

4.5.1 Data collection

Total neutron diffraction data were collected on GEM at the ISIS neutron spallation source. The samples were dried in a vacuum oven at 80 ˚C for 14 hours and the densities of the samples measured using a micropycnometer. The samples were loaded into vanadium foil cans and data collected at room temperature and 10 K.

Table 4.2 Details of the mixed-metal cyanide samples used in GEM data collection.

Sample	Weight / g	Density / gcm^{-3}	Integrated current at target/ μAh (10 K)	Integrated current at target/ μAh (300 K)
$(Cu_{0.50}Ag_{0.50})CN$	0.7710	3.513	895	*N/A*
$(Cu_{1/2}Au_{1/2})CN$	1.8100	5.224	900	701
$(Ag_{1/2}Au_{1/2})CN$	1.3646	5.689	761	*N/A*

The data were reduced as discussed in Chapter 2 to generate *Qi*(*Q*) (Figure 4.16).

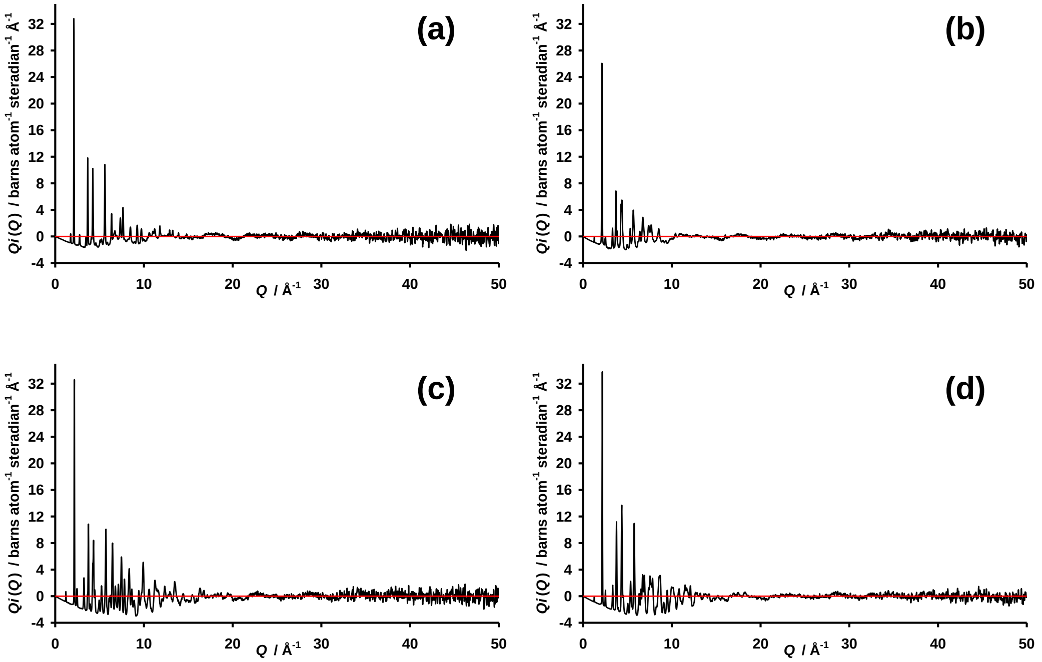

Figure 4.16 Qi(Q) for (a) $(Cu_{0.50}Ag_{0.50})CN$ at 10 K, (b) $(Cu_{1/2}Au_{1/2})CN$ at 10 K, (c) $(Ag_{1/2}Au_{1/2})CN$ at 10 K and (d) $(Cu_{1/2}Au_{1/2})CN$ at 300 K (Zero lines are shown in red).

The correlation function, $T(r)$, was obtained for each dataset, (Figure 4.17), by Fourier transforming the $Qi(Q)$ data with $Q_{\max} = 50$ Å^{-1} after applying a Lorch modification function.

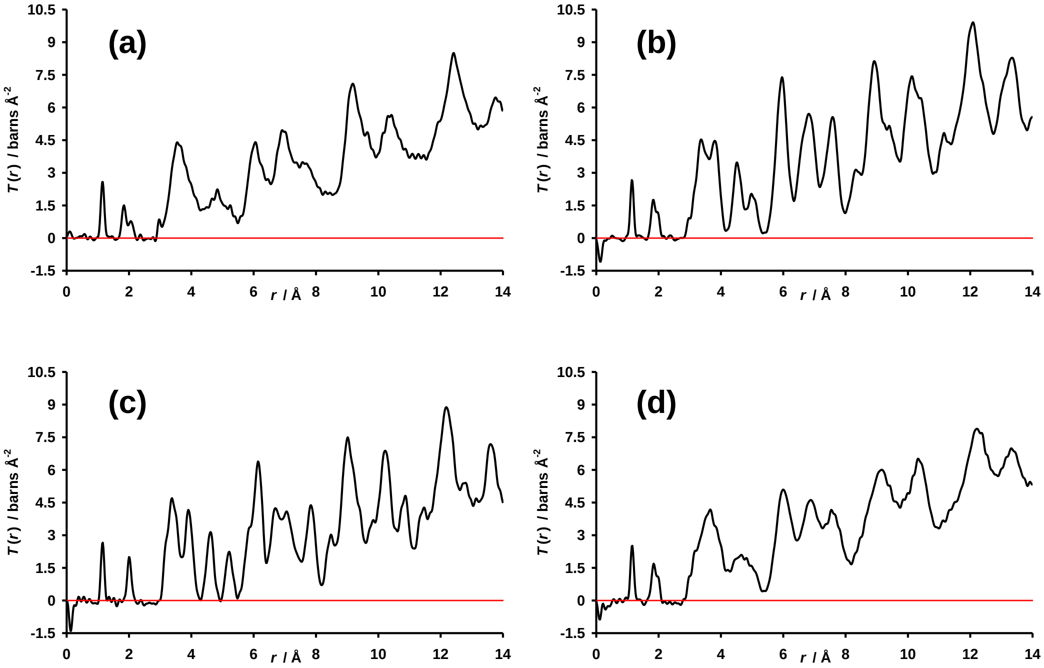

Figure 4.17 The correlation function T(r) for (a) $(Cu_{0.50}Ag_{0.50})CN$ at 10 K, (b) $(Cu_{1/2}Au_{1/2})CN$ at 10 K, (c) $(Ag_{1/2}Au_{1/2})CN$ at 10 K and (d) $(Cu_{1/2}Au_{1/2})CN$ at 300 K. (Zero lines are shown in red).

Fitting the first three peaks in $T(r)$ for $(Cu_{0.50}Ag_{0.50})CN$ and $(Cu_{1/2}Au_{1/2})CN$ gave the CN and two distinct M-C/N bond lengths, (Figure 4.18). For $(Ag_{1/2}Au_{1/2})CN$, only a single, but broad, peak was found in the M-C/N region, (Figure 4.18). The bond length values at 10 K are summarised in Table 4.3, along with the bond lengths of the parent metal cyanides.

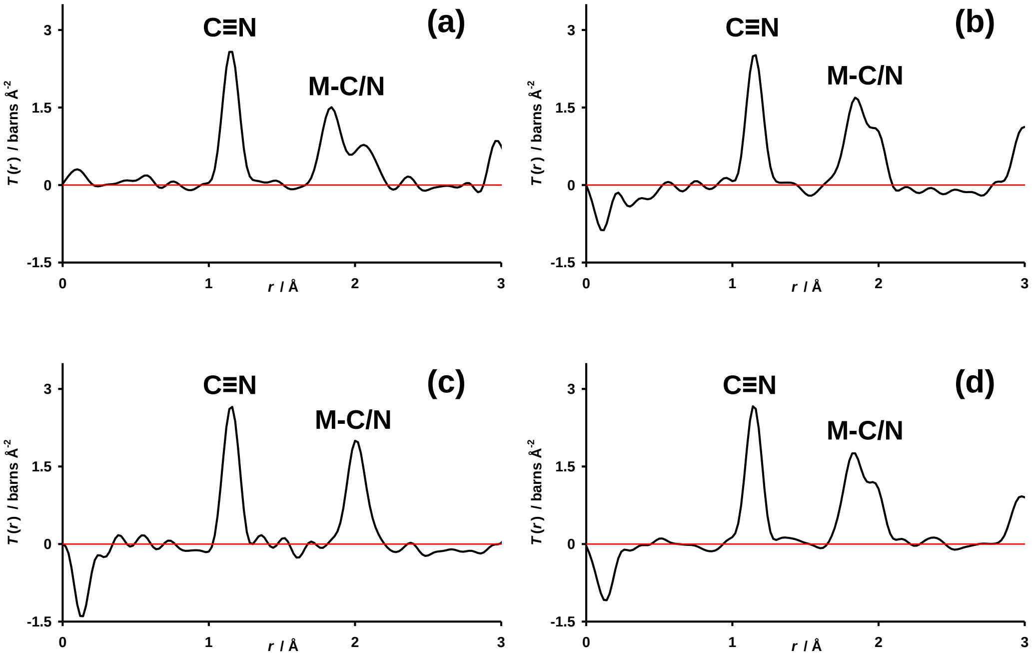

Figure 4.18 The low r region of T(r) containing the peaks from C≡N and M-C/N correlations for (a) $(Cu_{0.50}Ag_{0.50})CN$ at 10 K, (b) $(Cu_{1/2}Au_{1/2})CN$ at 10 K, (c) $(Ag_{1/2}Au_{1/2})CN$ at 10 K and (d) $(Cu_{1/2}Au_{1/2})CN$ at 300 K. (Zero lines are shown in red).

Table 4.3 Peak positions obtained from $T(r)_{exp}$

	$r_{C≡N}$ / Å	$r_{M\text{-}Z}$ / Å	$r_{M'\text{-}Z}$ / Å	Ref
HT-CuCN	1.1537(1)	1.8478(1)		[6]
AgCN	1.1552(1)	2.0679(1)		[6]
AuCN	1.1547(4)	1.9717(5)		[6]
$(Cu_{0.50}Ag_{0.50})CN$	1.1556(8)	1.842(2)	2.065(4)	
$(Cu_{1/2}Au_{1/2})CN$	1.151(2)	1.83(1)	1.99(1)	
$(Ag_{1/2}Au_{1/2})CN$	1.152(2)	2.011(4)		

For all the $(M_{1/2}M'_{1/2})CN$ compounds, ($(Cu_{0.50}Ag_{0.50})CN$, $(Cu_{1/2}Au_{1/2})CN$ and $(Ag_{1/2}Au_{1/2})CN$), two model chains were built incorporating the bond lengths from

Table 4.3. One model had the metal M bound to the nitrogen end of the cyanide group and the other had M bound to the carbon end.

4.5.2 Modelling the low *r* region of *T*(*r*) for $(Cu_{1/2}Au_{1/2})CN$

Figure 4.19 shows the low *r* region of the correlation function, *T*(*r*), for $(Cu_{1/2}Au_{1/2})CN$, together with the calculated correlation function for the two chain models with opposite C≡N ordering *i.e.* –[Cu-NC-Au-CN]– and –[Cu-CN-Au-NC]–. The model with chains which order –[Cu-NC-Au-CN]– gave the best fit to the data.

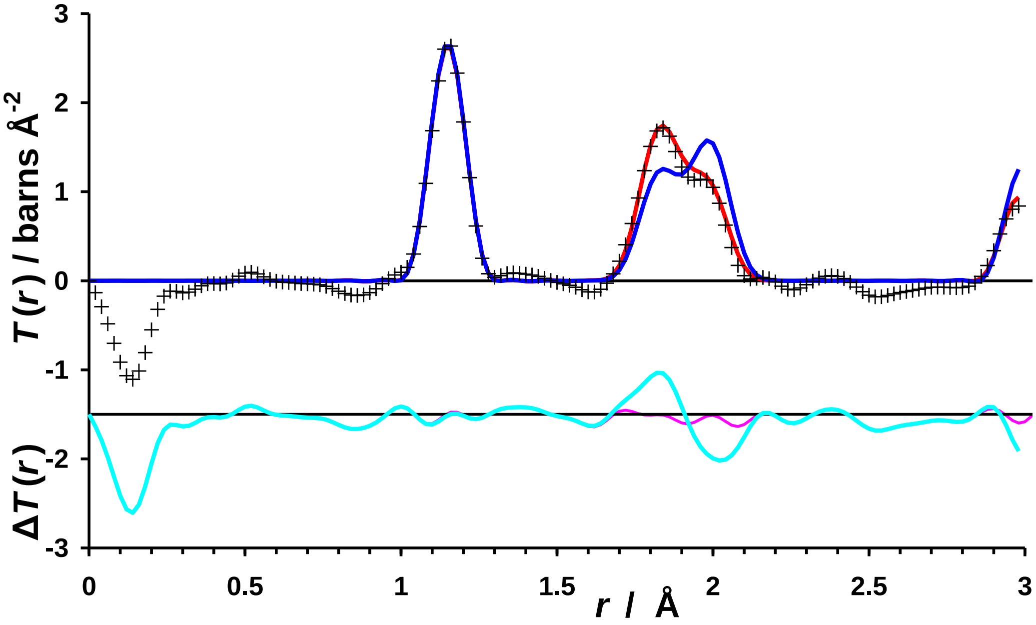

Figure 4.19 The low r region of T(r) for $(Cu_{1/2}Au_{1/2})CN$*, data (black crosses), –[Cu-NC-Au-CN]– model (red), difference (pink) and –[Cu-CN-Au-NC]– model (blue), difference (cyan). Note: the differences have been shifted by -1.5 on the y axis.*

4.5.3 Modelling the low *r* region of *T*(*r*) for $(Ag_{1/2}Au_{1/2})CN$

Only a single peak is seen in the M-C/N region of *T*(*r*) for $(Ag_{1/2}Au_{1/2})CN$ and the M-C and M-N contributions are not resolved. However, Figure 4.20 and Figure 4.21 show that it is still possible to determine the sense of CN ordering in the chains. Taking the M-C/N distances from the parent cyanides, $r_{\text{Ag-C/N}}$ and $r_{\text{Au-C/N}}$ values of 2.0679 and 1.9717 Å, respectively, produces a single peak in $T(r)_{\text{model}}$ but cannot reproduce the experimentally determined peak shape, whichever way round the CN groups are ordered.

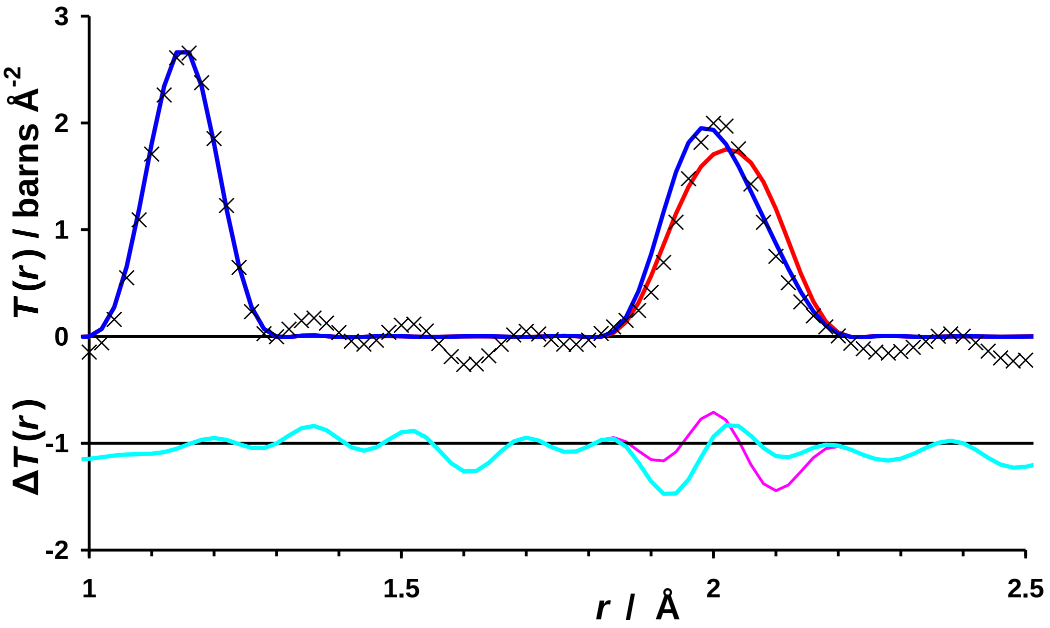

Figure 4.20 The low r region of T(r) for (Ag$_{1/2}$Au$_{1/2}$)CN, data (black crosses), –[Ag-NC-Au-CN]– model (red), difference (magenta) and –[Au-NC-Ag-CN]– model (blue), difference (cyan). The differences have been shifted by -1 on the y axis.

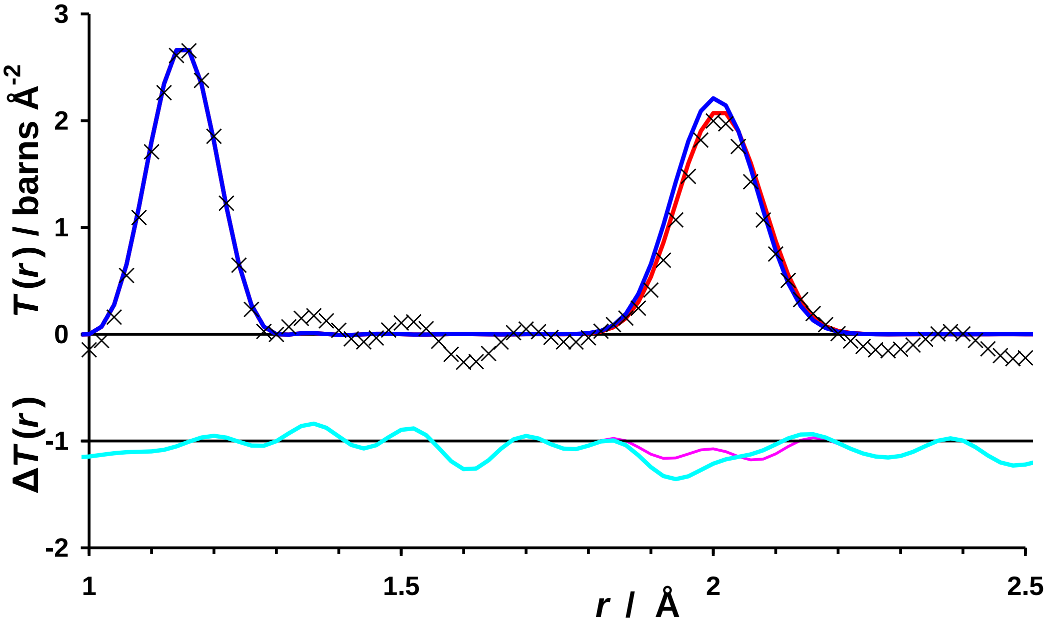

Figure 4.21 The low r region of T(r) for ($Ag_{1/2}Au_{1/2}$)CN, data (black crosses), –[Ag-NC-Au-CN]– model (red), difference (magenta) and –[Au-NC-Ag-CN]– model (blue), difference (cyan). The differences have been shifted by -1 on the y axis.

Figure 4.21 shows the best model in which nitrogen is attached to silver and carbon to gold with bond lengths adjusted to 2.03 and 1.99 Å, respectively. The new bond lengths are significantly different from the average Ag-C/N and Au-C/N values in the parents.

4.5.4 Modelling the low *r* region of *T*(*r*) for ($Cu_{0.50}Ag_{0.50}$)CN

Preliminary modelling showed that the both the metal and cyanide groups were ordered within the chains, and that the ordering is –[Cu-NC-Ag-CN]– and not –[Cu-CN-Ag-NC]– (Figure 4.22).

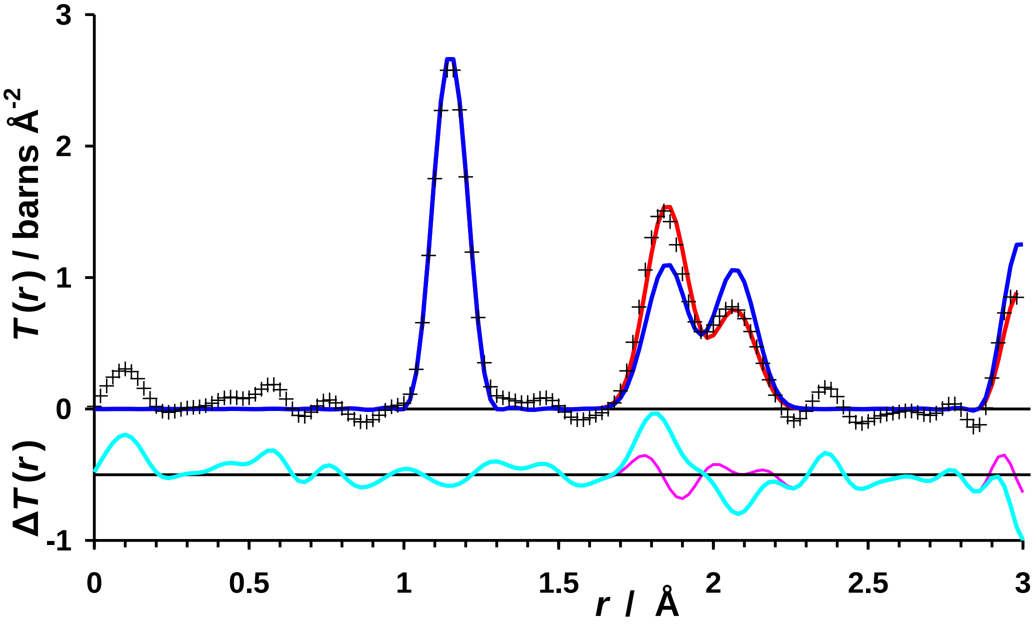

Figure 4.22 The low r region of T(r) for $(Cu_{0.50}Ag_{0.50})CN$, data (black crosses), –[Cu-NC-Ag-CN]– model (red), difference (pink) and –[Cu-CN-Ag-NC]– model (blue), difference (cyan). The differences have been shifted by -0.5 on the y axis.

4.5.5 Packing of the chains to model $T(r)$

The Bragg X-ray diffraction (Section 4.4) shows that there is no long-range order between the chains in any of the mixed-metal cyanides. However, the question remains as to whether there is any order in the arrangement of adjacent chains *i.e.* any local preference in the way the chains pack together. This is of interest particularly in the case of the gold-containing systems where it has been suggested that gold-gold (aurophilic) interactions are responsible for the adoption of the AuCN structure type, rather than the AgCN structure type.[7-8] For example, the chain-packing models shown in Figure 4.9 produce structures with different numbers of metal nearest neighbours of the same type. This is most clearly seen in Figure 4.8 which shows the relationship between metal atoms in each of the metal layers. In Figure 4.8(a), which produces *P6/mmm*[1], each gold atom has six gold near neighbours, in (b), which produces *Immm*[2], each gold has two gold near neighbours and in (c), which produces *P6/mmm*[3], there are two types of gold: one with three gold near neighbours and one with none, giving a weighted average of two near neighbours. The correlation function, $T(r)$, was calculated for these three models for both $(Cu_{1/2}Au_{1/2})CN$ and $(Ag_{1/2}Au_{1/2})CN$ over a larger length scale than used above and incorporating the information on bond distances obtained from fitting the low r region of $T(r)$. In the case of $(Cu_{0.50}Ag_{0.50})CN$, similar models were constructed in the two spacegroups *R-3m* and *P1*. However, in the AgCN structure type adopted here, the metals are not within bonding distances of each other, and it is therefore difficult to see any interaction which would produce a preference for one structure over the other.

4.5.6 Modelling $T(r)$ for $(Cu_{1/2}Au_{1/2})CN$

The three models built in Figure 4.9 were considered for $(Cu_{1/2}Au_{1/2})CN$. The full details of the atomic positions, lattice parameters and broadening factors for each model are given in Section 4.6.2 and the comparisons of the $T(r)_{exp}$ and $T(r)_{model}$ are shown in Figure 4.23 and 4.25.

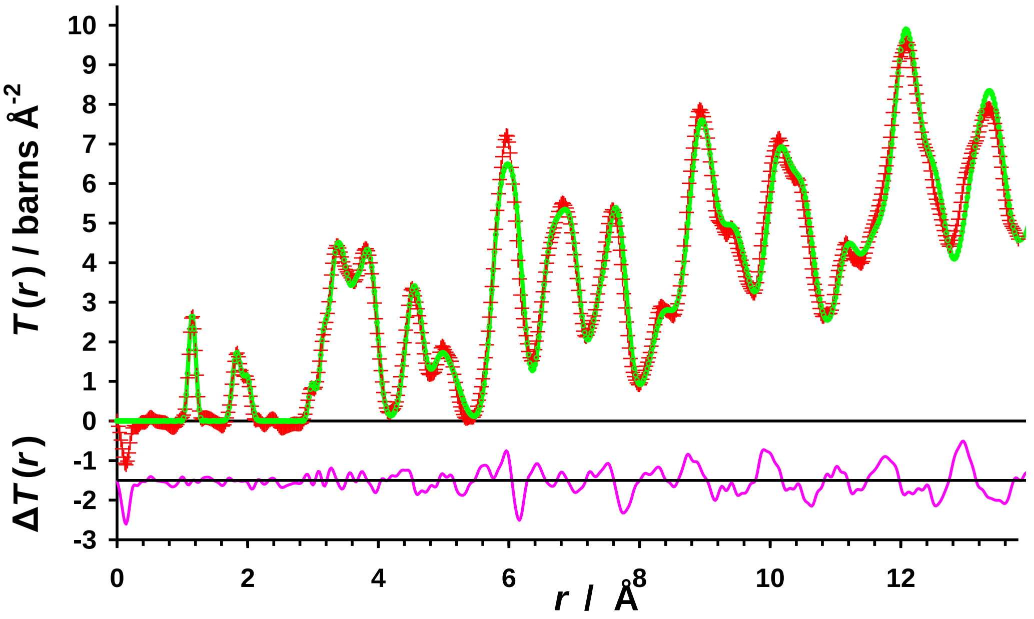

Figure 4.23 T(r) for ($Cu_{1/2}Au_{1/2}$)CN at 10 K, data (red crosses), P6/mmm[1] model (green line) and the difference between them shifted by -1.5 on the axes (pink line). $R_{T(r)}$ = 0.077

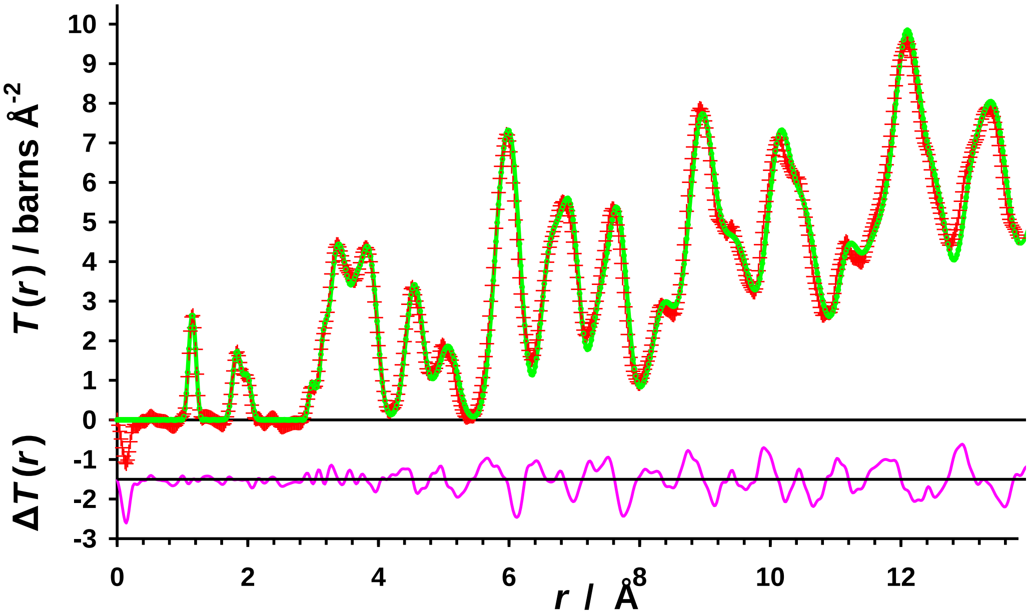

Figure 4.24 T(r) for ($Cu_{1/2}Au_{1/2}$)CN at 10 K, data (red crosses), Immm[2] model (green line) and the difference between them shifted by -1.5 on the axes (pink line). $R_{T(r)}$ = 0.082

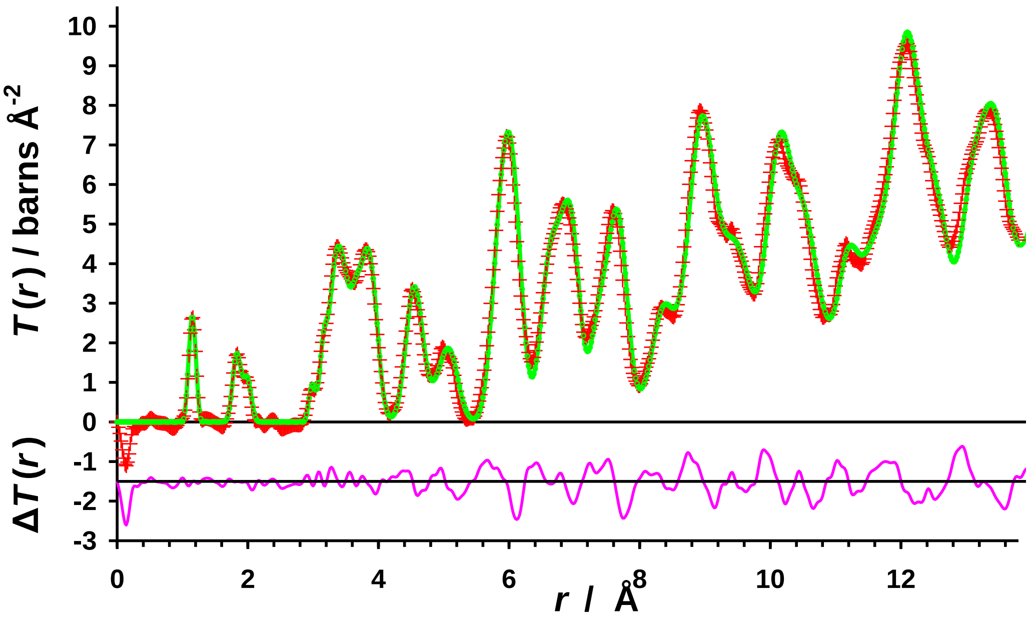

Figure 4.25 T(r) for $(Cu_{1/2}Au_{1/2})CN$ *at 10 K, data (red crosses), P6/mmm[3] model (green line) and the difference between them shifted by -1.5 on the axes (pink line).* $R_{T(r)} = 0.080$

All three models fit the data well (Table 4.4). Unfortunately, the values of $R_{T(r)}$ obtained from each are quite similar. This shows that although total neutron diffraction is the ideal tool to investigate the bonding within the chains, it cannot distinguish between the different possible local arrangements of these chains. For this purpose, total X-ray diffraction is a better tool for investigating the order. This is because Cu and Au have very different X-ray scattering lengths (as Z = 29 and 79, respectively), in contrast to their similar neutron scattering lengths (b_{Cu} = 7.718(4) and b_{Au} = 7.63(6) fm).

Table 4.4 The space groups and unit cells used for modelling ($Cu_{1/2}Au_{1/2}$)CN at 10 K

Model	a / Å	b / Å	c / Å	$R_{T(r)}$[§]
*P*6/*mmm*[1]	3.35	3.35	9.942	0.077
Immm[2]	3.35	5.802	9.942	0.082
*P*6/*mmm*[3]	5.802	5.802	9.942	0.080

[§] $R_{T(r)} = \sqrt{\sum \left| T(r_i)_{obs} - T(r_i)_{\mathrm{mod}} \right|^2 \Big/ \sum \left| T(r_i)_{obs} \right|^2}$

Figure 4.26 shows $T(r)_{\mathrm{exp}}$ for ($Cu_{1/2}Au_{1/2}$)CN at 300 K and $T(r)_{\mathrm{model}}$ for the *P*6/*mmm*[3] structure. It is notable how thermal motion broadens the features seen in $T(r)_{\mathrm{exp}}$ above r = 2.5 Å when compared with the 10 K data.

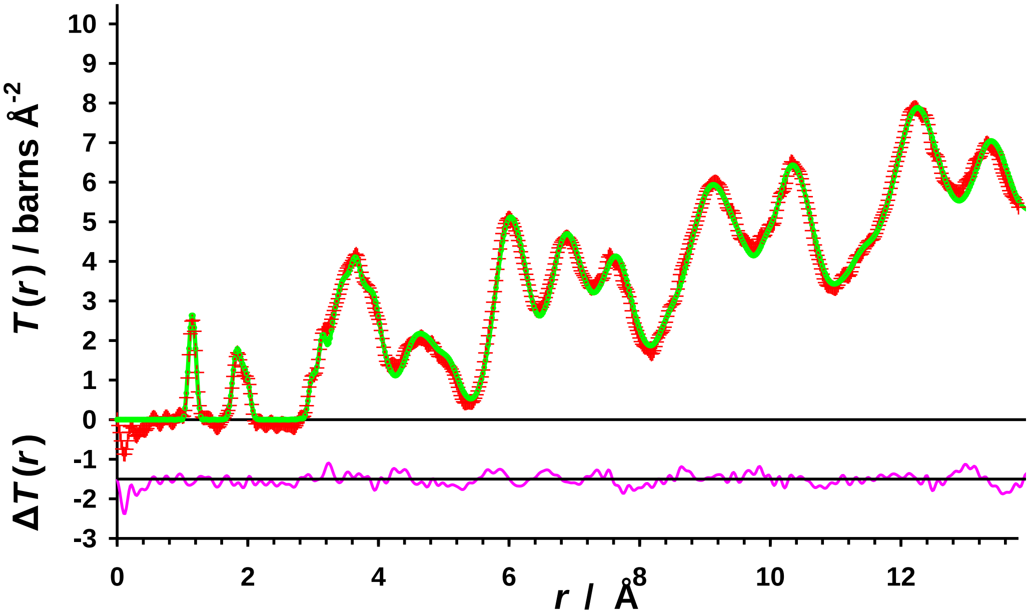

Figure 4.26 T(r) for ($Cu_{1/2}Au_{1/2}$)CN at 300 K, data (red crosses), P6/mmm[3] model (green line) and the difference between them shifted by -1.5 on the axes (pink line). $R_{T(r)}$ = 0.041

4.5.7 Modelling *T*(*r*) for ($Ag_{1/2}Au_{1/2}$)CN

The three models built in Figure 4.9 were used again for ($Ag_{1/2}Au_{1/2}$)CN. The full details of the atomic positions, lattice parameters and broadening factors for each model are given in Section 4.6.3 and the comparisons of the $T(r)_{\mathrm{exp}}$ and $T(r)_{\mathrm{model}}$ are shown in Figure 4.27 and 4.29.

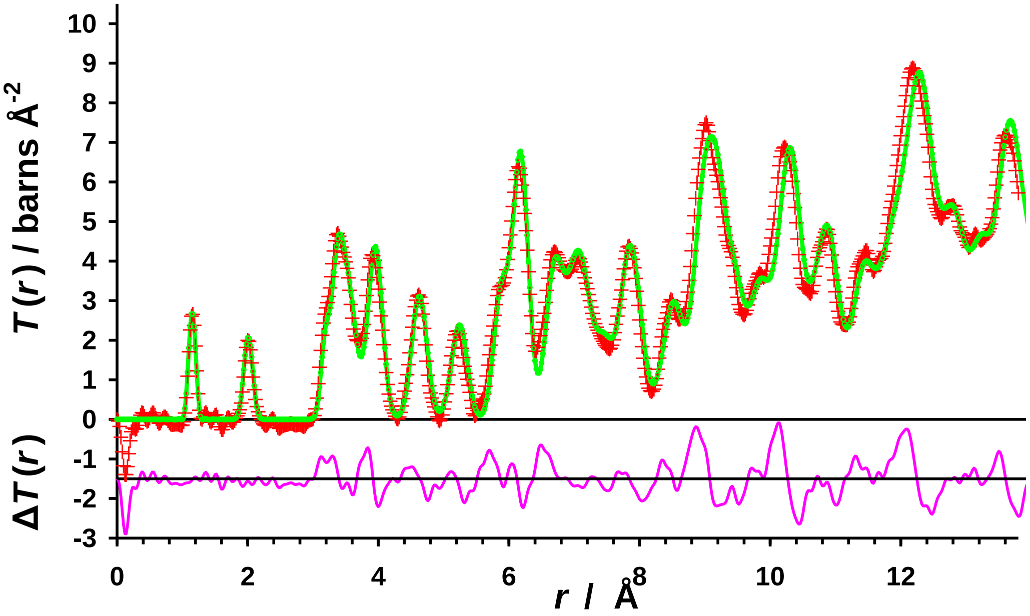

Figure 4.27 T(r) for ($Ag_{1/2}Au_{1/2}$)CN at 10 K, data (red crosses), P6/mmm[1] model (green line) and the difference between them shifted by -1.5 on the axes (pink line). $R_{T(r)}$ = 0.118

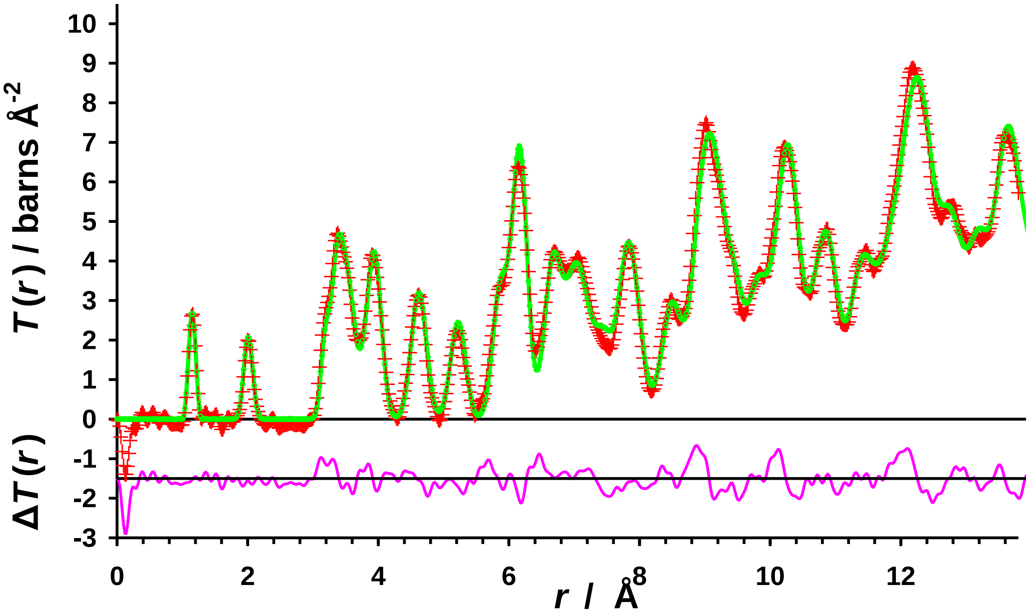

Figure 4.28 T(r) for ($(Ag_{1/2}Au_{1/2})CN$) at 10 K, data (red crosses), Immm[2] model (green line) and the difference between them shifted by -1.5 on the axes (pink line). $R_{T(r)}$ = 0.078

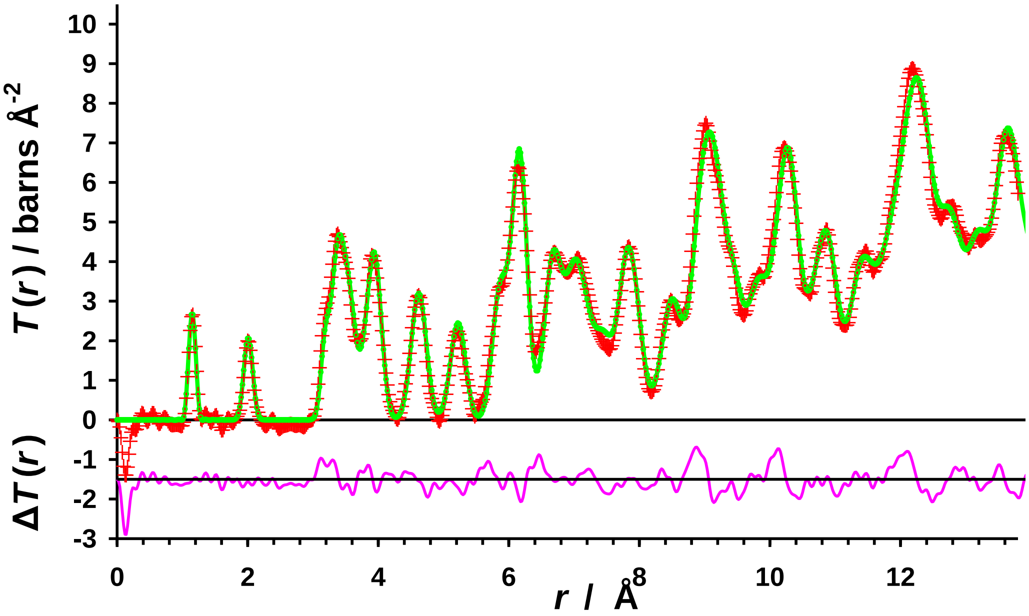

Figure 4.29 T(r) for ($(Ag_{1/2}Au_{1/2})CN$) at 10 K, data (red crosses), P6/mmm[3] model (green line) and the difference between them shifted by -1.5 on the axes (pink line). $R_{T(r)}$ = 0.076

Modelling of $T(r)_{\mathrm{exp}}$ shows that the model with homometallic layers, P6/mmm[1], which would maximise the aurophilic bonding interactions, is significantly worse than the other two models (Table 4.5). This is rather surprising as it was believed that the driving force for the formation of the AuCN structure type is the existence of aurophilic bonding. It is possible that in the mixed copper-gold system, other interchain interactions are important, such as non bonded C···N interactions between the chains, especially as there is now cyanide order within the chains, in contrast to the situation in AuCN.

Table 4.5 The space groups and unit cells used for modelling ($Ag_{1/2}Au_{1/2}$)CN at 10 K

Model	*a* / Å	*b* / Å	*c* / Å	$R_{T(r)}$
*P*6/*mmm*[1]	3.365	3.365	10.346	0.118
Immm[2]	3.365	5.828	10.346	0.078
*P*6/*mmm*[3]	5.828	5.828	10.346	0.076

4.5.8 Modelling *T*(*r*) for ($Cu_{0.50}Ag_{0.50}$)CN

The two models built in Figure 4.14 were used to model the data from ($Cu_{0.50}Ag_{0.50}$)CN. The full details of the atomic positions, lattice parameters and broadening factors for each model are given in Section 4.6.1 and the comparisons of the $T(r)_{\mathrm{exp}}$ and $T(r)_{\mathrm{model}}$ are shown in Figures 4.30 and 4.31.

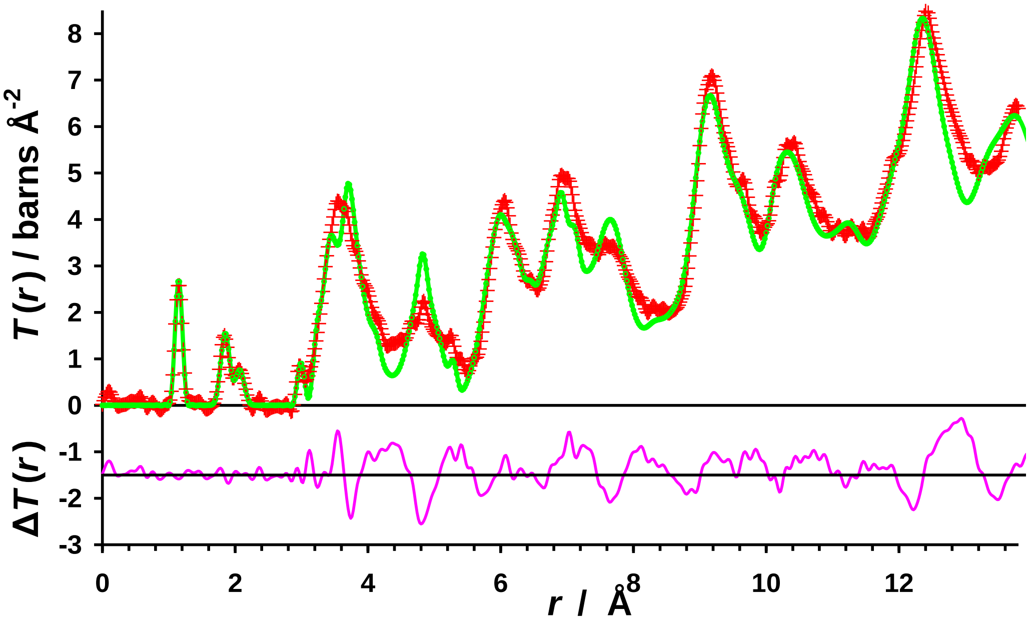

Figure 4.30 T(r) for ($Cu_{0.50}Ag_{0.50}$)CN at 10 K, data (red crosses), R-3m model (green line) and the difference between them shifted by -1.5 on the axes (pink line). $R_{T(r)}$ = 0.103.

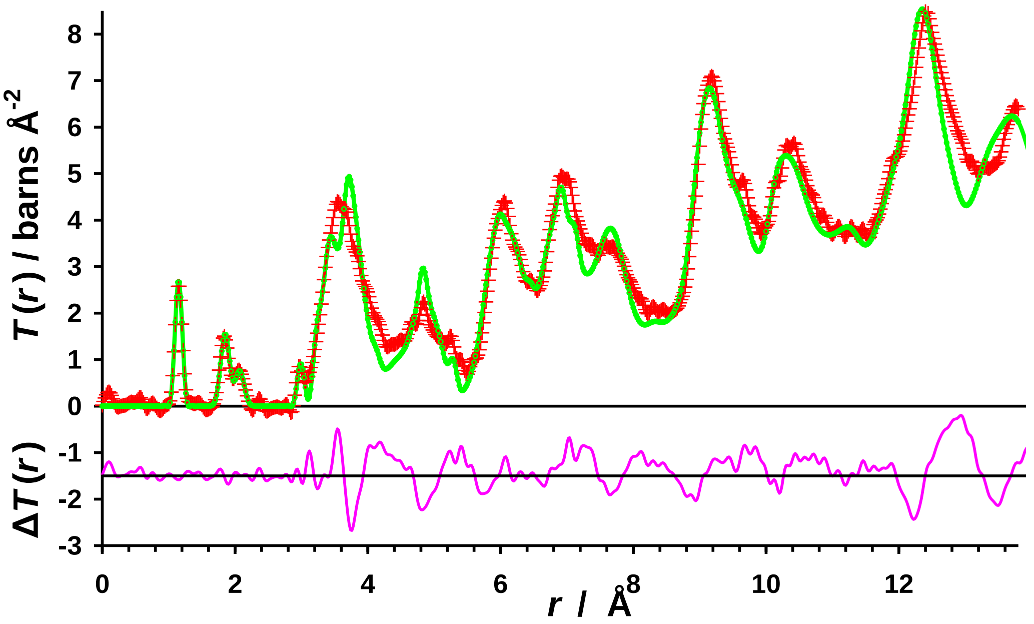

Figure 4.31 T(r) for ($Cu_{0.50}Ag_{0.50}$)CN at 10 K, data (red crosses), P1 model (green line) and the difference between them shifted by -1.5 on the axes (pink line). $R_{T(r)}$ = 0.105.

Both models give a reasonable fit to the data (Table 4.6) and confirm that the AgCN structure is adopted for this phase. More sophisticated modelling might be able to improve on the approach adopted here. Such methods and how they might be applied to all the mixed-metal cyanides are discussed below.

Table 4.6 The space groups and unit cells used for modelling ($(Cu_{0.50}Ag_{0.50})CN$) at 10 K

Model	a / Å	c / Å	$R_{T(r)}$
R-3m	5.91	10.1252	0.105
P1[*]	5.91	10.1252	0.103

[*] *Hexagonal metric used*

4.5.9 Structural conclusions

In summary, all three of the mixed group-11 metal cyanides, $(Cu_{0.50}Ag_{0.50})CN$, $(Cu_{1/2}Au_{1/2})CN$ and $(Ag_{1/2}Au_{1/2})CN$), contain chains in which the metal atoms order. The cyanide ligands are ordered demonstrating preferential binding to the carbon end of Au>Ag>Cu. In one case, $(Ag_{1/2}Au_{1/2})CN$), the rather surprising result was found that the gold atoms are not arranged on a local scale in homometallic layers with six near gold neighbours, as might be expected to maximise aurophilic interactions, but instead are found in mixed-metal layers. There are at least two possible ways to yield further structural information about the mixed-metal systems. The first approach is to use total X-ray diffraction, which is dominated by scattering from the metals, as a route to determining local metal-atom distributions within the layers. The second approach involves using Reverse Monte Carlo (RMC) methods to fit both neutron Bragg and total diffraction data as has been successfully undertaken for the parent cyanides.[9]

The models constructed in this work provide the ideal starting point for such studies.

4.6 Details for Creating the Correlation Function *T*(*r*)

4.6.1 The fractional coordinates and lattice parameters for the $(Cu_{0.50}Ag_{0.50})CN$ models

Table 4.7 The space groups and unit cells used for modelling $(Cu_{0.50}Ag_{0.50})CN$ at 10 K

Model	*a*=*b* / Å	*c* / Å	*α*=*β* / °	*γ* / °	$R_{T(r)}$
R-3m	5.91	10.1252	90	120	0.105
P1	5.91	10.1252	90	120	0.103

Table 4.8 $(Cu_{0.50}Ag_{0.50})CN$ model at 10 K in R-3m with –[Cu-NC-Ag-CN]– ordered chains.

Atom	*x*	*y*	*z*	Wyckoff position
Cu	0	0	0	3*a*
Ag	0	0	0.5	3*b*
C	0	0	0.2961	6*c*
N	0	0	0.1819	6*c*

Table 4.9 ($Cu_{0.50}Ag_{0.50}$)CN model at 10 K in P1 with –[Cu-NC-Ag-CN]– ordered chains.

Atom	*x*	*y*	*z*	Wyckoff position
Cu	0.0	0.0	0.0	1*a*
N	0.0	0.0	0.1819	1*a*
C	0.0	0.0	0.2961	1*a*
Ag	0.0	0.0	0.5000	1*a*
C	0.0	0.0	0.7039	1*a*
N	0.0	0.0	0.8181	1*a*
Cu	0.3333	0.6667	0.1667	1*a*
N	0.3333	0.6667	0.3486	1*a*
C	0.3333	0.6667	0.4627	1*a*
Ag	0.3333	0.6667	0.6667	1*a*
C	0.3333	0.6667	0.8706	1*a*
N	0.3333	0.6667	0.9847	1*a*
C	0.6667	0.3333	0.0373	1*a*
N	0.6667	0.3333	0.1514	1*a*
Cu	0.6667	0.3333	0.3333	1*a*
N	0.6667	0.3333	0.5153	1*a*
C	0.6667	0.3333	0.6294	1*a*
Ag	0.6667	0.3333	0.8333	1*a*

4.6.2 The fractional coordinates and lattice parameters for the ($Cu_{1/2}Au_{1/2}$)CN models

Table 4.10 The P6/mmm[1] model for ($Cu_{1/2}Au_{1/2}$)CN at 10 K with –[Cu-NC-Ag-CN]– ordered chains.

Atom	*x*	*y*	*z*	Wyckoff position
Cu	0	0	0	1*a*
Au	0	0	0.5	1*b*
C	0	0	0.2998	2*e*
N	0	0	0.1841	2*e*

Table 4.11 The Immm[2] model for ($Cu_{1/2}Au_{1/2}$)CN at 10 K with –[Cu-NC-Ag-CN]– ordered chains.

Atom	*x*	*y*	*z*	Wyckoff position
Cu	0	0	0	2*a*
Au	0.5	0.5	0	2*c*
C	0	0	0.2998	4*i*
N	0	0	0.1841	4*i*

Table 4.12 The P6/mmm[3] model for ($Cu_{1/2}Au_{1/2}$)CN at 10 K with –[Cu-NC-Ag-CN]– ordered chains.

Atom	*x*	*y*	*z*	Wyckoff position
Cu	0	0	0	1*a*
Au	0	0	0.5	1*b*
C	0	0	0.2998	2*e*
N	0	0	0.1841	2*e*
Cu	0.3333	0.6667	0.5	4*h*
Au	0.3333	0.6667	0.0	4*h*
C	0.3333	0.6667	0.2002	4*h*
N	0.3333	0.6667	0.3159	4*h*

Table 4.13 The P6/mmm[3] model for ($Cu_{1/2}Au_{1/2}$)CN at 300 K with –[Cu-NC-Ag-CN]– ordered chains.

Atom	*x*	*y*	*z*	Wyckoff position
Cu	0	0	0	1*a*
Au	0	0	0.5	1*b*
C	0	0	0.3006	2*e*
N	0	0	0.1844	2*e*
Cu	0.3333	0.6667	0.5	4*h*
Au	0.3333	0.6667	0.0	4*h*
C	0.3333	0.6667	0.1994	4*h*
N	0.3333	0.6667	0.3156	4*h*

Table 4.14 The space groups and unit cells used for modelling ($(Cu_{1/2}Au_{1/2})CN$ at 10 K

Model	a / Å	b / Å	c / Å	$R_{T(r)}^{\S}$
*P*6/*mmm*[1]	3.35	3.35	9.942	0.077
Immm[2]	3.35	5.802	9.942	0.082
*P*6/*mmm*[3]	5.802	5.802	9.942	0.080

4.6.3 The fractional coordinates and lattice parameters for the $(Ag_{1/2}Au_{1/2})CN$ models

Table 4.15 The disordered model for $(Ag_{1/2}Au_{1/2})CN$ model at 10 K inP6/mmm.

Atom	x	y	z	Wyckoff position
Au	0	0	0	1*a*
Z	0	0	0.3887	2*e*

Table 4.16 The P6/mmm[1] model for $(Ag_{1/2}Au_{1/2})CN$ at 10 K with –[Ag-NC-Au-CN]– ordered chains.

Atom	x	y	z	Wyckoff position
Au	0	0	0	1*a*
Ag	0	0	0.5	1*b*
C	0	0	0.1923	2*e*
N	0	0	0.3038	2*e*

Table 4.17 The Immm[2] model for $(Ag_{1/2}Au_{1/2})CN$ at 10 K with –[Ag-NC-Au-CN]– ordered chains.

Atom	x	y	z	Wyckoff position
Au	0	0	0	2*a*
Ag	0.5	0.5	0	2*c*
C	0	0	0.1923	4*i*
N	0	0	0.3038	4*i*

Table 4.18 The P6/mmm[3] model for ($Ag_{1/2}Au_{1/2}$)CN at 10 K with –[Ag-NC-Au-CN]– ordered chains.

Atom	*x*	*y*	*z*	Wyckoff position
Au	0	0	0	1*a*
Ag	0	0	0.5	1*b*
C	0	0	0.1923	2*e*
N	0	0	0.3038	2*e*
Au	0.3333	0.6667	0.5	4*h*
Ag	0.3333	0.6667	0.0	4*h*
C	0.3333	0.6667	0.1923	4*h*
N	0.3333	0.6667	0.3038	4*h*

Table 4.19 The space groups and unit cells used for modelling ($Ag_{1/2}Au_{1/2}$)CN at 10 K

Model	*a* / Å	*b* / Å	*c* / Å	$R_{T(r)}$
*P*6/*mmm*[1]	3.365	3.365	10.346	0.118
Immm[2]	3.365	5.828	10.346	0.078
*P*6/*mmm*[3]	5.828	5.828	10.346	0.076

4.7 Separating the different contributions to the calculated correlation function, $T(r)_{\text{calc}}$

To create $T(r)_{\text{model}}$, $T(r)_{\text{calc}}$ for a chain was subtracted from $T(r)_{\text{calc}}$ from the full model. The resulting set of delta functions came from atom pairs where the atoms were not in the same chain, (interchain correlations). The intrachain delta functions and interchain delta functions were then broadened separately and summed to generate $T(r)_{\text{model}}$. This was the method used to model $T(r)$ from HT-CuCN, AgCN and Au(CN).[10-12]

4.7.1 The broadening factors for the (Cu$_{0.50}$Ag$_{0.50}$)CN models

Table 4.20 The root-mean-square values used to broaden the individual partial correlation functions used to produce $T(r)_{model}$ *for* (Cu$_{0.50}$Ag$_{0.50}$)CN *at 10 K.*

Partial correlations in (Cu$_{0.50}$Ag$_{0.50}$)CN at 10 K			
Intrachain M-M	r = 0.0–14 Å $\langle u^2\rangle^{1/2}$ = 0.1 Å^2		
Intrachain Cu-C	r = 0.0–8.0 Å $\langle u^2\rangle^{1/2}$ = 0.03 Å^2	r = 8.0–14.0 Å $\langle u^2\rangle^{1/2}$ = 0.10 Å^2	
Intrachain Cu-N	r = 0.0–8.0 Å $\langle u^2\rangle^{1/2}$ = 0.055 Å^2	r = 8.0–14.0 Å $\langle u^2\rangle^{1/2}$ = 0.10 Å^2	
Intrachain Ag-C	r = 0.0–8.0 Å $\langle u^2\rangle^{1/2}$ = 0.055 Å^2	r = 8.0–14.0 Å $\langle u^2\rangle^{1/2}$ = 0.10 Å^2	
Intrachain Ag-N	r = 0.0–8.0 Å $\langle u^2\rangle^{1/2}$ = 0.03 Å^2	r = 8.0–14.0 Å $\langle u^2\rangle^{1/2}$ = 0.10 Å^2	
Intrachain Z-Z	r = 0.0–8.0 Å $\langle u^2\rangle^{1/2}$ = 0.035 Å^2	r = 0.08–14.0 Å $\langle u^2\rangle^{1/2}$ = 0.10 Å^2	
Interchain M-M	r = 0.0–7.0 Å $\langle u^2\rangle^{1/2}$ = 0.12 Å^2	r = 7.0–14.0 Å $\langle u^2\rangle^{1/2}$ = 0.16 Å^2	
Interchain M-Z	r = 0.0–4.5 Å $\langle u^2\rangle^{1/2}$ = 0.10 Å^2	r = 4.5–7.25 Å $\langle u^2\rangle^{1/2}$ = 0.16 Å^2	r = 7.25 –14.0 Å $\langle u^2\rangle^{1/2}$ = 0.18 Å^2
Interchain Z-Z	r = 0.0–4.5 Å $\langle u^2\rangle^{1/2}$ = 0.14 Å^2	r = 4.5–7.25 Å $\langle u^2\rangle^{1/2}$ = 0.18 Å^2	r = 7.25 –14.0 Å $\langle u^2\rangle^{1/2}$ = 0.24 Å^2

4.7.2 The broadening factors for the $(Cu_{1/2}Au_{1/2})CN$ models

Table 4.21 The root-mean-square values used to broaden the individual partial correlation functions used to produce $T(r)_{model}$ *for* $(Cu_{1/2}Au_{1/2})CN$ *at 10 K*

Partial correlations in $(Cu_{1/2}Au_{1/2})CN$ at 10 K			
Intrachain M-M	*r* = 0.0–14 Å $\langle u^2\rangle^{1/2}$ = 0.1 Å^2		
Intrachain Cu-C	*r* = 0.0–4.5 Å $\langle u^2\rangle^{1/2}$ = 0.03 Å^2	*r* = 4.5–14.0 Å $\langle u^2\rangle^{1/2}$ = 0.10 Å^2	
Intrachain Cu-N	*r* = 0.0–4.5 Å $\langle u^2\rangle^{1/2}$ = 0.048 Å^2	*r* = 4.5–14.0 Å $\langle u^2\rangle^{1/2}$ = 0.10 Å^2	
Intrachain Au-C	*r* = 0.0–4.5 Å $\langle u^2\rangle^{1/2}$ = 0.048 Å^2	*r* = 4.5–14.0 Å $\langle u^2\rangle^{1/2}$ = 0.10 Å^2	
Intrachain Au-N	*r* = 0.0–4.5 Å $\langle u^2\rangle^{1/2}$ = 0.03 Å^2	*r* = 4.5–14.0 Å $\langle u^2\rangle^{1/2}$ = 0.10 Å^2	
Intrachain Z-Z	*r* = 0.0–1.5 Å $\langle u^2\rangle^{1/2}$ = 0.036 Å^2	*r* = 1.5–4.5 Å $\langle u^2\rangle^{1/2}$ = 0.04 Å^2	*r* = 4.5–14.0 Å $\langle u^2\rangle^{1/2}$ = 0.10 Å^2
Interchain M-M	*r* = 0.0–8.0 Å $\langle u^2\rangle^{1/2}$ = 0.11 Å^2	*r* = 8.0–14.0 Å $\langle u^2\rangle^{1/2}$ = 0.14 Å^2	
Interchain M-Z	*r* = 0.0–8.0 Å $\langle u^2\rangle^{1/2}$ = 0.11 Å^2	*r* = 8.0–14.0 Å $\langle u^2\rangle^{1/2}$ = 0.16 Å^2	
Interchain Z-Z	*r* = 0.0–8.0 Å $\langle u^2\rangle^{1/2}$ = 0.12 Å^2	*r* = 8.0–14.0 Å $\langle u^2\rangle^{1/2}$ = 0.16 Å^2	

Table 4.22 The root-mean-square values used to broaden the individual partial correlation functions used to produce $T(r)_{model}$ for $(Cu_{1/2}Au_{1/2})CN$ at 300 K

Partial correlations in $(Cu_{1/2}Au_{1/2})CN$ at 10 K			
Intrachain M-M	r = 0.0–14 Å $\langle u^2 \rangle^{1/2}$ = 0.1 Å^2		
Intrachain Cu-C	r = 0.0–4.5 Å $\langle u^2 \rangle^{1/2}$ = 0.03 Å^2	r = 4.5–14.0 Å $\langle u^2 \rangle^{1/2}$ = 0.10 Å^2	
Intrachain Cu-N	r = 0.0–4.5 Å $\langle u^2 \rangle^{1/2}$ = 0.048 Å^2	r = 4.5–14.0 Å $\langle u^2 \rangle^{1/2}$ = 0.10 Å^2	
Intrachain Au-C	r = 0.0–4.5 Å $\langle u^2 \rangle^{1/2}$ = 0.048 Å^2	r = 4.5–14.0 Å $\langle u^2 \rangle^{1/2}$ = 0.10 Å^2	
Intrachain Au-N	r = 0.0–4.5 Å $\langle u^2 \rangle^{1/2}$ = 0.03 Å^2	r = 4.5–14.0 Å $\langle u^2 \rangle^{1/2}$ = 0.10 Å^2	
Intrachain Z-Z	r = 0.0–1.5 Å $\langle u^2 \rangle^{1/2}$ = 0.036 Å^2	r = 1.5–4.5 Å $\langle u^2 \rangle^{1/2}$ = 0.04 Å^2	r = 4.5–14.0 Å $\langle u^2 \rangle^{1/2}$ = 0.10 Å^2
Interchain M-M	r = 0.0–5.5Å $\langle u^2 \rangle^{1/2}$ = 0.16 Å^2	r = 5.5–14.0 Å $\langle u^2 \rangle^{1/2}$ = 0.19 Å^2	
Interchain M-Z	r = 0.0–5.5 Å $\langle u^2 \rangle^{1/2}$ = 0.2 Å^2	r = 5.5–8.0 Å $\langle u^2 \rangle^{1/2}$ = 0.22 Å^2	r = 8.0–14.0 Å $\langle u^2 \rangle^{1/2}$ = 0.28 Å^2
Interchain Z-Z	r = 0.0–5.5 Å $\langle u^2 \rangle^{1/2}$ = 0.2 Å^2	r = 5.5–8.0 Å $\langle u^2 \rangle^{1/2}$ = 0.23 Å^2	r = 8.0–14.0 Å $\langle u^2 \rangle^{1/2}$ = 0.28 Å^2

4.7.3 The broadening factors for the (Ag$_{1/2}$Au$_{1/2}$)CN models

Table 4.23 The root-mean-square values used to broaden the individual partial correlation functions used to produce T(r)$_{model}$ for (Ag$_{1/2}$Au$_{1/2}$)CN at 10 K

Partial correlations in (Ag$_{1/2}$Au$_{1/2}$)CN at 10 K				
Intrachain M-M	r = 0.0–14 Å $\langle u^2\rangle^{1/2}$ = 0.1 Å^2			
Intrachain Ag-C	r = 0.0–4.5 Å $\langle u^2\rangle^{1/2}$=0.052 Å^2	r = 4.5–14.0 Å $\langle u^2\rangle^{1/2}$ = 0.10 Å^2		
Intrachain Ag-N	r = 0.0–4.5 Å $\langle u^2\rangle^{1/2}$=0.040 Å^2	r = 4.5–14.0 Å $\langle u^2\rangle^{1/2}$ = 0.10 Å^2		
Intrachain Au-C	r = 0.0–4.5 Å $\langle u^2\rangle^{1/2}$=0.048 Å^2	r = 4.5–14.0 Å $\langle u^2\rangle^{1/2}$ = 0.10 Å^2		
Intrachain Au-N	r = 0.0–4.5 Å $\langle u^2\rangle^{1/2}$=0.052 Å^2	r = 4.5–14.0 Å $\langle u^2\rangle^{1/2}$ = 0.10 Å^2		
Intrachain Z-Z	r = 0.0–1.5 Å $\langle u^2\rangle^{1/2}$=0.035 Å^2	r = 1.5–4.5 Å $\langle u^2\rangle^{1/2}$ = 0.04 Å^2	r = 4.5–14.0 Å $\langle u^2\rangle^{1/2}$ = 0.10Å^2	
Interchain M-M	r = 0.0–5.5 Å $\langle u^2\rangle^{1/2}$ = 0.09 Å^2	r = 5.5–10 Å $\langle u^2\rangle^{1/2}$ = 0.1 Å^2	r = 10.0–14 Å $\langle u^2\rangle^{1/2}$ = 0.12Å^2	
Interchain M-Z	r = 0.0–6.75 Å $\langle u^2\rangle^{1/2}$ = 0.11 Å^2	r = 6.75–10 Å $\langle u^2\rangle^{1/2}$ = 0.13 Å^2	r = 10.–11. Å $\langle u^2\rangle^{1/2}$ = 0.16Å^2	r = 11.0–14 Å $\langle u^2\rangle^{1/2}$ = 0.18Å^2
Interchain Z-Z	r = 0.0–6.5 Å $\langle u^2\rangle^{1/2}$ = 0.10 Å^2	r = 6.5–11.0 Å $\langle u^2\rangle^{1/2}$ = 0.16 Å^2	r = 11.0–14. Å $\langle u^2\rangle^{1/2}$ = 0.18Å^2	

4.8 References

1. S. Kroeker, R. E. Wasylishen and J. V. Hanna, *J. Am. Chem. Soc.*, 1999, **121**, 1582.
2. D. L. Bryce and R. E. Wasylishen, *Inorg. Chem.*, 2002, **41**, 4131.
3. J. K. Harris and R. E. Wasylishen, *Inorg. Chem.*, 2009, **48**, 2316.
4. A. M. Chippindale, S. M. Cheyne and S. J. Hibble, *Angew. Chem. Int. Ed.*, 2005, **44**, 7942.
5. G. A. Bowmaker, B. J. Kennedy and J. C. Reid, *Inorg. Chem.*, 1998, **37**, 3968.
6. S. M. Cheyne, PhD Thesis, The University of Reading, 2004.
7. P. Pyykko, *Angew. Chem. Int. Ed.*, 2004, **43**, 4412.
8. M. O. Hakala and P. Pyykko, *Chem. Comm.*, 2006, 2890.
9. S. J. Hibble, G. B. Wood, E. J. Bilbe, A. H. Pohl, M. G. Tucker, A. C. Hannon and A. M. Chippindale, *Z. Kristallogr.*, 2010, **225**, 457-462.
10. S. J. Hibble, A. C. Hannon, S. M. Cheyne and S. G. Eversfield, *Inorg. Chem.*, 2002, **41**, 4990.
11. S. J. Hibble, S. M. Cheyne, A. C. Hannon and S. G. Eversfield, *Inorg. Chem.*, 2002, **41**, 1042.
12. S. J. Hibble, A. C. Hannon and S. M. Cheyne, *Inorg. Chem.*, 2003, **42**, 4724.

Chapter 5: The Bulk and Surface Structures of Nanocrystalline $Pd(CN)_2$ and $Pt(CN)_2$

5.1 Introduction

5.1.1 Synopsis

The work described in this chapter, following on from previous work on nickel cyanide,[1-2] proves that the basic structures of $Pd(CN)_2$ and $Pt(CN)_2$ are based on layers consisting of vertex-sharing square-planar $M(CN)_4$ units. The detailed structures of these sheets and the relationship between nearest-neighbour sheets have been determined using total neutron diffraction. Unlike in the case of nickel cyanide which has an extended layer structure, both palladium and platinum cyanides are nanocrystalline materials consisting of small stacks of sheets with approximate dimensions 30 Å × 30 Å. Both commercially available and synthesised samples have been investigated and the sheet sizes range from 10 Å × 10 Å to 80 Å × 80 Å. All palladium and platinum atoms in these nanocrystals are four coordinate and charge neutrality of the sheets is maintained by replacing some of the terminal $C\equiv N$ groups at the edges of the sheets by H_2O or NH_3 groups. In addition to total neutron diffraction, these materials have been characterised using a range of techniques including modelling of the X-ray diffraction patterns, vibrational spectroscopy and thermogravimetric analysis. The work has been published in *Inorganic Chemistry*.[3]

5.1.2 Background

Both palladium and platinum cyanide have been known in the literature since the beginning of the 19th Century. Palladium cyanide was first prepared by Wollaston in his separation of palladium metal from crude platinum, reported in 1804.[4-5] To separate palladium from an acidic solution of platinum, palladium and rhodium chlorides, he added aqueous mercuric cyanide to precipitate palladium cyanide, which on heating decomposed to afford palladium metal. In 1851, Bailey and Lamb attempted to use the thermal decomposition of palladium cyanide to determine the atomic weight of palladium metal but instead had to use another method because they were unable to dry their $Pd(CN)_2$ sample fully.[6] Although it is not entirely clear when the first sample of platinum cyanide was prepared, the decomposition of diammonium tetracyanoplatinate to produce platinum cyanide by Grünberg[7] in 1928 is widely cited as the only preparation which produces a water-free sample.[8-11]

Despite the fact that both $Pd(CN)_2$ and $Pt(CN)_2$ are commercially available, there is no structural information on them in the recent literature. In Linus Pauling's book, "The Nature of the Chemical Bond",[12] published in 1960, he predicts the structure of palladium cyanide (Figure 5.1) and by implication platinum cyanide. This structural prediction was based on magnetic measurements which show that $Pd(CN)_2$ is diamagnetic,[13] and hence contains square-planar Pd^{2+} (d^8) ions, and infrared spectroscopy which shows a single v(CN) at 2212 cm^{-1} indicative of bridging cyanide groups.[14]

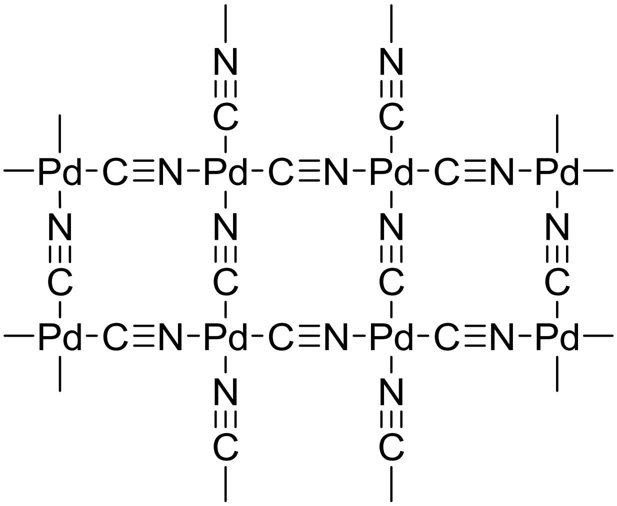

Figure 5.1 The structure of a $Pd(CN)_2$ sheet of proposed by L. Pauling.[12]

Palladium cyanide is sold as a catalyst for the quantitative and stereospecific ring opening of oxiranes,[15] it has also been used in the synthesis of olefinic cyanides from olefins[16] and can, like $PdCl_2$, be used in the dimerisation[17] or polymerisation[8, 16] of alkenes. Uses for platinum cyanide on the other hand appear to be entirely absent from the literature.

The structure of the first-row analogue, nickel cyanide, has recently been solved using total neutron diffraction[1] and consists of square-planar $Ni(CN)_4$ units fused together into sheets which retain *P*4 symmetry. The relationship between nearest-neighbour sheets is well defined and can be described by a unit cell in spacegroup *Pmmm* (Figure 5.2). There is however some difficulty in determining the relationship between next-nearest neighbour sheets.[2] This arises because although there is only one correct nearest-neighbour orientation, however, there are several possible next-nearest neighbour orientations, leading to disorder in the stacking sequence. The structures of the nickel-cyanide hydrates,

$Ni(CN)_2 \cdot nH_2O$ (where n = 1, 1½, 2 or 3), have also be been determined recently, all of which can easily be dehydrated to form anhydrous $Ni(CN)_2$.[18]

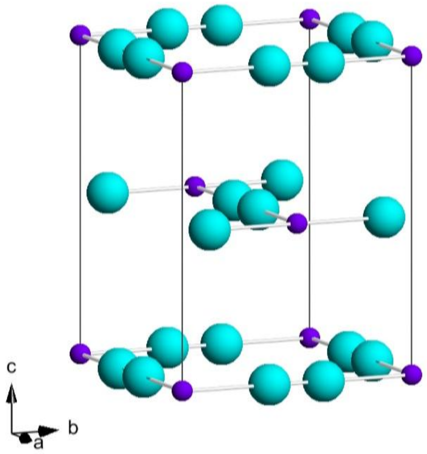

Figure 5.2 AB stacking of MZ_4 sheets in Pmmm. (Key: Metal (purple) and head-to-tail disordered cyanide (cyan)).

In contrast to the behaviour of nickel cyanide and its hydrates, both palladium and platinum cyanides are described in the literature as being difficult to dry[8] with water firmly bound within the structures. It is also stated that platinum cyanide made using aqueous methods has the approximate composition $Pt(CN)_2 \cdot 0.75H_2O$ and that this cannot be completely dried to form $Pt(CN)_2$ without further decomposition to spongy platinum metal.[19] This contrast in behaviour between the first and second/third row transition-metal cyanides suggested that there might be some differences in their structures and this indeed was found to be the case. A number of samples of palladium and platinum cyanides have been investigated, full experimental details are given in sections 5.8.1 - 5.8.5. The X-ray and neutron diffraction studies described below (sections 5.2.1 and 5.2.2), were carried out on dried commercially supplied palladium cyanide **(I)** and platinum cyanide **(II)**, synthesised by the decomposition of $(NH_4)_2[Pt(CN)_4]\cdot 2H_2O$. These materials have compositions $Pd(CN)_2\cdot 0.29H_2O$ **(I)** and $Pt(CN)_2\cdot 0.29NH_3$ **(II)**. Other routes to nanocrystalline palladium and platinum cyanides with a range of sheet sizes were also studied. For palladium cyanide, these include the thermal decomposition of *cis*-$Pd(CN)_2(NH_3)_2$ and its reaction with ethanoic acid, and for platinum cyanide, the reaction of $K_2Pt(CN)_4$ with K_2PtCl_4 in aqueous solution. These methods yield $Pd(CN)_2\cdot pNH_3$ **(V**, **VI)** and $Pt(CN)_2\cdot qH_2O$ **(VIII)**, demonstrating that it is possible to prepare ammonia and water terminated materials for both palladium and platinum cyanides. The smallest sheets prepared were 10 Å × 10 Å for $Pt(CN)_2\cdot qH_2O$ ($q = 0.67$) **(VIII)**. The high q value is a result of the small sheet size. Larger sized sheets of 80 Å × 80 Å, were produced for $Pd(CN)_2\cdot xH_2O$ ($x = 0.12$) **(IV)** by annealing under hydrothermal conditions and it was also possible to prepare a mixed-metal cyanide, $Pd_{1/2}Pt_{1/2}(CN)_2\cdot xH_2O$ ($x = 0.50$) **(IX)**, using a modified synthesis of **(VIII)**.

5.2 Results and Discussion

5.2.1 X-ray Diffraction

As shown in Figure 5.3, the powder X-ray diffraction patterns of $Pd(CN)_2\cdot 0.29H_2O$ **(I)** and $Pt(CN)_2\cdot 0.29NH_3$ **(II)** show clearly that these materials are much less crystalline than $Ni(CN)_2$.[1] Their powder patterns are not suitable for structure determination as they only contain a small number of very broad

Bragg reflections, which can be attributed to their very small crystallite sizes. The close resemblance of the two patterns to each other suggests however that palladium and platinum cyanides are isostructural.

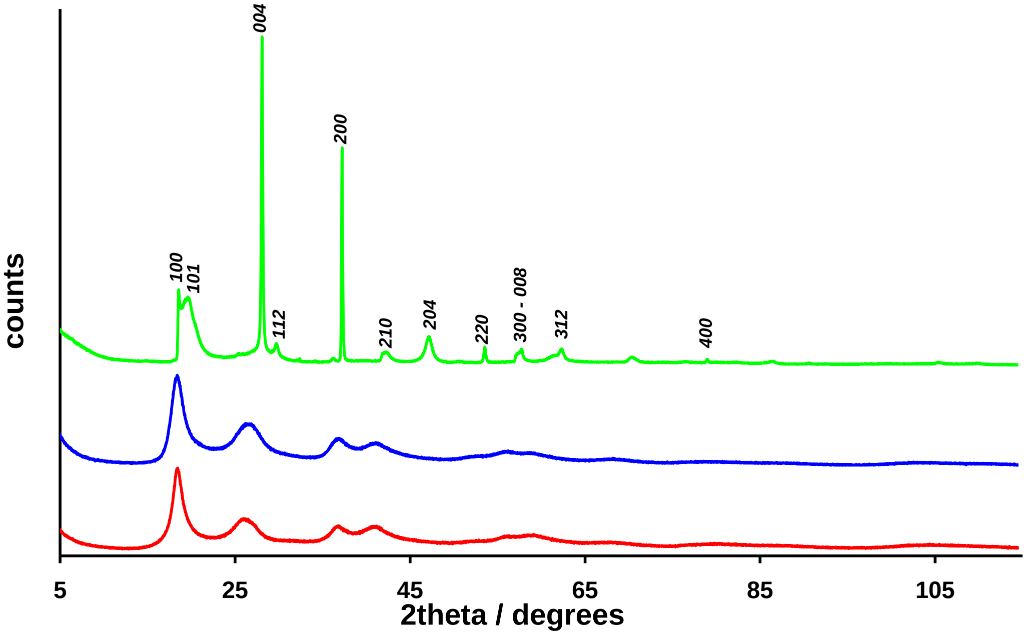

*Figure 5.3 Powder X-ray diffraction data for $Ni(CN)_2$ (green), $Pd(CN)_2{\cdot}0.29H_2O$ **(I)** (blue) and $Pt(CN)_2{\cdot}0.29NH_3$ **(II)** (red) measured at room temperature.*

Considering the proposed structure of the layer (Figure 5.1) and by analogy with the known tetragonal structure of $Ni(CN)_2$, the first peak (2θ ~18.2 °, d ~ 4.87 Å) might be assigned as the (*100*) reflection. For compounds **(I)** and **(II)** however, only two indices, (*hk*), are required to completely index the diffraction patterns. Unlike in the case of $Ni(CN)_2$, there are no sharp intense peaks corresponding to (*00l*) reflections indicating that the crystallite dimensions in the *c* direction must be very small. There is thus no information obtainable from Bragg diffraction on the third dimension. The Scherrer equation, Equation 5.1,[20] applied to the first reflection, (*10*), yields sheet dimensions, τ, of ~50 Å × 50 Å for both $Pd(CN)_2{\cdot}0.29H_2O$ **(I)** and $Pt(CN)_2{\cdot}0.29NH_3$ **(II)**.

$$\tau = \frac{k\lambda}{\beta(\cos\theta)} \tag{5.1}$$

Where k is the shape factor, taken to be 0.9, λ is the wavelength of the incident radiation (Cu K_α = 0.15406 nm) and β and θ are the full width half maximum and Bragg angle of the peak, respectively. More accurate sheet sizes have been obtained by modelling the X-ray diffraction data (section 5.2.5). In order to determine the structures of palladium and platinum cyanides, the results of the total neutron diffraction experiments are required (section 5.2.2).

5.2.2 Neutron Diffraction

Believing that the structures of palladium and platinum cyanides could readily be solved using total neutron diffraction, samples of $Pd(CN)_2{\cdot}xH_2O$ **(I)** and $Pt(CN)_2{\cdot}yNH_3$ **(II)** were taken to ISIS for neutron diffraction experiments on the GEM diffractometer.[21]

5.2.2.1 Data Collection

Neutron diffraction data were collected at 10 and 300 K for $Pd(CN)_2{\cdot}0.29H_2O$ **(I)** and $Pt(CN)_2{\cdot}0.29NH_3$ **(II)** on GEM. Data were collected on the sample of $Pd(CN)_2{\cdot}0.29H_2O$ **(I)** (5.0051 g) for 1500 μA h at 10 K and 970 μA h at 300 K.

Data were collected on the sample of $Pt(CN)_2 \cdot 0.29NH_3$ **(II)** (3.6740 g) for 1105 μA h at 10 K and 1180 μA h at 300 K.

Before the neutron diffraction experiment, the expectation was that $x = y \approx 0$ *i.e.* that both the cyanide samples were anhydrous. However from the first inspection of the data, it was clear that the samples contained hydrogenous material. By looking at the changes in the scattering levels with angle, it was calculated that the amount of hydrogen in the $Pd(CN)_2$ sample was ~⅔ of that in the $Pt(CN)_2$ sample. The first hypothesis was that there was water on the surface of the particles despite their careful drying and handling in an argon glovebox. In truth, the answer is much more interesting.

5.2.2.2 Data Reduction to Produce $T(r)_{exp}$

The data from detector banks 2, 3, 4 and 5, at mean scattering angles of 17.3, 34.3, 61.7 and 91.8°, were separately corrected for detector deadtime, multiple scattering, attenuation and inelasticity, and normalised to absolute scattering units. The contribution from the incoherent scattering due to hydrogen was then removed by subtracting a linear term to ensure that the total scattering oscillated about the self scattering calculated for $Pd(CN)_2$ and $Pt(CN)_2$. The calculated self scattering was then removed and the corrected data merged to yield an interference function, $Qi(Q)$, over the Q range 0.8–44 Å^{-1}, this was then extrapolated to Q = 0 Å^{-1} (Figure 5.4). The interference function was then multiplied by the Lorch modification function before $T(r)_{exp}$ was obtained *via* a Fourier transformation (Figure 5.5). All data reduction and manipulation was performed as described in Chapter 2.

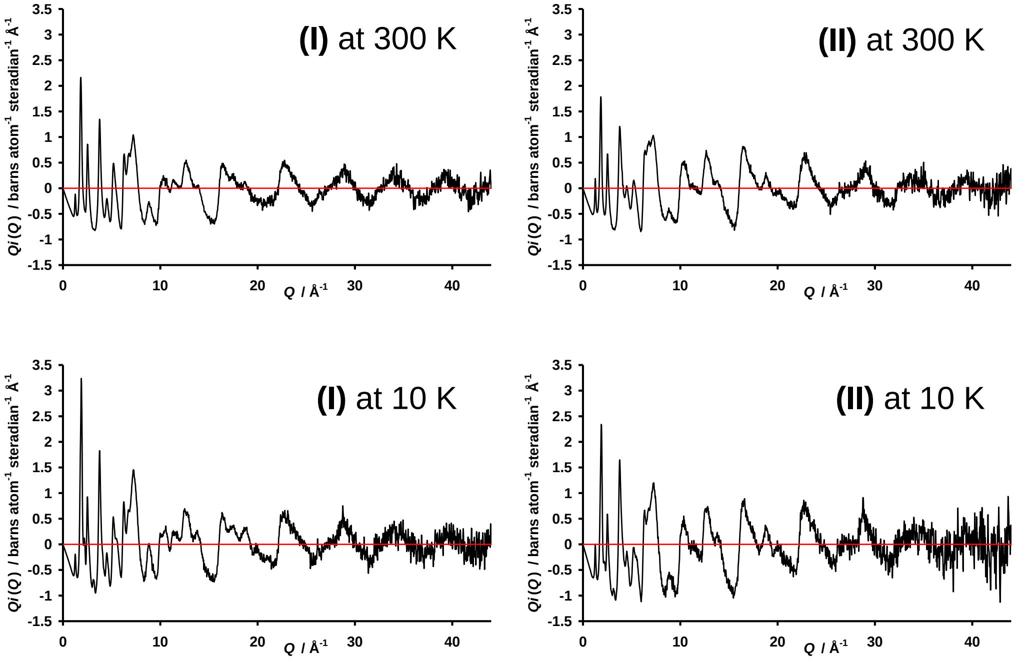

Figure 5.4 The interference functions, Qi(Q), for $Pd(CN)_2{\cdot}0.29H_2O$ ***(I)*** *(left) and $Pt(CN)_2{\cdot}0.29NH_3$* ***(II)*** *(right) at 10 and 300 K.*

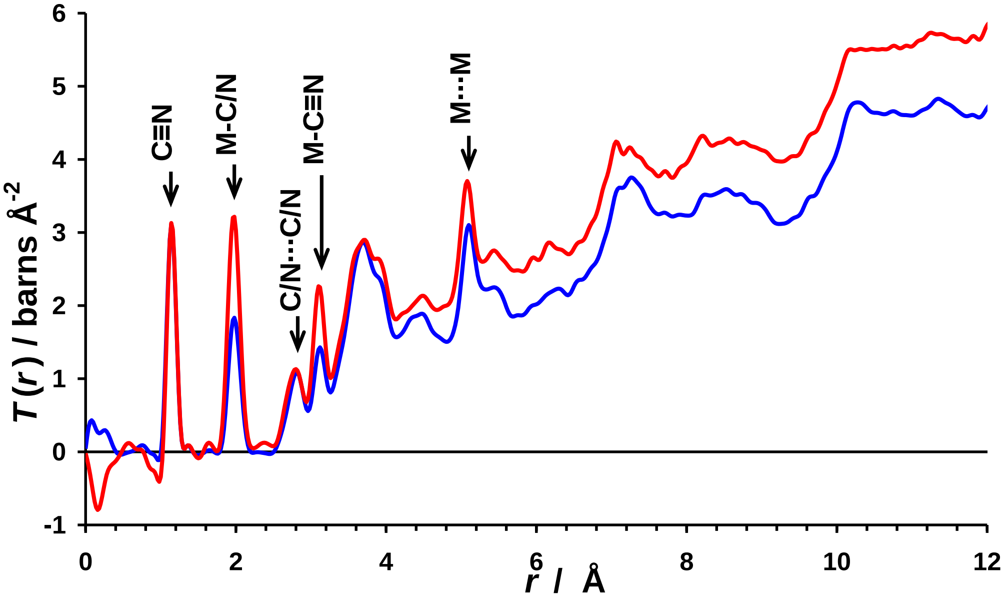

Figure 5.5 $T(r)_{exp}$ for $Pd(CN)_2$ (blue) and $Pt(CN)_2$ (red) both at 10 K.

Maxima in $T(r)_{\mathrm{exp}}$ correspond to frequently occurring interatomic distances in these compounds, and, at low r, can often be ascribed to “chemical bonds”.[22-23] Thus in the $Pd(CN)_2{\cdot}0.29H_2O$ **(I)** and $Pt(CN)_2{\cdot}0.29NH_3$ **(II)** correlation functions, the peaks at ~1.15 and ~1.98 Å correspond to the C≡N and M-C/N bond distances, respectively (Table 5.1). The equality, or near equality, of the M-C and M-N bond lengths is not unexpected, as it has been observed in a number of other metal cyanides *e.g.* in $Ni(CN)_2$[1] and the group 11 cyanides, CuCN,[24] AgCN[25] and AuCN.[26] It must be emphasised that this information on bond lengths is directly obtained and independent of any structural model (Table 5.1). The sharp peaks at ~5.09 Å correspond to the intralayer repeats *e.g.* Pd-(CN)-Pd in Figure 5.1. The first Bragg peaks in the X-ray diffraction patterns for both materials occur at $d \approx 4.8$ Å rather than at 5.1 Å, as would be the case if they were extended solids. This is consistent with their nanocrystallinity, as discussed in the X-ray Modelling (section 5.2.5).

Table 5.1 Bond lengths measured from each $T(r)_{exp}$ and angles calculated from them.

	$Pd(CN)_2$ **(I)**	$Pd(CN)_2$ **(I)**	$Pt(CN)_2$ **(II)**	$Pt(CN)_2$ **(II)**
Temp / K	10	300	10	300
1st peak $r_{C\equiv N}$ / Å	1.1487(8)	1.1580(8)	1.152(1)	1.1576(8)
2nd peak $r_{M\text{-}C/N}$ / Å	1.985(2)	1.983(2)	1.978(2)	1.979(1)
3rd peak $r_{C/N\cdots C/N}$ / Å	2.806(1)	2.807(2)	2.788(3)	2.792(1)
Z-M-Z angle (calc.) / °	89.95	90.11	89.62	89.72
$r_{M\cdots M}$ / Å	5.0988(2)	5.0869(4)	5.0787(2)	5.0709(1)

Over the full $T(r)$ range shown (Figure 5.5), the peaks in both correlation functions occur at almost identical positions providing further confirmation that the two materials are isostructural. The differences in peak intensities in the two correlation functions arise because of the smaller scattering length of palladium, 5.91 fm, compared to platinum, 9.60 fm. The intensities of peaks not involving metal atoms, for example, the peak at ~1.15 Å due to the C≡N correlations in the two materials, are identical in the two $T(r)$ plots. The divergence of the plots on increasing r reflects the different average scattering density of the two materials. The troughs in $T(r)$ at ~1 Å, just to the left of the peaks due to C≡N, and most evident in the platinum-cyanide correlation function, arise from the O-H and N-H correlations in palladium and platinum cyanides, respectively.

5.2.2.3 Confirming Pauling's Predicted Sheet Structure

Using the experimentally determined C≡N and M-C/N bond lengths (Table 5.1), a set of model sheets, one at each temperature for both compounds were generated. It should be emphasised at this point that total neutron diffraction is rather insensitive to C≡N order/disorder in the palladium and platinum cyanides as a consequence of the equality of the M-C and M-N bond lengths and it is appropriate to use a *pseudo* atom, Z, with a scattering length, $\bar{b}_Z$, where $\bar{b}_Z = (\bar{b}_C + \bar{b}_N)/2$ in place of distinct carbon or nitrogen atoms. From these MZ_4 sheets it was possible to predict longer-range correlations in $T(r)$. These are shown in Figure 5.6 for $Pd(CN)_2$ at 10 K. By comparing the predicted distances from this $Pd(CN)_2$ sheet with $T(r)_{exp}$ (Figure 5.7) it appears that Pauling's structural prediction is correct.

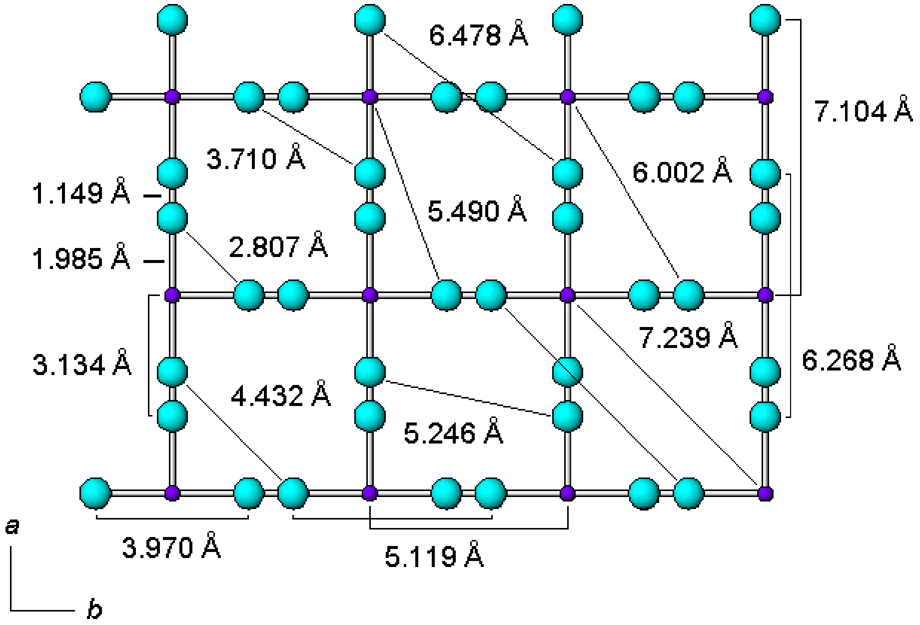

Figure 5.6 An MZ₄ layer as predicted by Pauling constructed using the C≡N and Pd-C/N bond lengths taken directly from $T(r)_{exp}$ for $Pd(CN)_2$ at 10 K. All other interatomic distances from 2 – 7.3 Å have been calculated. (Key: Metal (purple) and head-to-tail disordered cyanide (cyan)).

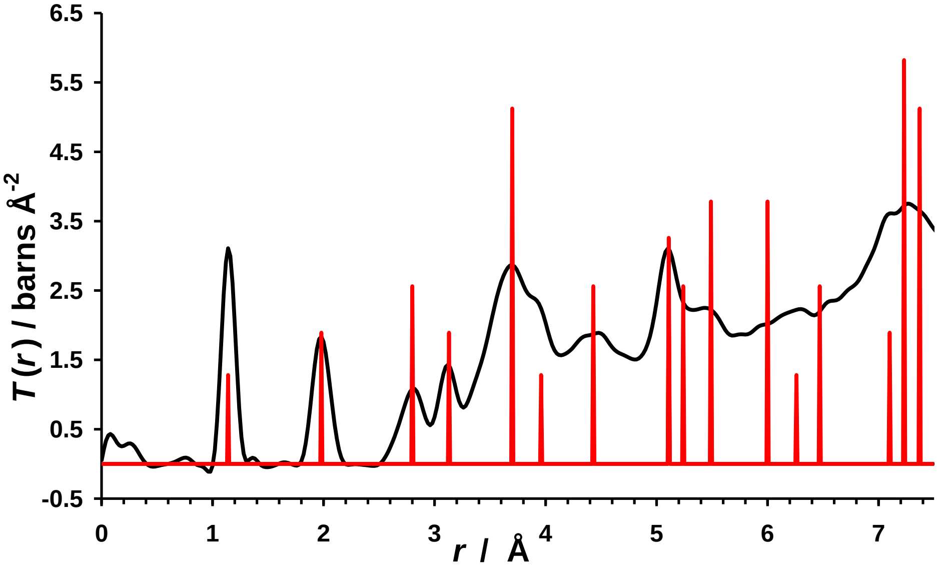

Figure 5.7 $T(r)_{exp}$ for $Pd(CN)_2$ at 10 K (black) along with the scaled delta functions from the predicted sheet (red). The excellent agreement between the predicted and observed peak positions confirms the Pauling's structural prediction is correct.

In addition to the fact that this model sheet correctly predicts the sharp peaks in $T(r)_{\text{exp}}$, the M-C/N bond length and the C/N-C/N non-bonded distance at ~2.8 Å, also given in Table 5.1, can be used to calculate the geometry around the metal atoms, which are indeed square planar. This is the first step in creating a complete model which fully explains $T(r)_{\text{exp}}$. The complete model requires, in addition to the sheet model, an interlayer separation and a stacking sequence for the sheets. The second two pieces of information are difficult to obtain in these materials because of the high level of interlayer disorder.

5.2.2.4 Scaling the Data

A more pressing issue was that the data reduction had not proceeded perfectly resulting in problems with the calculated coordination numbers. The true coordination number calculated from the position and area of the CN peak in $T(r)_{\text{exp}}$ must be 1.00 and from good data, collected on a well-behaved sample, it is possible to obtain this value to within 2 %. The coordination numbers of the first peaks in $T(r)_{\text{exp}}$ were calculated using Equation 2.1, in Chapter 2, to quantify how well the data reduction had been reduced, unfortunately the values obtained were all 4 % or more out (Table 5.2). When modelling $T(r)$, the scattering density of the model must match that of the data and usually only models with the correct scattering density should be considered. However, because there were complications with the data reduction due to the presence of hydrogen, it was decided that the $Qi(Q)$ data should be scaled so as to give $T(r)_{\text{exp}}$ with a scattering density which matched the model. Although this leads to more variables in the crystallographic model and a final $T(r)_{\text{exp}}$ which is model dependent, this method has led to not only good agreement between the data and the model, as of course it would, but also to a better agreement (less than 4 % difference) between the true and observed coordination numbers from the CN peak (Table 5.2).

Table 5.2 The coordination numbers before and after scaling $T(r)_{calc}$. Along with the final model used.

	$Pd(CN)_2$ **(I)**	$Pd(CN)_2$ **(I)**	$Pt(CN)_2$ **(II)**	$Pt(CN)_2$ **(II)**
Temp / K	10	300	10	300
N^* C≡N before scaling	1.08	0.93	1.04	0.85
Space group	$I4_1/amd$	$I4_1/amd$	$I4_1/amd$	$I4_1/amd$
$a_{T(r)}{}^{\S}$ / Å	5.119	5.124	5.108	5.116
$r_{M\cdots M}$ / Å	5.0988(2)	5.0869(4)	5.0787(2)	5.0709(1)
c / Å	13.60	13.76	13.60	13.76
scale factor	0.9613135	1.0448543	0.9676120	1.1619425
N^* C≡N after scaling	1.04	0.97	1.01	0.98

**N is the coordination number, $^{\S}a_{T(r)}$, is calculated from, $a_{T(r)} = r_{CN} + 2r_{M\text{-}C/N}$.*

5.2.3 The Bulk Structure of the Nanoparticles

5.2.3.1 Nearest-Neighbour Stacking Sequences

Having established unequivocally that Pauling's sheet model is correct, it is then necessary to determine how neighbouring sheets stack together. The sheets so far described have effective *P*4 symmetry because of the assumption that C and N are indistinguishable and that there is a single M-Z bond distance. The *a* lattice parameter used, $a_{T(r)}$, as defined above, along with the bond lengths obtained from the peaks at low *r* in *T*(*r*) (Table 5.1) were used to calculate the fractional atomic coordinates, x and y, for both metal and Z atoms in the unit cell (Section 5.9.2). It should be noted that the value of $a_{T(r)}$ is always larger than the corresponding $r_{\mathrm{M \cdots M}}$ value (Figure 5.5) because even at low temperatures, M-CN-M bending motions draw the metal atoms closer together. From $r_{\mathrm{C \equiv N}}$ and $r_{\mathrm{M\text{-}C/N}}$ the M-Z≡Z angle can be calculated and further discussions of this are given in section 5.5. At higher r, many correlations overlap in $T(r)$ (Figure 5.5) making it impossible to extract individual distances directly. However, $T(r)$ can be calculated for any structural model, $T(r)_{\mathrm{calc}}$, and once broadened, $T(r)_{\mathrm{model}}$, compared with that obtained experimentally. The models used are crystallographic and require a set of lattice parameters and atomic coordinates, obtained above, along with a space group. Plausible ways of stacking sheets together whilst retaining *P*4 sheet symmetry were then explored. During the modelling process, a variety of interlayer separations and stacking sequences were considered. The best final models use a lattice parameters, $a_{T(r)}$, calculated by, $a_{T(r)} = r_{\mathrm{CN}} + 2r_{\mathrm{M\text{-}C/N}}$, along with a stacking sequence with four sheets in the unit cell. The interlayer separations were estimated from density measurements to be ~3.4 Å. This value agrees with that obtained by scaling the interlayer separation found for $\mathrm{Ni(CN)_2}$ using the ratio of $r_{\mathrm{Pt\text{-}Z}}/r_{\mathrm{Ni\text{-}Z}}$. Subsequent modelling of the correlation functions, $T(r)$, yielded final values for the interlayer separations at 10 and 300 K of 3.40 and 3.44 Å for both materials, giving c lattice parameters of 13.6 and 13.76 Å, respectively. These separations give the best fit to the data for all models in which the sheets stack as shown in Figure 5.2 with spacegroup *Pmmm*. Other combinations of interlayer distances and stacking sequences were tested with none giving better fits to the data. For example, models with metal atoms stacked above each other, as in $K_2Pt(CN)_4Br_{0.3}{\cdot}3H_2O$,[27] did not reproduce $T(r)_{\mathrm{exp}}$ well, regardless of interlayer distance. In addition, body centred stacking sequences in spacegroup *Immm* (Figure 5.8) require a larger interlayer spacing (~3.5 Å) to obtain the best fit to $T(r)_{\mathrm{exp}}$. This necessary increase in interlayer spacing creates a problem: the densities of the models are much lower than the measured values resulting in the scaling factors required for the body centred models being further from 1 than the scaling factor for the *Pmmm* models. All this evidence strongly suggests that the nearest-neighbour sheets stack as shown for the *Pmmm* model.

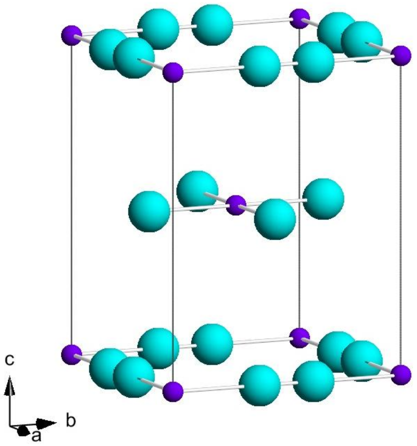

Figure 5.8 AB stacking sequence in Immm. (Key: Metal (purple) and head-to-tail disordered cyanide (cyan)).

5.2.3.2 Broadening

As discussed in Chaper 2, $T(r)_{\mathrm{calc}}$ generated from crystallographic models consist of sets of delta functions, one set per pair of atoms, which require broadening to generate $T(r)_{\mathrm{model}}$. In layered materials such as $Ni(CN)_2$, it is logical to broaden the inter and intra-sheet contributions to $T(r)_{\mathrm{calc}}$ separately. This is because distances between atoms within a sheet are more constrained than distances between atoms in different sheets. When comparing $T(r)_{\mathrm{exp}}$ with $T(r)_{\mathrm{calc}}$ with a model sheet for $\mathrm{Pd(CN)_2}$ and $\mathrm{Pt(CN)_2}$ (Figure 5.7), it can be seen that all of the sharp features in $T(r)$ are accounted for by just considering intralayer correlations. However not all of the peaks from within the layer seem to broaden at the same rate with increasing r, for example, the third peak at ~2.8 Å is broader that the fourth peak at ~3.1 Å. The intralayer correlations could be seen to be split into two classes (Figure 5.9) with one set of correlations coming from atom pairs along a single MCN chain, the other set coming from atoms in different chains (Figure 5.10). The correlations coming from atoms in a single MCN chain broaden less rapidly with r than the correlations coming from atoms in different chains, as is expected from geometry. More interestingly the increase in the broadening factors between these two sets of correlations is larger than would be expected purely from geometric considerations. By separating the correlations in this manner, a better fit to the data was obtained using a smaller number of broadening terms than was possible when employing the broadening regime used to model $\mathrm{Ni(CN)_2}$.[1] Not only is this broadening intuitive but by looking at the lowest energy vibrational modes calculated for $\mathrm{Ni(CN)_2}$,[2] this also leads to a better understanding of the sheet dynamics which are discussed in greater detail in 5.5. Full details of separating the correlations are given in Section 5.9.3.

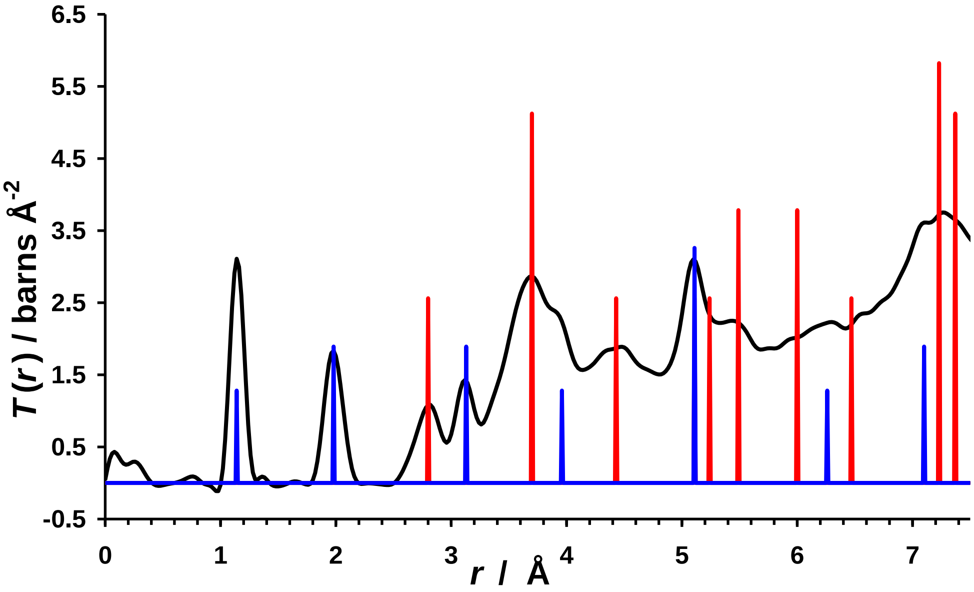

Figure 5.9 $T(r)_{exp}$ for $Pd(CN)_2$ at 10 K (black), along with scaled delta functions calculated from the model sheet, split into correlations from atom pairs within a chain (blue) and those in which the atoms are in different chains (red).

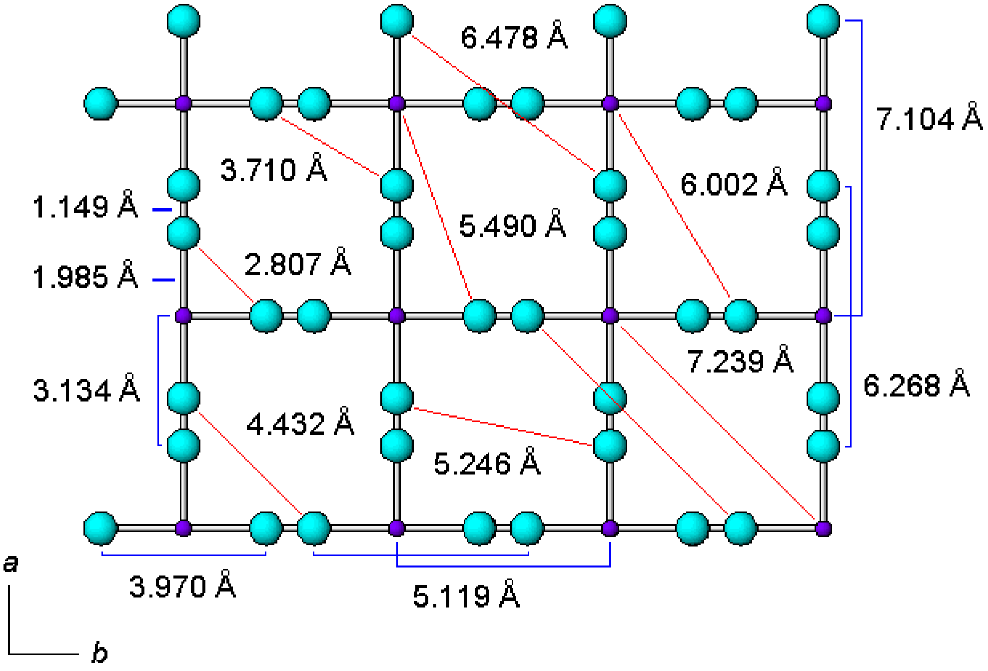

Figure 5.10 Calculated interatomic distances, within a $Pd(CN)_2$ layer, over the 0 – 7.3 Å range. Correlations from atom pairs within a chain are shown in blue, while those in which the atoms are in different chains are shown in red. (Key: Metal (purple) and head-to-tail disordered cyanide (cyan)).

5.2.3.3 Next Nearest-Neighbour Stacking Sequences

Having confirmed that the relationship between nearest-neighbour sheets in $Pd(CN)_2$ and $Pt(CN)_2$ is the same as seen in $Ni(CN)_2$, it is of interest to investigate the relationship between the next-nearest neighbour sheets in these materials. The next-nearest neighbour stacking sequence in $Ni(CN)_2$ has been contentious due to the high level of disorder between the sheets and how this can best be described. A function, p, describes the orientation of next-nearest neighbour sheets, when the next-nearest neighbour sheets are always identical, $p = 1$, (*e.g.* Figure 5.8) and when they are always different, $p = 0$ (Figure 5.11(b)).[2] In work done on $Ni(CN)_2$ using a crystallographic model, with the inter- and intra-sheet contributions broadened separately, it was found that a model in $P4_2/mmc$ (Figure 5.11(a)), with $p = 0.5$, gave the best fit to $T(r)_{\mathrm{exp}}$.[1, 18] In work done using the Reverse Monte Carlo (RMC) modelling, the value of p was determined to be close to 0.33, to describe such a stacking sequence a unit cell with a large number of sheets is required.

To explore the next-nearest neighbour stacking sequences in $Pd(CN)_2$ and $Pt(CN)_2$, models in spacegroups $Pmmm$, $P4_2/mmc$ and $I4_1/amd$ were compared. Although differences in the unbroadened correlation functions, $T(r)_{\mathrm{calc}}$, are apparent for the three models, where $r > 6.8$ Å, there was no significant difference in the agreement between $T(r)_{\mathrm{exp}}$ and $T(r)_{\mathrm{model}}$, with all models giving good agreement with the data. Because the degree of interlayer disorder is very high in these materials, larger root-mean-square displacements are needed to broaden the interlayer correlations than for the intralayer correlations. The interlayer broadening factors used to model $Pd(CN)_2$ and $Pt(CN)_2$ are even larger than is needed to model $Ni(CN)_2$.

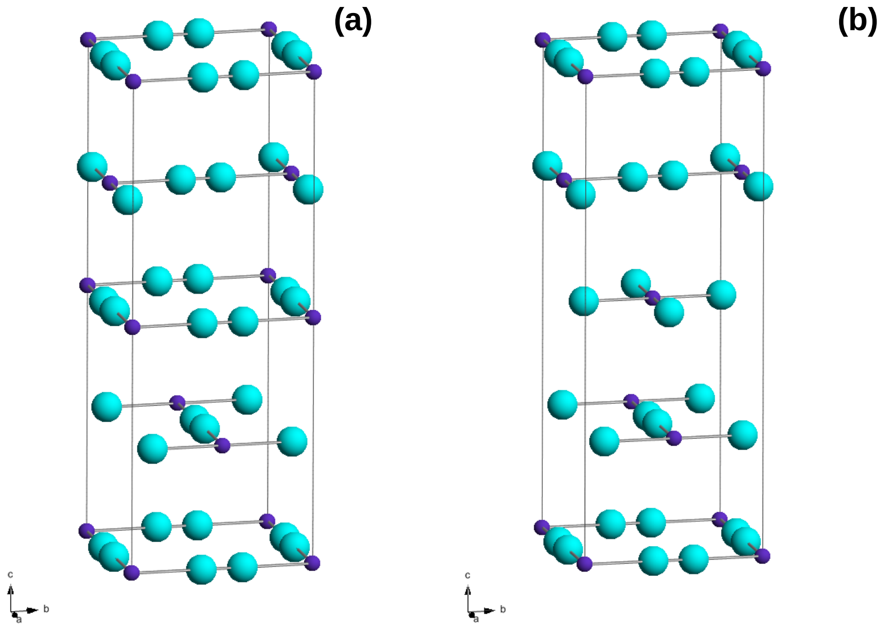

Figure 5.11 (a) The ABAB' stacking sequence in $P4_2/mmc$ used to model $Ni(CN)_2$ using a crystallographic unit cell,[1] and (b)The ABA'B' stacking sequence in $I4_1/amd$, used as the starting point to model $Ni(CN)_2$, using RMC modeling.[2] (Key: Nickel (purple) and head-to-tail disordered cyanide (cyan)).

This increase in disorder from $Ni(CN)_2$ to $Pd(CN)_2$ and $Pt(CN)_2$ explains the fact that no information about the third dimension is seen in the Bragg diffraction patterns from palladium and platinum cyanide, in contrast to the sharp *00l* reflections in seen in the diffraction pattern from nickel cyanide (Figure 5.3). The model in $I4_1/amd$ was chosen for the final modelling because it only requires two sets of fractional coordinates to define the structure; namely, one for M and one for Z. The full models, detailed in section 4.6, reproduce $T(r)_{exp}$ for both $Pd(CN)_2{\cdot}0.29H_2O$ **(I)** and $Pt(CN)_2{\cdot}0.29NH_3$ **(II)** at 10 K (Figure 5.12 and Figure 5.13) and at 300 K (Figure 5.14 and Figure 5.15).

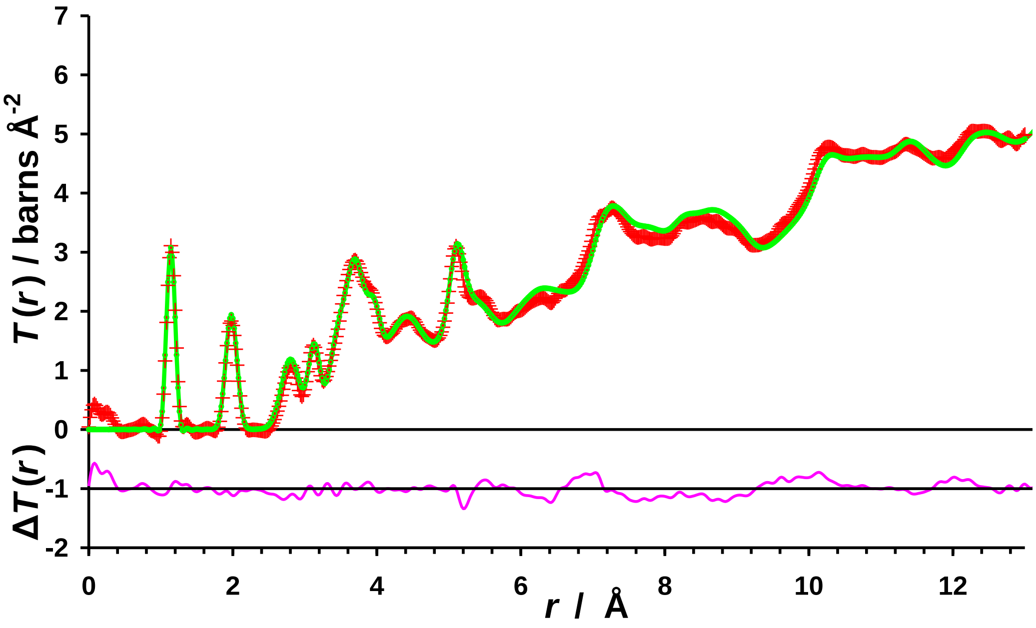

*Figure 5.12 T(r) for Pd(CN)$_2$·0.29H$_2$O **(I)** at 10 K, data (red crosses), model (green line) and the difference between them -1 (pink). $R_{T(r)}$ = 0.135, over the range 0 - 14 Å.*

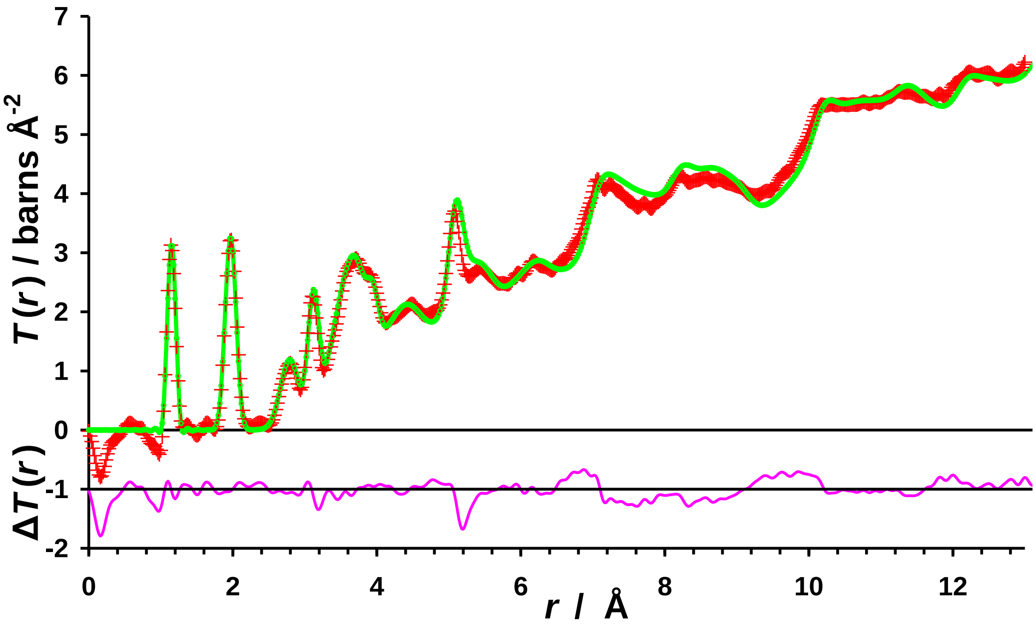

*Figure 5.13 T(r) for Pt(CN)$_2$·0.29NH$_3$ **(II)** at 10 K, data (red crosses), model (green line) and the difference between them -1 (pink). $R_{T(r)}$ = 0.125, over the range 0 - 14 Å.*

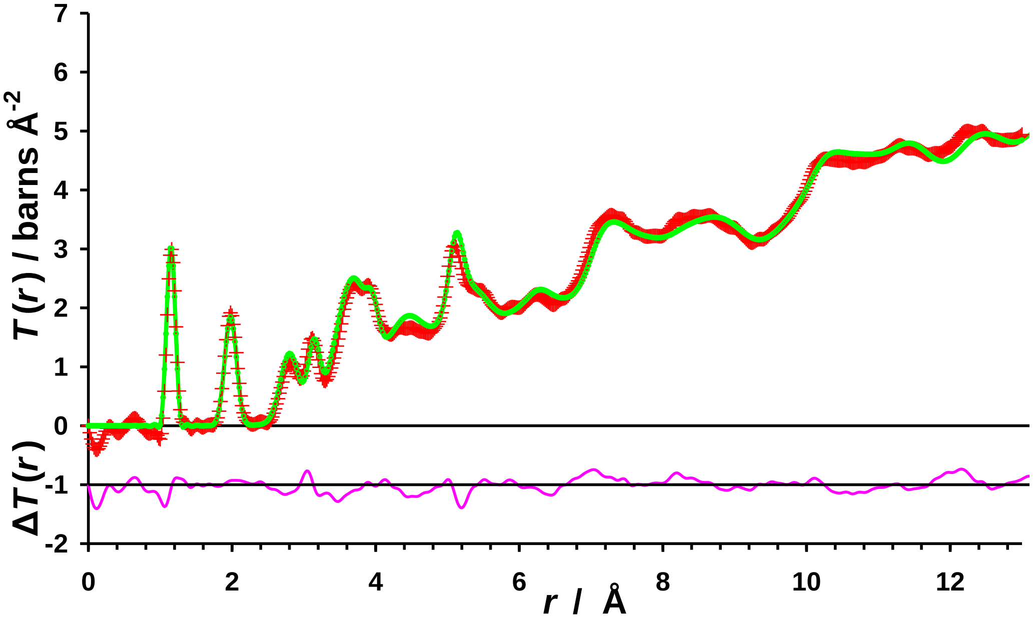

*Figure 5.14 T(r) for Pd(CN)$_2$·0.29H$_2$O **(I)** at 300 K, data (red crosses), model (green line) and the difference between them -1 (pink). R$_{T(r)}$ = 0.156, over the range 0 - 14 Å.*

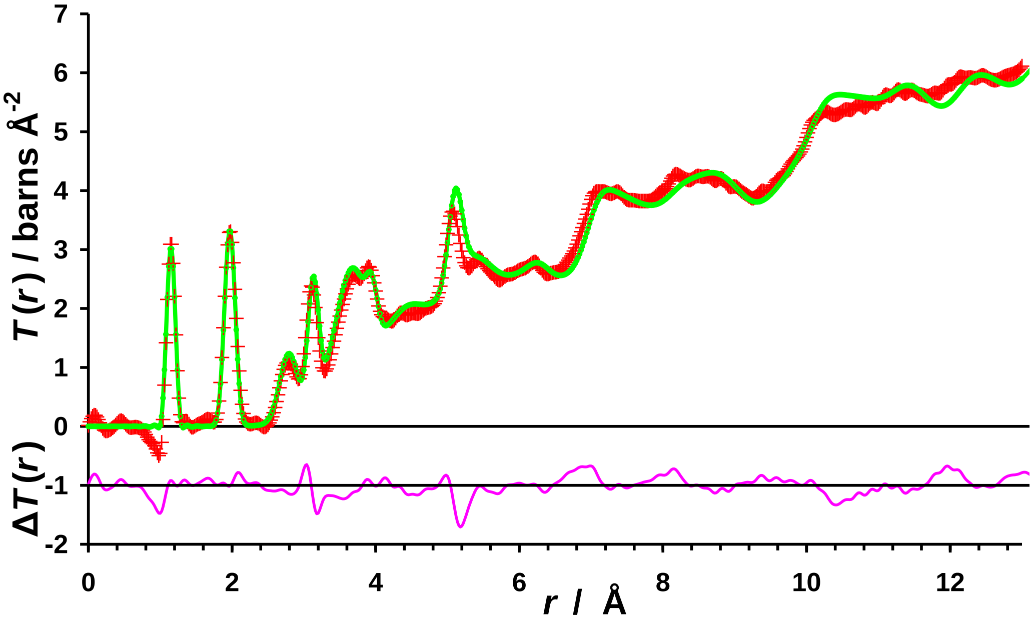

*Figure 5.15 T(r) for Pt(CN)$_2$·0.29NH$_3$ **(II)** at 300 K, data (red crosses), model (green line) and the difference between them -1 (pink). R$_{T(r)}$ = 0.145, over the range 0 - 14 Å.*

The two areas of significant deviation between $T(r)_{\text{model}}$ and $T(r)_{\text{exp}}$ for both compounds at 10 K and 300 K, are at around $r \approx 5.1$ Å, as discussed in section 5.2.3.1, and where $r < 1$ Å. Some noise at low r in $T(r)_{\text{exp}}$ is caused by imperfections in the data reduction but the peak at just under 1 Å is sample dependent, as explained in section 5.2.4.

5.2.4 The Edges of the Nanoparticles

One feature visible in both $T(r)_{\text{exp}}$ plots for compounds **(I)** and **(II)**, and not yet accounted for, is a negative peak at r just less than 1 Å. This feature must arise from correlations involving hydrogen because hydrogen has a negative coherent scattering length and so produces troughs rather than peaks in $T(r)_{\text{exp}}$. This feature is more pronounced in $T(r)_{\text{exp}}$ for the platinum cyanide sample. Based on the relative intensities of these features, they can be ascribed to N-H correlations from NH_3 groups in the platinum cyanide sample and to O-H correlations from H_2O in the palladium cyanide sample. The ratio of the intensities of the negative peaks for equimolar amounts of NH_3 and H_2O, calculated from the average coherent scattering lengths, $\bar{b}_c$, of the appropriate atoms and the number of N-H and O-H correlations is 2.42, $\left(\left(6\bar{b}_N\bar{b}_H\right) \div \left(4\bar{b}_O\bar{b}_H\right)\right)$. Figure 5.16 shows the low r region of $T(r)_{\text{exp}}$, together with calculations of models of $Pt(CN)_2{\cdot}yNH_3$ with ($0.1 \leq y \leq 0.3$). The best agreement is for $y = 0.30$. A small positive peak at 1.62 Å, arising from the H···H correlations in NH_3, would be predicted if the $Pt(CN)_2$ sample contained ammonia, which is indeed observed. The amounts of water and ammonia in the two compounds are equal, and in the case of $Pd(CN)_2{\cdot}xH_2O$ $x = 0.30$ also gives a good fit to $T(r)_{\mathrm{exp}}$ (Figure 5.17).

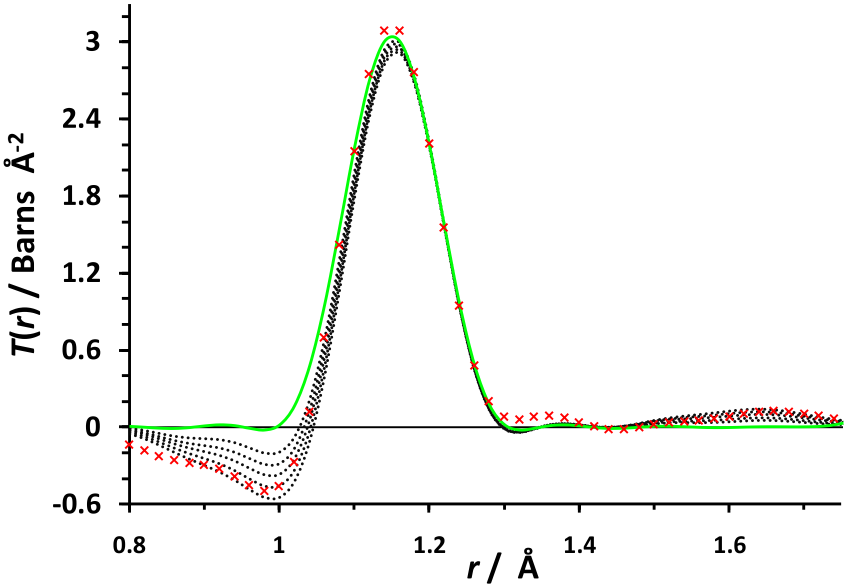

Figure 5.16 Modelling the low r region of T(r) for $Pt(CN)_2{\cdot}yNH_3$. $T(r)_{exp}$ (red crosses), $T(r)_{model}$ for $y = 0$ (green line) and $T(r)_{model}$ for $y = 0.1$, 0.15, 0.20, 0.25 and 0.30 (black dotted curves, with $y = 0.30$ reaching the most negative value).

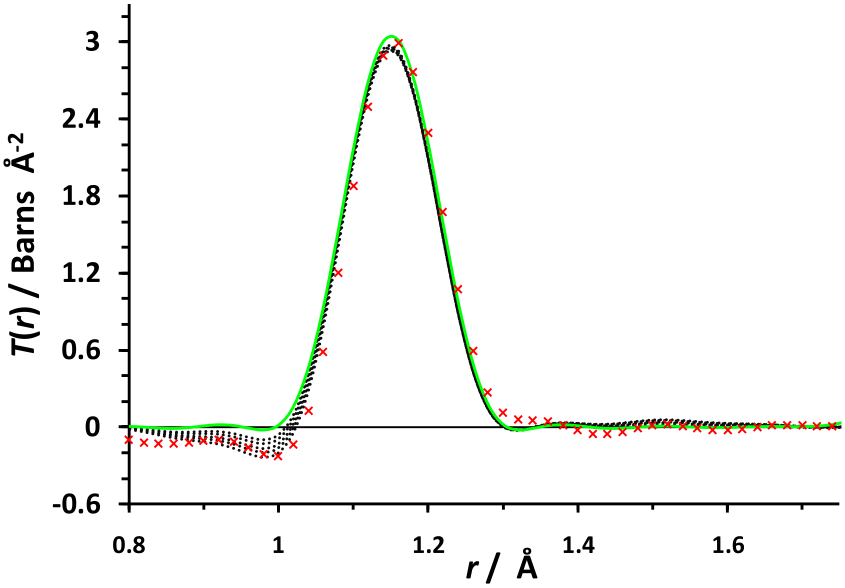

Figure 5.17 Modelling the low r region of T(r) for $Pd(CN)_2{\cdot}xH_2O$. $T(r)_{exp}$ (red crosses), $T(r)_{model}$ for $x = 0$ (green line) and $T(r)_{model}$ for $x = 0.1$, 0.15, 0.20, 0.25 and 0.30 (black dotted curves, with $x = 0.30$ reaching the most negative value).

These *x* and *y* values are in good agreement with the thermogravimetric analysis for these materials (section 5.10) and are in line with the modelling of the X-ray data described below.

The presence of significant amounts of water and ammonia in these palladium and platinum cyanides is a consequence of their nanocrystalline nature. In nanocrystalline materials the terminating groups, in this case water and ammonia, represent a significant fraction of the material composition. Figure 5.18 shows the "ultimate" nanoparticles, $Pd_4(CN)_8(H_2O)_4$ and $Pt_4(CN)_8(NH_3)_4$, in which four water or ammonia molecules are required to maintain the square-planar coordination around the metal atoms whilst maintaining charge neutrality.

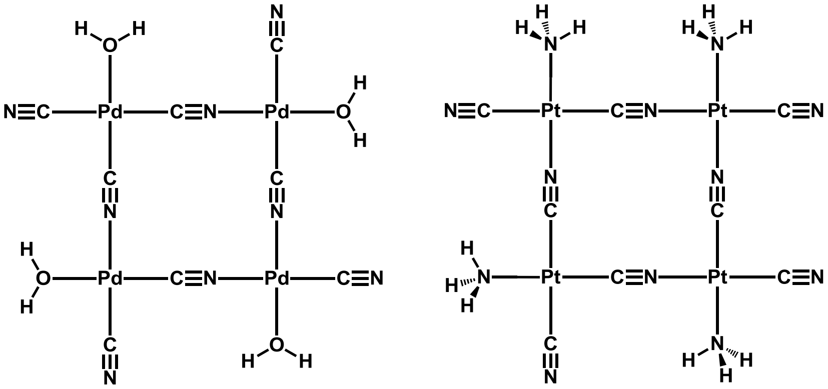

Figure 5.18 The "ultimate" nanoparticles, $Pd_4(CN)_8(H_2O)_4$ and $Pt_4(CN)_8$ $(NH_3)_4$.

The empirical formulae of these nanoparticles, $Pd(CN)_2{\cdot}xH_2O$ and $Pt(CN)_2{\cdot}yNH_3$, have $x = y = 1$ hence the sheet sizes of the nanoparticles with $x = y = 0.29$ clearly must be larger than the "ultimate" nanoparticles. Table 5.3 shows how *x* and *y* depend on the sheet size in terms of both Pt-CN-Pt or Pd-CN-Pd repeats in Å, assuming that both charge neutrality and square-planar coordination around M are maintained. A further assumption that the sheets are square simplifies the table, and has proven to be reasonable from the X-ray modelling study (section 5.2.5).

Table 5.3 The relationship between model sheet size and the composition in nanocrystalline $Pd(CN)_2$ and $Pt(CN)_2$, together with the calculated ratio of terminal : bridging cyanide groups.

Sheet size[§] (Å × Å)	1 × 1 (5×5)	2 × 2 (10×10)	3 × 3 (15×15)	4 × 4 (20×20)	5 × 5 (25×25)	6 × 6 (30×30)	7 × 7 (35×35)	8 × 8 (40×40)	9 × 9 (45×45)	10 × 10 (50×50)	20 × 20 (100×100)
n for $M(CN)_2 \cdot nH_2O$ and $M(CN)_2 \cdot nNH_3$	1.00	0.67	0.50	0.40	0.33	0.29	0.25	0.22	0.20	0.18	0.10
(no. terminal CN) / (no. bridging CN)	1:0	1:2	1:3	1:4	1:5	1:6	1:7	1:8	1:9	1:10	1:20

[§] Sheet size is expressed in terms of number of M-CN-M repeats and the corresponding approximate size in Ångstroms, assuming that the M-CN-M repeat is 5 Å.

Using Table 5.3 sheet sizes of 30 Å × 30 Å (6 × 6 M-CN-M repeats) are obtained for both $Pd(CN)_2 \cdot 0.29H_2O$ **(I)** and $Pt(CN)_2 \cdot 0.29NH_3$ **(II)**, which are a little smaller than the crystallite sizes obtained from the Scherrer equation. The sheet sizes obtained for $Pd(CN)_2\cdot 0.29H_2O$ **(I)** and $Pt(CN)_2\cdot 0.29NH_3$ **(II)** determined and derived using a variety of methods are given in Table 5.4.

*Table 5.4 Sheet sizes and compositions for the neutron samples $Pd(CN)_2\cdot xH_2O$ **(I)** and $Pt(CN)_2\cdot yNH_3$**(II)** determined and derived by a variety of methods*[§]

Experimental Method	$Pd(CN)_2\cdot xH_2O$ **(I)**		$Pt(CN)_2\cdot yNH_3$ **(II)**	
	x	Sheet size / Å × Å	*y*	Sheet size / Å × Å
From width of (*10*) reflection in powder XRD[†]	*0.18*	**50 × 50**	*0.15*	**60 × 60**
From modelling powder XRD[$]	*0.29*	**30 × 30**	*0.29*	**30 × 30**
TGA$_{>100^\circ\mathrm{C}}$[¥]	**0.29**	*30 × 30*	**0.22**	*40 × 40*
Modelling peak at ~1 Å in *T*(*r*)	**0.30**	*30 × 30*	**0.30**	*30 × 30*
From longest-range correlations in *D*(*r*)[#]	*~0.29*	**~30 × 30**	*~0.29*	**~30 × 30**

[§] *Experimentally determined values are given in **bold** and derived ones in italics from information in Table 5.3.*

[†] *Sheet size determined using the Scherrer equation, Equation 5.1.*

[$] *Sheet size determined by comparison of the experimental powder XRD pattern with those calculated for a range of sheet sizes for $Pd(CN)_2$ (Figure 5.21) and $Pt(CN)_2$ (Figure 5.19) as discussed in section 5.2.5.*

[¥] *Calculated assuming $M(CN)_2\cdot nH_2O/NH_{3(s)}\rightarrow M_{(s)}+(CN)_{2(g)}+nH_2O/NH_{3(g)}$ as detailed in section 5.10.*

[#] *Assuming square sheets, each sheet edge is (longest correlation)/$\sqrt{2}$ (Figure 5.22).*

5.2.5 X-Ray Diffraction Modelling

X-ray diffraction patterns were calculated by Dr Simon Hibble using the DISCUS program[28] for individual $Pd(CN)_2$ and $Pt(CN)_2$ square sheets all with *P*4 symmetry, but with differing extents. In each case, the M···M distance (*i.e.* M-CN-M repeat) from *T*(*r*) was used as the lattice parameter. The modelling of the X-ray data of platinum cyanide shows that the peak positions, shapes and widths all vary as a function of the sheet extent (Figure 5.19). The 30 Å × 30 Å (6 × 6 Pt-CN-Pt repeats) sheet size produces the best fit across the whole pattern to the experimental pattern for $Pt(CN)_2{\cdot}0.29NH_3$ **(II)** (Figure 5.20) in good agreement with the values obtained for the sheet sizes using other methods (Table 5.4). A notable feature is that the first reflection, (*10*), is calculated to have a *d*-spacing of 4.84 Å, as measured experimentally, even though the Pt···Pt distance used is 5.0709 Å (Table 5.2). This deviation is a consequence of the small extent of the sheets. The simulations for palladium cyanide (Figure 5.21) show similar behaviour, also yielding a sheet size of 30 Å × 30 Å for $Pd(CN)_2{\cdot}0.29H_2O$ **(I)**. Remarkably, these two-dimensional models can account for the entire experimental X-ray diffraction patterns and no (*00l*) or (*hkl*) reflections are observed. This behaviour is consistent with the high degree of disorder as seen in the interlayer correlations determined from the total neutron diffraction study. In contrast, in the X-ray pattern of $Ni(CN)_2$ (Figure 5.3) the interlayer reflections are very sharp indicating that hundreds, if not thousands, of sheets are stacked together.[1-2]

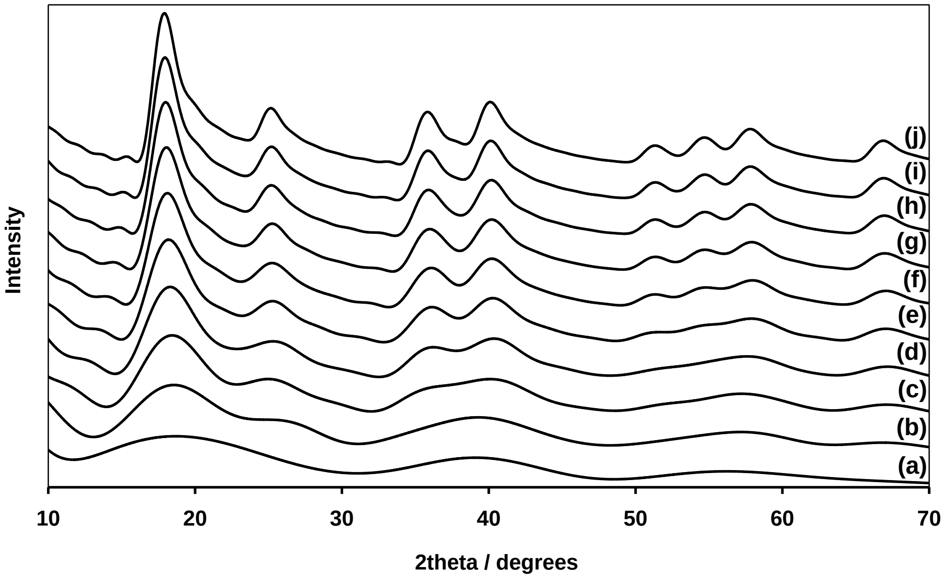

Figure 5.19 Modelling of X-ray diffraction patterns for Pt(CN)$_2$ sheets with sheet sizes varying from 5 Å × 5 Å to (j) 50 Å × 50 Å in increments of 5 Å × 5 Å.

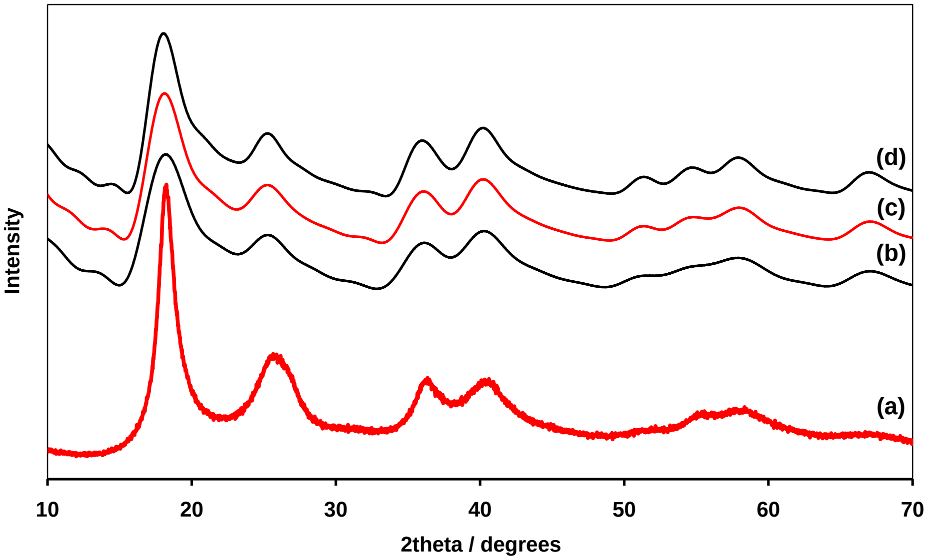

*Figure 5.20 Experimental X-ray diffraction pattern of (a) Pt(CN)$_2$.0.29NH$_3$ **(II)** compared to calculated patterns for Pt(CN)$_2$ sheets with sheets sizes of (b) 25 Å × 25 Å, (c) 30 Å × 30 Å and (d) 35 Å × 35 Å.*

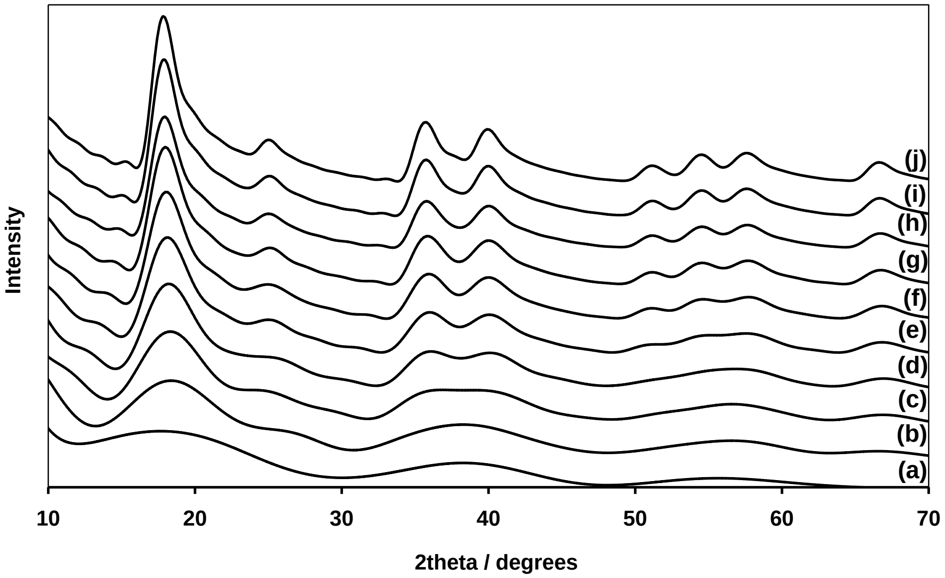

Figure 5.21 Modelling of X-ray diffraction patterns for $Pd(CN)_2$ sheets with sheet sizes varying from (a) 5 Å × 5 Å to (j) 50 Å × 50 Å in increments of 5 Å × 5 Å.

5.2.6 Long Range *D*(*r*)

The correlation function, *D*(*r*), further confirms the small-sheet sizes of both palladium and platinum cyanides. No correlations are visible in *D*(*r*) for **(I)** and **(II)** beyond ~42 Å (Figure 5.22). Assuming this value corresponds to a maximum M···M distance across the sheet diagonal for a square sheet, this gives a sheet edge length of $42/\sqrt{2}$ ≈ 30 Å *i.e.* a sheet size of 30 Å × 30 Å. *D*(*r*) for $Ni(CN)_2$, also determined using data from the GEM diffractometer,[1] (Figure 5.22) has correlations clearly visible even at 100 Å. This highlights the structural differences between nanocrystalline palladium and platinum cyanides, consisting of short stacks of small sheets, and disordered crystalline nickel cyanide, with essentially the same structure, in which there are a greater number of effectively infinite sheets per stack.

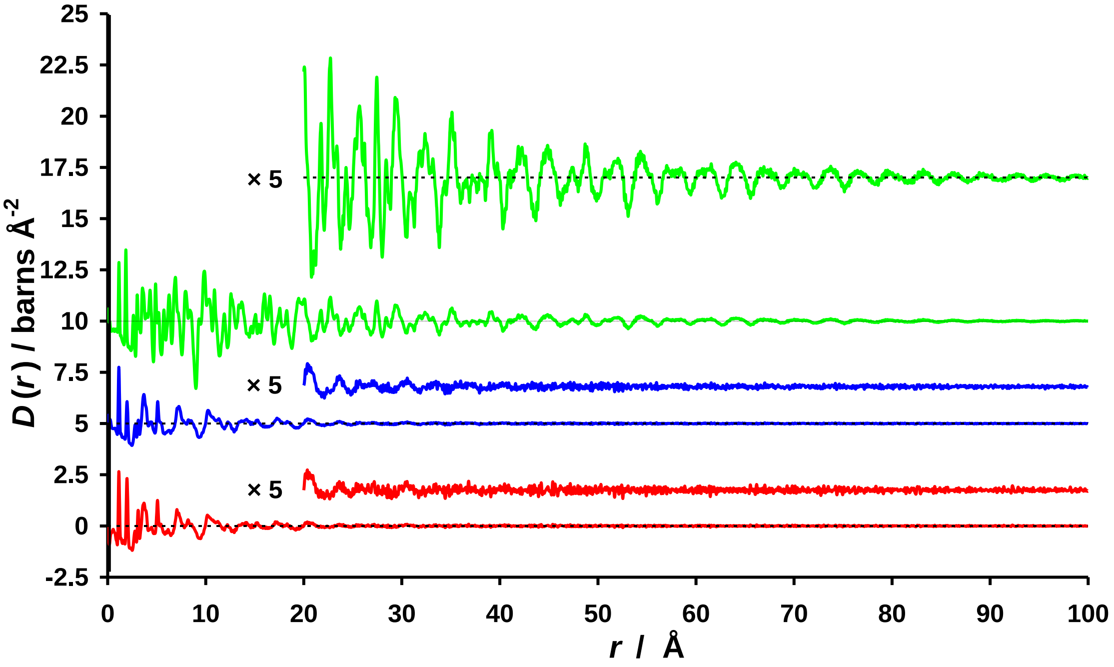

Figure 5.22 The differential correlation function, D(r), for $Pt(CN)_2.0.29NH_3$ ***(II)*** *(red),* $Pd(CN)_2.0.29H_2O$ ***(I)*** *(blue) (offset by 5 barns* $Å^{-2}$*) and* $Ni(CN)_2$ *(green),*[2] *(offset by 10 barns* $Å^{-2}$*). D(r) is also shown for each compound with 5-fold magnification over the 20-100 Å region.*

5.3 Characterisation of Nanocrystalline Compounds (III) – (IX)

Additional nanocrystalline palladium and platinum cyanides were prepared **(IV)**–**(IX)** including examples in which the terminating groups were varied; *i.e.* palladium cyanide nanoparticles terminated by ammonia, $Pd(CN)_2{\cdot}pNH_3$, and platinum cyanide nanoparticles terminated by water, $Pt(CN)_2{\cdot}qH_2O$. Full experimental details are given in sections 5.8.3 and 5.8.4 respectively. Their compositions and sheet sizes are shown in Table 5.5. Rational syntheses of $Pd(CN)_2{\cdot}pNH_3$ and $Pt(CN)_2{\cdot}yNH_3$ were achieved by heating the crystalline precursors, *cis*-$Pd(CN)_2(NH_3)_2$ and *cis*-$Pt(CN)_2(NH_3)_2$, which have ammonia and cyanide already attached to the metal centres.

Table 5.5 Summary of nanocrystalline palladium and platinum cyanides, $M(CN)_2\cdot nH_2O$ and $M(CN)_2\cdot nNH_3$, together with their corresponding sheet sizes and compositions

	Sample (origin)	Terminal Groups	Sheet Size / Å× Å	n_{derived}	n_{TGA}[§]
I	$Pd(CN)_2.nH_2O$ (neutron sample)	H_2O	30 × 30[$] 50 × 50[†]	0.29[$] 0.18[†]	0.29
II	$Pt(CN)_2.nNH_3$ (neutron sample)	NH_3	30 × 30[$] 60 × 60[†]	0.29[$] 0.15[†]	0.22
III	$Pd(CN)_2.nH_2O$ (Aldrich as purchased)	H_2O	30 × 30[$] 50 × 50[†]	0.29[$] 0.18[†]	0.30
IV	$Pd(CN)_2.nH_2O$ (hydrothermally treated (**III**))	H_2O	80 × 80[$] 90 × 90[†]	0.12[$] 0.11[†]	~0.2
V	$Pd(CN)_2.nNH_3$ (heated *cis*-$Pd(CN)_2(NH_3)_2$)	NH_3	20 × 20[$] 30 × 30[†]	0.40[$] 0.29[†]	0.30
VI	$Pd(CN)_2.nNH_3$ (*cis*-$Pd(CN)_2(NH_3)_2$ + AcOH)	NH_3	25 × 25[$] 40 × 40[†]	0.33[$] 0.22[†]	NA*
VII	$Pt(CN)_2.nNH_3$ (heated *cis*-$Pt(CN)_2(NH_3)_2$)	NH_3	15 × 15[$] 25 × 25[†]	0.50[$] 0.33[†]	NA
VIII	$Pt(CN)_2.nH_2O$ (precipitate from $K_2Pt(CN)_4$ + K_2PtCl_4)	H_2O	10 × 10[$] 20 × 20[†]	0.67[$] 0.40[†]	0.45
IX	$Pd_{1/2}Pt_{1/2}(CN)_2.nH_2O$ (precipitate from $K_2Pd(CN)_4$ + K_2PtCl_4)	H_2O	15 × 15[$] 30 × 30[†]	0.50[$] 0.29[†]	0.39

[$] *Sheet size determined from X-ray modelling with composition derived from Table 5.3.*

[†] *Sheet size determined from Scherrer equation, 5.1 with composition derived from Table 5.3.*

[§] *Composition determined from thermogravimetric analysis.*

* *Sample contained acetic acid impurity so n was not determined from thermogravimetric analysis.*

The synthetic method used to prepare $Pt(CN)_2{\cdot}qH_2O$, involving the reaction of $Pt(CN)_4^{2-}$ and $PtCl_4^{2-}$, was easily modified to produce a mixed palladium-platinum cyanide, $Pd_{1/2}Pt_{1/2}(CN)_2{\cdot}0.50H_2O$ by replacing $Pt(CN)_4^{2-}$ by $Pd(CN)_4^{2-}$. Full experimental details are given in section 5.8.5. The sheet sizes for compounds **(V)**–**(IX)**, as determined by X-ray modelling and the Scherrer equation, were smaller than those found for the neutron samples **(I)** and **(II)** and are in reasonable agreement with the *p* and *q* values determined from TGA analyses (Table 5.4 and section 5.10). The smallest sheet size produced was 10 Å × 10 Å in $Pt(CN)_2{\cdot}0.67H_2O$ **(VIII)**, which clearly shows much broader reflections in the X-ray diffraction pattern compared to $Pt(CN)_2{\cdot}0.29NH_3$ **(II)** (Figure 5.23). The sheet, complete with terminating water molecules, is shown in Figure 5.24.

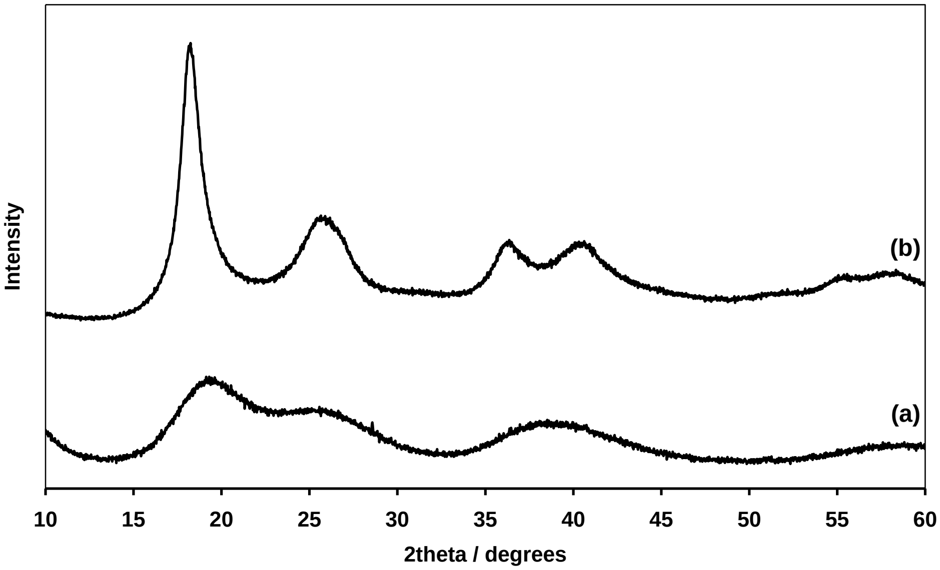

*Figure 5.23 Experimental X-ray diffraction patterns of (a) $Pt(CN)_2.0.67H_2O$ **(VIII)** (sheet size 10 Å × 10 Å) and (b) $Pt(CN)_2.0.29NH_3$ **(II)** (sheet size 30 Å × 30 Å).*

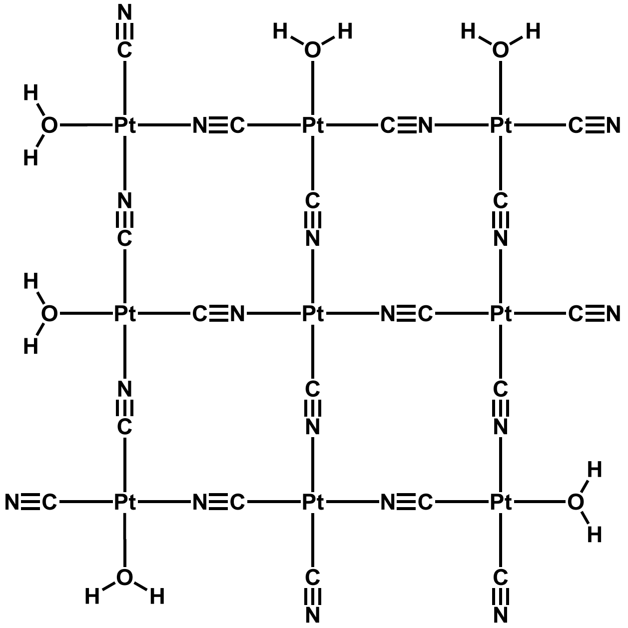

*Figure 5.24 A 10 Å × 10 Å (2 × 2 Pt-CN-Pt repeat units) nanosheet found in $Pt(CN)_2{\cdot}0.67H_2O$ **(VIII)** with water molecules as sheet-terminating groups.*

Attempts to produce highly crystalline $Pd(CN)_2$ and $Pt(CN)_2$ by heating nanocrystalline samples in an autoclave in water with a small amount of KCN, to act as a mineraliser, were not successful. This hydrothermal treatment of palladium cyanide produced $Pd(CN)_2{\cdot}0.12H_2O$ **(IV)**, which shows a moderate increase in sheet size, determined from X-ray modelling as 80 Å × 80 Å, and the onset of interlayer ordering (Figure 5.25).

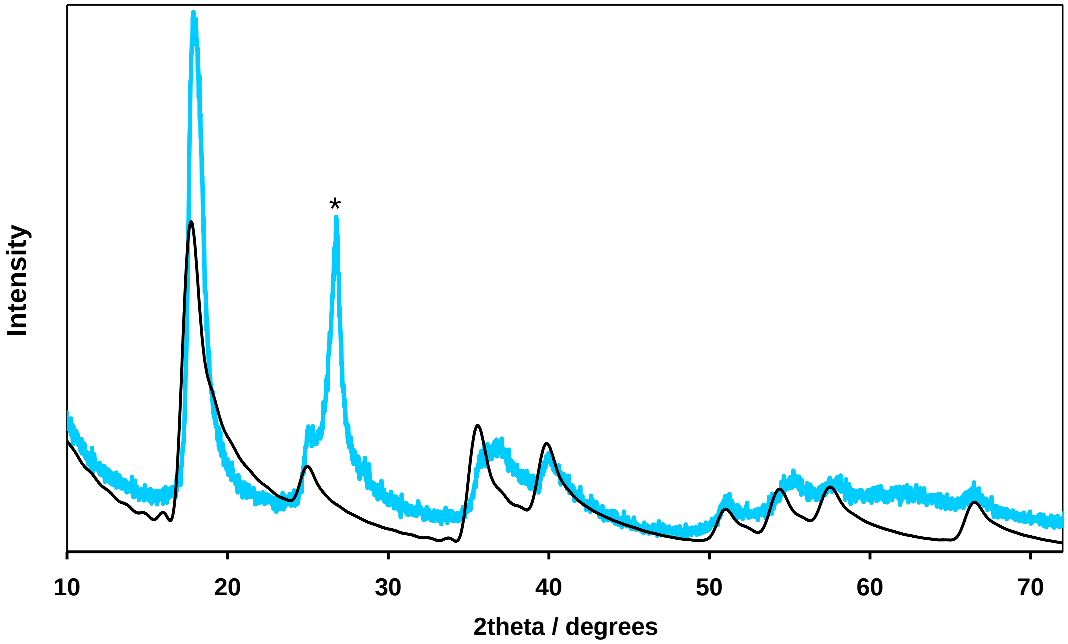

Figure 5.25 Experimental powder X-ray diffraction pattern for Pd(CN)$_2$0.12H$_2$O ***(IV)*** *(pale blue) together with the calculated pattern for a sheet of size 80 Å × 80 Å (black). The additional peak in the experimental pattern indicated by * shows the development of the interlayer order.*

The shift in the position of the (*10*) peak, as a function of peak width (Figure 5.26) for the compounds **(I)-(IX)** all lie on a common curve, reinforcing the idea that they form a family.

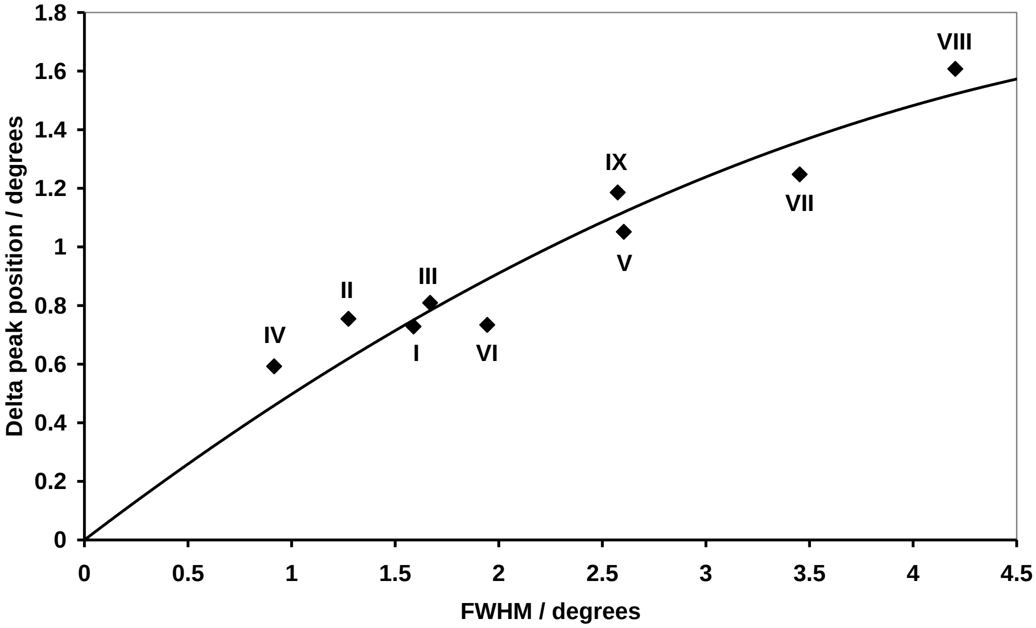

Figure 5.26 The measured shift in the (1,0) peaks in the powder X-ray diffraction patterns for compounds (I)-(VIII) (as defined in Table 5.5) from those calculated for the theoretical infinite M(CN)$_2$ sheets (M= Pd, Pt) as a function of the peak width (i.e. a measure of the particle size). The solid line is an aid to the eye.

5.4 Infrared and Raman Spectra

The vibrational spectra of the palladium and platinum cyanide materials provide supporting information on the sheet sizes and their terminating groups, Figure 5.27, Figure 5.28 and Figure 5.29. Coordinated ammonia and water both show vibrations at ~1600 cm^{-1} in the IR corresponding to δ_{as}(NH$_3$) and δ(OH$_2$) respectively, but they can be distinguished because the ammonia-containing compounds show an additional vibration, δ_s(NH$_3$), in the region 1200-1300 cm^{-1}. This can clearly be seen by comparing the fingerprint regions in Figure 5.27(b) and Figure 5.28(b).

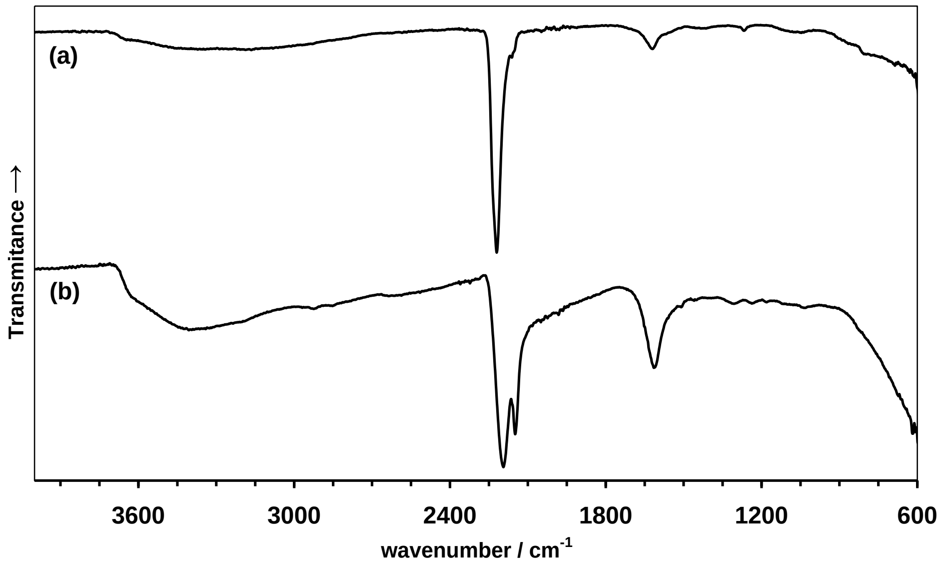

*Figure 5.27 Infrared spectra of (a) $Pd(CN)_2.0.29H_2O$ **(I)** and (b) $Pt(CN)_2.0.67H_2O$ **(VIII)**.*

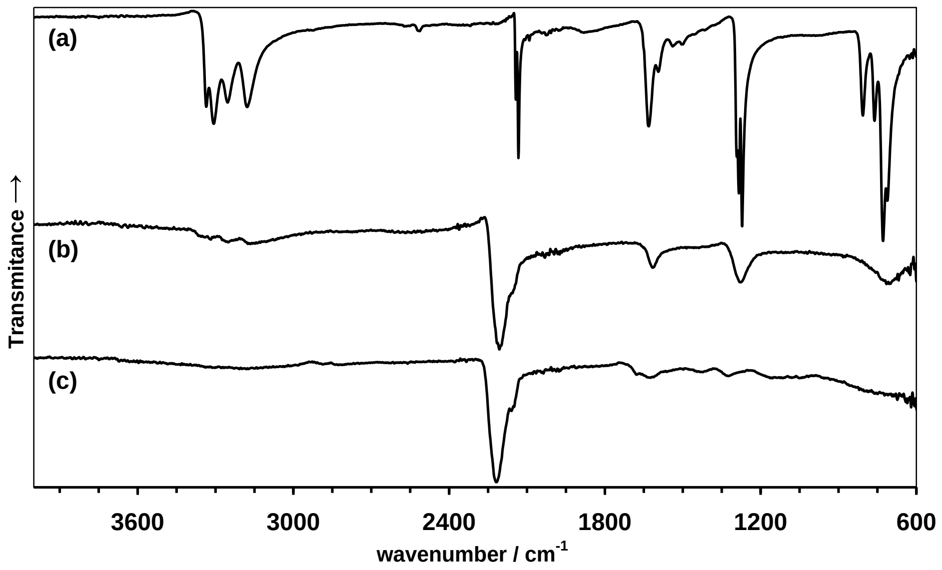

*Figure 5.28 Infrared spectra of (a) cis-$Pd(CN)_2(NH_3)_2$, (b) $Pd(CN)_2.0.40NH_3$ **(V)** and (c) $Pt(CN)_2.0.29NH_3$**(II)**.*

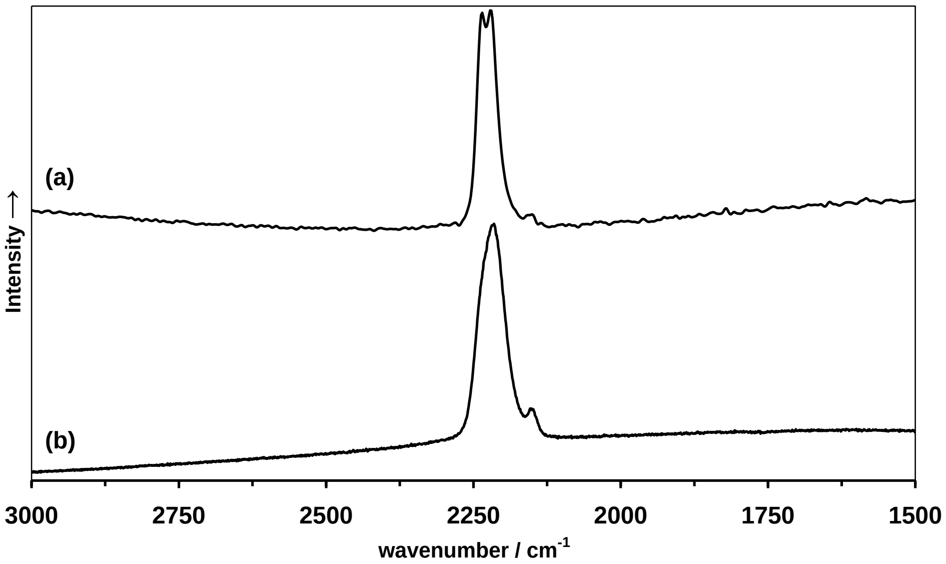

Figure 5.29 Raman spectra of (a) $Pd(CN)_2.0.29H_2O$ ***(I)*** *and (b) $Pt(CN)_2.0.67H_2O$* ***(VIII)****.*

The proposed models of nanocrystalline palladium and platinum cyanides, which are of finite extent, predict the presence of two types of cyanide group, namely bridging and terminal, as illustrated in Figure 5.18 and Figure 5.24. In contrast only bridging cyanides occur in infinite sheets. The two types can indeed be distinguished in the IR spectra as $\nu(CN)_{bridging}$ modes occur at ~2220 cm^{-1} and $\nu(CN)_{terminal}$ modes at ~2160 cm^{-1}. The latter have stretching frequencies close to those found in the $[M(CN)_4]^{2-}$ ions[29] and in *cis*-$M(CN)_2(NH_3)_2$ (M= Pd,[30] Figure 5.28(a) and Pt[31]). On decreasing the sheet size, the relative absorbance of the terminal to bridging $\nu(CN)$ modes increases, as predicted in Table 5.3. This is most clearly seen in Figure 5.27, for $Pd(CN)_2{\cdot}0.29H_2O$ **(I)** and $Pt(CN)_2{\cdot}0.67H_2O$ **(VIII)** which have sheet sizes of 30 Å × 30 Å and 10 Å × 10 Å respectively. That the number of terminal water groups increases as the sheet size is reduced can also be seen from the change in relative absorbencies of the $\delta(OH_2)$ and $\nu(CN)_{bridging}$ modes.

The Raman spectra, although rather insensitive to vibrations involving ammonia and water, are consistent with the above observations and interpretation. Both $v(CN)_{bridging}$ and $v(CN)_{terminal}$ modes can be seen (Figure 5.29) and changes in their relative intensities again reflect changes in the sheet sizes. The ratio of the peaks intensities of $v(CN)_{terminal}$: $v(CN)_{bridging}$ modes is however lower in the Raman than the IR spectra. In $Pd(CN)_2{\cdot}0.29H_2O$ **(I)**, there are two $v(CN)_{bridging}$ frequencies observed in the Raman spectrum. These, together with the single non-coincident $v(CN)_{bridging}$ peak in the IR spectrum, reflect the square-planar coordination around the metal centres in the interior of the sheet. In the Raman spectrum of $Pt(CN)_2{\cdot}0.67H_2O$ **(VIII)**, the different $v(CN)_{bridging}$ modes are not fully resolved. This can be ascribed to an increase in the widths of the peaks due to the reduced sheet size. Looking at Figure 5.24, it can be seen that the average metal environment no longer has *P*4 symmetry.

5.5 Thermal Behaviour

It has been shown that nickel cyanide undergoes 2-D NTE with $\alpha_a = -6.5 \times 10^{-6}$ K^{-1} and at the beginning of the work on $Pd(CN)_2$ and $Pt(CN)_2$ it was anticipated that both of these materials would also shown 2-D NTE. Conventional measurements of thermal expansion require powder diffraction patterns to be indexed at multiple temperatures, with changes in the unit cell lengths being used to calculate the coefficients of thermal expansion, α. In the cases of nanocrystalline materials, such as palladium and platinum cyanides, it is not possible to determine changes in the *a* lattice parameter because of the large peak breadth in the diffraction patterns, however this does not mean that the thermal behaviour of these materials cannot be investigated. By looking at changes in the pair correlation functions at 10 and 300 K, it has been possible to directly observe not only a decrease in the M···M distance, determined from the peak at ~5.1 Å, but also to identify the low energy vibrational modes which are responsible for this behaviour. The contraction within the $Pd(CN)_2$ and $Pt(CN)_2$ sheets, $\alpha_{M\cdots M}$, is -8.05×10^{-6} and -5.30×10^{-6} K^{-1} respectively, comparable with the contraction seen in $Ni(CN)_2$.

There are two vibrational modes which maintain the square-planar coordination around the metal atoms, in side-step modes both atoms of the cyanide group are displaced in the same direction from the M···M axis (Figure 5.30). In the shorter wavelength kinked modes, the atoms of the cyanide group are displaced in opposite directions from the M···M axis (Figure 5.31).

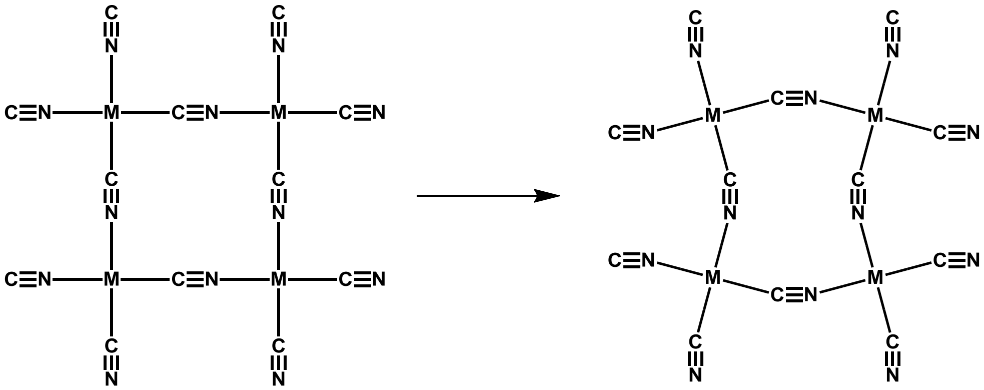

Figure 5.30 Side-step mode, in which the both atoms of the cyanide group are displaced in the same direction from the M···M axis, in a section of an $M(CN)_2$ sheet.

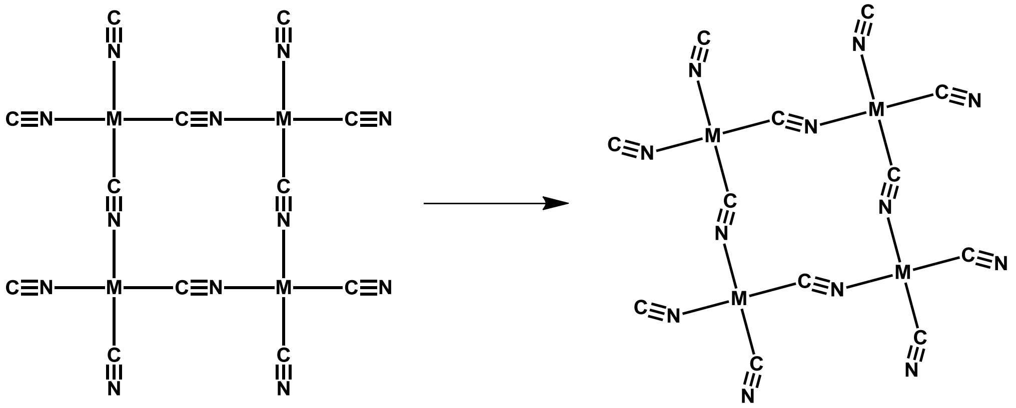

Figure 5.31 Kinked modes, in which the atoms of the cyanide group are displaced in opposite directions from the M···M axis, in a section of an $M(CN)_2$ sheet.

Using the 1st, 2nd and 4th peaks in *T*(*r*) it is possible to calculate the average M-Z≡Z angle (Table 5.6).

Table 5.6 Calculated M···M distances, the bond lengths and angles used to calculate them, along with the measured value from $T(r)_{exp}$.

Sample	$Pd(CN)_2$ **(I)**	$Pd(CN)_2$ **(I)**	$Pt(CN)_2$ **(II)**	$Pt(CN)_2$ **(II)**
Temp / K	10	300	10	300
r C≡N / Å	1.1487(8)	1.1580(8)	1.152(1)	1.1576(8)
r M-C/N / Å	1.985(2)	1.983(2)	1.978(2)	1.979(1)
4th peak ~3.1 Å / Å	3.1156(6)	3.113(1)	3.1074(8)	3.1085(6)
M-Z≡Z angle (calc.) / °	167.2	164.1	165.7	164.1
r M···M ($a_{T(r)}$) / Å	5.0988(2)	5.0869(4)	5.0787(2)	5.0709(1)
$\alpha_{M\cdots M}$ / K^{-1}	-8.05×10^{-6}		-5.30×10^{-6}	
$M\cdots M_{calc}$ / Å (side-step)	5.0287	4.978	4.992	4.9576
$M\cdots M_{calc}$ / Å (kinky modes)	5.096	5.08	5.08	5.082

From this information it is possible to calculate the M···M distances which would be expected from both vibrational modes, by comparing this with the observed M···M distances it can be seen that the kinked modes give better agreement with the data. It should be noted that the large broadening of the 3rd peak in $T(r)$ is a consequence of scissor-like distortions around the metal atoms, symmetry B_{1g} which should be seen in the Raman at around 100 – 200 cm^{-1}.

5.6 Conclusions

It can now be seen why it has taken so long to verify that Pauling's proposed structure for palladium and platinum cyanides is essentially correct. Palladium and platinum cyanides have turned out not to be simple extended solids as was originally envisaged, but are nanocrystalline materials consisting of small sheets of vertex sharing square-planar $M(CN)_4$ units of sheet sizes ranging from 10 Å × 10 Å to 80 Å × 80 Å. They are not in fact stoichiometric $Pd(CN)_2$ or $Pt(CN)_2$, but always contain ammonia or water molecules on the edges of the nanosheets. Using a range of techniques it has been possible to show how and why these molecules are bound. It has also been shown that it is possible to vary the sizes of the nanosheets within limited bounds. Thus it is possible to represent the structures of palladium and platinum cyanides as large molecules or clusters (Figure 5.24).

Commercial samples of "$Pd(CN)_2$" and "$Pt(CN)_2$", from Aldrich, are in fact $Pd(CN)_2{\cdot}0.29H_2O$ and $Pt(CN)_2{\cdot}0.29NH_3$ and are described well by the detailed structures of **(I)** and **(II)** given in this work. Given the distinctive yellow colour, it is highly likely that the Aldrich sample of $Pt(CN)_2{\cdot}0.29NH_3$ is prepared from the thermal decomposition of $(NH_4)_2Pt(CN)_4$ or its hydrate.

Both palladium and platinum cyanides exhibit 2-D NTE, as expected from previous work on nickel cyanide. The values of α_a obtained are -8.05×10^{-6} and -5.30×10^{-6} K^{-1} for compounds **(I)** and **(II)**, comparable with $\alpha_a = -6.5(1) \times 10^{-6}$ K^{-1} for $Ni(CN)_2$.[1] More interestingly, it has been possible to identify the vibrations responsible for this phenomenon.

5.7 Further Work

Preliminary work has shown that it is possible to prepare mixed $NiM(CN)_4{\cdot}nH_2O$ (were M = Pd and Pt, and n = 0, 2, 3 and 6) which are highly crystalline and unit cells have been proposed for some of the hydrates. More interestingly the dehydrated compounds appear to be nanocrystalline materials like $Pd(CN)_2$ and $Pt(CN)_2$, this mixture of the properties of nickel cyanide and of palladium and platinum cyanides is worthy of further study.

Because palladium cyanide is used as a heterogeneous catalyst, the particle size is very likely to have an effect of on its catalytic action. Further investigation of this could be of interest to organic or industrial chemists who use $Pd(CN)_2$ as a catalyst. There is also the possibility that $Pd(CN)_2{\cdot}pNH_3$ could be used in reactions which are water sensitive.

5.8 Sample Preparation

Palladium and platinum Cyanides for Neutron Studies, $Pd(CN)_2.xH_2O$ and $Pt(CN)_2.yNH_3$ were prepared as follows:

5.8.1 $Pd(CN)_2\cdot 0.29H_2O$ (sample I).

A sample purchased as $Pd(CN)_2$ from Aldrich (6 g) as an off-white powder **(III)** was dried under vacuum at 120 °C for 3 hours in a constricted glass ampoule, to produce **(I)**. The IR spectrum (Figure 5.27(a)), showed the presence of water in the material. The neutron analysis results, supported by thermal analysis, gave the composition of the dried sample **(I)** as $Pd(CN)_2\cdot 0.29H_2O$ (Table 5.4 and Figure 5.33). The pycnometrically measured density was 2.81(2) g cm^{-3}.

IR (Figure 5.27): ν(OH) 3165 (vvw, v broad); ν(CN) 2220(s), 2164(w); $\delta(OH_2)$ 1623(w), $\rho(OH_2)$ 1040 (vvw, broad); ν(PdC, PdN) 554(s) cm^{-1}.

Raman (Figure 5.29): ν(CN) 2240(s), 2224(s), 2153(vw); ν(PdC, PdN) 565(vw), 468(vw); low frequency bends: 360(vw), 322(vw), 231(vw) cm^{-1}.

5.8.2 $Pt(CN)_2\cdot 0.29NH_3$ (sample II).

$Pt(CN)_2\cdot 0.29NH_3$ was prepared as a yellow powder by decomposition of $(NH_4)_2Pt(CN)_4\cdot 2H_2O$ at 300 °C under vacuum in a constricted glass ampoule for 17 hours.[7] The ammonium salt was first prepared by mixing solutions of $BaPt(CN)_4\cdot 2.6H_2O$ (Aldrich) (7.3875 g, 15.28 mmol) in H_2O (110 mL) and $(NH_4)_2SO_4$ (2.2363 g, 16.92 mmol) in H_2O (10 mL) at room temperature. The immediate precipitate, $BaSO_4$, was filtered off and the remaining solution allowed to evaporate almost to dryness at room temperature over a few days to produce bright yellow crystals of $(NH_4)_2Pt(CN)_4\cdot 2H_2O$, the crystal structure of which has been solved by Dr Ann Chippindale, details are given in 5.9. Because excess ammonium sulphate was used, the $(NH_4)_2Pt(CN)_4\cdot 2H_2O$ hydrate was contaminated with $(NH_4)_2SO_4$, this was removed by sublimation during the decomposition of the diammonium tetracyanoplatinate to form compound **(II)**. The IR spectrum (Figure 5.28(c)), showed the presence of ammonia in the material. Analysis of the neutron data, together with thermal analysis (Figure 5.34) gave the composition of the sample as $Pt(CN)_2\cdot 0.29NH_3$. The pycnometrically measured density was 4.32(2) g cm^{-3}.

IR (Figure 5.28(c)): ν(NH) 3200 (vw, v broad); ν(CN) 2217(s), 2158(m); $\delta_{as}(NH_3)$ 1675(w), 1625(w); $\delta_s(NH_3)$ 1322(w) cm^{-1}.

Raman: not collected, sample fluoresced.

5.8.3 Other Palladium Cyanides, $Pd(CN)_2\cdot xH_2O$ and $Pd(CN)_2\cdot pNH_3$

$Pd(CN)_2\cdot xH_2O$ **(III)** and **(IV)**. The effect of hydrothermal treatment on the particle size of $Pd(CN)_2\cdot xH_2O$ was investigated. $Pd(CN)_2$ from Aldrich (0.0311 g, 0.1962 mmol) **(III)** was heated in an autoclave with H_2O (5 mL) in the presence of a small quantity of KCN (0.0056 g, 0.086 mmol), to act as a mineraliser, at 150 °C for 4 weeks. The powder X-ray diffraction pattern of the product **(IV)** showed some sharpening of the peaks (Figure 5.25) consistent with an increase in sheet size from 30 Å × 30 Å to 80 Å × 80 Å, (Table 5.5).

(III) IR: ν(CN) 2217(s), 2165(w); $\delta(OH_2)$ 1622(w); $\rho(OH_2)$ 1037(w, broad); ν(PdC, PdN) 550(s) cm^{-1}.

(III) Raman: ν(CN) 2238(s), 2224(s); ν(PdC, PdN) 558 (vvw), 470(vvw); low frequency bend: 362(vvw) cm^{-1}.

(IV) IR: ν(OH) 3350 (vw, v broad); ν(CN) 2234(s), 2220(s), 2154(w); δ(OH_2) 1623(w); ρ(OH_2) 1030(vvw, broad); ν(PdC, PdN) 550(s) cm^{-1}.

cis-$Pd(CN)_2(NH_3)_2$ was prepared for use as a crystalline precursor to $Pd(CN)_2{\cdot}pNH_3$ by dissolving $Pd(CN)_2$ (Aldrich) (0.1572 g, 0.9921 mmol) in aqueous NH_3 (35%, 50 mL). After 3 days, crystals in the form of colourless needles grew in the solution. The crystals were filtered off and allowed to dry in air. A full structure determination confirmed that the crystals were *cis*-$Pd(CN)_2(NH_3)_2$ (lattice parameters at 150 K: a = 6.7416(3), b = 12.6824(4), c = 6.7431(3) Å; β = 110.675(5)°; spacegroup $P2_1/n$)[32] and the IR spectrum was in close agreement with that reported by Šoptrajanova *et al*.[30]

IR (Figure 5.28(a)): ν(NH) 3344(m), 3306(m), 3252(m), 3177(m); ν(CN) 2143(m), 2133(s); δ_{as}(NH_3) 1629(s), 1592(w); δ_s(NH_3) 1288(s), 1284(s), 1271(s); ρ(NH_3) 805(m), 760(m), 727(s), 710(s) cm^{-1}.

Raman: ν(CN) 2146(s), 2135(mw); δ_s(NH_3) 1284(vw), 1267(vw), 1099(vw, broad); ν(PdC, PdN) 489(vw), 469(mw), 435(vw), 414(vvw), 399(vw); low frequency bends: 378(vvw), 263(w), 150(w) cm^{-1}.

$Pd(CN)_2{\cdot}pNH_3$ **(V)** and **(VI)** were prepared from *cis*-$Pd(CN)_2(NH_3)_2$ by two methods:

(1) Heating crystals of *cis*-$Pd(CN)_2(NH_3)_2$ under nitrogen in the thermogravimetric apparatus from 20-200 °C led to the evolution of ammonia and the formation of nanocrystalline $Pd(CN)_2{\cdot}0.40NH_3$ (Table 5.5) **(V)**.

IR (Figure 5.28(b)): *v*(NH) 3326(w), 3243(w), 3144(w); *v*(CN) 2205(s), 2154(m); $\delta_{as}(NH_3)$ 1609(m); $\delta_s(NH_3)$ 1270(ms); *v*(PdC, PdN) 696(m) cm^{-1}.

Raman: *v*(NH) 3271(w), 3190(w); *v*(CN) 2217(s), 2154(w); $\delta_s(NH_3)$ 1296(w); *v*(PdC, PdN) 559(w), 495(mw), 471(mw); low frequency bend: 361(w) cm^{-1}.

(2) Crystals of *cis*-$Pd(CN)_2(NH_3)_2$ (0.0415 g, 0.2155 mmol) were added to aqueous CH_3CO_2H (10 mL, 1.5 M) and left for 15 weeks.[14] A powder X-ray diffraction pattern showed that the white product, which retained the morphology of the original needles, was nanocrystalline. The sheet size, as determined by the X-ray modelling (Table 5.5), corresponds to the composition $Pd(CN)_2 \cdot 0.33NH_3$ **(VI)**. The IR spectrum showed that the product contained peaks corresponding to acetic acid impurity and hence the composition could not be determined by thermogravimetric analysis.

IR: *v*(NH) 3050(w, v broad); *v*(CN) 2213(s), 2159(m); $\delta_{as}(NH_3)$ 1618(w); $\delta_s(NH_3)$ 1272(w) cm^{-1}. (Note: the additional peaks due to acetic acid have been omitted).

Raman: *v*(CN) 2222(s), 2158(w); *v*(PdC, PdN) 565(w), 495(vw), 471(w); low frequency bends: 359(vw), 238(vw) cm^{-1}.

5.8.4 Other Platinum Cyanides, $Pt(CN)_2 \cdot qH_2O$ and $Pt(CN)_2 \cdot yNH_3$

$Pt(CN)_2 \cdot 0.50NH_3$ **(VII)** was prepared as a orange-brown solid by heating a mixture of $Pt(CN)_2(NH_3)_2$ and $Pt(CN)_2 \cdot yNH_3$, produced by the evaporation of a solution of $Pt(CN)_2$ (Aldrich, 0.2463g, 0.9967 mmol) in aqueous NH_3 (35%, 50 mL) under N_2 to 240 °C. The composition given is that corresponding to the sheet size of 15 Å × 15 Å, as determined by the X-ray modelling (Table 5.5).

$Pt(CN)_2 \cdot 0.67H_2O$ **(VIII)** was prepared by adding a solution of $K_2Pt(CN)_4$ (0.1887 g, 0.5001 mmol, in 5 mL water) to a solution of K_2PtCl_4 (0.2078 g, 0.5006 mmol, in 5 mL water). A yellow-brown gel formed over a period of two to three weeks. This was repeatedly washed with water and allowed to dry in air. The reflections in the powder X-ray pattern were very broad (Figure 5.23), consistent with the very small sheet size, 10 Å × 10 Å, of this sample (Table 5.5).

IR (Figure 5.27(b)): ν(OH) 3440(w, v broad); ν(CN) 2201(s), 2152(s); $\delta(OH_2)$ 1611(w) cm^{-1}.

Raman (Figure 5.29(b)): ν(CN) 2216(vs), 2151(w); ν(PtC, PtN) 616(w, broad), 504(w), 477(w); low frequency bend: 357(w) cm^{-1}.

5.8.5 Mixed Palladium–Platinum Cyanide, $Pd_{1/2}Pt_{1/2}(CN)_2 \cdot xH_2O$

$Pd_{1/2}Pt_{1/2}(CN)_2 \cdot 0.50H_2O$ **(IX)**, a nanocrystalline mixed palladium-platinum cyanide, was prepared by adding a solution of $K_2Pd(CN)_4$ (0.1447 g, 0.5012 mmol, in 5 mL water) to a solution of K_2PtCl_4 (0.2078 g, 0.5006 mmol, in 5 mL water). A cream powder formed over a period of 6 to 8 weeks. This was filtered, repeatedly washed with water and allowed to dry in air. The powder X-ray pattern is given in Figure 5.32.

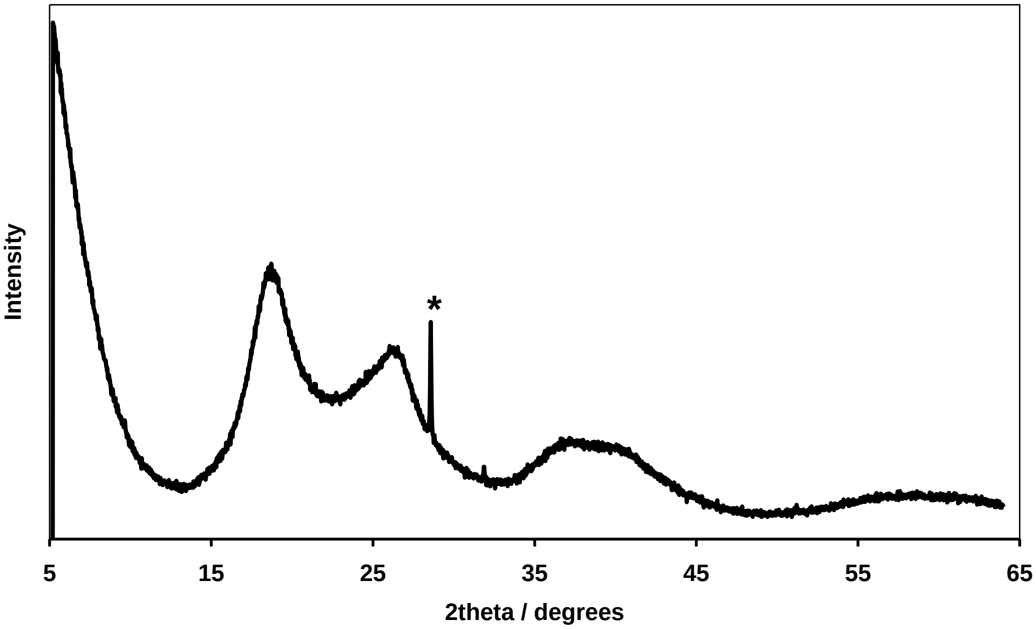

Figure 5.32 Experimental powder X-ray diffraction patterns for $Pd_{1/2}Pt_{1/2}(CN)_2{\cdot}0.50H_2O$ ***(IX)****. The reflection labelled * is from KCl, an impurity from the synthesis method.*

Thermogravimetric analysis gave the composition as $Pd_{1/2}Pt_{1/2}(CN)_2{\cdot}0.39H_2O$, in reasonable agreement with the composition determined from the X-ray modelling. The powder X-ray diffraction pattern of the final product after heating to 600 ˚C could be indexed on the basis of a cubic unit cell with lattice parameter a = 3.9036(2) Å, in excellent agreement with the value of 3.903 Å found for the alloy $Pd_{1/2}Pt_{1/2}$.[33]

IR: ν(OH) 3400(w, very broad); ν(CN) 2202(s), 2150(m); $\delta(OH_2)$ 1614(m); $\rho(OH_2)$ 1089(w, broad) cm^{-1}.

Raman: ν(CN) 2219(vs), 2151(w); ν(Pd/PtC, Pd/PtN) 598(w, broad), 472(w); low frequency bend: 348(w) cm^{-1}.

5.9 Details for Creating the Correlation Function $T(r)$

5.9.1 The Unit Cells

Table 5.7 The space groups and unit cells used for modelling (I) and (II) at 10 and 300 K

	Space group	a / Å	c / Å
$Pd(CN)_2$ at 10 K	$I4_1/amd$	5.119	13.600
$Pt(CN)_2$ at 10 K	$I4_1/amd$	5.108	13.600
$Pd(CN)_2$ at 300 K	$I4_1/amd$	5.124	13.760
$Pt(CN)_2$ at 300 K	$I4_1/amd$	5.116	13.760

5.9.2 The Atomic Positions

*Table 5.8 $Pd(CN)_2$ **(I)** at 10 K*

Atom	x	y	z	Wyckoff position
Pd	0	0	0	4*a*
Z (C/N)	0.3878	0	0.0	16*h*

*Table 5.9 $Pt(CN)_2$ **(II)** at 10 K*

Atom	x	y	z	Wyckoff position
Pt	0	0	0	4*a*
Z (C/N)	0.3872	0	0.0	16*h*

*Table 5.10 $Pd(CN)_2$ **(I)** at 300 K*

Atom	x	y	z	Wyckoff position
Pd	0	0	0	4*a*
Z (C/N)	0.3870	0	0.0	16*h*

*Table 5.11 $Pt(CN)_2$ **(II)** at 300 K*

Atom	x	y	z	Wyckoff position
Pd	0	0	0	4*a*
Z (C/N)	0.3878	0	0.0	16*h*

5.9.3 Separating the Contributions to $T(r)_{calc}$

To create $T(r)_{model}$, $T(r)_{calc}$ for a sheet was subtracted from $T(r)_{calc}$ for the full model to generate a set of delta functions which came from atom pairs where the atoms were not in the same layer, as had been done in the case of $Ni(CN)_2$.[1] The correlations from within the layer were then separated into those which ran along a chain in the layer, and those which came from atoms that were not within the same chain. This was achieved by multiplying $T(r)_{calc}$ from an MZ_2 chain by 1.2 and subtracting this from $T(r)_{calc}$ from a sheet. The scaling by 1.2 is required because a chain and a layer have different compositions, *e.g.* MZ_2 and MZ_4 respectively. The result of this is that in a chain the metal atoms have a smaller coordination number and that there are proportionally less carbon and nitrogen atoms, than in a sheet. This leads to an overall reduction in the areas of the peaks, by ~83.3%. The proof for this was deduced by Alex Hannon, for which I am very grateful and is given in Appendix 5.

5.9.4 Broadening Factors

Table 5.12 The root-mean-square values used to broaden the individual partial correlation functions used to produce $T(r)_{model}$ *for* $Pd(CN)_2$ *at 10 K.*

Partial correlations in $Pd(CN)_2$ at 10 K					
Interlayer	r = 0.0–3.8 Å $\langle u^2\rangle^{1/2}$ = 0.095 Å^2	r = 3.8–4.0 Å $\langle u^2\rangle^{1/2}$ = 0.43 Å^2	r = 4.0–6.0 Å $\langle u^2\rangle^{1/2}$ = 0.60 Å^2	r = 6.0–9.0 Å $\langle u^2\rangle^{1/2}$ = 0.70 Å^2	r = 9.0–15 Å $\langle u^2\rangle^{1/2}$ = 0.90 Å^2
Intralayer cross chain	r = 0.0–3.0 Å $\langle u^2\rangle^{1/2}$ = 0.12 Å^2	r = 3.0–3.85 Å $\langle u^2\rangle^{1/2}$ = 0.145 Å^2	r = 3.85–5.8 Å $\langle u^2\rangle^{1/2}$ = 0.175 Å^2	r = 5.8–8.0 Å $\langle u^2\rangle^{1/2}$ = 0.2 Å^2	r = 8.0–15 Å $\langle u^2\rangle^{1/2}$ = 0.26 Å^2
Intralayer along chain	r = 0.0–1.5 Å $\langle u^2\rangle^{1/2}$ = 0.035 Å^2	r = 1.5–4.0 Å $\langle u^2\rangle^{1/2}$ = 0.065 Å^2	r = 4.0–6.15 Å $\langle u^2\rangle^{1/2}$ = 0.085 Å^2	r = 6.15–15.0 Å $\langle u^2\rangle^{1/2}$ = 0.14 Å^2	

Table 5.13 The root-mean-square values used to broaden the individual partial correlation functions used to produce $T(r)_{model}$ *for* $Pt(CN)_2$ *at 10 K.*

Partial correlations in $Pt(CN)_2$ at 10 K					
Interlayer	r = 0.0–3.8 Å $\langle u^2\rangle^{1/2}$ = 0.14 Å^2	r = 3.8–4.0 Å $\langle u^2\rangle^{1/2}$ = 0.43 Å^2	r = 4.0–6.0 Å $\langle u^2\rangle^{1/2}$ = 0.60 Å^2	r = 6.0–9.0 Å $\langle u^2\rangle^{1/2}$ = 0.70 Å^2	r = 9.0–15.0 Å $\langle u^2\rangle^{1/2}$ = 0.90 Å^2
Intralayer cross chain	r = 0.0–3.0 Å $\langle u^2\rangle^{1/2}$ = 0.12 Å^2	r = 3.0–3.85 Å $\langle u^2\rangle^{1/2}$ = 0.15 Å^2	r = 3.85–5.8 Å $\langle u^2\rangle^{1/2}$ = 0.19 Å^2	r = 5.8–8.0 Å $\langle u^2\rangle^{1/2}$ = 0.24 Å^2	r = 8.0–15 Å $\langle u^2\rangle^{1/2}$ = 0.3 Å^2
Intralayer along chain	r = 0.0–1.5 Å $\langle u^2\rangle^{1/2}$ = 0.031 Å^2	r = 1.5–4.0 Å $\langle u^2\rangle^{1/2}$ = 0.062 Å^2	r = 4.0–6.15 Å $\langle u^2\rangle^{1/2}$ = 0.085 Å^2	r = 6.15–15.0 Å $\langle u^2\rangle^{1/2}$ = 0.14 Å^2	

Table 5.14 The root-mean-square values used to broaden the individual partial correlation functions used to produce $T(r)_{model}$ for $Pd(CN)_2$ at 300 K.

Partial correlations in $Pd(CN)_2$ at 300 K						
Interlayer	r = 0.0–3.8 Å $\langle u^2\rangle^{1/2}$ = 0.20 Å^2	r = 3.8–4.0 Å $\langle u^2\rangle^{1/2}$ = 0.40 Å^2	r = 4.0–6.0 Å $\langle u^2\rangle^{1/2}$ = 0.62 Å^2	r = 6.0–15.0 Å $\langle u^2\rangle^{1/2}$ = 0.90 Å^2		
Intralayer cross chain	r = 0.0–3.0 Å $\langle u^2\rangle^{1/2}$ = 0.12 Å^2	r = 3.0–3.85 Å $\langle u^2\rangle^{1/2}$ = 0.18 Å^2	r = 3.85–5.8 Å $\langle u^2\rangle^{1/2}$ = 0.24 Å^2	r = 5.8–8.0 Å $\langle u^2\rangle^{1/2}$ = 0.27 Å^2	r = 8.0–15.0 Å $\langle u^2\rangle^{1/2}$ = 0.28 Å^2	
Intralayer along chain	r = 0.0–1.5 Å $\langle u^2\rangle^{1/2}$ = 0.035 Å^2	r = 1.5–4.0 Å $\langle u^2\rangle^{1/2}$ = 0.06 Å^2	r = 4.0–6.15 Å $\langle u^2\rangle^{1/2}$ = 0.085 Å^2	r = 6.15–6.6 Å $\langle u^2\rangle^{1/2}$ = 0.14 Å^2	r = 6.6–8.0 Å $\langle u^2\rangle^{1/2}$ = 0.16 Å^2	r = 8.0–15.0 Å $\langle u^2\rangle^{1/2}$ = 0.20 Å^2

Table 5.15 The root-mean-square values used to broaden the individual partial correlation functions used to produce $T(r)_{model}$ for $Pt(CN)_2$ at 300 K.

Partial correlations in $Pt(CN)_2$ at 300 K						
Interlayer	r = 0.0–3.8 Å $\langle u^2\rangle^{1/2}$ = 0.20 Å^2	r = 3.8–4.0 Å $\langle u^2\rangle^{1/2}$ = 0.40 Å^2	r = 4.0–6.0 Å $\langle u^2\rangle^{1/2}$ = 0.62 Å^2	r = 6.0–15.0 Å $\langle u^2\rangle^{1/2}$ = 0.90 Å^2		
Intralayer cross chain	r = 0.0–3.0 Å $\langle u^2\rangle^{1/2}$ = 0.12 Å^2	r = 3.0–3.85 Å $\langle u^2\rangle^{1/2}$ = 0.18 Å^2	r = 3.85–5.8 Å $\langle u^2\rangle^{1/2}$ = 0.24 Å^2	r = 5.8–8.0 Å $\langle u^2\rangle^{1/2}$ = 0.27 Å^2	r = 8.0–15.0 Å $\langle u^2\rangle^{1/2}$ = 0.28 Å^2	
Intralayer along chain	r = 0.0–1.5 Å $\langle u^2\rangle^{1/2}$ = 0.035 Å^2	r = 1.5–4.0 Å $\langle u^2\rangle^{1/2}$ = 0.06 Å^2	r = 4.0–6.15 Å $\langle u^2\rangle^{1/2}$ = 0.085 Å^2	r = 6.15–6.6 Å $\langle u^2\rangle^{1/2}$ = 0.14 Å^2	r = 6.6–8.0 Å $\langle u^2\rangle^{1/2}$ = 0.16 Å^2	r = 8.0–15.0 Å $\langle u^2\rangle^{1/2}$ = 0.20 Å^2

5.10 Thermogravimetric Analysis

The amounts of water or ammonia in $Pd(CN)_2 \cdot xH_2O$, $Pd(CN)_2 \cdot pNH_3$, $Pt(CN)_2 \cdot yNH_3$ and $Pt(CN)_2 \cdot qH_2O$ were determined by thermogravimetric analysis in which small quantities of samples were decomposed to metal and cyanogen gas under flowing nitrogen gas, typically over the temperature range 20-600 ˚C. The samples started to lose weight immediately, corresponding to loss of surface-adsorbed water molecules. The weight loss taken below 100 ˚C was therefore ignored. A weight loss of 34.42 % from **(I)** (Figure 5.33) corresponds to a starting formula $Pd(CN)_2 \cdot 0.29H_2O$.

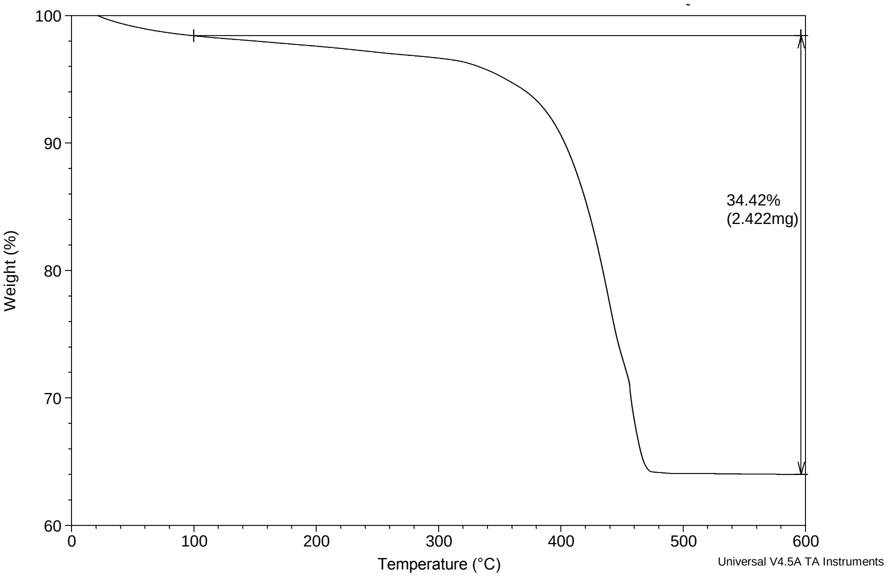

Figure 5.33 Thermogravimetric Analysis of $Pd(CN)_2 \cdot 0.29H_2O$ ***(I)***

A weight loss of 21.99 % from **(II)** (Figure 5.34) corresponds to a starting formula $Pt(CN)_2 \cdot 0.22NH_3$.

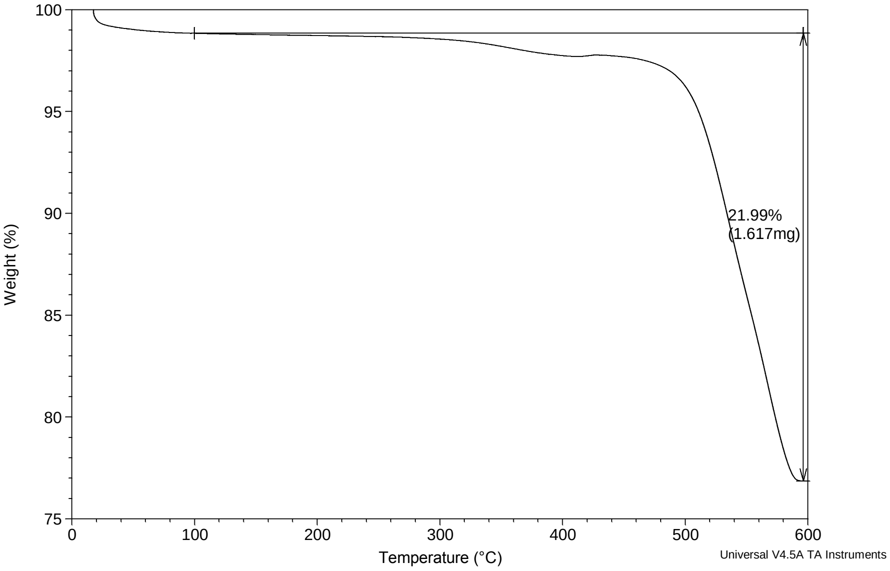

Figure 5.34 Thermogravimetric Analysis of $Pt(CN)_2 \cdot 0.29NH_3$ ***(II).***

5.11 References

1. S. J. Hibble, A. M. Chippindale, A. H. Pohl and A. C. Hannon, *Angew. Chem. Int. Ed.*, 2007, **46**, 7116.
2. A. L. Goodwin, M. T. Dove, A. M. Chippindale, S. J. Hibble, A. H. Pohl and A. C. Hannon, *Phys. Rev. B*, 2009, **80**, 054101.
3. S. J. Hibble, A. M. Chippindale, E. J. Bilbe, E. Marelli, P. J. F. Harris and A. C. Hannon, *Inorg. Chem.*, 2011, **50**, 104-113.
4. W. H. Wollaston, *Philos. Trans. R. Soc. London*, 1805, 316.
5. W. H. Wollaston, *Philos. Trans. R. Soc. London*, 1804, 419.
6. G. H. Bailey and T. Lamb, *J. Chem. Soc.*, 1892, **61**, 745.
7. A. A. Grinberg, *Izn. Inst. Izuch Platiny*, 1928, **6**.
8. A. G. Sharpe, *The Chemistry of Cyano Complexes of the Transition Metals*, Academic Press, London, 1976.
9. H. E. Williams, *Cyanogen Compounds*, 2nd edn., Edward Arnold & Co., London, 1945.
10. P. Nagy, PhD Thesis, University of Debrecen, Hungary, 2004.
11. F. R. Hartley, *The Chemistry of Platinum and Palladium*, Applied Science Publishers, Bristol, 1973.
12. L. Pauling, *The Nature of the Chemical Bond*, 3rd edn., Cornell University Press, 1960.
13. R. B. Janes, *J. Am. Chem. Soc.*, 1935, **57**, 471.
14. R. D. Gillard, *J. Inorg. Nucl. Chem.*, 1964, **21**, 1321.
15. K. Imi, N. Yanagihara and K. Utimoto, *J. Org. Chem.*, 1987, **52**, 1013.

16. Y. Odaira, T. Oishi, T. Yukawa and S. Tsutsumi, *J. Am. Chem. Soc.*, 1966, **88**, 4105.
17. A. D. Ketley, L. P. Fisher, A. J. Berlin, C. R. Morgan, E. H. Gorman and T. R. Steadman, *Inorg. Chem.*, 1967, **6**, 657.
18. A. H. Pohl, PhD Thesis, The University of Reading, 2008.
19. I. B. Baranovskii and Y. Y. Kharitonov, *Doklady Akad. Nauk. SSSR (English translation)*, 1966, **169**, 805.
20. H. P. Klug and L. E. Alexander, *X-ray Diffraction Procedures*, 2nd edn., Wiley-Interscience, 1974.
21. A. C. Hannon, *Nucl. Instrum. Methods Phys. Res., Sect. A*, 2005, 88.
22. S. J. L. Billinge and M. G. Kanatzidis, *Chem. Commun.*, 2004, 749.
23. S. J. Hibble, A. C. Hannon and I. D. Fawcett, *J. Phys.: Condens. Matter*, 1999, **11**, 9203.
24. S. J. Hibble, A. C. Hannon, S. M. Cheyne and S. G. Eversfield, *Inorg. Chem.*, 2002, **41**, 4990.
25. S. J. Hibble, S. M. Cheyne, A. C. Hannon and S. G. Eversfield, *Inorg. Chem.*, 2002, **41**, 1042.
26. S. J. Hibble, A. C. Hannon and S. M. Cheyne, *Inorg. Chem.*, 2003, **42**, 4724.
27. G. Heger, H. J. Deiseroth and H. Schulz, *Acta Cryst. B*, 1978, **34**, 725.
28. T. Proffen and R. B. Neder, *J. Appl. Crystallogr.*, 1997, **30**, 171.
29. G. J. Kubas and L. H. Jones, *Inorg. Chem.*, 1974, **13**, 2816.
30. L. Soptrajanova, B. Soptrajanov and G. Jovanovski, *J. Mol. Struc.*, 1986, **142**, 63.
31. Y. Y. Kharitonov, O. N. Evstafeva, I. B. Baranovskii and G. Y. Mazo, *Russ. J. Inorg. Chem.*, 1969, **14**, 248.
32. M. Penavic, *Acta Cryst. C*, 1986, **42**, 1283.
33. J. B. Darby and K. M. Myles, *Metall. Trans.*, 1972, **3**, 653.

Appendices

A.1 The Crystal Structure of $[Ag(NH_3)_2][AgCu_3(CN)_5]$

A suitable crystal was mounted on a glass fibre using Superglue and slowly cooled to 150 K. The structure was solved by direct methods using the program SIR92[1] and least-squares refinement carried out within CRYSTALS[2]. All the C≡N groups in the framework are ordered as verified by refinement and all hydrogen atoms of the ammonia groups were located in difference Fourier maps. Their coordinates were refined with distance and angle restraints applied (N-H distances restrained to be 0.850(5) Å).

Table A.1 Crystallographic details for $[Ag(NH_3)_2][AgCu_3(CN)_5]$

Formula	$[Ag(NH_3)_2][AgCu_3(CN)_5]$
Crystal Colour	Colourless rod
Crystal System, space group	Monoclinic, $P2_1/n$
a/Å	7.9266 (2)
b/Å	12.7620 (3)
c/Å	12.1104 (3)
α/°	90
β/°	97.460(3)
γ/°	90
V/Å^3	1214.71
T/K	150 slow cooled
R, R_w	0.0239, 0.0255

The local structure is shown in Figure A1.1. There are three crystallographically distinct Cu(I) atoms, all of which are bonded to three CN groups in approximately trigonal planar coordination. There are two distinct

Ag(I) atoms. One of the Ag atoms Ag(2), is coordinated to two NH_3 groups to form a linear cation, $[Ag(NH_3)_2]^+$. The second, Ag(1) has rather unusual $\mu_{1,2,2}$ coordination in that it is bonded at a normal distance to one CN group, (Ag(1)-C(1) = 2.073(3) Å, and also interacts with the C atoms of two more distant CN groups, Ag(1) - C(2) = 2.549(3) Å and Ag(1) - C(4) = 2.495(3) Å. Overall, these units pack together to form layers of formula $[AgCu_3(CN)_5]^-$ (Figure A1.2). The layers stack along the *a* axis in pairs, held together by the $[Ag(NH_3)_2]^+$ units, which are located in rings within the layers bounded by 5 metal atoms (Figure A1.3).

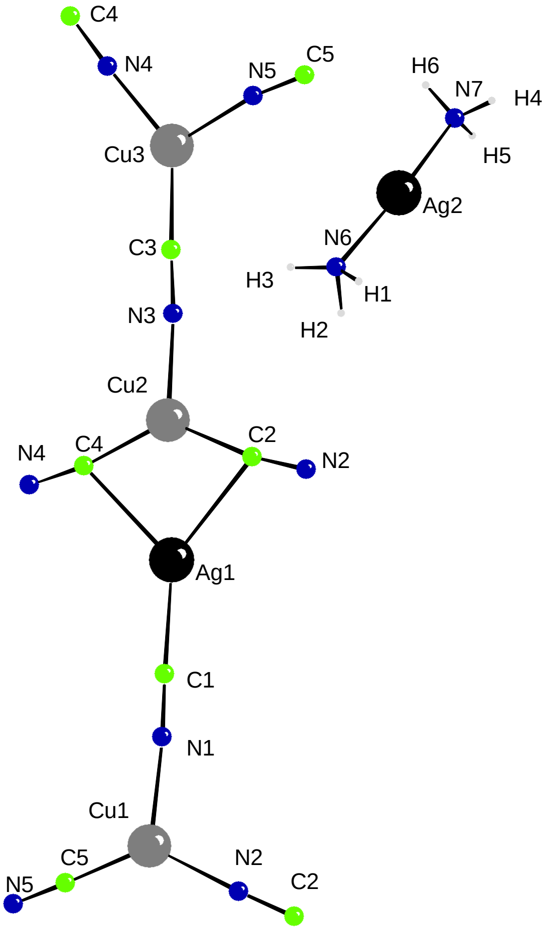

Figure A1.1 The local structure and numbering scheme for $[Ag(NH_3)_2][AgCu_3(CN)_5]$

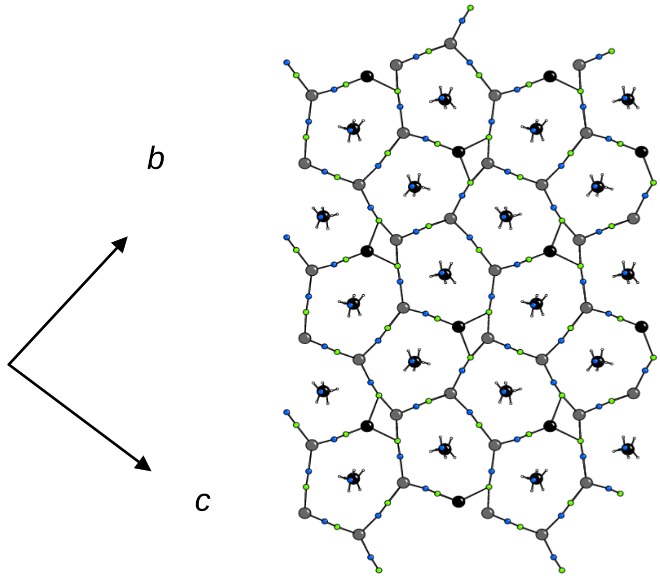

Figure A1.2: View along the a axis of a single layer showing the linear $[NH_3\text{-}Ag\text{-}NH_3]^+$ *cations lying in the rings formed by linking of Cu-Ag-CN units into layers of formula (Key copper (grey), silver (black), carbon (green), nitrogen (blue))*

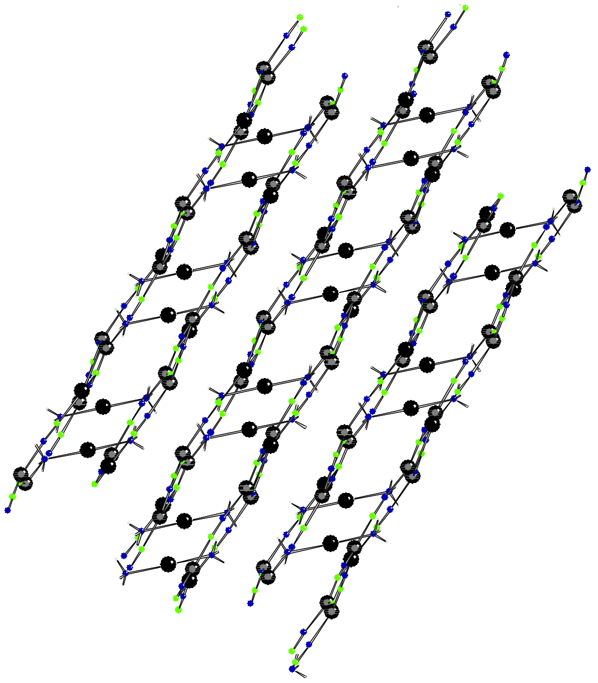

Figure A1.3: View along the b axis showing how pairs of layers are linked together by the $[NH_3\text{-}Ag\text{-}NH_3]^+$ *cations.* (Key copper (grey), silver (black), carbon (green), nitrogen (blue))

Table A.2 Selected bond lengths (Å) and angles (°) in $[Ag(NH_3)_2][AgCu_3(CN)_5]$

Ag(1) - C(1)	2.073(3)	N(6) - Ag(2) - N(7)	175.78(12)
Ag(1) - C(2)	2.549(3)	N(1) - Cu(1) - N(2)	109.88(11)
Ag(1) - C(4)	2.495(3)	N(1) - Cu(1) - C(5)	115.22(12)
Ag(2) - N(6)	2.137(3)	N(2) - Cu(1) - C(5)	133.78(12)
Ag(2) - N(7)	2.138(3)	N(3) - Cu(2) - C(2)	111.73(12)
Cu(1) - N(1)	1.984(3)	N(3) - Cu(2) - C(4)	113.50(12)
Cu(1) - N(2)	1.928(3)	C(2) - Cu(2) - C(4)	134.63(12)
Cu(1) - C(5)	1.886(3)	N(4) - Cu(3) - N(5)	104.40(11)
Cu(2) - N(3)	1.948(3)	N(4) - Cu(3) - C(3)	137.55(12)
Cu(2) - C(2)	1.927(3)	N(5) - Cu(3) - C(3)	117.78(12)
Cu(2) - C(4)	1.930(3)	Cu(1) - N(1) - C(1)	172.8(3)
Cu(3) - N(4)	1.936(3)	Cu(1) - N(2) - C(2)	174.3(3)
Cu(3) - N(5)	1.967(3)	Cu(2) - N(3) - C(3)	174.1(3)
Cu(3) - C(3)	1.884(3)	Cu(3) - N(4) - C(4)	174.8(3)
N(1) - C(1)	1.156(4)	Cu(3) - N(5) - C(5)	171.3(3)
N(2) - C(2)	1.153(4)	Ag(1) - C(1) - N(1)	178.2(3)
N(3) - C(3)	1.152(4)	Ag(1) - C(2) - N(2)	121.6(2)
N(4) - C(4)	1.154(4)	Cu(2) - C(2) - N(2)	171.1(3)
N(5) - C(5)	1.158(4)	Cu(3) - C(3) - N(3)	175.7(3)
C(1) - Ag(1) - C(2)	135.82(11)	Ag(1) - C(4) - N(4)	119.6(2)
C(1) - Ag(1) - C(4)	132.64(11)	Cu(2) - C(4) - N(4)	171.5(3)
C(2) - Ag(1) - C(4)	89.8(1)	Cu(1) - C(5) - N(5)	178.0(3)

A.2 The Crystal Structure of [$Ag_4Cu(CN)_5(NH_3)_3$]

A suitable crystal was mounted on a loop using polyfluoroether oil and flash cooled to 150 K. The structure was solved by direct methods using the program SIR92[1] and least-squares refinement carried out within CRYSTALS[2]. All the C≡N groups in the framework are ordered as verified by refinement and all hydrogen atoms of the ammonia groups were located in difference Fourier maps. Their coordinates were refined with distance and angle restraints applied (N-H distances restrained to be 0.850(5) Å).

Table A.3 Crystallographic details for [$Ag_4Cu(CN)_5(NH_3)_3$]

Formula	[$Ag_4Cu(CN)_5(NH_3)_3$]
Crystal Colour	Colourless plate
Crystal System, space group, *Z*	Triclinic, *P*-1, 2
a/Å	6.9039 (5)
b/Å	7.1336 (7)
c/Å	14.5273 (14)
α/°	92.011 (8)
β/°	97.466 (7)
γ/°	95.150 (7)
V/Å^3	705.75
T/K	150
R, R$_w$	0.0270, 0.0355

The asymmetric unit, consisting of a molecule of approximately C_{3v} symmetry, is shown in Figure A2.1. There are four crystallographically distinct Ag(I) atoms, all of which have linear coordination. One of the Ag atoms is bonded to two C≡N groups and the other three are bonded to a

C≡N group and an ammonia molecule. The central atom, Cu(1), has tetrahedral coordination. The molecules pack as shown in Figure A2.2 with hydrogen bonds between the nitrogen atom of Ag(4)-C(5)N(5) groups and ammonia groups in neighbouring molecules (in the range 3.019(1) to 3.376(1) Å) serving to hold the structure together.

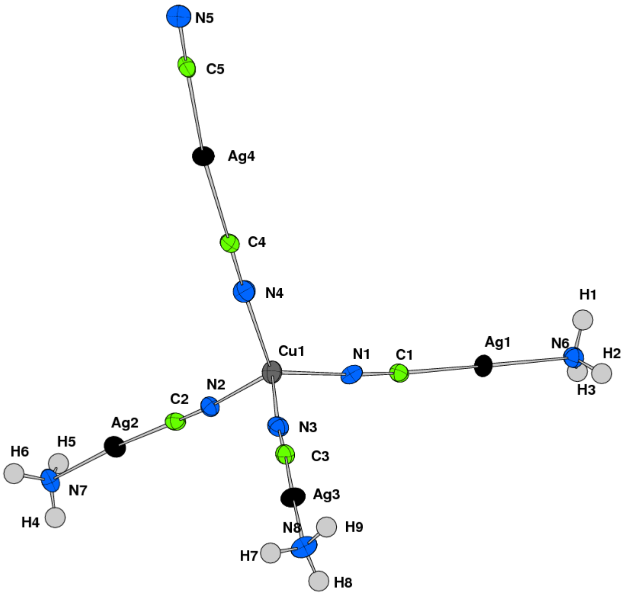

Figure A2.1 The asymmetric unit and numbering scheme for $[Ag_4Cu(CN)_5(NH_3)_3]$ (Key copper (grey), carbon (green), nitrogen (blue))

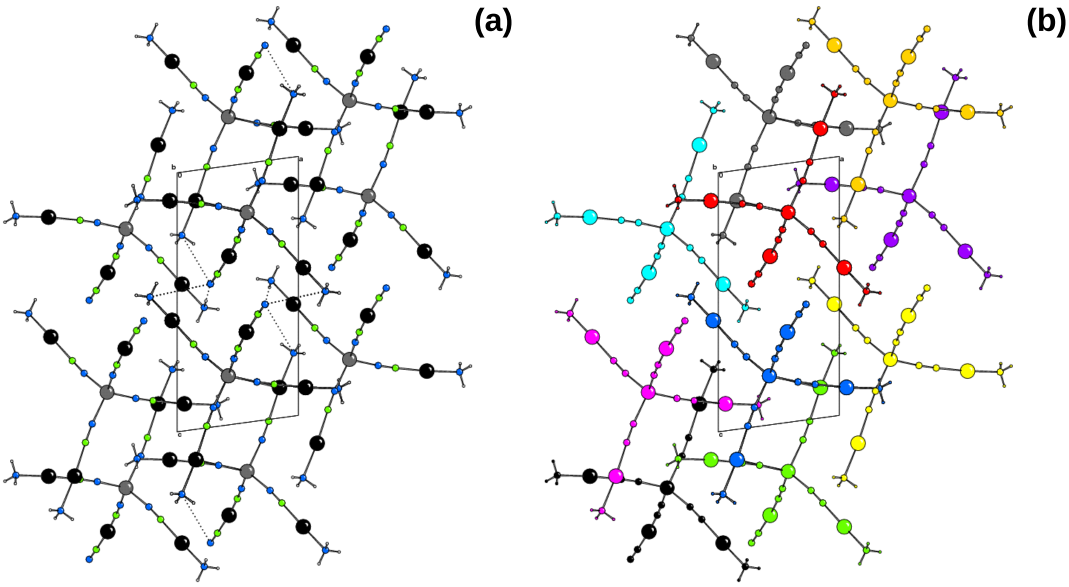

Figure A2.2 View along the b axis showing the packing of [Ag$_4$Cu(CN)$_5$(NH$_3$)$_3$] molecules. (a) (Key copper (grey), carbon (green), nitrogen (blue)) *The dotted lines correspond to hydrogen bonding interactions between N(5) of the Ag(4)-C(5)N(5) group and ammonia groups in neighbouring molecules. (b) Each tetrahedron has been colourer separately to emphasis the packing.*

Table A.4 Selected bond lengths (Å) and angles (°) in [Ag$_4$Cu(CN)$_5$(NH$_3$)$_3$]

Ag(1) - C(1)	2.054(4)	N(6) - Ag(1) - C(1)	176.48(17)
Ag(1) - N(6)	2.145(4)	N(7) - Ag(2) - C(2)	174.81(16)
Ag(2) - C(2)	2.061(4)	N(8) - Ag(3) - C(3)	176.30(16)
Ag(2) - N(7)	2.154(4)	C(4) - Ag(4) - C(5)	173.81(17)
Ag(3) - C(3)	2.041(5)	N(1) - Cu(1) - N(2)	107.63(16)
Ag(3) - N(8)	2.132(4)	N(1) - Cu(1) - N(3)	107.29(16)
Ag(4) - C(4)	2.067(4)	N(2) - Cu(1) - N(3)	108.50(16)
Ag(4) - C(5)	2.067(5)	N(1) - Cu(1) - N(4)	115.83(16)
Cu(1) - N(1)	1.991(4)	N(2) - Cu(1) - N(4)	108.46(17)
Cu(1) - N(2)	2.006(4)	N(3) - Cu(1) - N(4)	108.93(16)
Cu(1) - N(3)	2.013(4)	Cu(1) - N(1) - C(1)	176.2(4)
Cu(1) - N(4)	1.978(4)	Cu(1) - N(2) - C(2)	173.5(4)
N(1) - C(1)	1.162(6)	Cu(1) - N(3) - C(3)	173.9(4)
N(2) - C(2)	1.150(6)	Cu(1) - N(4) - C(4)	177.7(4)

N(3) - C(3)	1.159(6)	Ag(1) - C(1) - N(1)	176.9(4)
N(4) - C(4)	1.161(6)	Ag(2) - C(2) - N(2)	178.2(4)
N(5) - C(5)	1.157(6)	Ag(3) - C(3) - N(3)	174.8(4)
		Ag(4) - C(4) - N(4)	176.8(4)
		Ag(4) - C(5) - N(5)	178.2(4)

A.3 The Crystal Structure of $Cu(NH_3)_4[Au(CN)_2]$

A suitable crystal was mounted on a glass fibre using Superglue and flash cooled to 150 K. The structure was solved by direct methods using the program SIR92[1] and least-squares refinement carried out within CRYSTALS[2]. The C(4)≡N(4) group in the framework and the terminal C≡N groups around Au(1) are ordered as verified by refinement and all hydrogen atoms of the ammonia groups were located in difference Fourier maps. Their coordinates were refined with distance and angle restraints applied (N-H distances restrained to be 0.850(5) Å and H-N-H angles 109(5)°).

Table A.5 Crystallographic details for $Cu[Ag(CN)_2][(NC)Ag(NH_3)]_3$

Formula	$[Au(NH_3)_4][Cu_2(CN)_4]$
Crystal Colour	Blue block
Crystal System, space group	Orthorhombic, $P2_1/n$
a/Å	7.2283 (15)
b/Å	9.9066 (15)
c/Å	8.8785 (3)
V/Å^3	635.76
T/K	150
R, R_w	0.0383, 0.0432

The local structure is shown in Figure A3.1. There are two crystallographically distinct Cu atoms. Cu(1), in oxidation state I and with trigonal planar coordination, is connected to three C≡N groups, one of which is ordered, C(4)≡N(4), and two equivalent ones which show head-to-tail disorder by symmetry, C(3)≡N(3). Cu(2), in oxidation state II, is approximately square pyramidal, being coordinated to N(4) of the ordered cyanide group and four equivalent ammonia molecules. There is also one

Au(I) atom coordinated to two C≡N groups to form a linear cation, $[Au(CN)_2]^-$.

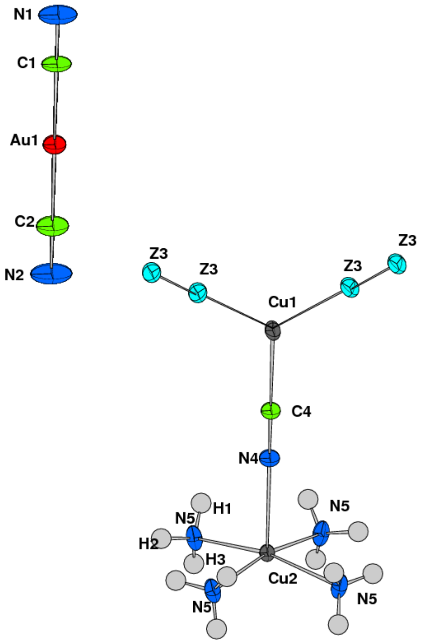

Figure A3.1 The local structure and numbering scheme for $[Au(NH_3)_4][Cu_2(CN)_4]$. Note Z(3)≡Z(3) corresponds to a fully disordered cyanide group i.e. each Z(3) site is occupied by 50% C(3) and 50% N(3).

The extended structure consists of Cu(1)CN chains, with pendant $Cu(2)(NC)(NH_3)_4$ groups, which run parallel to the *c* axis (Figure A3.2) These chains pack together with $[Au(CN)_2]^-$ units lying parallel to the *b* axis between adjacent chains (Figure A3.3 and A3.4).

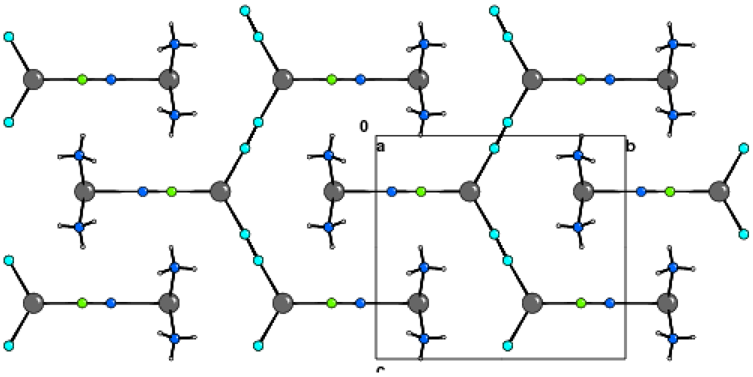

Figure A3.2 View along the a axis showing zigzag chains of Cu(1)CN with pendant Cu(2)(NC)(NH$_3$)$_4$ groups. The linear [NC-Au-CN]$^-$ anions have been omitted. (Key copper (grey), carbon (green), nitrogen (blue) and disordered carbon / nitrogen (cyan).

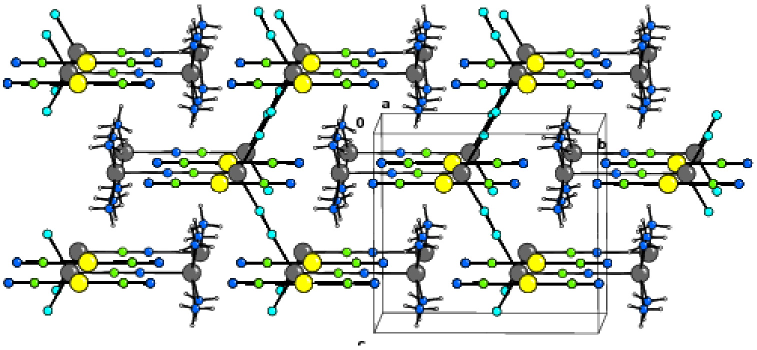

Figure A3.3 View along the a axis showing zigzag chains of Cu(1)CN with pendant Cu(2)(CN)(NH$_3$)$_4$ groups and the linear [NC-Au-CN]$^-$ anions. (Key copper (grey), gold (yellow), carbon (green), nitrogen (blue) and disordered carbon / nitrogen (cyan).

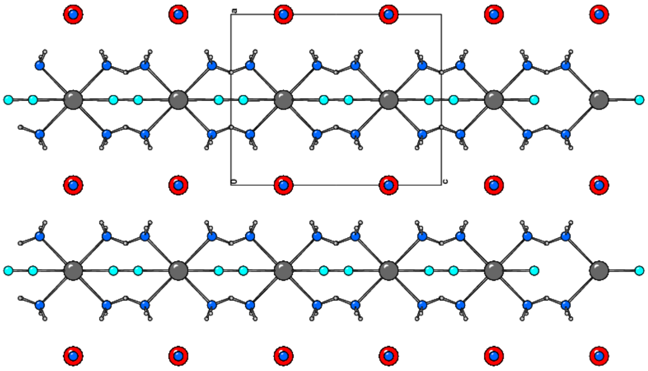

Figure A3.4 View along the b axis showing the location of the [NC-Au-CN]$^-$ anions between the layers. (Key copper (grey), gold (red), nitrogen (blue) and disordered *carbon / nitrogen (cyan*).

Table A.6 Selected bond lengths (Å) and angles (°) in [Au(NH$_3$)$_4$][Cu$_2$(CN)$_4$]

Au(1) - C(1)	1.948(9)	C(1) - Au(1) - C(2)	180
Au(1) - C(2)	1.971(11)	Au(1) - C(1) - N(1)	180
Cu(1) - Z(3)	1.961(7)	Au(1) - C(2) - N(2)	180
Cu(1) - C(4)	1.938(9)	Z(3) - Cu(1) - Z(3)’	120.1(4)
Cu(2) - N(4)	2.291(9)	Z(3) - Cu(1) - C(4)	119.96(19)
Cu(2) - N(5)	2.043(4)	N(4) - Cu(2) - N(5)	96.27(13)
Cu(2) - C(4)	1.930(3)	N(5) - Cu(2) - N(5)’	91.0(2)
Cu(3) - N(4)	1.936(3)	N(5) - Cu(2) - N(5)’’	167.5(3)
Cu(3) - N(5)	1.967(3)	N(5)’ - Cu(2) - N(5)’’	87.7(2)
Cu(3) - C(3)	1.884(3)	Cu(1) - Z(3) - Z(3)’	177.0(8)
N(1) - C(1)	1.190(14)	Cu(1) - N(4) - C(4)	180
N(2) - C(2)	1.151(16)	Cu(2) - C(4) - N(4)	180
Z(3) - Z(3)	1.169(13)		
N(4) - C(4)	1.148(13)		
N(5) - C(5)	1.169(13)		

A.4 The Crystal Structure of $(NH_4)_2Pt(CN)_4{\cdot}2H_2O$

Although a number of structures of hydrates of alkali metal tetracyanoplatinates, $K_2Pt(CN)_4.nH_2O$ (n = 3,[3] 1[4] and 0[4]), $Rb_2Pt(CN)_4{\cdot}nH_2O$ (n = 1.5,[5] 1[6] and 0[7]) and $Cs_2Pt(CN)_4{\cdot}H_2O$[8] have been reported previously, there are no structural reports of any ammonium analogues.

Diammonium tetracyanoplatinate dihydrate was prepared as described in Chapter 5, section 5.8.2 by mixing aqueous solutions of $BaPt(CN)_{4(aq)}$ and $(NH_4)_2SO_{4(aq)}$ at room temperature. After the immediate precipitate, $BaSO_4$, was filtered off a small portion of the remaining solution was removed and allowed to slowly evaporate at room temperature over the course of 4-6 weeks to produce bright yellow crystals of composition $(NH_4)_2Pt(CN)_4{\cdot}2H_2O$. Weight lost from 20 - 120 ˚C under flowing nitrogen corresponding to 1.8 H_2O. (2.080 mg to 1.899 mg, small sample)
(IR data: v(OH) 3420(w) 3198(w); v(NH) 3026(w) 2833(w); v(CN) 2119(s), 2083(sh, w); $\delta(OH_2)$ 1625(m); δ (NH_4^+) 1428(s), 1400(s); 1083; v(Pt-C) 613(sh, w) cm^{-1}).

A suitable crystal was mounted on a loop using perfluoroether and flash cooled to 150 K. The structure was solved by direct methods by Dr Ann Chippindale using the program SIR92 and least-squares refinement carried out within CRYSTALS. All hydrogen atoms were located in difference Fourier maps. Their coordinates were refined with distance and angle restraints applied (O-H and N-H distances restrained to be 0.850(5) and H-

O-H and H-N-H angles to be 109(5)°). The Flack parameter was refined to a value of 0.48(2), indicating that the crystal is a racemic twin.

Table A.7 Table Crystallographic details for $(NH_4)_2Pt(CN)_4{\cdot}2H_2O$

Formula	$(NH_4)_2Pt(CN)_4.2H_2O$
Crystal Colour	Yellow block
Crystal System, space group	Orthorhombic, $Pna2_1$
a / Å	6.5019(3)
a / Å	14.5080(4)
c/ Å	11.0697(4)
V / Å^3	1044.21(6)
T / K	150 (flash cooled)
R, R_w	0.0197, 0.0272

The asymmetric unit is shown in Figure A4.1 and consists of a $Pt(CN)_4^{2-}$ ion with two crystallographically distinct NH_4^+ as counterions and two water molecules.

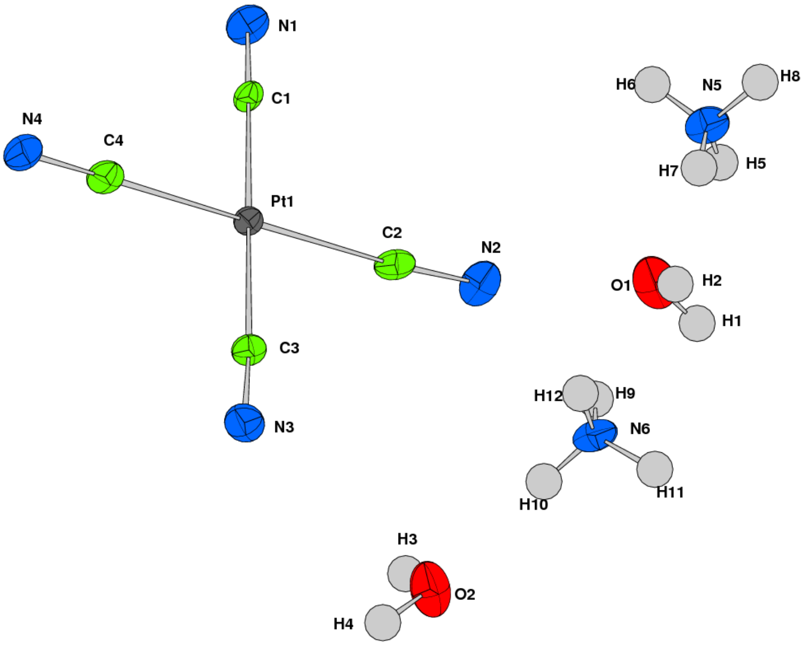

Figure A4.1 The asymmetric unit of $(NH_4)_2Pt(CN)_4{\cdot}2H_2O$.

Table A.8 Bond Lengths (Å) and Angles (°) in $(NH_4)_2Pt(CN)_4{\cdot}2H_2O$

Pt(1) - Pt(1)	3.25180(13)	C(1) - Pt(1) - C(2)	89.7(3)
Pt(1) - C(1)	1.965(10)	C(1) - Pt(1) - C(3)	179.4(2)
Pt(1) - C(2)	2.005(7)	C(2) - Pt(1) - C(3)	89.9(4)
Pt(1) - C(3)	2.017(10)	C(1) - Pt(1) - C(4)	90.8(4)
Pt(1) - C(4)	1.982(7)	C(2) - Pt(1) - C(4)	178.8(3)
N(1) - C(1)	1.146(8)	C(3) - Pt(1) - C(4)	89.6(3)
N(2) - C(2)	1.154(8)	Pt(1) - C(1) - N(1)	178.9(4)
N(3) - C(3)	1.150(8)	Pt(1) - C(2) - N(2)	175.9(6)
N(4) - C(4)	1.151(8)	Pt(1) - C(3) - N(3)	177.1(5)
		Pt(1) - C(4) - N(4)	178.0(6)

The $Pt(CN)_4^{2-}$ ion is square-planar as expected for Pt^{2+} (d^8) species. The bond lengths and angles (Table A.8) show that the ion is almost regular although not required to be so by symmetry. The $Pt(CN)_4^{2-}$ ions stack on top of each other along the *a* axis (Figure A4.2) in a staggered manner to form chains in which the Pt…Pt distance is 3.252(1) Å, rather shorter than the distances of 3.478(1) and 3.421(2) Å observed in $K_2Pt(CN)_4{\cdot}3H_2O$[3] and $Rb_2Pt(CN)_4.1.5\ H_2O$,[5] respectively, which contain similar stacked chains. The torsion angle C-Pt…Pt-C between neighbouring $Pt(CN)_4^{2-}$ units is ~41°.

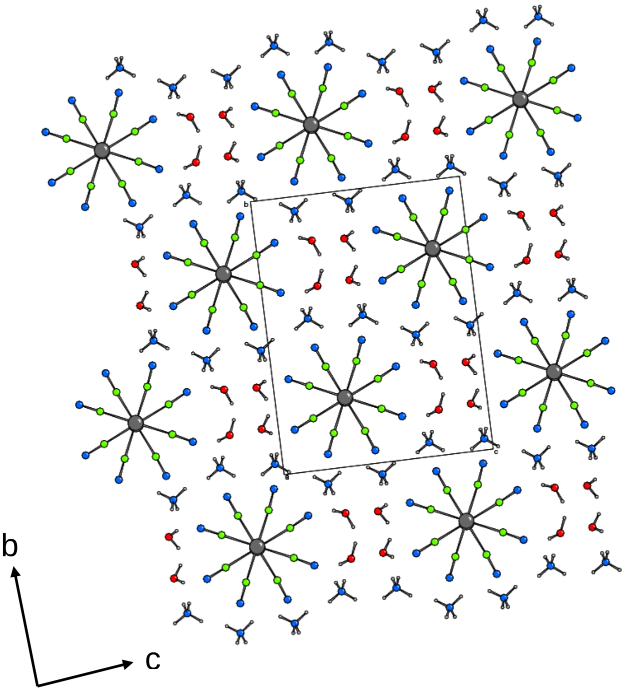

Figure A4.2 View along the a axis showing the stacking of the $Pt(CN)_4^{2-}$ ions in a staggered manner. (Key: platinum (grey), carbon (green), nitrogen (blue), oxygen (red) and hydrogen (white)).

The chains then pack along *a* as shown in Figure A4. with ammonium ions and water molecules between neighbouring chains. A network of hydrogen bonds involving cyanide groups, water molecules and ammonium ions serves to hold the structure together (Figure A4.4).

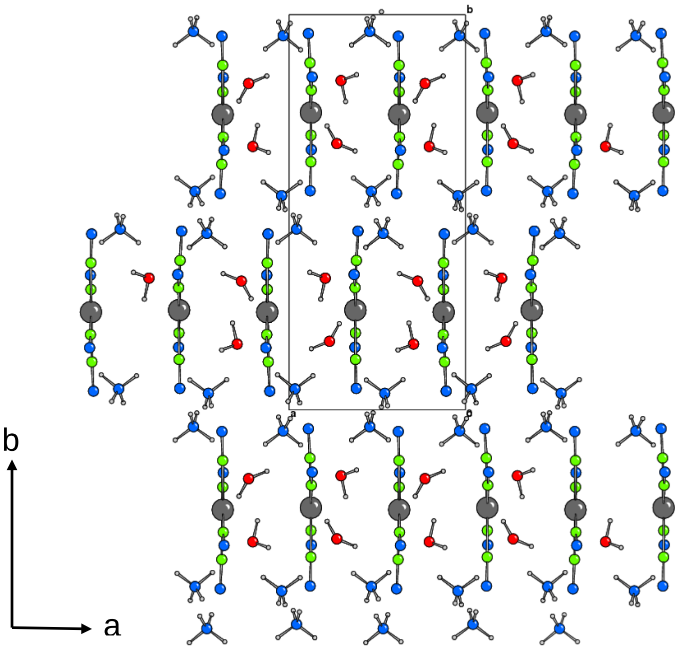

Figure A4.3 View along the c axis showing how the chains of Pt(CN)$_4^{2-}$ ions pack together. Key: platinum (grey), carbon (green), nitrogen (blue), oxygen (red) and hydrogen (white).

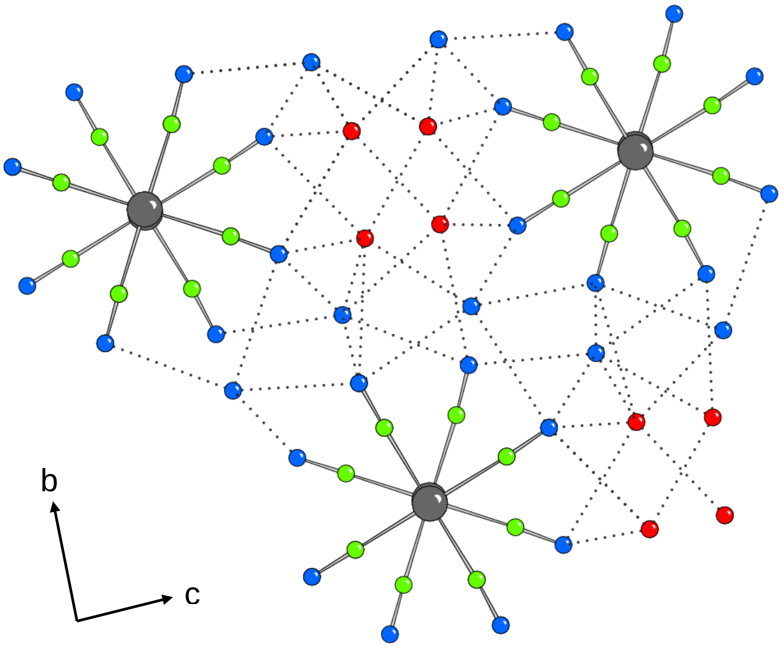

Figure A4.4 Hydrogen bonding interactions shown as dotted lines between CN groups, ammonium ions and water molecules. All distances shown as dotted lines are shorter than 3.4 Å. Key: platinum (grey), carbon (green), nitrogen (blue) and oxygen (red). The hydrogen atoms have been excluded for clarity.

References

1. A. Altomare, G. Cascarano, C. Giacovazzo, A. Guagliardi, M. C. Burla, G. Polidori and M. Camalli, *J. Appl. Cryst.*, 1994, **27**, 435.
2. D. J. Watkin, C. K. Prout and L. J. Pearce, Chemical Crystallography Laboratory, University of Oxford, Oxford, Editon edn., 1996.
3. D. M. Washecheck, S. W. Peterson, A. H. Reis and J. M. Williams, *Inorganic Chemisty*, 1976, **15**, 74-78.
4. C. Mühle, J. Nuss, R. E. Dinnebier and M. Jansen, *Z. Anorg. Allg. Chem*, 2004, **630**, 1462-1468.
5. T. R. Koch, P. L. Johnson and J. M. Williams, *Inorg. Chem.*, 1977, **16**, 640-645.
6. L. Dupont, *Bull. Soc. Royale des Sciences de Liege*, 1967, **36**, 40.
7. C. Muehle, A. Karpov and M. Jansen, *Zeitschrift fuer Naturforschung*, 2009, **B60**, 1269 - 1272.
8. P. L. Johnson, T. R. Koch and J. M. Williams, *Acta Cryst.*, 1977, **B33**, 1293-1295.
9. A. C. Hannon, in *Encyclopedia of Spectroscopy and Spectrometry*, eds. J. Lindon, G. Tranter and J. Holmes, Academic Press, London, Editon edn., 2000, vol. 2, pp. 1493-1503.

A.5 Proof for $1.2(T(r)^{\text{chain}}) = T(r)^{\text{layer}}$

Alex Hannon's proof that 1.2(1D chain) = (2D sheet) as sent to me in "Correlations for 1D chains in 2D layers.doc" 6-7-09.

Separating correlations for 1D chains from 2D layers.

Background

Edd Bilbé has been broadening the correlations in a layer differently, depending on whether the atom pair are in a chain or not. He has done this by hand satisfactorily (i.e. by manually identifying which distances are in a chain and giving each of them the smaller broadening width). However, when he tried to do this in a more automated way, by using XTAL to calculate *T(r)* for both chain and layer, he found that *T(r)* for the chain was not consistent with *T(r)* for the layer. This is not because there is anything wrong with XTAL, but because the situation is a little more subtle.

Derivation of Results

The situation is more subtle because (considering $Pt(CN)_2$) each CN is in one chain, whereas each Pt is in two chains. The basic problem is that when Edd calculates the correlation function, $T^{1D}(r)$, for the chain, it does not predict the correct area for the chain peaks in the correlation function, $T^{2D}(r)$, for the layer.

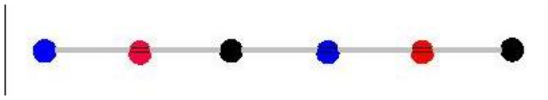

Figure A5.1 1D Chain

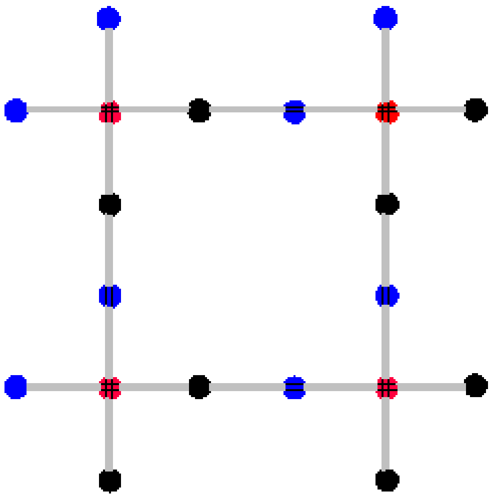

Figure A5.2 2D Layer (red=Pt, black=C, blue=N)

In order to work out how to solve this problem, we first need to express the total correlation function, *T(r)*, for each model in terms of its partial correlation functions. Considering the structure to be head-tail disordered (this is just done to reduce the number of atom types so that the number of terms in the equations is reduced), the correlation function of Pt cyanide is given by [9]…

$$T(r) = c_{\mathrm{Pt}} \bar{b}_{\mathrm{Pt}}^{2} t_{\mathrm{Pt\text{-}Pt}}(r) + c_{\mathrm{C/N}} \bar{b}_{\mathrm{C/N}}^{2} t_{\mathrm{C/N\text{-}C/N}}(r) + 2 c_{\mathrm{Pt}} \bar{b}_{\mathrm{Pt}} \bar{b}_{\mathrm{C/N}} t_{\mathrm{Pt\text{-}C/N}}(r), \tag{1}$$

where C/N means carbon and nitrogen, c_j is the atomic fraction of element *j*, and $t_{jk}(r)$ is the partial correlation function for the atom pair *j-k*. This equation is correct for either the layer or the chain.

The layer has composition $\mathrm{Pt(CN)_2}$ (i.e. c_{Pt}=0.2, $c_{\mathrm{C/N}}$=0.8), so that its correlation function is given by…

$$T^{\mathrm{2D}}(r) = 0.2 \bar{b}_{\mathrm{Pt}}^{2} t_{\mathrm{Pt\text{-}Pt}}^{\mathrm{2D}}(r) + 0.8 \bar{b}_{\mathrm{C/N}}^{2} t_{\mathrm{C/N\text{-}C/N}}^{\mathrm{2D}}(r) + 0.4 \bar{b}_{\mathrm{Pt}} \bar{b}_{\mathrm{C/N}} t_{\mathrm{Pt\text{-}C/N}}^{\mathrm{2D}}(r). \tag{2}$$

The chain has composition PtCN (i.e. c_{Pt}=0.333, $c_{\mathrm{C/N}}$=0.667), so that its correlation function is given by…

$$T^{\mathrm{1D}}(r) = 0.333 \bar{b}_{\mathrm{Pt}}^{2} t_{\mathrm{Pt\text{-}Pt}}^{\mathrm{1D}}(r) + 0.667 \bar{b}_{\mathrm{C/N}}^{2} t_{\mathrm{C/N\text{-}C/N}}^{\mathrm{1D}}(r) + 0.667 \bar{b}_{\mathrm{Pt}} \bar{b}_{\mathrm{C/N}} t_{\mathrm{Pt\text{-}C/N}}^{\mathrm{1D}}(r). \tag{3}$$

Now we need to consider the partial correlation functions, because this is easy to think about in terms of the structural models.

First consider the 1D chain. At each interatomic distance an atom has 2 neighbors. i.e. at each of the distances that occurs between atoms, the coordination number is 2. That is to say, the area under each peak of a chain partial correlation function, $t^{\mathrm{1D}}_{j-k}(r)$, gives a coordination number of 2.

Second consider a 2D layer. We are only considering the contributions to the 2D layer correlation function which arise from interatomic distances between two atoms which are in the same chain as each other; we will denote these contributions by ‘2D,chain’. Each C or N is in one chain, and so for each interatomic distance starting from a C or N the coordination number is 2, the same as for the chain. i.e. the area under each peak of a C/N-centered partial correlation function, $t^{\mathrm{2D,chain}}_{\mathrm{C/N}-k}(r)$, gives a coordination number of 2. However, the situation is different for a Pt; for each interatomic distance starting from a Pt there is a coordination number of 4. . i.e. the area under each peak of a Pt-centered partial correlation function, $t^{\mathrm{2D,chain}}_{\mathrm{Pt}-k}(r)$, gives a coordination number of 4.

Using these considerations of the coordination numbers, we can deduce the relations between the partial correlation functions of the chain and the layer;

$$t^{\mathrm{2D,chain}}_{\mathrm{C/N}-k}(r) = t^{\mathrm{1D}}_{\mathrm{C/N}-k}(r), \tag{4}$$

$$t^{\mathrm{2D,chain}}_{\mathrm{Pt}-k}(r) = 2t^{\mathrm{1D}}_{\mathrm{Pt}-k}(r). \tag{5}$$

The chain contribution to the total correlation function of the 2D layer can then be evaluated by using these relations in Eq.(2)…

$$T^{\mathrm{2D,chain}}(r) = 0.4\bar{b}^2_{\mathrm{Pt}} t^{\mathrm{1D}}_{\mathrm{Pt\text{-}Pt}}(r) + 0.8\bar{b}^2_{\mathrm{C/N}} t^{\mathrm{1D}}_{\mathrm{C/N\text{-}C/N}}(r) + 0.8\bar{b}_{\mathrm{Pt}}\bar{b}_{\mathrm{C/N}} t^{\mathrm{1D}}_{\mathrm{Pt\text{-}C/N}}(r). \tag{6}$$

It surprised me to find this, but the right hand side of Eq.(6) is in proportion to the right hand side of Eq.(3). Therefore

$$T^{2\mathrm{D,chain}}(r) = 1.2T^{1\mathrm{D}}(r) \tag{7}$$

Since this result is surprising, it should be checked.

“I had predicted that the scaling factor would be 1.2 by looking at the peak areas for the C-N and M-C/N correlations in both the chain model after scaling and the full sheet model. After subtracting the chain correlations scaled by 1.2 from the correlations from the model sheet, no negative peaks are observed in the resulting correlation function, which would be a sign that there was a problem with the calculation.”